UNSATURATED SOIL BEHAVIOR UNDER MONOTONIC AND CYCLIC STRESS STATES

A Dissertation

by

BYOUNG-JAE MUN

Submitted to the Office of Graduate Studies of
Texas A&M University
in partial fulfillment of the requirements for the degree of

DOCTOR OF PHILOSOPHY

December 2004

Major Subject: Civil Engineering

UNSATURATED SOIL BEHAVIOR UNDER MONOTONIC AND CYCLIC STRESS STATES

A Dissertation

by

BYOUNG-JAE MUN

Submitted to Texas A&M University
in partial fulfillment of the requirements
for the degree of

DOCTOR OF PHILOSOPHY

Approved as to style and content by:

Robert L. Lytton (Chair of Committee)	James D. Murff (Member)
Charles P. Aubeny (Member)	Christopher C. Mathewson (Member)

Paul Roschke
(Head of Department)

December 2004

Major Subject: Civil Engineering

ABSTRACT

Unsaturated Soil Behavior under Monotonic and Cyclic Stress States. (December 2004)
Byoung-Jae Mun, B.Eng., Chung-Ang University;
M.Eng., Texas A&M University
Chair of Advisory Committee: Dr. Robert L. Lytton

The objectives of this dissertation are to measure and calculate surface free energies of soil particles, to understand the mechanical behavior of unsaturated silty sand through first studying the stress-strain relationship, the effects of matric suction and pore water chemistry and second to interpret the behavior by the critical state frame work, to develop a method to predict cone tip resistance in unsaturated soils, and to present the concept of pseudo strain and dissipated pseudo strain energy.

Universal Sorption Device (USD) is developed to measure surface free energies of soil particles. The test results on a soil sample shows that specific surface area increased with decreasing particle size. The components of surface free energies and the work of adhesion increased with decreasing particle size.

A servo controlled triaxial testing device is developed to test 15.24 cm in height and 7.62 cm in diameter, recompacted specimens of unsaturated soil under varying matric suction and different pore chemistry. During the test, the matric suction is maintained constant. Results from the triaxial drained tests are used for validation of the constitutive models proposed by Alonso et al. (1990). Predictions from the model are in good agreement with experimental results.

The critical state model for unsaturated soil is used to calculate cone tip resistance in unsaturated silty sand. The calculated cone tip resistance is used to evaluate the liquefaction potential of unsaturated soils. The results from the stress based liquefaction potential analysis reveal that even in an unsaturated condition soil is susceptible to liquefaction.

By applying the pseudo strain concept, it is possible to account for the viscous resistance of water during cyclic loading. The results of undrained cyclic triaxial tests are used to calculate pseudo-strain and dissipated pseudo strain energy. The results of calculated dissipated pseudo strain energy suggest that the effect of initial matric suction is evident. On the other hand, the effect of surface tension increase or decrease due to existence of chemical on the pore water is negligible.

ACKNOWLEDGMENTS

This research was sponsored by the National Science Foundation (NSF) and its support is gratefully acknowledged.

First of all, I would like to express my deep gratitude and appreciation to my advisor, Dr. Robert L. Lytton, whose guidance, patience, and encouragement over the past three years have been invaluable, especially in those periods when I doubted successful completion of this research; but above all, for his extraordinary positiveness.

My appreciation is extended to Dr. Charles Aubeny for his constant help and advice on this research and teaching efforts during my stay at Texas A&M University.

I am deeply indebted to Dr. James D. Murff for his teaching efforts. His discipline, knowledge, creativeness, and warmness over the past five years have been an inspiration to me.

I would like to express special thanks to Dr Christopher Mathewson for serving on the advisory committee.

I am grateful to Dr Jayson E. Barfknecht for passing me his knowledge on triaxial apparatus and helping me on the calibration of equipment. I would like to say thank to Dr. Lianxi Ma for providing me USD testing knowledge and test results.

I also would like to thank the Korean students in the Geotechnical Engineering Division for their friendship, in particular those relaxing times. Special thanks to Dr. Seungwoon Han for his friendship and invaluable discussion during my study.

I am extremely grateful to the support, encourage and love offered by my wife, Jinkyung Han. Most importantly, I would like to thank my father and mother, Giljoo Mun and Jeungsook Cho for unconditional love and support throughout all my life.

TABLE OF CONTENTS

Page

LIST OF FIGURES

FIGURE Page

FIGURE Page

FIGURE Page

FIGURE Page

LIST OF TABLES

CHAPTER I
INTRODUCTION

1.1 General

Historically, geotechnical engineers have studied soil and rock materials using concepts from mechanics of solids and fluids. Analytical models were developed and material characteristics evaluated from a macroscale point of view. Shear strength and compressibility were the primary characteristics of interest in soil mechanics and foundation engineering. Order-of-magnitude estimates of permeability also were needed for the analysis of seepage through dams and into excavations. Conventional methods for analyzing slope stability, consolidation, and seepage developed largely from the study of saturated soils, although the behavior of dry granular soil also is fairly well understood.

The reality is that neither saturated nor completely dry condition is correct. A vast portion of the earth's surface is subjected to arid and semi-arid climatic conditions, and as a result, soil is frequently used as an engineering material in an unsaturated condition. Indeed, in most land areas, unsaturated soil conditions are dominant. Despite ample existence of unsaturated soils, unsaturated soil behavior is relatively new area of study, and only in recent years many of the theoretical derivations in this discipline have become thoroughly and readily available to engineers. This fact might be attributed to several difficulties:

1) Generally, unsaturated soil properties are nonlinear functions of pore water pressure
2) Highly negative pore water pressure are difficult to measure
3) Laboratory and field testing for unsaturated soil has proven to be costly, time consuming, and difficult to conduct

---

This dissertation follows the style and format of the *Journal of Geotechnical and Geoenvironmental Engineering.*

4) Unsaturated soil theories have been viewed as relatively complex by most geotechnical practitioners
5) The uncertainty associated with the measurement and/or prediction of unsaturated soil properties has not been addressed in details by researchers.

Lastly, determining of stress state variable also adds to these difficulties. Several pioneering studies, such as that of Bishop and Blight (1963), were directed at quantifying a single effective stress in unsaturated soils. The concept of two independent stress states variables was proposed by Fredlund and Morgenstern (1977). These are, typically, the net normal stress $(\sigma - u_a)$ and matric suction $(u_a - u_w)$; where σ is the total stress, and u_a and u_w are the pore air and pore water pressures, respectively. These independent stress state variables are becoming increasingly accepted in the study of unsaturated soil mechanics practice.

Considerable attention has been paid to developing fundamentals of unsaturated soil mechanics. In recent years, this effort has been mainly directed toward developing models that rationalize the constitutive behavior of unsaturated soil. The proposed models incorporate many of the features of unsaturated soil behavior. However, there is still some room for model enhancements, further elaboration, and inclusion of other features of an unsaturated soil. The present dissertation work was motivated by these research needs. In order to do these, experimental data and their thorough analysis are needed.

1.2 Problem Statement and Research Objectives

In the past four decades, the study of liquefaction has been dealt with assuming saturated soil conditions. It may be true that enough pore pressure will not be generated to reach a liquefaction condition in unsaturated soils. The existence of air in the soil will lead to volume change rather than pore pressure increase since pore air is more highly compressible than pore water during earthquake loading. However, it is a fact that the unsaturated soils undergo significant loss of its strength or large deformations, hence susceptible to earthquake.

In this research, an attempt will be made to increase the knowledge and understanding of the mechanical response of unsaturated soils upon being subjected to different stress states, matric suction and pore-fluid chemistry, in order to facilitate more elaborate analytical solutions in geotechnical problems involving soils with negative pore water pressure. The results of the investigation may enhance the analysis of the liquefaction or cyclic mobility potential of unsaturated soil. In order to accomplish this goal, the results of a number of drained, suction controlled monotonic and undrained suction controlled cyclic triaxial tests on recompacted silty sand (SM) specimens will be used.

Since the effect of surface tension on unsaturated soil is evident, the variation of mechanical response of unsaturated soil due to changes in pore fluid chemistry will be monitored in the triaxial tests set up. Furthermore, the monotonic triaxial compression test results will be interpreted by the critical state framework. An elasto-plastic constitutive relation by Alonso, Gens, and Josa (1990) will be used to evaluate the ability of the model. The reason for this model is that the model is a pioneering work for unsaturated soil and this model can be a starting point for its improvements. In this research, the model is further evaluated by applying the pseudo-strain concept. The use of the pseudo-strain domain enables us to separate the viscoelastic resistance of material behavior. After the validation of the model, it will be used further to evaluate the liquefaction or cyclic mobility potential of the unsaturated soil.

Cyclic triaxial tests will be performed in order to see the effect of cyclic loading. The test data will be used to study the effect of the energy dissipation mechanism. There are two major energy dissipation mechanisms. One is the energy dissipation due to viscous resistance (viscous damping). The other is the energy dissipation due to friction (frictional damping). In this research, energy dissipation due to friction will be analyzed in the pseudo strain domain.

Specific objectives of this research are as follows:

1) Development of a general particle model to verify the effect of surface tension in unsaturated soils.

2) Measurement of surface free energy of soil particles.
3) Determination of the suction level at which unsaturated soil is susceptible to substantial loss of strength due to earthquake loading.
4) Review of previously proposed critical state-based constitutive models for unsaturated soil.
5) Validation of the previously proposed critical state-based constitutive model and application of the pseudo-strain concept to the critical state model for unsaturated soils. Application of the unsaturated constitutive model to predict cone penetration resistance.
6) Application of the dissipated pseudo-strain energy concept to analyze cyclic triaxial tests of unsaturated soils.

1.3 Organization of the Dissertation

Chapter II presents the review the published literature regarding the fundamental aspects of matric suction and capillary forces acting in an unsaturated soil. These will include a review of microscale analysis of unsaturated soil. Also the particle level study of unsaturated soils will be extended to various particle shapes and sizes to see the effects of surface tension of water and pore-water chemistry.

Chapter III illustrates the fact that surface free energy, which reflects physical-chemical surface characteristics of water and soil particles, has a good potential to be utilized in unsaturated soil mechanics. Surface free energy of soil particles will be measured by using the Universal Sorption Device (USD) method, which can accommodate peculiar shape, size, mineralogy, and surface roughness characteristics of particles. The principles and testing protocol will be studied. The methods are applied to soils, which are collected at the Texas A&M Riverside Campus, will be tested and the results will be presented.

Chapter IV summarizes a stress-based approach for evaluating liquefaction potentials using in-situ cone penetration tests. Also methods to predict cone penetration tip resistance are reviewed in this chapter. Focus will be on the determination of matric

suction at which soil undergoes large deformation or substantial loss of strength under earthquake loading.

Chapter V presents the elasto-plastic critical state-based constitutive model for unsaturated soils developed by Alonso, Gens, and Josa (1990). Mechanics of energy dissipation is presented as well as the pseudo-strain concept to account for viscous resistance.

Chapter VI is devoted to describing the main features of the suction controlled triaxial testing device used in this study. Description of the computer control of the equipment, computer controlled data acquisition, triaxial cell, four axis actuators, and the control used in controlling the test environment is presented in detail. The calibration of each measuring device is also included in this chapter.

Chapter VII presents the comparison between the drained suction controlled experiments and the numerical simulations in order to validate the previously proposed elasto-plastic critical state model. Furthermore the elasto-plastic model is used to predict cone penetration in unsaturated soil media. The undrained cyclic triaxial tests also are presented along with the calculation of the dissipated pseudo strain energy.

Chapter VIII presents the conclusions of the research and recommendations for future research.

CHAPTER II
UNSATURATED SOIL MECHANICS FUNDAMENTALS

Fundamental theories of soil mechanics have been used in the past to explain or predict soil behavior. The improvement and expansion of these theories over the years has resulted in more advanced models that can be applied to a broader range of soil problems.

This chapter commences with soil suction in unsaturated soils. This is followed by pore water in unsaturated soil and degree of saturation. Then soil water characteristic curve is reviewed briefly. Thereafter, particle level study of unsaturated soil is covered. The analyses of different particle size and shape and effect of pore-chemistry are performed to gain insight into the nature of matric suction and subsequent equivalent effective stress analyses. Then the stress state variables of relevance in solving engineering problems associated with shear strength behavior are highlighted. The last part of the chapter deals with the axis-translation technique in the laboratory.

2.1 Soil Suction in Unsaturated Soil

A free energy of pore water in soil is often referred to as soil suction-water. The free energy of the water in the soil can be measured in terms of the partial vapor pressure. Soil suction, an energy quantity, can be used to evaluate the capability of a soil to attain or hold water. When water enters into unsaturated soils, the water can be absorbed and stored by the soil and the applied energy per unit volume of water is called soil suction or total suction (Lee and Wray 1995, Park 2000).

The soil suction (the free energy) and partial pressure of the pore water vapor can be written as follow:

$$-h_t = \frac{RT}{mg}\ln\left(\frac{P}{P_o}\right) \tag{2.1}$$

where R = the universal gas constant (8.31432 J/mole K),

T = the absolute temperature,

m = molecular mass of water vapor (18.016 g/mole),

P = the partial pressure of pore water vapor pressure (kPa),

P_o = the saturation pressure of water vapor over a flat surface of pure water at the same temperature (kPa), and

g = gravitational constant.

The total suction has two components, matric and osmotic suction. Addition of two components is total suction as follow:

$$-h_t = -h_m - h_o \tag{2.2}$$

where h_t = total suction (m),

h_m = matric suction (m), and

h_o = osmotic suction (m).

Osmotic suction is the result of the lowering of the relative humidity of the pore fluid by the presence or concentration of soluble salts in the pore water and can be expressed by using Van't Hoffs' Equation.

$$-h_o = \pi = \frac{vRTC\phi}{g} \tag{2.3}$$

where, π = osmotic suction,

ν = ionic activity,

C = molar concentration (moles/liter), and

ϕ = osmotic coefficient.

Matric suction is the negative pore water pressure or capillary stress across the air-water interface and is associated with the capillary phenomenon from the surface tension of water. The pressure difference between the pore-air pressure, u_a, and the pore-

water pressure, u_w, also depends on the curvature of the air-water interface. In the absence of osmotic suction, Equation 2.1 can be expressed as following equation:

$$\Delta u = -\left(u_a - u_w\right) = \frac{RT\rho}{m} \ln \frac{p}{p_s} = -T_s \left(\frac{1}{r_1} + \frac{1}{r_2}\right) \tag{2.4}$$

where T_s = surface tension of pore fluid (kN/m),

r_1 = radius of air bubble (m),

r_2 = radius of water (m), and

p_s = vapor pressure above a flat surface of water with a molar concentration of salt, C.

In an unsaturated soil specimen being tested in the laboratory, the air-pressure is greater than the water pressure. However, in an unsaturated soil with a continuous air phase in the field, the pore-air pressure, u_a, is typically equal to atmospheric pressure, and then the pore-water pressure u_w is then negative relative to atmospheric pressure.

2.2 Pore Water in Unsaturated Soil and Degrees of Saturation

Sharma (1998) explains that voids in an unsaturated soil can be either water-filled or air-filled. The shape of the voids in soil gives the explanation on water-filled or air-filled voids. The shape of voids can be idealized as forms of a tube which is the minimum cross-sectional dimension of void. Assuming the radius of the tube r, the diameter of voids other than smallest dimension of voids will be larger than 2r. The consideration of geometry of air-water interface filling a tube of radius r, the Equation 2.4 becomes:

$$u_a - u_w = \frac{2T_s}{r} \tag{2.5}$$

The Equation 2.5 shows that the matric suction is inversely proportional to the radius of the tube. This implies that, if air can enter the tube of a void at certain value of suction, the air will occupy the rest of the voids with larger cross-sectional dimension. This is because the matric suction value is higher than the matric suction value for the voids with larger cross-sectional dimension. This suggests that voids are not likely to be filled partly with air and partly with water. The voids will be filled with either air or water. In a drying process, voids will empty of water and fill with air progressively to form voids with larger sized tubes than those with smaller tubes (Sharma 1998).

According to Wheeler and Karube (1996), three forms of pore water in an unsaturated soil are categorized: adsorbed water, bulk water, and meniscus water. The adsorbed water is tightly bound to the soil particles. Bulk water is the water which is flooded in the void spaces. The meniscus water is meniscus water surrounds the interparticle contacts and is not part of the bulk water.

The fundamental influences of pore water pressure and pore air pressure on the behavior of an unsaturated soil depend on the relative amounts of water in bulk and meniscus forms. The pore water pressure in the bulk water influences the soil behavior in a similar way as the pore water pressure in saturated soils. In contrast, pore-water pressure within meniscus water affect inter-particle forces at the particle contacts, reducing the possibility of slippage and making the particle assembly more stable. The effect of adsorbed water is not significant since it is part of the soil particle.

As water starts to evaporate or drain from saturated soil, menisci of water are drawn inward resulting in a suction pressure increase as in Equation 2.4. There is not much change in water content. However, the change in suction and resulting effective stress has an important effect on the soil mass.

Bear (1979) classifies the soil in terms of the degree of saturation as follows:

1) “Pendular saturation”; the state characterized by a very low degree of saturation. The water is retained in menisci formed around the grain contact points. These menisci do not form a continuous water phase. However, the air phase is continuous.

2) “Funicular saturation”; the state characterized by the coexistence of continuous air and water phases.
3) “Insular air (or occluded) saturation”; the state where the pore air loses its continuity and some parts become trapped in the water as air bubbles.

The compressibility of the unsaturated soil under undrained conditions will be different depending on the degree of saturation. Following classification system can be used.

At high degrees of saturation (S>90%): the air-water mixture is more rigid than the soil skeleton. With this condition, any external loading induces the same increment of pressure in both the air and water. This increment of pressure in both phases is equal to the external loading applied. It can be used for the formulation of equations for the compressibility of the air-water mixture. Increasing and instantaneous deformations can be expected with decreasing degrees of saturation.

The compressibility of water-air mixture at degrees of saturation between 90 % and 70 % is similar to that of the soil skeleton. The compressibility of the unsaturated soil is related to the structural behavior of the soil skeleton. The air-water mixture is highly compressible at degrees of saturation less than 70 %. Also the compressibility of the soil depends on the structural behavior of the soil skeleton.

2.3 Soil-Water Characteristic Curve

The soil-water characteristic curve relates matric suction of an unsaturated soil with the water content or degree of saturation. The shape of the soil-water characteristic curve depends on the soil macro-pores and micro-pores. The soil characteristics curve is one of the significant physical properties of unsaturated soil and is influenced by the type of minerals in the soil, the void size distribution and particle structures. The soil-water characteristic curve is also dependent on soil texture. Studies have shown that clay soils tend to retain more water than sandy soils. Another factor that has been shown to affect the soil characteristic curve is soil compaction. It is generally accepted that a

dense soil tends to retain more water in comparison to a loose one because of more closely packed pore spaces.

The soil-water characteristic curve can be either an adsorption (wetting) or a desorption (drying) curve. Usually, the wetting and drying curves are different due to hysteresis. Thus, at a particular suction level, the degree of saturation or water content will be different. The non-uniform pore size distribution in a soil, as well as the presence of entrapped air in the pore-water, are considered to be the main causes for hysteresis in the soil-water characteristics curve (Hoyos 1998). Also, the advancing contact angle during wetting and receding contact angle between a soil particle and the air-water interface affects hysteresis of soil-water characteristic curve.

2.4 Particle Study

The purpose of this section is to highlight the influence of air in a soil-water mixture. Laplace's Equation is employed in predicting the force induced due to the formation of menisci around soil particles. Thus, the prediction of equivalent stresses is possible as a function of the size of soil particle and either gravimetric or volumetric water content. Also, the presence of chemicals in the water is studied. The study is strictly limited to the micro-scale level. However, the interpretation of the study will be applied to the macro-scale level of unsaturated soil behavior and characteristics. The particle shapes studied are spherical, ellipsoidal, and platy particles.

2.4.1 Spherical Particles

As in Figure 2.1, two spheres with radius of R are in contact. Meniscus water collects at the particle contact forming an annular ring with double curvature represented by radii r_1 and r_2. Assumptions are made in using spherical geometry. First, the surface of the solid is smooth. Second, the effect of gravity on the geometry of the meniscus is ignored. Also, this model is limited to the pendular stage of the degree of saturation.

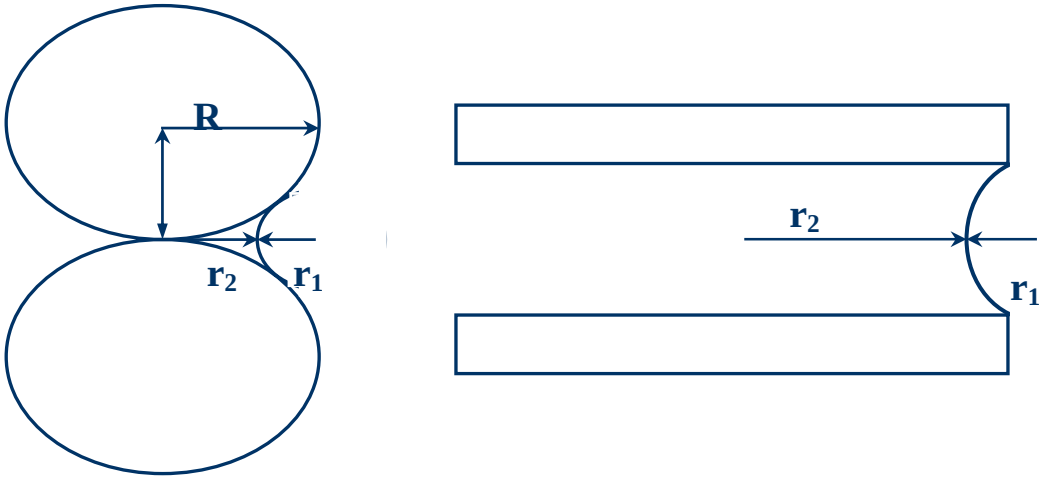

Figure 2.1 Spherical and Flat Particles in Contact with Water Meniscus

The water inside the ring is at a pressure u_w and the air outside the ring is at a pressure u_a. The expression for matric suction (u_a-u_w) can be written as:

$$\Delta u = -(u_a - u_w) = \frac{T_s}{R\alpha}\left(\frac{2}{\alpha} - 3\right) \qquad (2.6)$$

where $\alpha = \frac{r_2}{R}$.

This expression shows that the matric suction is a function of the particle size R and the ratio r_2/R, and it can be used to estimate the values of suction corresponding to different particle sizes and the ratio r_2/R. Figure 2.2 shows a plot of matric suction against r_2/R for different sizes of particles with surface tension of $73\times10^{-6} kN/m$. Figure 2.2 shows that the matric suction increases inversely with the radius of particle, R.

The presence of water in the ring-shaped menisci at the particle contact gives rise to an additional inter-particle normal force, which can be determined by considering equilibrium of the particles. In the absence of external force, the force applied due to adhesion of water to particles becomes:

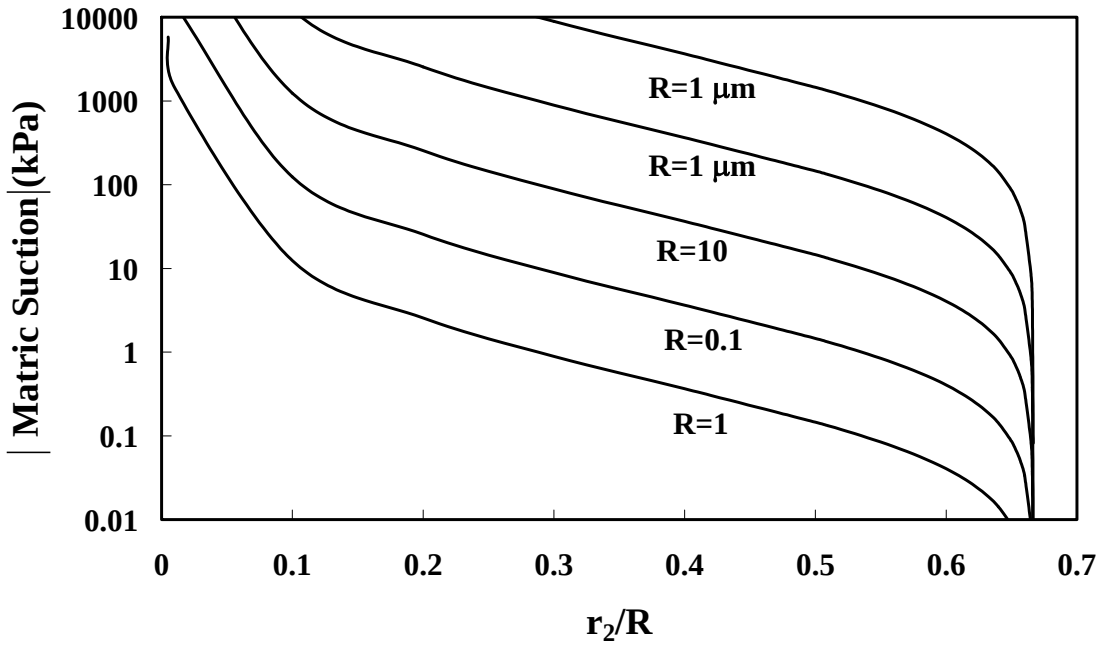

Figure 2.2 Variation of Suction with Different Particle Sizes

$$F = \Delta u(\pi r_2^2) + T_s(2\pi r_2) \tag{2.7}$$

Assuming that the increase in inter-particle force can be expressed as an averaged increase of stress over a square region of area $4R^2$, an expression for the stress increase can be written as:

$$\sigma_{eff} = \frac{\pi T_s}{4R}(2-\alpha) \tag{2.8}$$

Equation 2.8 shows that the additional component of inter-particle stress arising from the presence of meniscus water at the inter-particle contact increases from $\pi T_s/2R^2$ as suction tends to infinity (when r_2/R tends to zero). Figure 2.3 shows the value of effective stress at α value of 0 against particle radius at $73\times10^{-6} kN/m$ of surface

tension. At relatively large particle sizes, the induced effective stress is very small and negligible. However, as the particle gets smaller, the effective stress becomes larger and cannot be neglected.

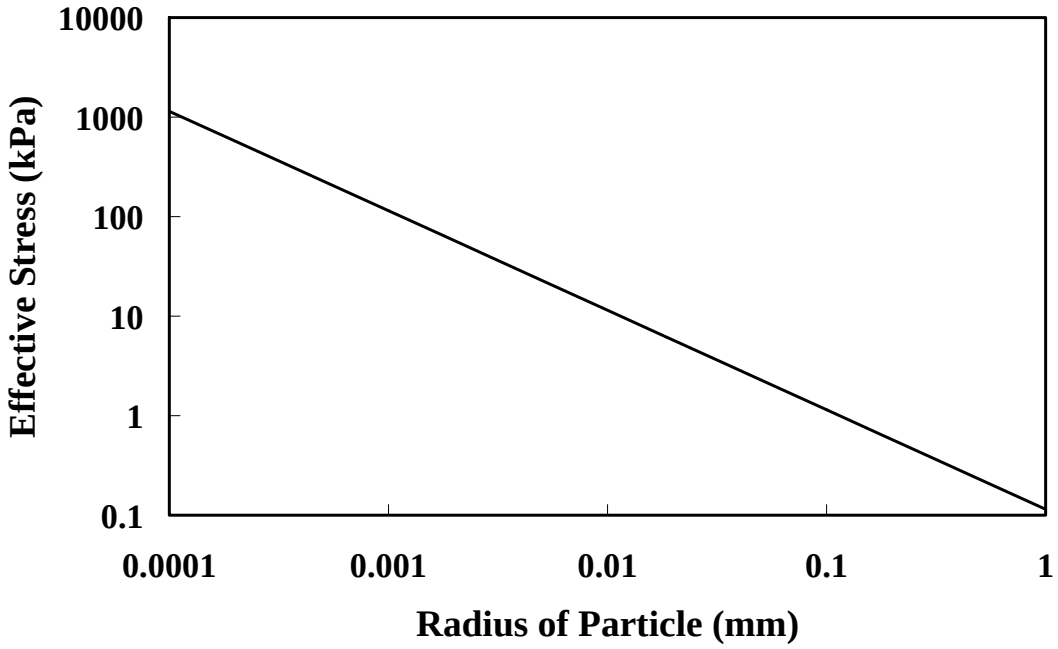

Figure 2.3 Variation of Equivalent Effective Stress with Different Particle Sizes

The volume of water can be calculated considering the geometry of the meniscus. This volumetric water content can also be used to calculate gravimetric water content as well. Cho (2000) showed the derivation of the water content as a function of r_2/R (= α) and the equation is as follow:

$$w = \frac{9}{8Gs}\left(\frac{\alpha^4}{1-\alpha^2}\right)\left(1-\frac{\alpha(2-\alpha)}{2(1-\alpha)}arc\sin\left(\frac{2(1-\alpha)}{\alpha^2+2(1-\alpha)}\right)\right) \tag{2.9}$$

When tetrahedral packing is considered, the effective stress is:

$$(\sigma_{eq})_{TH} = 2\sqrt{2}(\sigma_{eq})_{SC} \tag{2.10}$$

where $(\sigma_{eq})_{SC} = \frac{\pi T_s}{4R^2}(2-\alpha)$ and SC stands for surface-centered cubic.

2.4.2 Platy Particles

The purpose of analyzing a contact between platy particles is that the shape of a clay platelet cannot be described as approximately spherical. In the platy particle analysis, $1/r_2$ is normally neglected, since r_2 is significantly larger than r_1 in its geometry consideration as in Figure 2.1. The expression for matric suction for this case is as follow:

$$-\Delta u = T_s \frac{1}{r_1} = T_s(\frac{SSA\gamma_w}{wg}) \tag{2.11}$$

where SSA = specific surface area.

Gravimetric water content can be calculated considering the specific surface area of the particle with the given particle dimensions.

$$w = \frac{W_w}{W_s} = SSAr_1 \frac{\gamma_w}{g} \tag{2.12}$$

For the disk geometry, the equivalent effective stress contributed by capillarity is π/4 of suction pressure. Particle size is not present in this equation. Instead, specific surface appears as a more meaningful parameter in the context of small platy particles. (Cho 2000).

As water dries, either particles move together or the meniscus recedes between the particles at constant r_1. The parallel particle model applies to dispersed-aggregate systems. The analysis of flocculated fabrics with edge-to-face contacts leads to a lesser effect of capillarity than the effect of capillarity on a perfectly smooth disk. The analysis of equilibrium must also include the localized reaction at asperities and inter-particle electrical forces (Nagaraj and Srinivasa Murthy 1985, Fam and Satamarina 1996, and Cho 2000).

2.4.3 Ellipsoidal Particles

Previous studies on effects of transition between sphere and flat particles do not exist. In this study, ellipsoidal particle will be studied. As in Figure 2.4, two equal sizes of elliptic particles are in contact. Unlike the spherical particles, there are two particle radii, R_1 as a major radius and R_2 as a minor radius of the particles. The shape of the particle is generated by rotating the elliptical cross-section around the vertical (or minor) axis. The water meniscus is bounded by two particles and by the air-water interface with radius r_1 as the radius of air bubble and radius r_2 as the radius around the point of contact. A contact angle can be specified where the air-water interface is in contact with each of the soil particles. The same assumptions are made as in sphere and platy particles. The complete derivation of suction and volumetric water content is not simple and the calculation procedures are iterative.

As in Figure 2.4, the following equation can be derived by considering geometry of particles:

$$\frac{x^2}{R_1^2}+\frac{y^2}{R_2^2}=1 \tag{2.13}$$

where x $= r\cos\theta$ and

y $= r\sin\theta$

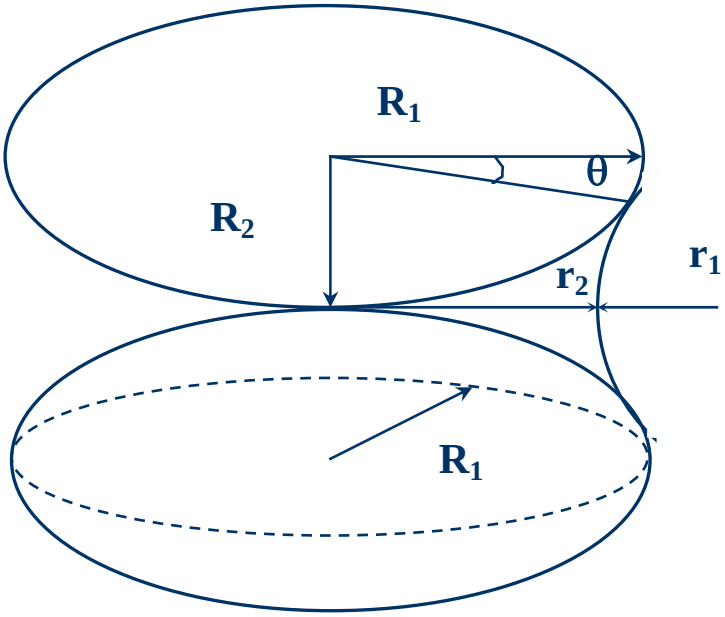

a)

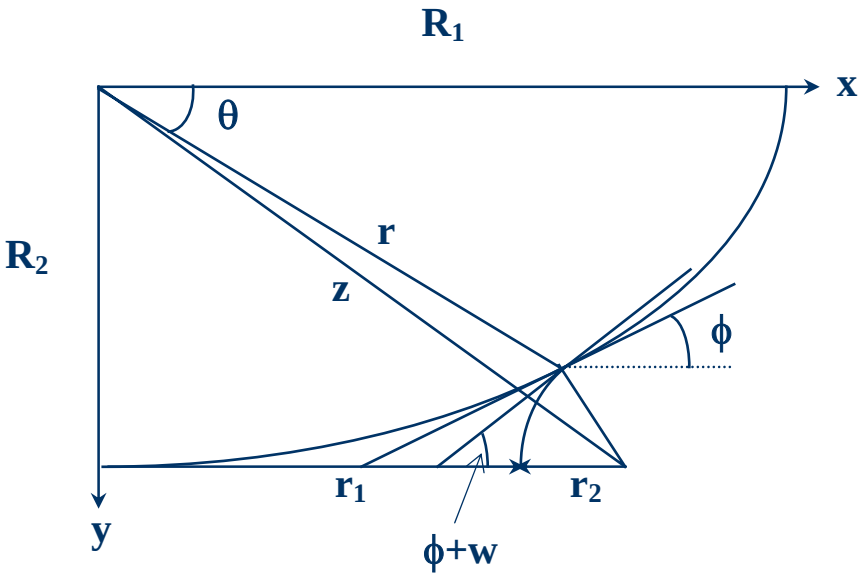

b)

Figure 2.4 Ellipsoidal Particles in Contact with Water Meniscus: a) Ellipsoidal Particles in Vertical Packing; b) Close Up View of Ellipsoidal Particle

Substituting x and y into Equation 2.13, the above equation can be solved for r as follow:

$$r^2 = \frac{1}{\frac{r^2\cos^2\theta}{R_1^2} + \frac{r^2\sin^2\theta}{R_2^2}} = \frac{R_2^2}{\sin^2\theta + (\frac{R_2}{R_1})^2\cos^2\theta} \tag{2.14}$$

Also Equation 2.13 further yields the following equation:

$$\tan\phi = \frac{dy}{dx} = (\frac{R_2}{R_1})^2\cot\theta \tag{2.15}$$

Other relations are also possible from the geometry in consideration of Figure 2.4:

$$r_1\sin(90-\phi-w) = R_2 - r\sin\theta \tag{2.16}$$

$$\frac{r_1}{r_2} = [(\frac{z}{r_2})^2 - (\frac{R_2}{r_2})^2]^{1/2} - 1 \tag{2.17}$$

$$z^2 = \left[\frac{R_1\sin\theta}{B} + r_1\cos(\phi+w)\right]^2 + \left[\frac{R_1\cos\theta}{B} + r_1\sin(\phi+w)\right]^2 \tag{2.18}$$

where $B = [(\frac{R_1}{R_2})^2\sin^2\theta + \cos^2\theta]^{1/2}$ and

$$z = (r_1 + r_2)^2 + R_2^2$$

Thus, the radius of water can be expressed as the following:

$$r_2 = R_1\{[\frac{\sin\theta}{B} + (\frac{r_1}{R_1})\cos(\phi+w)]^2 + [\frac{\cos\theta}{B} + \frac{r_1}{R_1}\sin(\phi+w)]^2 - (\frac{R_2}{R_1})^2\}^{1/2} - r_1 \tag{2.19}$$

By letting, $\frac{r_1}{R_1} = \beta$, $\frac{r_1}{r_2} = \gamma$, and $\frac{R_1}{R_2} = \delta$, $\frac{r_2}{r_1} = \alpha$, then Equation 2.19 can be rewritten as following:

$$\alpha = \{[\frac{\sin\theta}{B\beta} + \cos(\phi + w)]^2 + [\frac{\cos\theta}{\beta B} + \sin(\phi + w)]^2 - (\frac{1}{\beta\delta})^2\}^{1/2} - 1 \qquad (2.20)$$

The α–value calculated in Equation 2.20 is not final. The α will be recalculated by calculating ϕ in the following Equation 2.21. This procedure will continue until the specified convergence of θ using Equation 2.15 is reached.

$$\delta^2 \tan\phi - \frac{\alpha\beta + \beta[1 - \sin(\phi + w)]}{\frac{1}{\delta} - \beta\cos(\phi + w)} = 0 \qquad (2.21)$$

Finally, using the Laplace Equation as in Equation 2.5, suction and equivalent effective stress can be calculated as following:

$$\Delta u = (u_a - u_w) = \frac{T_s}{R_1\alpha\beta}(\frac{1}{\gamma} - 1) \qquad (2.22)$$

$$\sigma'_{eq} = \frac{F}{4R_1^2} = \frac{T_s}{R_1}\frac{\pi}{4}(\alpha + 1)\alpha\beta \qquad (2.23)$$

Once the radius of water r_2 is calculated, the volumetric water content can also be calculated. Figure 2.5 shows that the volume of water can be calculated from the rotation of three areas, A1, A2, and A3. Then the total volume of water is expressed as follows:

$$V = V_1 - V_2 + V_3 \qquad (2.24)$$

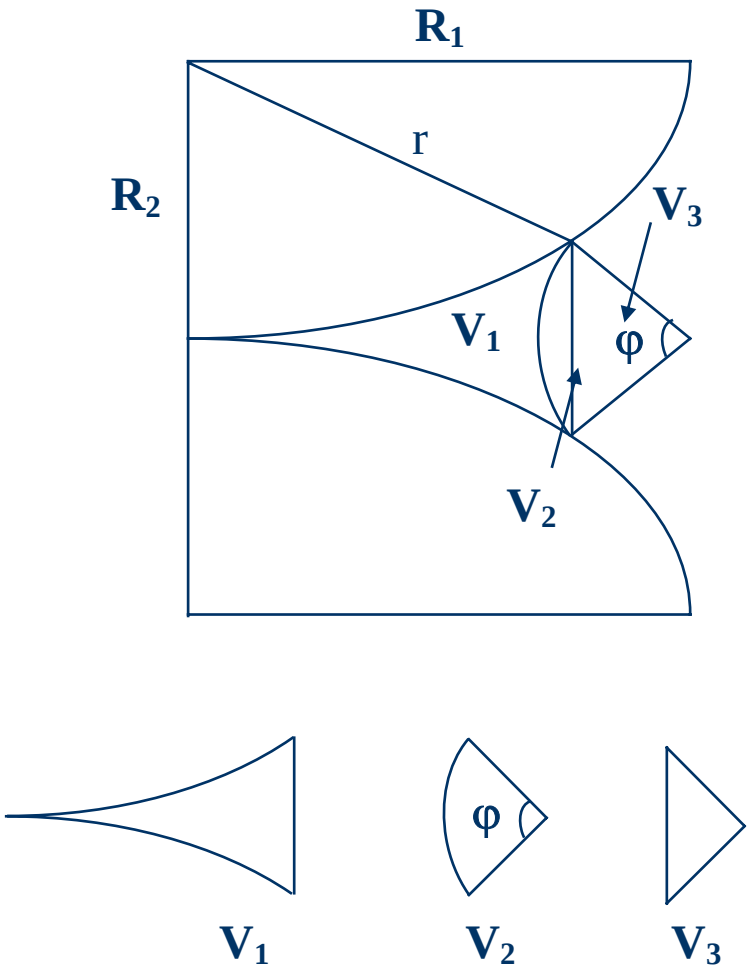

Figure 2.5 Volume of Water Calculation

Using the Equation (2.13), the Volume, V_1, is calculated as follows:

$$V_1 = \int_{x=0}^{x=r\cos\theta} 2\pi x(R_2 - y)dx = 2\pi R_2 \int_o^{r\cos\theta} x\left[1-\left(1-\frac{x^2}{R_1^2}\right)^{\frac{1}{2}}\right]dx \qquad (2.25)$$

In the calculation the volume V_2, we need to calculate the area of the sector with angle φ and the centroidal distance of the sector. The centroidal distance is calculated considering the area moment of the sector and the ratio of the area moment to area of the sector. Then, the volume can be calculated by rotating the area of the sector as in the following equation:

$$\text{Area of sector} = r_1^2\varphi$$

$$\text{Centroidal Distance} = \frac{2}{3}r\frac{\sin\varphi}{\varphi}$$

$$V_2 = 2\pi r_1^2\left(r_1 + r_2 - \frac{2}{3}r_1\frac{\sin\varphi}{\varphi}\right)\varphi \tag{2.26}$$

The volume of triangle, V_3, can also be calculated from the rotation of the area of the triangle as in Equation 2.27. Again, the centroidal distance can be calculated considering area moment of the triangle.

$$\text{Area of Sector} = r_1^2\sin\varphi\cos\varphi$$

$$\text{Centroidal Distance} = \frac{2}{3}r_1\cos\varphi$$

$$\text{V}_3 = 2\pi r_1^2\left(r_1 + r_2 - \frac{2}{3}r_1\cos\varphi\right)\sin\varphi\cos\varphi \tag{2.27}$$

Finally, the volume of water bounded by particles and air-water interface is as follow:

$$\begin{aligned} V = {} & \pi R_2^3\cos^2\theta\left(\frac{\delta^2}{B^2}\right) + \frac{2\pi}{3}\frac{R_1^3}{\delta}\left\{\left[1-\frac{\cos^2\theta}{B^2}\right]^{3/2} - 1\right\} \\ & -2\pi r_1^2\left\{r_1\left[\varphi - \frac{2}{3}\sin\varphi - \sin\varphi\cos\varphi + \frac{2}{3}\sin\varphi\cos\varphi^2\right] + r_2\left[\varphi - \sin\varphi\cos\varphi\right]\right\} \end{aligned} \tag{2.28}$$

So far, matric suction, effective stress, and volume of water were derived based on the vertical packing of particle. Matric suction, equivalent effective stress, and volume of water also can be derived based on horizontal packing of particles as in Figure 2.6. However, the derivation of suction based on the procedures developed for the vertical packing can not be used due to numerical error. One possible way to do is to keep the suction constant. Then, r_3 can be calculated using the Laplace Equation as follow:

$$(u_a - u_w)_{vert} = (u_a - u_w)_{hori} = T_s\left(\frac{1}{r_1} - \frac{1}{r_3}\right) \tag{2.29}$$

The equation for the equivalent effective stress is as follows:

$$F = (u_a - u_w)(\pi r_1 r_3) + T_s(2\pi\sqrt{\frac{r_1^2 + r_3^2}{2}})$$

$$\sigma'_{eq} = \frac{F}{4R_1R_2} \tag{2.30}$$

For the calculation of the volumetric water content, the same procedure will be used as in the vertical case. However, unlike the vertical case, the integration of area involves an elliptical integral. Three volumes can be calculated, V_1, V_2, and V_3 as follows:

$$V_1 = 2\pi R_1\sqrt{\frac{1+\delta^2}{2}}\int_{y=0}^{y=r\sin\xi} y dy - \sqrt{\frac{1+\delta^2}{2}}\int_{y=0}^{y=r\sin\xi}\sqrt{1-\frac{y^2}{R_2^2}}\,y dy$$

$$V_2 = 2\pi(r_1 + r_3 - \frac{2}{3}r_1\frac{\sin\eta}{\eta})\sqrt{\frac{r_1^2 + r_3^2}{2}}r_1^2\eta$$

$$V_3 = 2\pi\left[r_1 + r_3 - \frac{2}{3}r_1\cos\eta\right]\sqrt{\frac{r_1^2 + r_3^2}{2}}r_1^2\sin\eta\cos\eta$$

$$V = V_1 - V_2 + V_3 = \pi R_1^3 \sqrt{\frac{1+\delta^2}{2}} \frac{\sin \xi^2}{C^2} + \frac{2\pi}{3} \sqrt{\frac{1+\delta^2}{2}} R_1 R_2^2 \left[\left(1 - \frac{\sin^2 \xi}{R_2^2} \frac{R_1^2}{C^2} \right)^{\frac{3}{2}} - 1 \right]$$
$$-2\pi r_1^2 \sqrt{\frac{1+\delta^2}{2}} \left\{ r_1 \left[\eta - \frac{2}{3} \sin \eta - \sin \eta \cos \eta + \frac{2}{3} \sin \eta \cos \eta^2 \right] + r_3 \left[\eta - \sin \eta \cos \eta \right] \right\} \quad (2.31)$$

where C $= \left[\cos^2 \xi + \delta^2 \sin^2 \xi \right]^{\frac{1}{2}}$

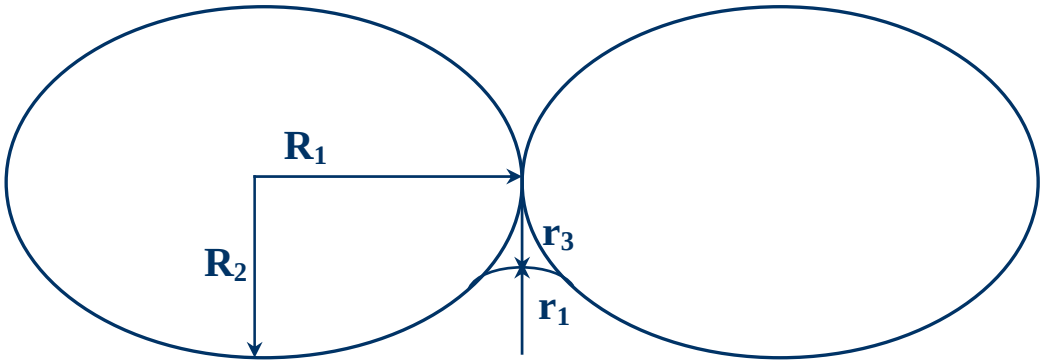

a)

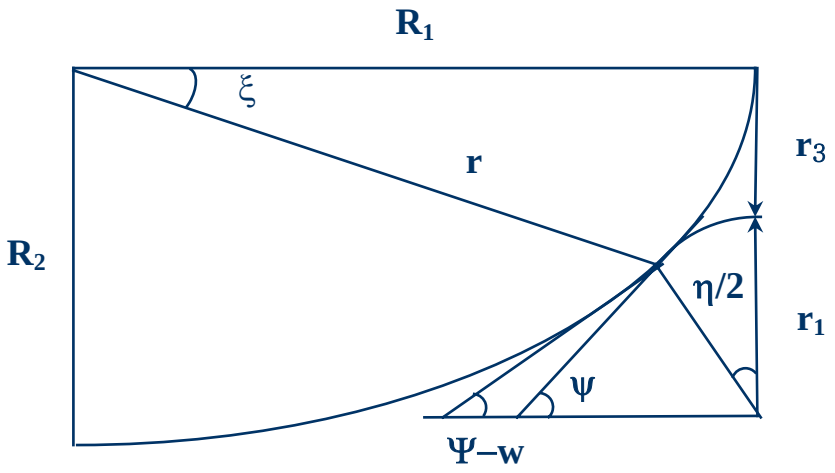

b)

Figure 2.6 Ellipsoidal Particles in Horizontal Packing: a) Ellipsoidal Particles in Horizontal Packing; b) Close Up View of Ellipsoidal Particle

2.4.4 Verification of Ellipsoidal Particle Model and Discussions

For comparison with the spherical particle and platy particle, values of matric suction and equivalent effective stress calculated from the ellipsoidal particle are tabulated in Table 2.1.

Table 2.1 Comparison of Matric Suction and Equivalent Effective Stress

	δ=1	δ=10	δ=100	δ=500	Spherical	Flat
Δu (kPa)	7005	7293	7298	7299	7005	7300
σ'_{ver} (kPa)	1.5	151	1427	2650	1.5	5733.4
σ'_{hor} (kPa)	1.5	169	1965	4128	1.5	N.A.

The matric suction and effective stress calculated in the above table was based on particle size, $R_1=75*10^{-6}$ (m), $T_s=73*10^{-6}$ (kN/m), and $r_1=10^{-8}$ (m). As in the above table, at δ=1, which is a spherical particle ($R_1/R_2=1$), the matric suction and effective stress are the same in the spherical particle. As δ becomes larger, which means that particle becomes flatter, the suction and effective stress increase. At δ=500 ($R_1/R_2=500$), suction was close to the suction value of flat particle. The vertical effective stress for the elliptical stress at δ=500 is much smaller than the value for the flat particle. This is due to the difference in geometry of two particle model. The horizontal effective stress is larger than vertical effective stress since horizontal area ($A=4*R_1^2$) is smaller than the vertical area ($A=4R_1*R_2$). However, the inter-particle vertical force induced by the surface tension was much larger than that of the horizontal. If there is any repulsive force on the edge of particle, the inter-particle force in horizontal direction will be reduced hence the horizontal effective stress will be smaller than the calculated value.

From the results in the Table 2.1, the ellipsoidal particle model is capable of predicting suction and effective stress for the range of particle shape from a spherical to

a flat particle. This elliptical model will be used to study the effect of surface tension effect on suction and inter-particle forces with different particle shapes and sizes.

Table 2.2 and 2.3 shows the change of surface tension due to different concentrations of pore water chemistry. It is a known fact that the surface tension goes up with increasing concentration of inorganic salts. On the other hand, the surface tension decreases with an increase in organic salt concentration.

Table 2.2 Surface Tension of Inorganic Solutes in Water (Lide 2000)

Concentration (moles/1000g)	$CaCl_2$ (25 ^oC)	KCl (20 ^oC)	NaCl (20 ^oC)	$MgCl_2$ (20 ^oC)
0	71.97	72.75	72.75	72.75
0.1	72.32	72.91	72.92	73.07
0.5	73.47	73.45	73.57	74.27
1.0	75.17	74.15	74.39	75.75
2.0	78.87	75.55	76.05	79.15
3.0	82.97	76.95	77.65	82.85
5.0			80.95	85.75

Note: Units of surface tension in ergs/cm^2

Table 2.3 Surface Tension of Organic Solutes in Water (Lide 2000)

Acetone (25^{o}C)	Phenol (20^{o}C)	Ethyl alcohol (30^{o}C)	Acetic Acid (30^{o}C)
55.5 (0.05)	72.6 (0.024)	66.1 (0.01)	68.0 (0.01)
48.9 (0.1)	66.5 (0.417)	61.6 (0.02)	60.1 (0.05)
41.1 (0.2)	61.0 (0.941)	54.2 (0.05)	43.6 (0.3)
38.3 (0.25)	46 (3.76)	45.9 (0.1)	38.4 (0.5)
30.4 (0.25)	42.3(5.62)	34.1 (0.25)	34.3 (0.7)

Note: Values in the parenthesis are % dilution. Surface tension in ergs/cm^2

Figure 2.7 shows the increase or decrease of the matric suction due to the change of surface tension on a 75 μm particle size. For elliptical particles, this will be the larger radius, R_1. For all cases, the suction increases with increasing surface tension and particle flatness. On the other hand, the decrease in surface tension due to the presence of organic chemicals in the water resulted in decrease in the matric suction.

The effect of the surface tension on the equivalent effective stress is shown on Figure 2.8. The effective stress also shows the similar trends with change in the surface tension of the water.

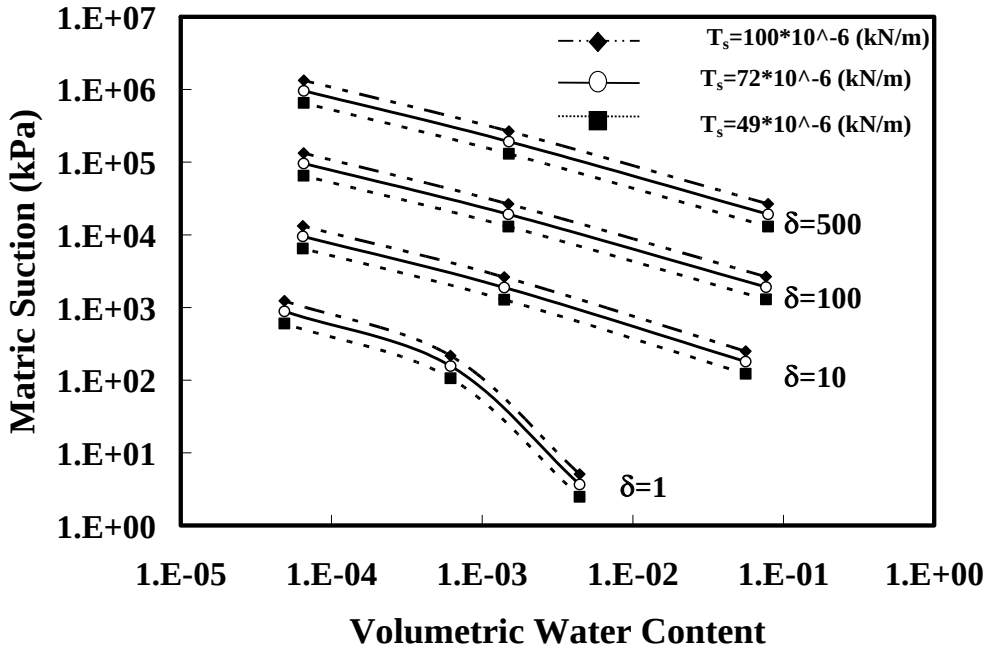

Figure 2.7 Variation of Matric Suction with Different Particle Shape and Surface Tension

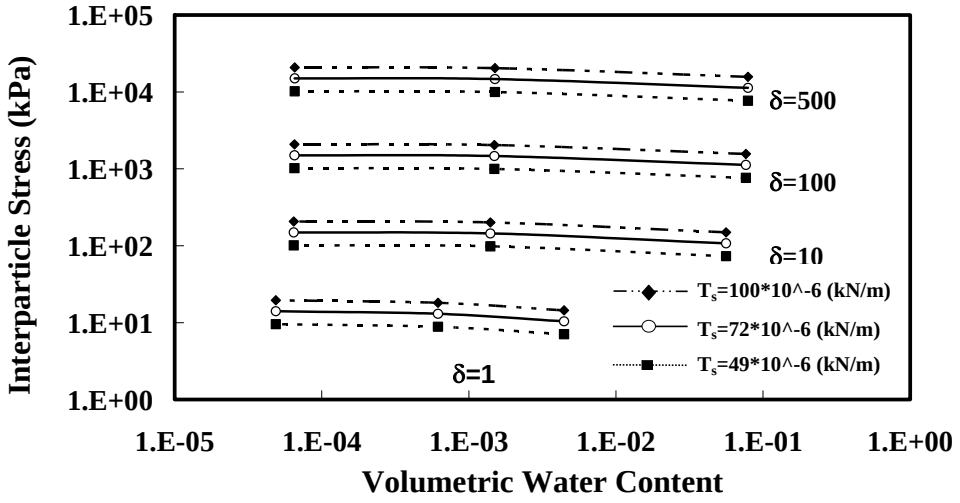

Figure 2.8 Variation of Equivalent Effective Stress with Different Particle Shape and Surface Tension

2.5 Behavior of Unsaturated Soils

2.5.1 Effective Stress Approach

Classical soil mechanics was developed predominantly from the study of saturated soils. The principle of effective stress for saturated soil was first stated by Terzaghi (1936) and is commonly expressed in the following form:

$$\sigma' = \sigma - u_w \tag{2.32}$$

where σ' = effective normal stress,

σ = total normal stress, and

u_w = pore-water pressure.

Equation 2.32 is a definition of the stress state variable for saturated soils. The mechanical aspects of a saturated soil are governed only by the effective stress.

Satisfactory stress state variables for an unsaturated soil have been considerably more difficult to establish. Since it is desirable that the concept of effective stress for

saturated soils be extended unsaturated soils, all proposed effective stress equations for an unsaturated soil have attempted to provide a single-value stress state variable. The most widely quoted effective stress equation was that proposed by Bishop (1959):

$$\sigma' = \sigma - u_a + \chi(u_a - u_w) \tag{2.33}$$

where u_a is the pore-air pressure and χ is a soil parameter related to the degree of saturation of the soil. The magnitude of the χ parameter varies between zero for a dry soil and unity for a saturated soil, where the traditional effective stress equation for saturated soils is recovered. The relationship between χ and S_r is not unique and is influenced by the soil type and the stress paths. It is noted that a soil parameter, χ, is incorporated into Equation 2.33 to describe the stress state, which produces a constitutive relation. Hence, it becomes questionable to use Equation 2.33 as a stress state variable from a continuum mechanics standpoint (Fung 1977).

Further investigations conducted by Jennings and Burland (1962) questioned the use of Equation 2.33 for unsaturated soils and pointed out that the proposed effective stress equation could not fully explain the volumetric behavior for most unsaturated soils below a critical degree of saturation. Bishop and Blight (1963), Blight (1967), and Burland (1964) suggested that the mechanical behavior of an unsaturated soil should be independently related to the stress state variables, σ-u_a and σ-u_w. A change in u_a-u_w did not correspond to the same change in effective stress as did a change in σ-u_a. This was attributed to surface tension in pore-water acting over only part of the surface area of the soil particles. Further research on volume change behavior of unsaturated soils conducted by Aitchison and Woodburn (1969), Matyas and Radhakrishna (1968), Barden et al. (1969), and Brackely (1971) also suggested the use of independent stress state variables.

The brief literature review presented above shows that considerable effort has been expended in the establishment of a single-valued effective stress equation for an unsaturated soil. Unfortunately, the research results have demonstrated that the effective

stress is not single-valued for an unsaturated soil. Furthermore, many researchers suggested the use of independent stress state variables to describe the mechanical behavior of an unsaturated soil. The use of independent stress state variables has resulted in more meaningful explanation of unsaturated soil behavior.

2.5.2 Independent Stress State Variables

In the late seventies, Fredlund and Morgenstern (1977) presented the use of two independent stress state variables for unsaturated soils. These variables were based on a stress analysis consistent with that used in multiple component (mixture) continuum mechanics. The two independent stress state variables are expressed in terms of physically measurable quantities, i.e., the total stress, σ, the pore-water pressure, u_w, and the pore-air pressure, u_a: and they have also been experimentally tested (Fredlund 1973).

The unsaturated soil was considered as a four-phase system. Besides, the solid soil grains, water and air, the air-water interface (meniscus) was included as the fourth independent phase. The assumptions in the stress analysis are that the solid and the water phase are incompressible and the soil is treated as though it were chemically inert. The preferred stress state variables are

$$\left[\sigma_{ij} - u_a \delta_{ij}\right] \text{ and } \delta_{ij}\left[u_a - u_w\right] \tag{2.34}$$

The first tensor contains the net normal stress terms and the conventional shear stress components. The second tensor represents the matric suction stress.

Fredlund and Morgenstern (1977) also carried out he null-type test by varying the individual components (σ, u_a, and u_w) of the stress sate variables in a such way that the stress state variables remained constant assuming that this would produce no distortion or volumetric change of the soil. Based on the results of the null tests, the above stress state variables were qualified for describing the mechanical behavior of unsaturated soils.

2.5.3 Shear Strength of Unsaturated Soil

As soil is subjected to a combination of normal and shear stresses, its strength increases up to a point where it can no longer withstand shear stresses. An expression for the maximum shear strength in classical soil mechanics for saturated soil is the Mohr-Coulomb failure criterion:

$$\tau = c' + (\sigma - u_w)\tan\phi' \tag{2.35}$$

where τ = shear stress along failure plane,

c' = effective cohesion,

σ = total stress,

u_w = pore water pressure, and

ϕ' = effective friction angle.

The shear strength of an unsaturated soil using two independent stress state variables was formulated by Fredlund et al (1978) as follow:

$$\tau = c' + (\sigma - u_a)\tan\phi' + (u_a - u_w)\tan\phi^b \tag{2.36}$$

where σ-u_a = net normal stress,

ϕ' = friction angle due to the net normal stress,

u_a-u_w = matric suction, and

ϕ^b = the angle relating the rate of change of shear strength with matric suction.

Rearranging of Equation 2.36 results in the following equation:

$$\tau = c + (\sigma - u_a)\tan\phi' \tag{2.37}$$

where c = $c' + (u_a - u_w)\tan\phi^b$.

Though Equation 2.36 and 2.37 shows a linear relationship between shear strength and matric suction, experimental evidence (Fredlund and Rahardjo 1987) studies have shown that shear strength in unsaturated soils increases non-linearly with an increase in matric suction. With an increase in matric suction, shear strength increases at first in a linear manner up to a matric suction value above which increases in strength become non-linear. At higher matric suction, the strength may remain constant or even drop (Fredlund and Rahardjo 1993).

Further developments include work done by Lamborn (1986). He used reversible thermodynamic principles to describe the stress generated on the soil skeleton due to tension in the pore water. He used the soil-water characteristics curve to predict the shear strength of unsaturated soils. The formulation is as follows:

$$\sigma_{ij} = \theta \frac{\partial F_w}{\partial \left(\varepsilon_{ij}\right)_w} \tag{2.38}$$

where F_w = the Helmholtz free energy in the water,

ε_{ij} = strain in the water,

θ = volumetric water content, and

σ_{ij} = stress on the soil due to the water.

Since matric suction is a derivative of the Helmholtz free energy, the stress due to soil suction can be redefined as follows:

$$\sigma = -f\theta h_m \tag{2.39}$$

where f = the unsaturated shear strength function,

h_m = matric suction,

θ = volumetric water content, and

σ = stress on the soil due to water.

Lytton (1995) proposed the following shear strength using two stress variables and Lamborn's approach as follows:

$$\tau = c' + \left[(\sigma - u_a) + f\,\theta(u_a - u_w)\right]\tan\phi' \tag{2.40}$$

The above equation includes a term that accounts for the transition zone between the air entry point and the suction at which continuous air void starts. Lytton (1995) also describes that the $\tan\phi^b$ term is bound by the product of $\theta\tan\phi'$ and the upper and lower bound of values of unsaturated shear strength function in the transition zone as in Figure 2.9. The upper and lower bound of unsaturated shear strength function in the transition zone is given in the following equations:

$$f_1 = \left(\frac{\theta_a - \theta}{\theta_a - \theta_u}\right) + \frac{1}{\theta}\left(\frac{\theta - \theta_u}{\theta_a - \theta_u}\right) \tag{2.41}$$

$$f_2 = \frac{1}{\left(\frac{\theta_a - \theta}{\theta_a - \theta_u}\right) + \theta\left(\frac{\theta - \theta_u}{\theta_a - \theta_u}\right)} \tag{2.42}$$

where θ = volumetric water content at current suction,

θ_a = volumetric suction at air entry, and

θ_u = volumetric water content at unsaturation (continuous air void).

Vanapalli et al. (1996) also proposed the shear strength equation using the soil-water characteristic curve. They developed two similar shear strength equations based on the volumetric water content and the degree of saturation as follows:

$$\tau = c' + (\sigma - u_a)\tan\phi' + (u_a - u_w)\tan\phi'\left(\frac{\theta - \theta_r}{\theta_s - \theta_r}\right) \tag{2.43}$$

where θ = volumetric water content at current matric suction,

θ_s = volumetric water content at saturation,

θ_r = residual volumetric water content.

$$\tau = c' + (\sigma - u_a)\tan\phi' + (u_a - u_w)\tan\phi'\left(\frac{S - S_r}{100 - S_r}\right) \qquad (2.44)$$

where S = the degree of saturation in percent at current suction and

S_r = the residual degree of saturation.

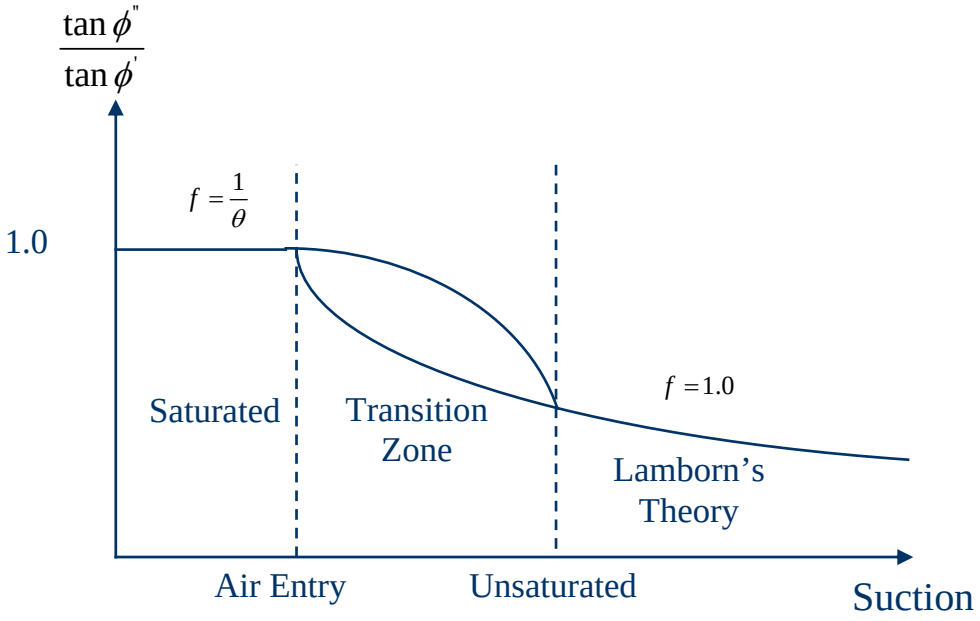

Figure 2.9 Transition of Friction Angle due to Matric Suction from Saturated to Unsaturated State (redrawn after Lytton 1995)

2.6 Axis Translation Technique

For unsaturated soils with high matric suction, water cavitation is a problem. Water in a measuring system may cavitate when the water pressure approaches -1 atm. As a result, occluded air bubbles accumulate in the measuring system. This causes an error in the measurement of pore-water pressure. The difficulty of measurement of negative pore-water pressure in an unsaturated soil can be overcome by applying an axis-translation technique to a soil specimen.

The procedure involves a translation of the reference or pore-air pressure. The pore-water pressure can then be referenced to a positive air pressure (Hilf 1956; Olson and Langfelder 1965; Fredlund 1989; Hoyos 1998). In other words, the axis translation technique simply translates the origin of reference for the pore-water pressure from standard atmospheric conditions to the final positive air pressure. This technique has been successfully applied to the volume change and shear strength testing of an unsaturated soil (Bishop and Donald 1961; Gibbs and Coffey 1969; Fredlund 1973; Ho and Fredlund 1982; Gan et al. 1988; Fredlund and Rahardjo 1993; Hoyos 1998).

Axis translation requires continuity of air space in the specimen. This technique may not be applicable when the degree of saturation in the specimen exceeds 70 %. Hence, application of the axis translation is limited to the range of high suction. Limitations of this technique are described by Bocking and Fredlund (1980).

Laboratory testing of unsaturated soil under high matric suction conditions involves the axis-translation. The general idea is to translate both the pore-air pressure and pore-water pressure into a positive range by creating an artificial atmospheric pressure greater than 101.5 kPa. As a result, the negative gauge pore-water pressure is also raised by an equal amount to a positive pressure, so that matric suction of the unsaturated soil specimens remains constant regardless of the magnitude of the pore-air pressure.

CHAPTER III
SURFACE FREE ENERGY OF SOIL PARTICLES

Recent developments in many modern technologies involve new material or processes in which interfaces or surfaces play essential roles. Knowledge of surfaces and interfaces has great impact on many basic industries, such as data processing, medicine, agriculture, transportation, and civil engineering. This chapter will introduce the basics about the surface energy concept, measurement and calculation of surface free energy of soil, and the calculation of the work of adhesion and cohesion.

3.1 Surface Free Energy

By definition, the surface free energy of a solid or liquid is the energy needed to create a new element area of surface under vacuum conditions. Unsaturated soil behavior is related to adhesive bonding within the water-aggregate system. And the adhesive bonding is related the surface free energy characteristics of the system. The surface free energy theory has been widely used in colloid, lubrication, adhesive coating, and the painting industry for many years.

The surface free energies of aggregates are mainly comprised of an apolar component and a polar (acid-base) component. Equation 3.1 is used to describe the total surface free energy and its components:

$$\Gamma = \Gamma^{LW} + \Gamma^{AB} \tag{3.1}$$

where Γ = surface free energy of aggregate,

Γ^{LW} = Lifshitz-van der Waals components of the surface free energy (apolar), and

Γ^{AB} = acid-base component of the surface free energy (polar).

The Lifshitz-van der Waals force contains at least three components: London dispersion force, Debye induction force, and Keesom orientation force.

The acid-base interaction includes all interaction of electron donor (proton acceptor) - electron acceptor (proton donor) type bonds including hydrogen bonding. The relationship between the polar surface energy, Γ^{AB}, and its components is in Equation 3.2.

$$\Gamma^{AB} = 2\sqrt{\Gamma^{+}\Gamma^{-}} \tag{3.2}$$

where Γ^{+} = Lewis acid component of surface energy interaction and

Γ^{-} = Lewis base component of surface energy interaction.

3.2 Surface Free Energy Measurement of Soil

Surface free energies of soils are measured using the Universal Sorption Device (USD) method. The USD method utilized the gas adsorption characteristics of selected solvents, whose surface free energy components are known, to indirectly measure the surface free energies of soil particles.

The USD was developed to measure the surface free energy of soil. A schematic view of the USD is shown in Figure 3.1. It is mainly comprised of a so-called Rubotherm magnetic suspension balance, its data acquisition computer, a pressure transducer, vacuum regulator, solvent container, and temperature control circulator. The balance is able to measure up to 200g with accuracy of 10^{-5} g and the accuracy of the pressure transducer is 0.1% with range of 15 psi. The whole system is basically connected with quarter inch copper tubing. The sample cell temperature is kept at 25 °C and the temperature of the other parts is kept at a few degrees higher than the sample to avoid vapor condensation on the transportation tubing wall. A 6.4 L stainless steel container is connected to the vapor transferring tube as ballast to keep the vapor pressure stable in the condition that either an adsorption or a desorption occurs. This container is effective also in preventing a sudden unexpected large change of pressure when the pressure is increased or decreased to get isotherms. After equilibrium is established

between the sample and the adsorptive vapor (so the sample's weight did not change with time), the difference in weight of the sample prior to and after treatment is regarded as the amount adsorbed.

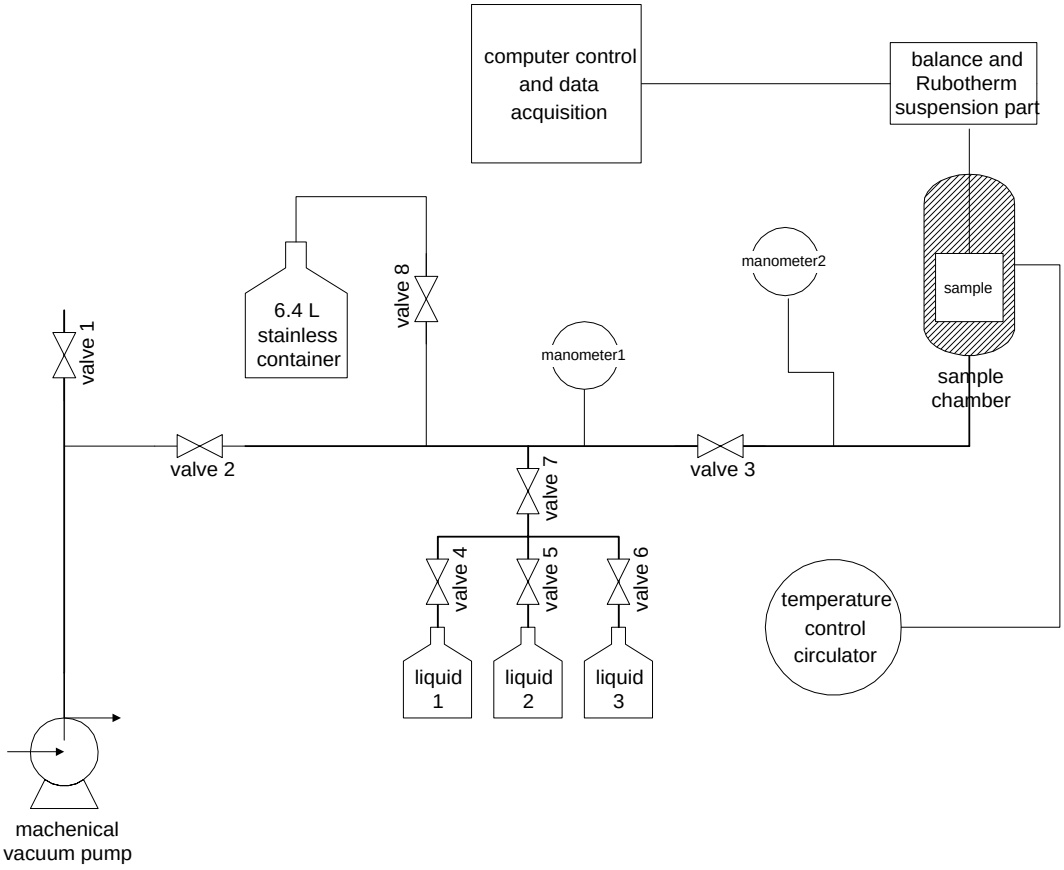

Figure 3.1 Schematic View of USD

Theoretically, the surface free energy of soils will not be affected by the size of the soil because the size is accounted for during the calculation process. The total and component surface free energies of three solvents: n-Hexane, Methyl Propyl Ketone

(MPK), and distilled water at 25^{o}C, were obtained from the literature and are listed in Table 3.1.

Table 3. 1 Surface Free Energies of the Solvents for Soils (Units: ergs/cm^2)

Absorbate	Γ	Γ^{LW}	Γ^{AB}	Γ^{+}	Γ^{-}
n-Hexane	18.4	18.4	0	0	0
MPK	24.7	24.7	0	0	19.6
Water	72.8	21.8	51.0	25.5	25.5

3.3 Testing Procedure

About 100 g of each type of soils to be used in the surface free energy tests by the USD method is prepared. The soils are washed using distilled water and then put into a 120^{o}C oven and dried for at least 8 hours. The soil samples are then moved into a vacuum desiccator at about 1 torr and 120^{o}C for at least 24 hours to degas. The soil sample container is washed carefully with distilled water and acetone and dried in an oven at 120^{o}C for an hour. Then soil with its weight measured is placed in the container. Once the container is hung on the hook of the magnetic suspension balance, the balance is activated and calibrated. Next the vacuum pump is used to evacuate below one torr for one day while the chamber is heated to 60^{o}C. Then the chamber temperature is reduced and maintained at 25^{o}C under vacuum of below one torr for eight hours. From this point, solvent vapor is injected into the system until pressure reaches the first predetermined value by using a micro-adjustment valve. After the steady state adsorption mass is reached and measured by the system, the pressure is changed to the next setting point. Tests are repeated with the remaining solvents in the following order: n-hexane, MPK, and water. The measured results are used to calculate the surface free energy components of the soil.

3.4 Theory and Calculation of USD Method

In this research, three solvents, n-hexane (apolar), MPK (mono polar), and water (bi polar) were selected. From the test, measurement of the specific amount of solvent adsorbed on the surface of the adsorbent and simultaneously measurement of vapor pressure at the surface of soil are taken. Once measurements are taken, correction of the adsorption data for solvent vapor buoyancy by using the generalized Pitzer correlation (Smith et al. 1996) is made. Buoyancy corrected experimental data were reduced and plotted and two parameter BET model was applied to the experimental data. According to BET theory, adsorption can be represented by the following linear equation:

$$\frac{p}{n(p_o - p)} = \left(\frac{c-1}{n_m c}\right)\frac{p}{p_o} + \frac{1}{n_m c} \tag{3.3}$$

where p = vapor pressure,

p_o = saturated vapor pressure,

n = specific amount adsorbed on the surface of the adsorbent, and

n_m = monolayer specific amount of vapor adsorbed on the surface of soil. Equation 3.3 is typically applicable over the range of p/p_o from 0 to 0.5, so that n_m can be obtained from the slope and the intercept of the straight line best fitting the plot $p/n(p-p_o)$ versus p/p_o.

For the case of a vapor adsorbed on a solid, the spreading pressure at saturation vapor pressure, π_e, for each solvent can be calculated using the following Gibbs adsorption equation:

$$\pi_e = \frac{RT}{A}\int_0^{p_o} \frac{n}{p}\,dp \tag{3.4}$$

where π_e = spreading pressure at saturation vapor pressure of the solvent,

R = the universal gas constant,

T = the absolute temperature, and

A = the specific surface area of the adsorbent.

This equation indicates that for any equilibrium pressure and temperature, the spreading pressure is dependent on the surface excess concentration n. The value of spreading pressure, for any surface excess concentration, may be calculated from the adsorption isotherm drawn with the coordinates n/p and p, by integrating between the initial state (n=0, p=0) and the liquid's saturation vapor pressure p_o.

In the vapor adsorption process, the work of adhesion of a liquid on a solid, W_A, in terms of the surface tension (surface free energy) of the liquid, Γ_l, and the equilibrium spreading pressure of adsorbed vapor on the solid surface, π_e, is shown as in Equations 3.5 and 3.6.

$$W_A = \pi_e + 2\Gamma_l = \Delta G_{sl} \tag{3.5}$$

$$\Delta G_{sl} = \Delta G_{sl}^{LW} + \Delta G_{sl}^{AB} = 2\sqrt{\Gamma_s^{LW}\Gamma_l^{LW}} + 2\sqrt{\Gamma_s^{+}\Gamma_l^{-}} + 2\sqrt{\Gamma_s^{-}\Gamma_l^{+}} \tag{3.6}$$

where the subscript s and l refer to solid and liquid, respectively. The superscripts LW, AB, +, and -, represents the Lifshitz-van der Waals components, Acid-Base component, Acid component, and Base component of surface free energy, respectively.

In case that the adsorptive is apolar where Γ^+ and Γ^- become zero, we can get the Lifshitz- van der Waals component of surface free energy of the solid:

$$\Gamma_s^{LW} = \frac{(\pi_e + 2\Gamma_l)^2}{4\Gamma_l^{LW}} \tag{3.7}$$

In the case that the adsorptive is mono polar in which $\Gamma_l^+ = 0$ (or $\Gamma_l^- = 0$) we can get the acid component of the surface free energy of a solid:

$$\Gamma_s^+ = \frac{(\pi_{em} + 2\Gamma_{lm} - \sqrt{\Gamma_s^{LW}\Gamma_{lm}^{LW}})^2}{4\Gamma_{lm}^-} \tag{3.8}$$

In which the subscript m means the monopolar adsorptive. In the case that the adsorptive is bipolar in which neither $\Gamma_l^+ = 0$ nor $\Gamma_l^- = 0$, we can get the base component of surface free energy:

$$\Gamma_s^- = \frac{(\pi_{eb} + 2\Gamma_{lb} - 2\sqrt{\Gamma_s^{LW}\Gamma_{lb}^{LW}} - 2\sqrt{\Gamma_s^+\Gamma_{lb}^-})^2}{4\Gamma_{lb}^+} \tag{3.9}$$

At last, we can get the total surface energy of the solid:

$$\Gamma_s = \Gamma_s^{LW} + 2\sqrt{\Gamma_s^+\Gamma_s^-} \tag{3.10}$$

3.5 Verification of USD

Uniformly sized standard glass balls with diameter of 4 mm and density of 2.5792 g/cm^3 were prepared in order to verify the accuracy and precision of the USD. The glass ball sample was obtained from VWR Co., Inc. As mentioned, three kinds of adsorptives: n-hexane, which is apolar, was obtained from EM SCIENCE, A Division of EM Industries, Inc; methyl propyl ketone (MPK), which is monopolar, was obtained from Aldrich Chemical Co., Inc; distilled water, which is bipolar, was obtained from biochemical group in Department of Chemical Engineering, Texas A&M University.

3.5.1 Testing Results of Glass Balls

There were 6 testing results of distilled water. As in the Figure 3.2, curves 2 and 5 were results of adsorption tests in which the adsorption mass were measured at each vapor pressure step while the vapor was introduced into the sample chamber of the USD. Curves 1, 3, and 4 were conducted as desorption tests in which the desorption mass was

measured at each vapor pressure step which the vapor was vacuumed out of the sample chamber of the USD. Curve 6 shows that adsorption test was conducted first followed by a desorption test. Figure 3.2 shows that all the curves are close to each other. Also shown in the figure is that the desorption curves are not significantly different from the adsorption curves. This means that there is small hysteresis between the adsorption and desorption tests. Over all test results with distilled water were repeatable and the accuracy and precision the USD was established.

Figure 3.3 shows the four testing results of n-hexane with glass balls. Curves 1 and 3 were the results of adsorption tests and curves 2 and 4 were results of the desorption tests. Figure 3.4 illustrates the results of seven tests with MPK. Curves 2, 3, 5, and 6 were adsorption tests and curves 1, 4, and 7 are desorption tests. From two figures, it can be said that tests were pretty much repeatable. Again, hysteresis are very small. The BET theory is used to measure the SSA (Specific Surface Area). Figures 3.5, 3.6, and 3.7 show the curve fitting of the BET equation.

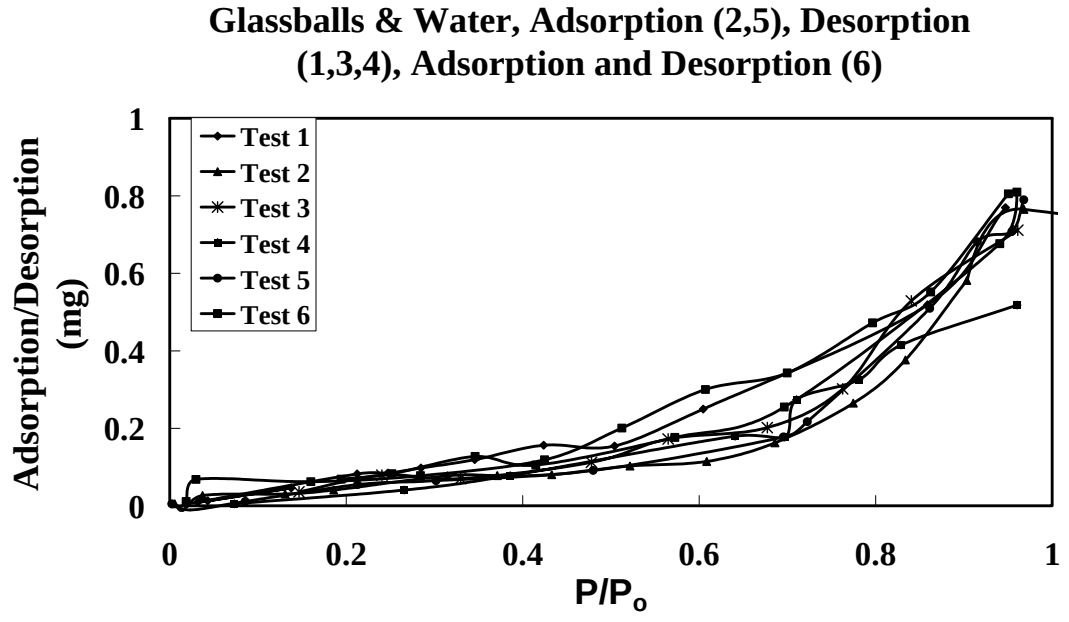

Figure 3.2 The Adsorption and Desorption Isotherms of Water Vapor onto Glass Balls

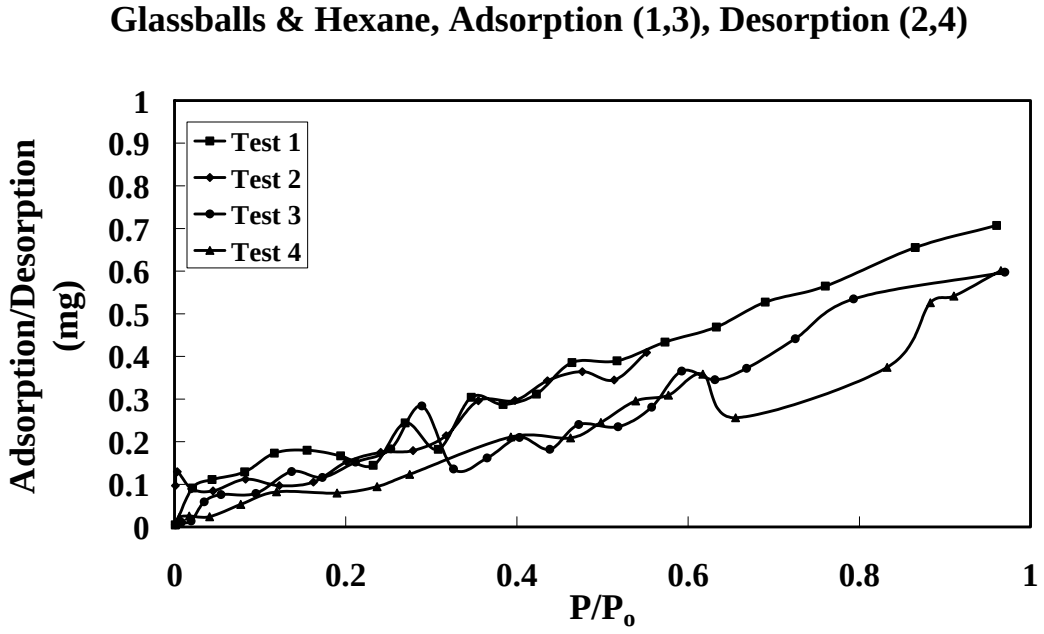

Figure 3.3 The Adsorption and Desorption Isotherms of n-Hexane Vapor onto Glass Balls

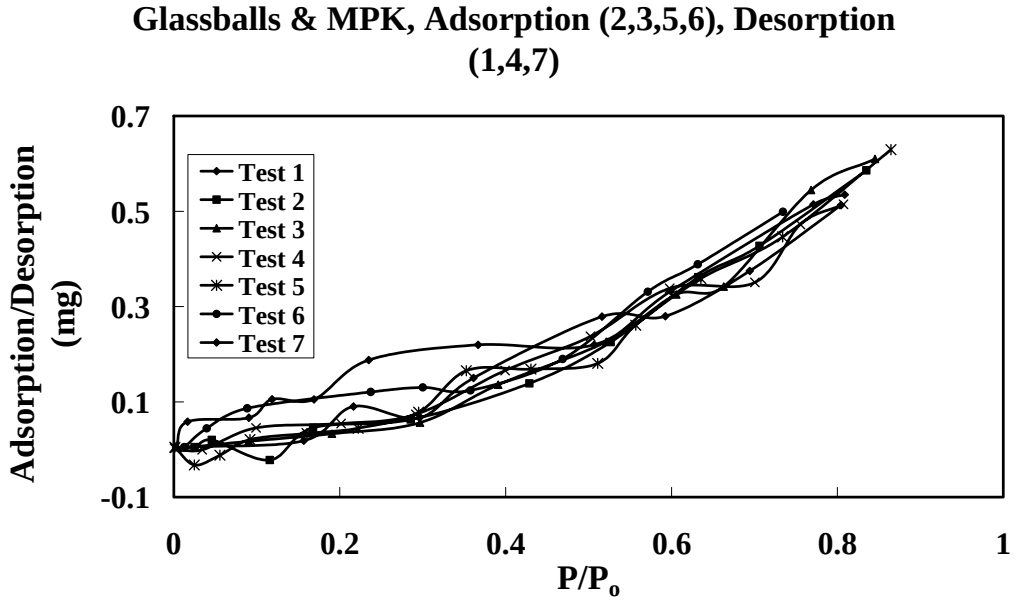

Figure 3.4 The Adsorption and Desorption Isotherms of MPK Vapor onto Glass Balls

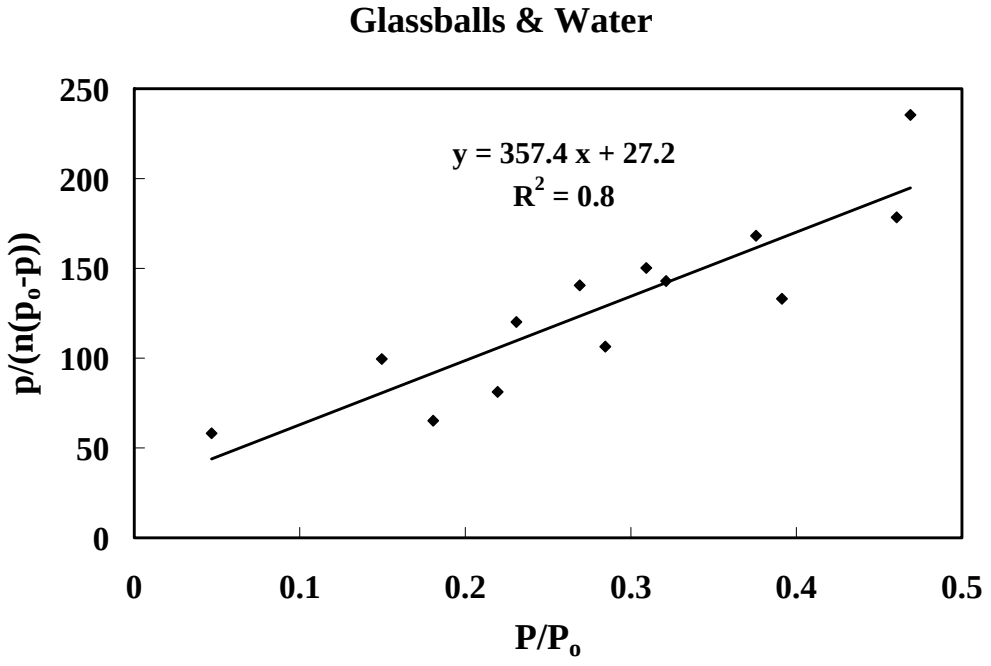

Figure 3.5 The Curve Fitting of BET Theory of Water Vapor onto Glass Balls

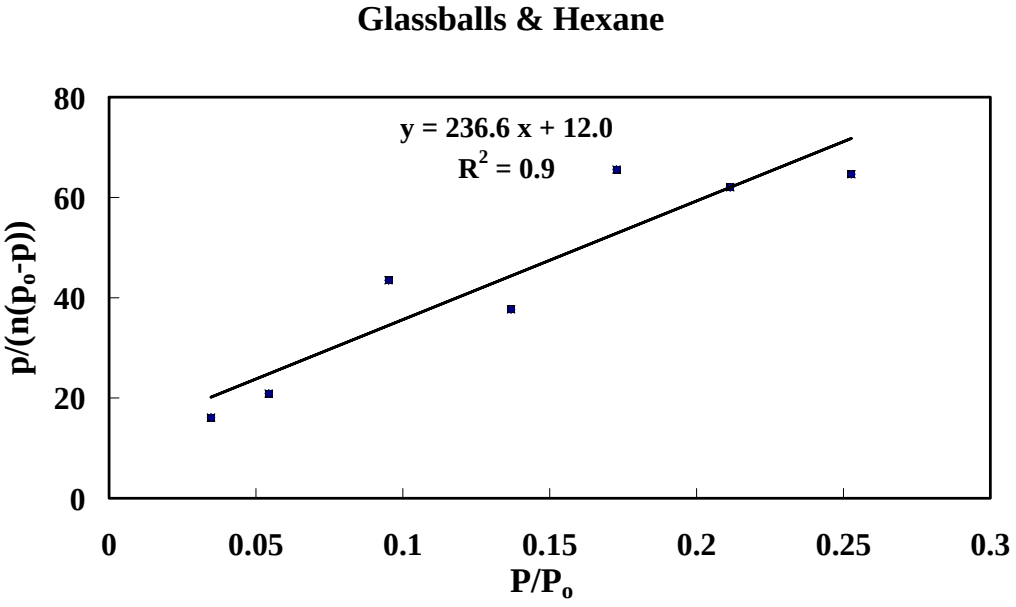

Figure 3.6 The Curve Fitting of BET Theory of n-Hexane Vapor onto Glass Balls

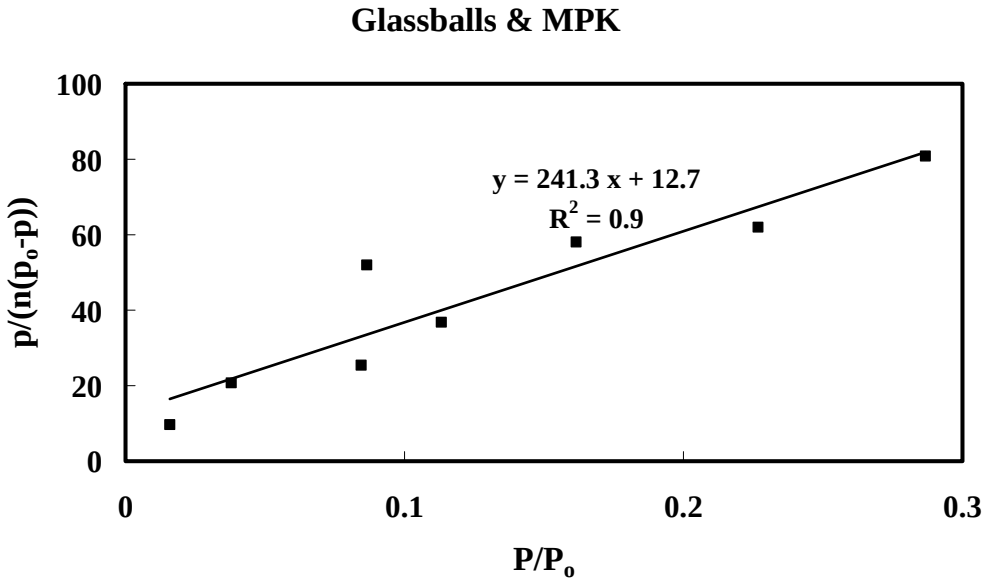

Figure 3.7 The Curve Fitting of BET Theory of MPK Vapor onto Glass Balls

Based on the above test results of distilled water, n-hexane, and MPK, the specific surface area, spreading pressure, and the surface free energy and its components for the glass balls were calculated and are tabulated in Table 3.2 and 3.3.

Table 3.2 Specific Surface Area and Spreading Pressure of the Glass Balls

	$A(m^2/g)$	π_e (ergs/cm^2)
Water	0.0061	280
n-Hexane	0.012	89.3
MPK	0.0106	124.4

Table 3.3 Surface Energy and Its Components of the Glass Balls (Unit: ergs/cm^2)

Γ^{LW}	Γ^{+}	Γ^{-}	Γ^{AB}	Γ
216.1	9.8	646.3	159.1	375.1

3.6 Surface Free Energy of Soil

USD was used to measure the surface free energy of soil. Soil samples were obtained as described in the following. Three soil samples are prepared: composite sample, sand sample, and clay sample. The composite sample is the composite of sand and clay sizes and a raw sample, which was collected from the Riverside Campus of Texas A&M University. The sand sample was the soil that passed the #40 sieve and was retained on the #200 sieve. A total of 200 grams of soil were collected and soaked in distilled water. After a night of soaking, it was stirred well and then sieved over a #200 sieve and the water was caught in a larger beaker. Sand was washed several times until the water was clear. Then the sieve was placed with the sand on it in the oven along with the beaker with the water and clay. Once dried, a clay sample and a clean sand sample were obtained. No measurements were made on the clay sizes.

Typical adsorption and desorption isotherms with the sand and the composite samples are shown in Figures 3.8 through 3.19. Unlike the results of glass balls, hysteresis is observed in all three isotherms. However, in this research, adsorption data were used to calculate specific surface areas and surface free energies.

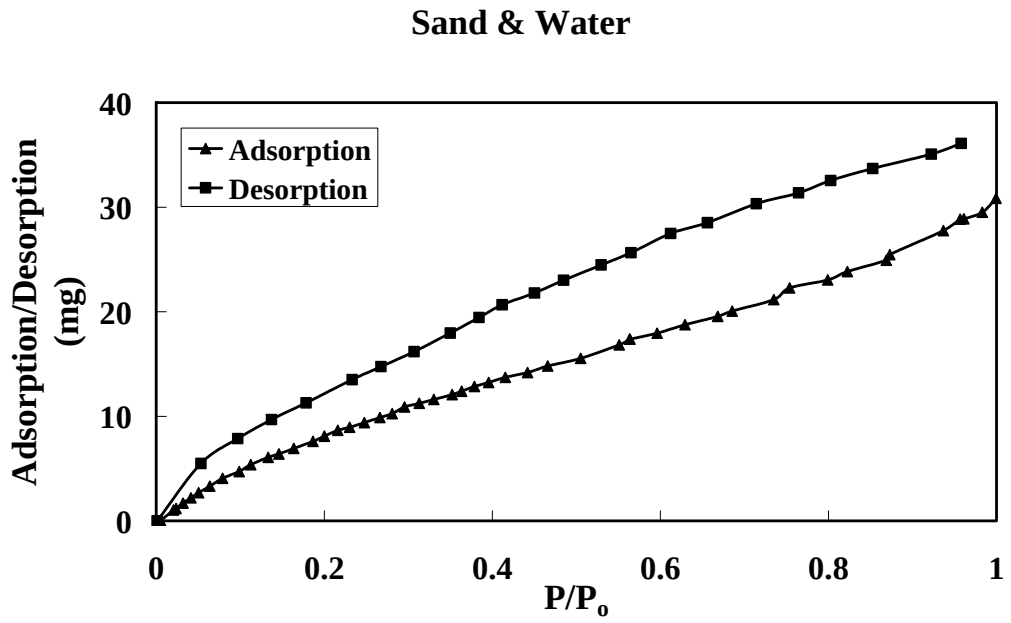

Figure 3. 8 The Adsorption and Desorption Isotherms of Water Vapor onto Sand

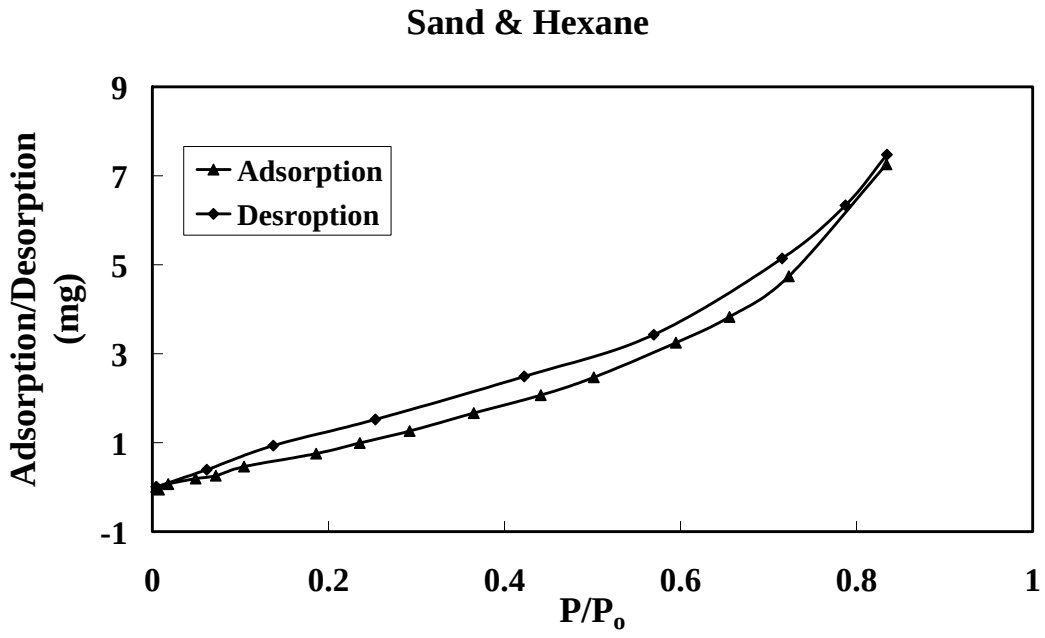

Figure 3. 9 The Adsorption and Desorption Isotherms of n-Hexane Vapor onto Sand

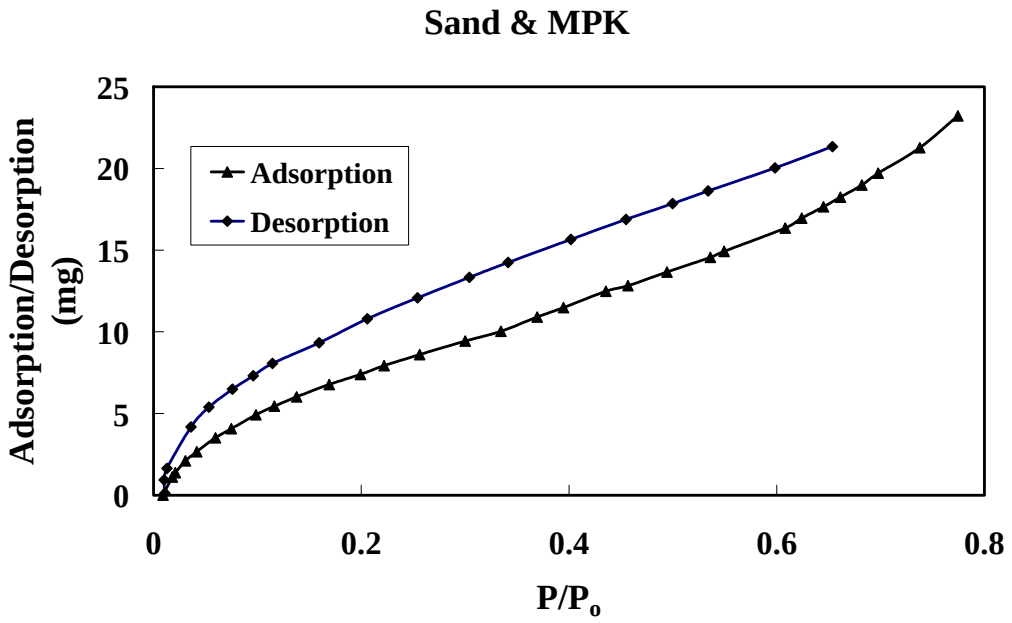

Figure 3. 10 The Adsorption and Desorption Isotherms of MPK Vapor onto Sand

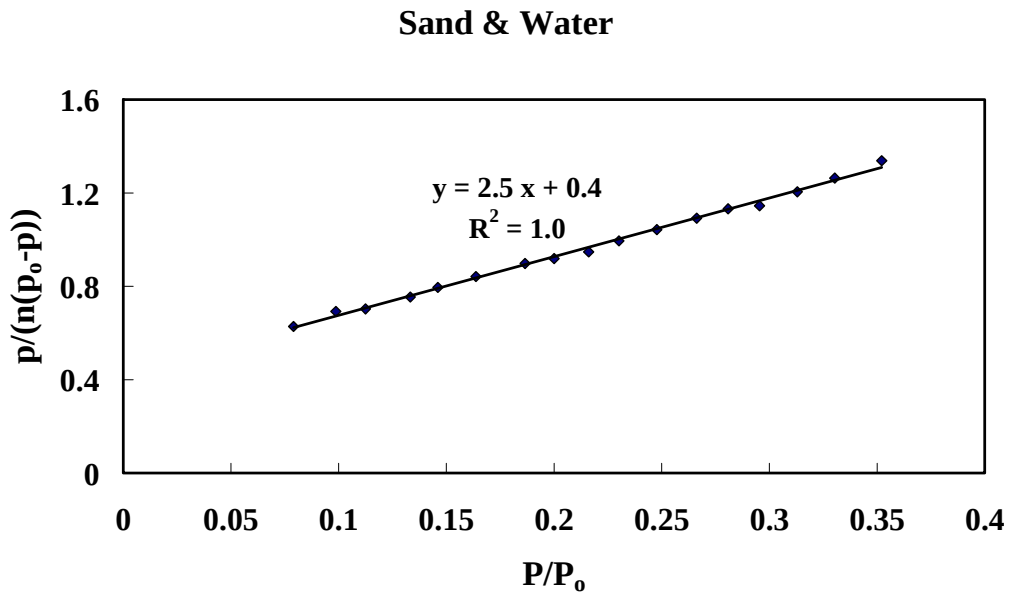

Figure 3. 11 The Curve Fitting of BET Theory of Water Vapor onto Sand

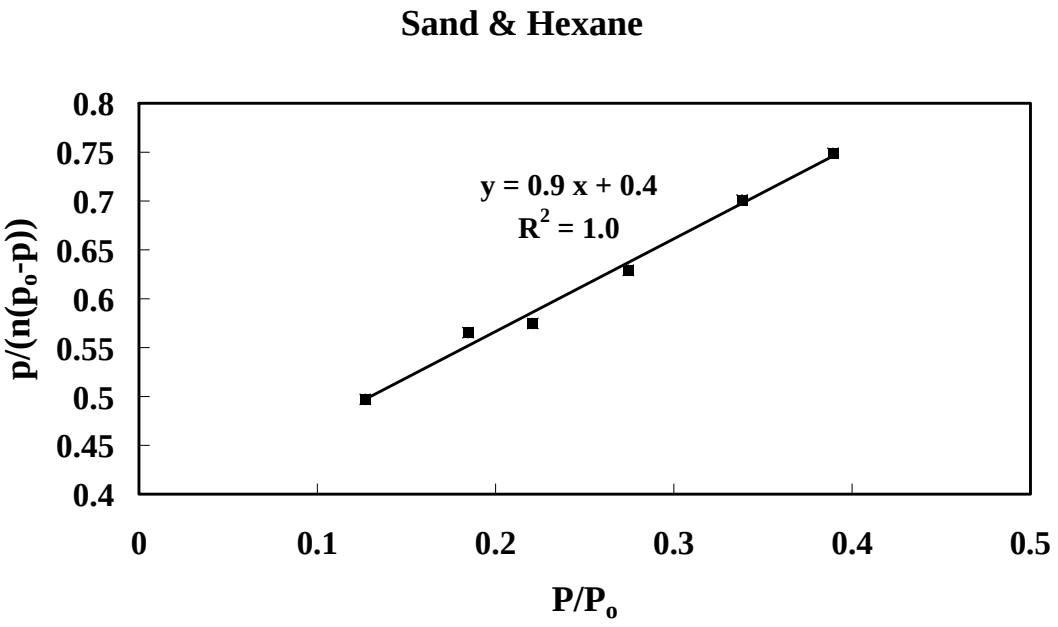

Figure 3. 12 The Curve Fitting of BET Theory of n-Hexane Vapor onto Sand

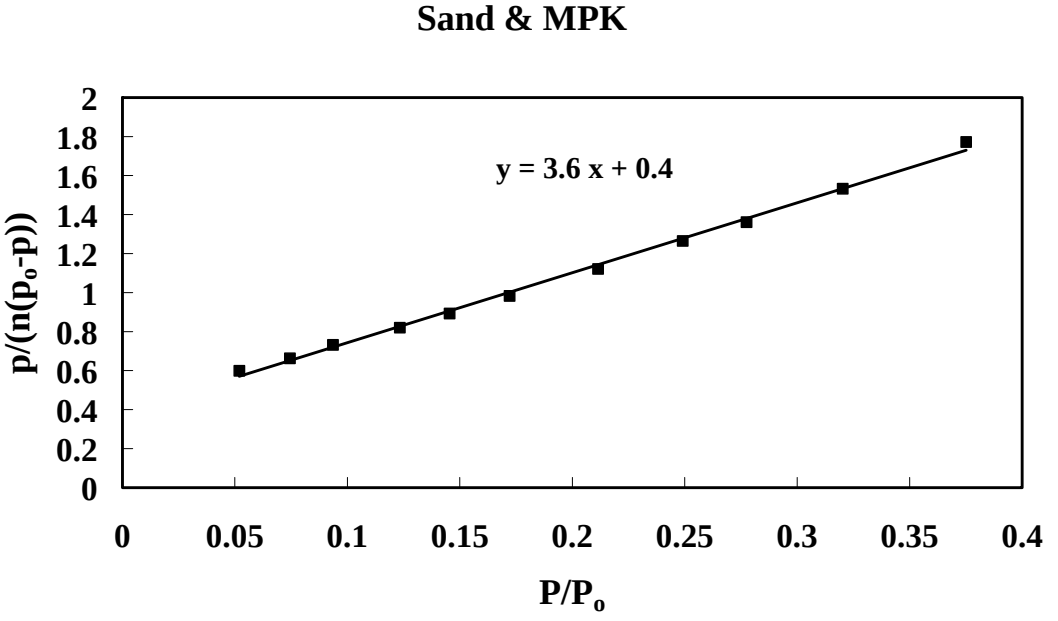

Figure 3. 13 The Curve Fitting of BET Theory of MPK Vapor onto Sand

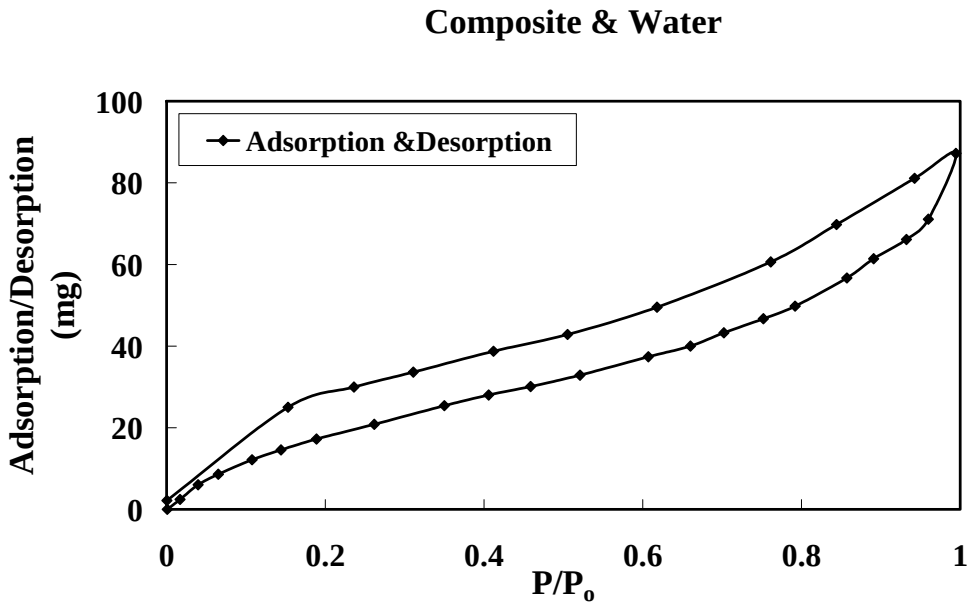

Figure 3. 14 The Adsorption and Desorption Isotherms of Water Vapor onto the Composite Soil Sample

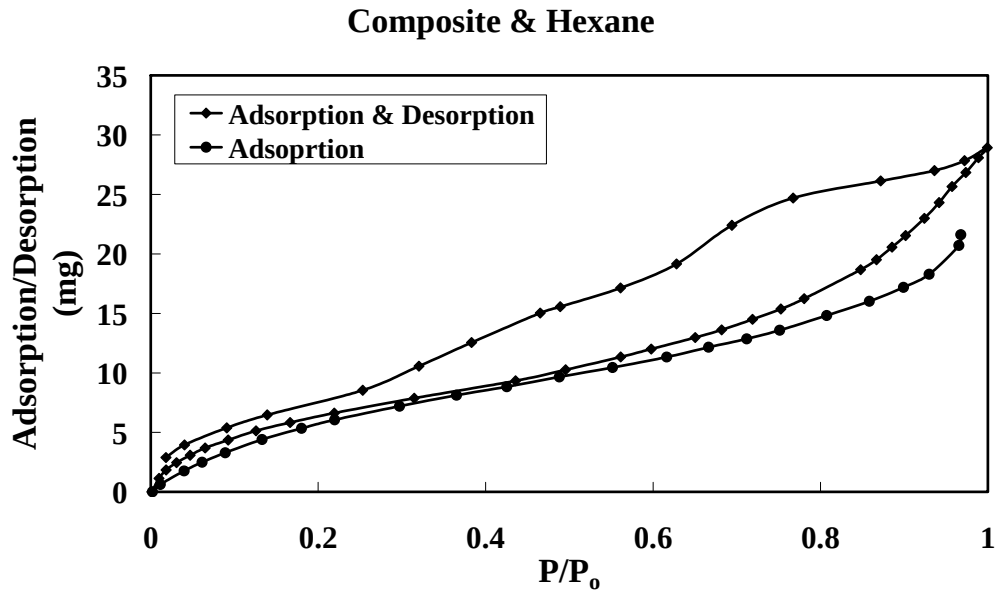

Figure 3. 15 The Adsorption and Desorption Isotherms of n-Hexane Vapor onto Composite Soil Sample

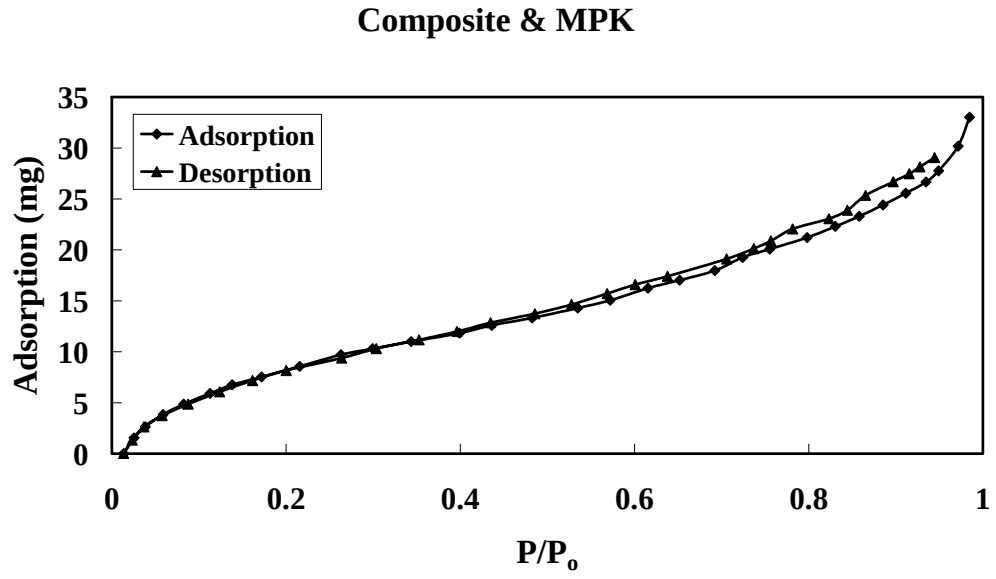

Figure 3. 16 The Adsorption and Desorption Isotherms of MPK Vapor onto the Composite Soil Sample

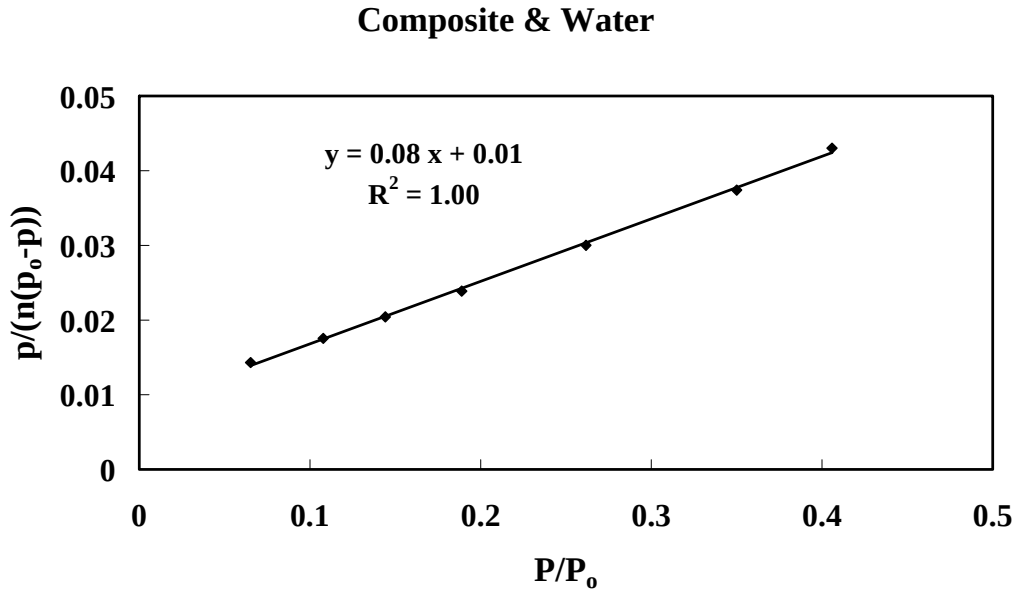

Figure 3. 17 The Curve Fitting of BET Theory of Water Vapor onto the Composite Soil Sample

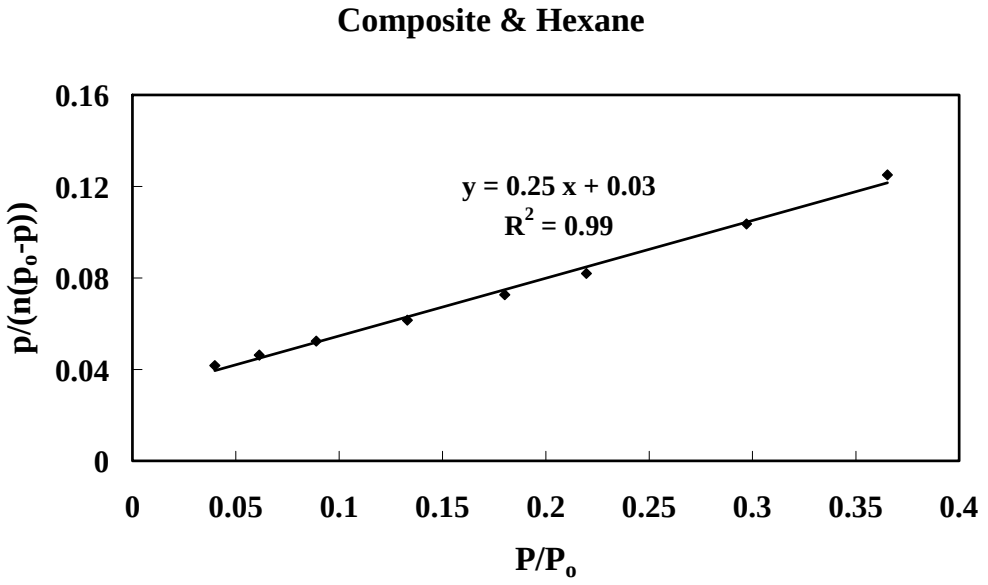

Figure 3. 18 The Curve Fitting of BET Theory of n-Hexane Vapor onto the Composite Soil Sample

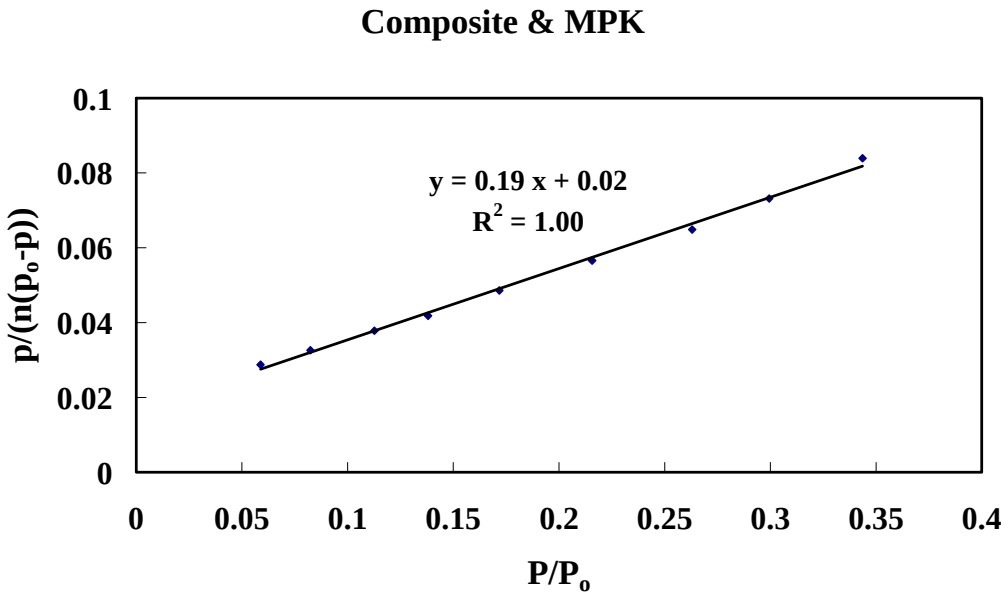

Figure 3.19 The Curve Fitting of BET Theory of MPK Vapor onto Composite Soil Sample

The specific surface area and spreading pressure of the sand and composite soil using the adsorption isotherm of the three solvents are listed in Table 3.4.

Table 3.4 Specific Surface Area and Spreading Pressure of the Sand and Composite

	Sand		Composite	
	SSA (m^2/g)	π_e ($ergs/cm^2$)	SSA (m^2/g)	π_e ($ergs/cm^2$)
Water	1.18	124.7	34.3	173
n-Hexane	2.02	37.5	9.32	45.1
MPK	0.72	39.9	10.7	50.4

Table 3.5 Surface Free Energies of the Sand and Composite

	Γ^{LW}	Γ^{+}	Γ^{-}	Γ^{AB}	Γ
Sand	74	1.51	286.8	41.6	115.6
Composite	91.1	0.31	536.2	25.7	116.8

Soil surface energies are affected by their particle sizes as shown in Table 3.5. In general, as the particle size decrease, the specific surface area of the particle increases and the component of surface energies and total surface free energy increase except for the acid component of surface free energy.

3.7 Particle Model and USD Test Results

Kelvin's equation in Equation 2.1 enables us to calculate the relative humidity (p/p_o) with given adsorbent properties (ie, Water and n-Hexane). In this section, the particle model was used to calculate the relative humidity with the given adsorbent properties. This is compared to the USD test data of glass ball and soil.

Figure 3.20 shows the plot of relative humidity against water or liquid content of the glass balls. The spherical particle model is used to calculate the gravimetric liquid content and relative humidity. As in the Figure 3.20, there is a discrepancy in the measurement and the calculated water or liquid content from the particle model. Water and liquid content were calculated considering a tetrahedral packing of particles. One possible explanation of this difference is due to the idealization of particle model.

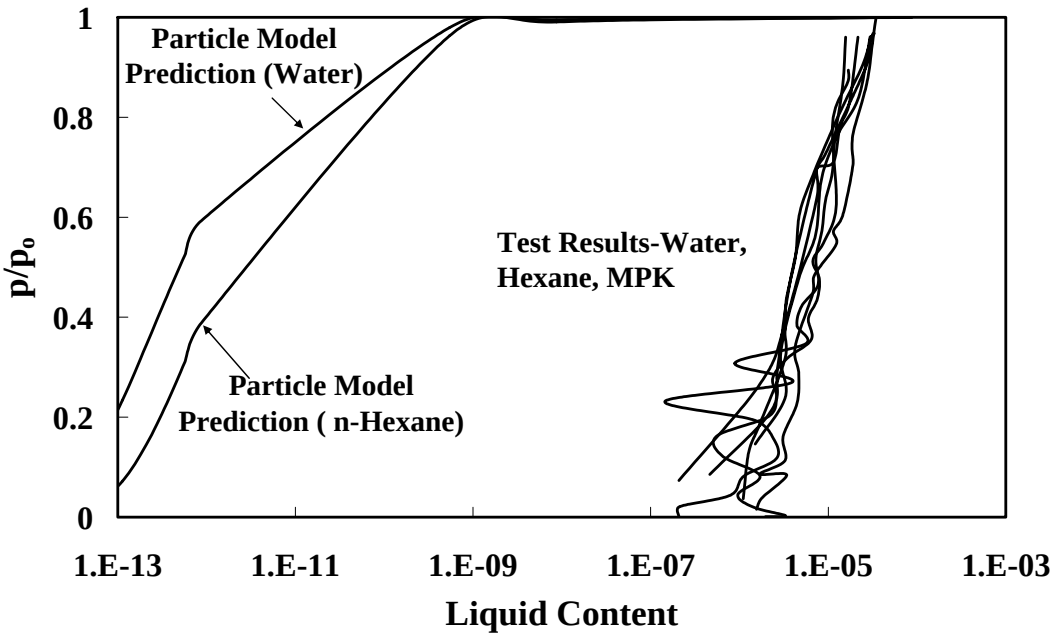

Figure 3.20 Relationship Between Normalized Vapor Pressure and Liquid Content (Glass Balls)

In the particle model, the assumption is that no water exists around particles except those areas bounded by particles and the air-water interface. However, the reality is not likely this condition. During adsorption or desorption, there will be adsorptives on

the surface of adsorbents (Glass Balls) and this will contribute to the increase of liquid content. Another difference raises the problem of texture: whether the glass balls are smooth enough, even though they were washed with distilled water and acetone before the tests.

The images of the Scanned Electronic Microscope, which are shown in Figure 3.21, show that the glass balls are far from smooth. There are many dust particles on its surface, which may contaminated by the dust in air. Also there are many pits on the surface of the glass balls. Both the dust particles and the pits will increase the liquid content during an adsorption and a desorption process. The lack of smoothness of surface also results in different specific surface area. From the consideration of a perfectly smooth surface of sphere with radius of 2.0 mm and density of 2.5792 g/cm^3, the calculated specific surface area was $5.8\times10^{-4} m^2/g$. This specific surface area is 10 to 20 times less than less than those measured.

Figure 3.22 shows the plot of the relative humidity against liquid content of sand. In the calculation of water content using the particle model, the radius of the particle was chosen 75 μm. As in the case of glass balls, the predicted liquid content and measured value are different. The liquid adsorbed on the sand is greater than the predicted. This results in an increase in specific surface area. This also means that sand particles have rugged surface.

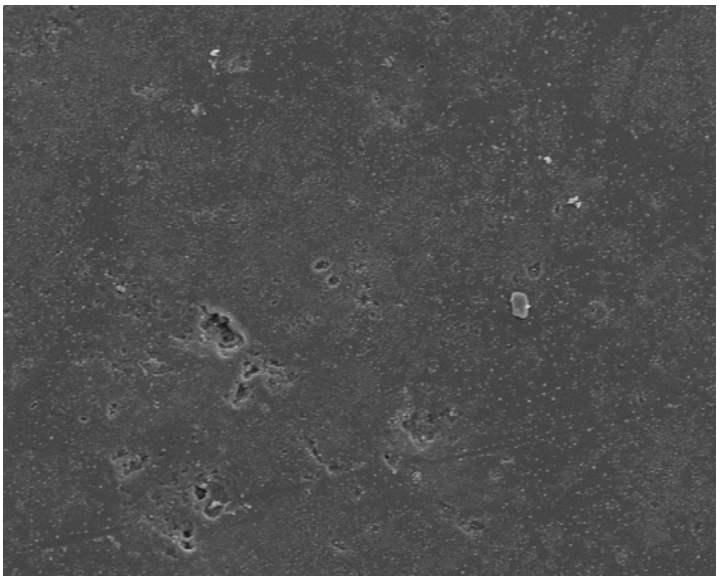

a)

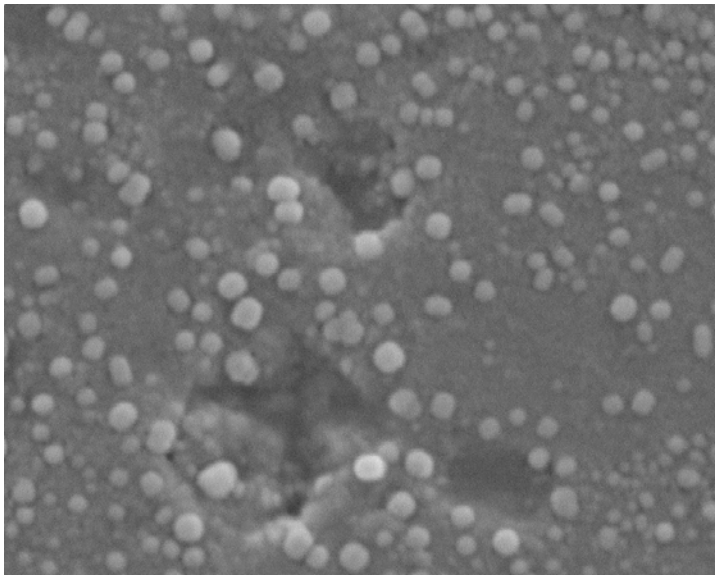

b)

Figure 3.21 Scanning Electron Microscopy Picture of Glass Balls: a) Enlargement of x900; b) Enlargement of x15,000

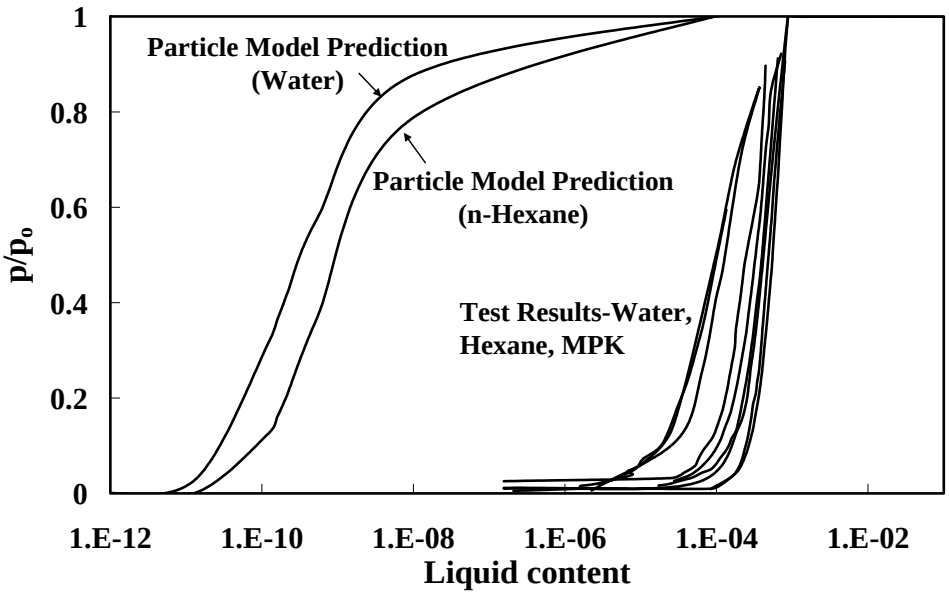

Figure 3.22 Relationship Between Normalized Vapor Pressure and Liquid Content (Sand)

3.8 Cohesion and Adhesion

The interfacial strength between water and aggregate is called adhesion. The strength inside the water itself is called cohesion. The cohesive and adhesive bonding among water-soil systems mainly arises from Lifshitz-van der Waals intermolecular forces and acid-base intermolecular forces. In certain circumstances, for example, the interactions between colloidal particles dispersed in a polar liquid, the electrostatic (EL) interaction of the particles must be taken into account. In this study, EL interactions are not dominant and neglected.

The free energy of cohesion is the formation of a cohesive unit area of the union of two bodies of the same material under the vacuum condition shown in Figure 3.23 and the following Equation 3.11 (Good and van Oss 1991):

$$\Delta G_i^c = 2\Gamma_i \tag{3.11}$$

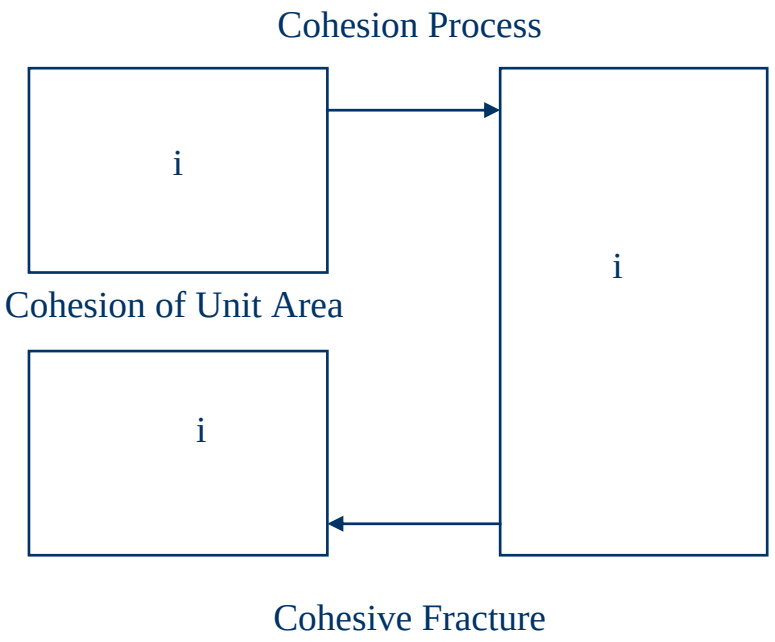

Figure 3.23 Graphical Representation of Cohesive Process

The free energy of cohesion has two components, the Lifshitz-van der Waals components, ΔG_i^{cLW}, and Acid-Base components, ΔG_i^{cAB}, as shown in Equation 3.12.

$$\Delta G_i^c = \Delta G_i^{cLW} + \Delta G_i^{cAB} \tag{3.12}$$

Similar to cohesion, the surface free energy of adhesion between the water and soil system corresponds to the creation of a unit crack area at the interface between two dissimilar bodies in a vacuum condition as shown in Figure 3.24. Adhesion is defined by the following equations:

$$\Delta G_{ij}^a = \Gamma_i + \Gamma_j - \Gamma_{ij} \tag{3.13}$$

$$\Delta G_{ij}^a = \Delta G_{ij}^{aLW} + \Delta G_{ij}^{aAB} \tag{3.14}$$

where Γ_{ij} = the interfacial surface energy between i and j.

There are two components for interfacial surface free energy as described in Equation 3.15.

$$\Gamma_{ij} = \Gamma_{ij}^{LW} + \Gamma_{ij}^{AB} \tag{3.15}$$

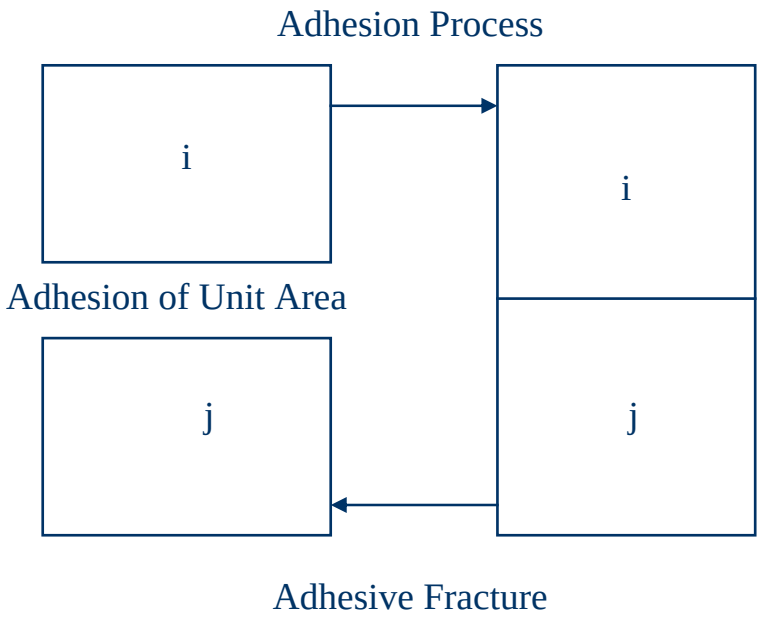

Figure 3.24 Graphical Representation of Adhesive Process

The Berthelot geometric mean is used to calculate the Lifshitz-van der Waals components of surface free energy as follows (Good 1992):

$$\Gamma_{ij}^{LW} = \left(\sqrt{\Gamma_i^{LW}} - \sqrt{\Gamma_j^{LW}}\right)^2 \tag{3.16}$$

$$\Delta G_{ij}^{aLW} = 2\sqrt{\Gamma_i^{LW}\Gamma_j^{LW}} = \sqrt{\Delta G_i^{aLW}\Delta G_j^{aLW}} \tag{3.17}$$

Equations 3.18 and 3.19 define the acid-base component of surface free energy:

$$\Gamma_{ij}^{AB} = 2(\sqrt{\Gamma_i^+} - \sqrt{\Gamma_j^-})(\sqrt{\Gamma_i^-} - \sqrt{\Gamma_j^+}) \tag{3.18}$$

$$\Delta G_{ij}^{aAB} = 2\sqrt{\Gamma_i^+ \Gamma_j^-} + 2\sqrt{\Gamma_i^- \Gamma_j^+} \tag{3.19}$$

The surface energy of adhesion reflects the adhesive bond between the water and soil particles. The higher the surface energy of adhesion, the higher the bond between the water and soil particles will be. The work of adhesion between particles and water are presented in Table 3.6.

Table 3.6 Work of Adhesion Between Solid Particles and Water (Unit: ergs/cm2)

	G^{AB}	G^{LW}	G
Glass ball	272	139	410
Sand	189	81	270
Composite	232	89	321

CHAPTER IV
LIQUEFACTION LITERATURE REVIEW AND CONE TIP RESISTANCE

This chapter lays out the definition of liquefaction. In particular, the liquefaction definition in unsaturated soils is presented. In the light of assessment of the liquefaction potential, a review of a stress based liquefaction evaluation is introduced. Subsequently, methods to calculate the tip resistance of cone penetration test are presented. Finally, the chapter is concluded with the liquefaction potential evaluation of unsaturated soils based on cone penetration prediction using the centerline solution for sandy soil.

4.1 Liquefaction Definition in Unsaturated Soil

The concept of liquefaction drew worldwide attention after two large earthquakes in Alaska, USA and Niigata, Japan. Since these earthquakes, a lot of work has been done in the past 40 years. Much was learned through the vast research works but there seems to be a discrepancy in the literature relating to a standard definition for liquefaction. The proper definition for soil liquefaction has been the subject of a continuing debate within the geotechnical profession.

The word liquefaction literally means a state change from solid to a liquid. Castro (1975) stated that true liquefaction refers to the flow of soil under a static shear stress that exceeds the undrained residual shear resistance of a contractive soil. He observed large post peak strength loss and subsequent positive pore pressures during undrained shear of soil above the constant void ratio line. Liquefaction of loose cohesionless soils can be observed under both monotonic and cyclic loading. Castro and Poulus (1977) restricted the use of the term liquefaction to describe flow failure.

The propensity of dense, saturated sands to progressively soften in undrained cyclic shear, but achieve limiting strains under subsequent static loading, is more precisely described as cyclic mobility (Castro 1975 and Castro and Poulus 1977). Soils subjected to cyclic mobility will first soften under cyclic loading, but stiffen under undrained monotonic loading. Generally, cyclic mobility is considered as liquefaction. It

shows built up of pore pressure during undrained cyclic shear even though it does not result in catastrophic failure like a flow failure does.

In unsaturated soils, the occurrence of flow liquefaction is not likely to happen since the increase of pore pressure is very small compared to saturated soil. However, unsaturated soil will be still subjected to loss of its strength under earthquake loading depending on the suction level in the soils. The liquefaction in unsaturated soil will be the presence of large strain with evidence of settlement or lateral spreading. Hence, liquefaction in unsaturated soil is a cyclic mobility type of failure.

4.2 Evaluation of Liquefaction Potential

Estimation of liquefaction is analogous to a slope stability investigation, since it can be represented as a factor of safety. The variables that are required are demand and capacity. Demand is the seismic stress imparted by an earthquake, which is expressed in terms of the Cyclic Stress Ratio (CSR). Capacity is the resistance of a soil layer and is expressed in terms of the Cyclic Resistance Ratio (CRR). The factor of safety is simply the ratio of CSR to CRR.

Numerous methods have been proposed for evaluating the liquefaction potential of soil deposits. The methods are the stress based procedure, the strain based procedure, and the energy based procedure. In the following section, only the stress based procedure is presented.

4.2.1 Stress Based Approach

The most widely used method for evaluating liquefaction is the stress-based approach. This procedure is largely based on empirical observations of laboratory and field data and has been continually refined as a result of newer studies and the increase in the number of liquefaction case histories (NRC 1985, NCEER 1997, and Youd et al. 2001). This approach is conceptually simple. The stress induced by earthquake load is compared to the resistance of the soil.

The amplitude of the earthquake stress is calculated by the Cyclic Stress Ratio (CSR). Seed and Idriss (1971) formulated the following equation for the calculation of the cyclic stress ratio:

$$CSR = \frac{\tau_{ave}}{\sigma_{vo}^{'}} = 0.65 \frac{a_{\max}}{g} \frac{\sigma_{vo}}{\sigma_{vo}^{'}} r_d \qquad (4.1)$$

where CSR = Cyclic stress ratio,

$a_{\max}$ = Peak ground surface acceleration,

g = Acceleration of gravity,

$\sigma_{vo}^{'}$ = Effective vertical stress,

σ_{vo} = Total vertical stress, and

r_d = Stress reduction factor

As shown in Figure 4.1, r_d is a function of depth. The average value of r_d can be calculated using the following equation (NCEER 1997):

$$r_d = 1.0 - 0.00765z \text{ for z} \leq 9.15\text{m}$$
$$r_d = 1.174 - 0.0267z \text{ for } 9.15\text{m} < z \leq 23m$$
$$r_d = 0.744 - 0.008z \text{ for } 23\text{m} < z \leq 30m$$
$$r_d = 0.5 \text{ for z} > 30\text{m} \qquad (4.2)$$

For spread sheet calculation, the following equation, which is based on Equation 4.2 (NCEER 1997), may be used:

$$r_d = \frac{(1.0 - 0.4113z^{0.5} + 0.04052z + 0.001753z^{1.5})}{(1.0 - 0.4177z^{0.5} + 0.05729z - 0.006205z^{1.5} + 0.001210z^{2})} \qquad (4.3)$$

Magnitude Scaling Factors (MSF) are applied to the CSR to consider the duration of the earthquake motions.

$$CSR_{M\,7.5} = \frac{CSR}{MSF} = \frac{\tau_{ave}}{MSF\,\sigma'_{vo}} = \frac{\tau_{M\,7.5}}{\sigma'_{vo}} \tag{4.4}$$

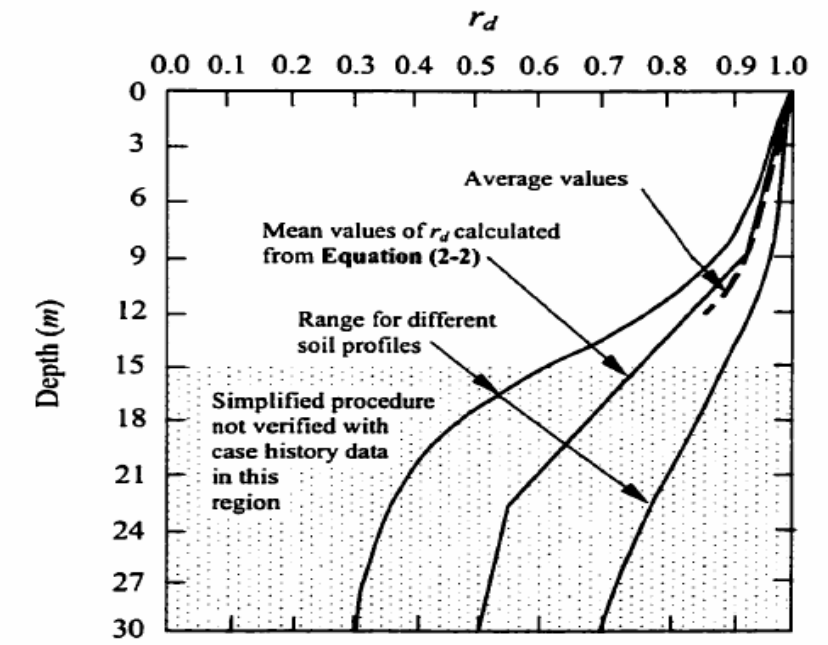

Figure 4.1 r_d versus Depth Curves (NCEER 1997)

Different correlations for MSF have been proposed and presented in Figure 4.2. The average values of the NCEER(1997) recommended range for the MSF can be determined by the following equation:

$$MSF_{ave} = \begin{bmatrix} \left(\frac{MSF_{Andrus-Stokoe} + MSF_{Idriss}}{2} \right) & for \quad M \le 7.5 \\ MSF_{Idriss} & for \quad M \ge 7.5 \end{bmatrix} \tag{4.5}$$

where $MSF_{Andrus-Stokoe} = \left[\frac{M}{7.5} \right]^{-3.3}$

$$MSF_{Idriss} = \frac{10^{2.24}}{M^{2.56}}$$

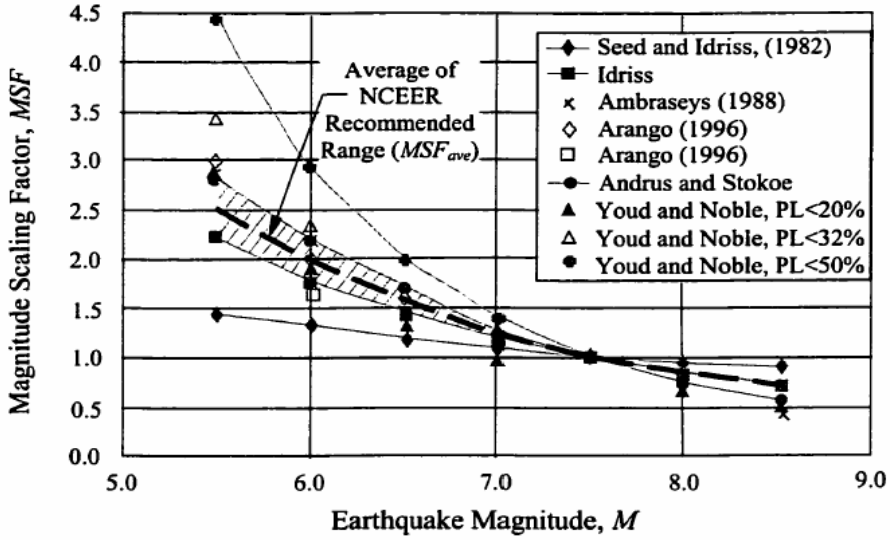

Figure 4.2 Magnitude Scaling Factors Derived by Various Investigators (NCEER 1997)

The resistance of the soil is represented as a Cyclic Resistance Ratio (CRR). Ideally the best method for evaluating CRR is to retrieve and test undisturbed soil specimens in the laboratory. Unfortunately, sampling of undisturbed sand is too difficult to yield good results and preservation of the in situ stress state is literally impossible. As

a result, in situ testing has been the standard practice in the evaluation of liquefaction procedures. Standard Penetration Test (SPT), Cone Penetration Test (CPT), and shear-wave velocity measurements have been used for the evaluation of liquefaction potential investigation procedures. In this research, the CPT based liquefaction potential evaluation is presented.

Figure 4.3 provide curves prepared by Robertson and Wride for direct determination of CRR for clean sand ($FC \le 5\%$) from the CPT data and was developed by analyzing earthquake case histories. For each of the case histories, the cyclic stress ratio was estimated using equation 4.4 and plotted against normalized CPT resistance, q_{c1N}. The CRR curve separates regions of the plot with data indicative of liquefaction from regions indicative of nonliquefaction. The clean sand base curve in Figure 4.3 can be approximated using the following equation (Robertson and Wride 1998):

$$\text{If } q_{c1N} < 50 \qquad CRR_{7.5} = 0.833[(q_{c1N})_{cs}/1000] + 0.05 \qquad (4.6\text{ a})$$

$$\text{If } 50 \le q_{c1N} < 160 \qquad CRR_{7.5} = 93[(q_{c1N})_{cs}/1000)]^3 + 0.08 \qquad (4.6\text{ b})$$

where $(q_{c1N})_{cs}$ = clean sand cone penetration resistance normalized to 1 atm.

The normalization of CPT resistance can be calculated using the following equations:

$$q_{c1N} = C_q(q_c / p_a) \qquad (4.7\text{ a})$$

$$C_q = (p_a / \sigma'_{vo})^n \qquad (4.7\text{ b})$$

where p_a = 1 atm of pressure in the same unit used for σ'_{vo},

n = exponent that varies with soil type, and

q_c = field cone penetration resistance measured at the tip.

The value of the exponent, n, varies from 0.5 to 1.0 depending on the grain characteristics of the soil (NCEER 1997).

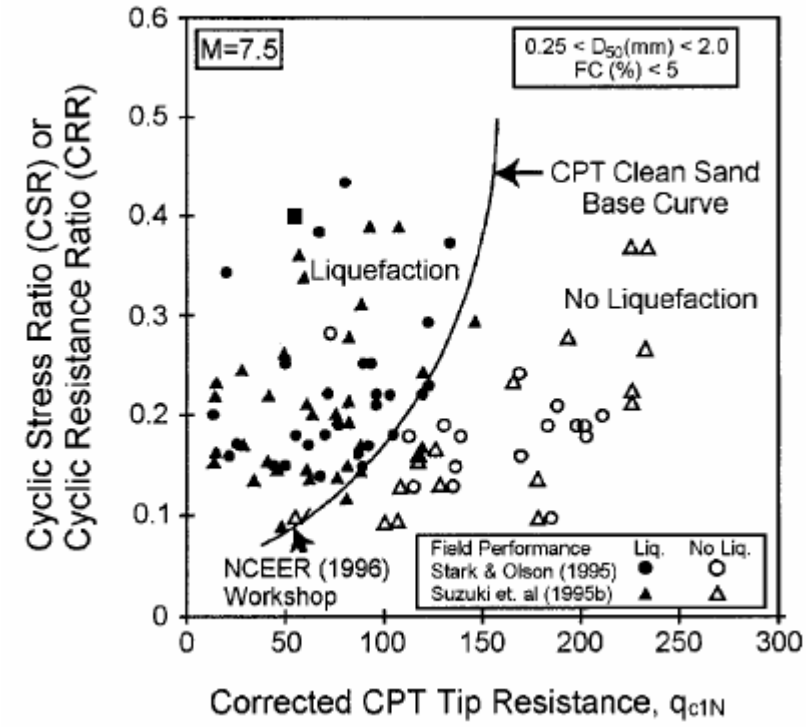

Figure 4.3 CPT Cyclic Resistance Curve (Youd et al. 2001)

The normalized penetration resistance, q_{c1N} , is for all soil. The normalized penetration resistance for silty sands should be corrected to an equivalent clean sand value, $(q_{c1N})_{cs}$, by the following relationship (Youd et al. 2001):

$$(q_{c1N})_{cs} = K_c q_{c1N} \tag{4.8}$$

where K_c is a correction factor for grain characteristics and is defined by the following equation (Youd et al. 2001):

For $I_c \le 1.64$ $\quad K_c = 1.0$ (4.9 a)

For $I_c > 1.64$ $\quad K_c = -0.403 I_c^4 + 5.58 I_c^3 - 21.63 I_c^2 + 33.75 I_c - 17.88$ (4.9 b)

where I_c is termed the soil behavior type index and is calculated from the following equation (Youd et al. 2001):

$$I_c = [(3.47 - \log Q)^2 + (1.22 + \log F)^2]^{0.5} \quad (4.10\text{ a})$$

$$Q = [(q_c - \sigma_{vo}) / p_a][(p_a / \sigma'_{vo})^n] \quad (4.10\text{ b})$$

$$F = [f_s / (q_c - \sigma_{vo})] \times 100\% \quad (4.10\text{ c})$$

where f_s is the sleeve resistance of the CPT (The units are the same as those in which q_c and σ_{vo} are expressed).

The detailed calculation procedure of the I_c index for different soil types is given in Youd et al. (2001).

4.3 Cone Tip Resistance

The liquefaction potential evaluation procedure discussed in the previous section needs the calculation of the cone penetration tip resistance in the absence of field cone penetration tests. This section identifies the studies conducted up to date on the mechanics and the models associated with penetration into geomaterials and to determine the capabilities and limitations of the existing models and methods.

4.3.1 Existing Theories for Penetration

Three general approaches are commonly used to estimate the cone penetration resistance of sand: 1) Bearing Capacity, 2) Cavity Expansion Theory, and 3) Strain Path Method. In this chapter, the strain path method is discussed somewhat in detail. two other methods are explained briefly.

4.3.1.1 Bearing Capacity Approach

The initial approach for estimating the penetration resistance of a soil deposit was based on bearing capacity theory. The approach assumes that the cone penetration

resistance is equal to the failure load of a deep foundation. The magnitude of this load is defined through either limit equilibrium or slip line methods, which are based on either conditions of global equilibrium or conditions of equilibrium and the assumed failure criterion. In general, bearing capacity calculations are based on the plane strain solutions for rigid-plastic material at a shallow depth. Corrections are then introduced to incorporate geometry. Modifications are based on the empirical relations, which make bearing capacity theory an empirical approach. Therefore, the application of this is limited to the cases with a rich data base. Elghaib (1989) summarized the limitations of the bearing capacity method:

1) Failure patterns are not based on direct experimental evidence and offer no interpretation of the mechanics of steady state penetration.
2) The soil is modeled as a rigid plastic material, such that no account is given of the energy absorbed in elastic straining outside the failure zone in the soil.
3) No or little account can be made of more realistic mechanical and hydraulic properties of real soil, such as the dependency of the failure envelope on the mean effective stress for sands and pore pressure generation for clays.

4.3.1.2 Cavity Expansion

The cavity expansion approach for estimating the penetration resistance assumes that the pressure required to advance a cone into a soil mass is equal to the pressure needed to expand a cavity from a finite radius of cone penetrometer. The approach requires the computation of a limit pressure during the expansion of the cavity, which is in turn related to the penetration resistance. The shape of the cavity is either cylindrical or spherical. This leads to the condition that the stress and strain is strictly one dimensional. In most applications, the tip resistance is calculated using the spherical expansion and the side resistance is calculated using the cylindrical expansion.

4.3.1.3 Strain Path Method

The strain path method is an approximate analytical technique developed by Baligh (1985a and 1985b) to describe the fundamental mechanisms of deep penetration in soil. It is assumed that due to the severe kinematic constraints involving deep penetration problems, deformations and strains are independent of the shearing resistance of the soil. Therefore, deep penetration problems are considered as strain controlled and deformations and strains are calculated based on kinematic considerations and boundary conditions. Shear stresses can be calculated using an appropriate constitutive model and pore pressure can be determined by imposing equilibrium conditions (Elghaib 1989). The usage of the Strain Path Method (SPM) in determining the stress field can be summarized as follows (Elghaib 1989):

1) The strain field induced by a penetrator is estimated from the velocity field of an incompressible and inviscid fluid. The assumption is that due to severe kinematic constraints in deep penetration problems, strains generated are independent of the shearing resistance of surrounding soils.
2) Along the streamline, the deviatoric stresses are determined from the strain by using an appropriate constitutive model for soils.
3) Using the equilibrium equation, the octahedral stress is obtained from the spatial gradient of the deviatoric stresses.

Although complete stress fields can be generated using the SPM by following the above procedures, only the calculation of tip resistance of the penetrator is of interest in this research. Therefore, in the following sections, the application of the Strain Path Method to cone penetration is strictly focused on the equilibrium along the centerline of the penetrometer. The analytical centerline solution developed by Elghaib (1989) is summarized and the numerical method for the centerline solution is presented in the next sections.

4.3.2 Centerline Solution

4.3.2.1 Centerline Solution for Frictional Material

In the centerline solution method, the tip resistance is equated with the equilibrium along the centerline of the penetrator. The following sections summarize the analysis proposed by Elghaib (1989) using a bilinear elastic-perfectly plastic model.

Along the centerline of the simple pile, soil elements are subjected to triaxial compression mode of shearing. The vertical strain along the centerline can be approximated as follow:

$$\varepsilon_{zz} = \frac{R^2}{4z^2} \tag{4.11}$$

where R is radius of a simple pile.

The extent of the plastic zone ahead of the pile tip is then:

$$\frac{z_p}{R} = \sqrt{\frac{1}{4\varepsilon_y}} \tag{4.12}$$

where ε_y is the axial yield strain.

An extended von Mises criterion is used to describe plastic failure:

$$S^2 - \frac{2}{3}k'^2\sigma'^2 = 0 \tag{4.13}$$

where, S is the second invariant of deviatoric stress and k' is the friction ratio (the ratio of the shear stress to normal effective stress) at failure.

In triaxial stress space, this reduces to:

$$S_1 = \sqrt{3}k'\sigma' \tag{4.14}$$

where S_1 is the deviatoric stress.

The friction ratio, k', can be defined in terms of the friction angle measured in triaxial compression, ϕ', by equating the von Mises criterion with the Mohr-Coulomb failure criterion:

$$k' = 2\sqrt{3}\frac{\sin\phi'_{tc}}{3-\sin\phi'_{tc}} \tag{4.15}$$

For the centerline solution of the simple pile, the octahedral stress can be obtained by integration of the equilibrium equation in the vertical direction (z-direction). In the elastic zone ($z < -z_p$), the mean effective stress remains constant and is equal to the initial isotropic effective stress σ'_o. In the plastic zone ($z > -z_p$), the vertical equilibrium condition reduces to the following first order differential equation:

$$\frac{d\sigma'}{dz} = -\frac{4\sin\phi'}{3(1+\sin\phi')}\frac{6}{(2+(\frac{z}{z_p})^2)z}\sigma' \tag{4.16}$$

The integration of Equation 4.16 results in the normalized octahedral effective stress induced in the plastic zone as follow:

$$\frac{\sigma'}{\sigma'_o} = (\frac{1}{3}+\frac{2}{3}(\frac{z_p}{z})^2)^{\chi} \tag{4.17}$$

where $\chi = \frac{2\sin\phi'}{1+\sin\phi'}$

At the tip of the pile (z/R=-1/2), the mean effective stress is found to be:

$$\frac{\sigma'_{tip}}{\sigma'_o} = (\frac{1}{3} + \frac{8}{3}(\frac{z_p}{R})^2)^{\chi} \tag{4.18}$$

The point resistance factor N_σ $(= q_c / \sigma'_o = (\sigma'_{zz})_{tip} / \sigma'_o)$, where $\sigma_{zz} = \sigma'_{zz} + u_o$ and u_o is the initial pore pressure, is then obtained from the Mohr's circle of stress in the plastic zone:

$$N_\sigma = \frac{3(1+\sin\phi')}{(3-\sin\phi')}(\frac{1}{3} + \frac{8}{3}(\frac{z_p}{R})^2)^{\chi} \tag{4.19}$$

The above equation shows that N_σ is a function of the friction angle ϕ' and the plastic zone, which is expressed by Equation 4.12.

Hence, the simple pile solution for the tip resistance factor (in an incompressible material) can be written as:

$$N_\sigma = \frac{3(1+\sin\phi')}{(3-\sin\phi')}(\frac{1}{3} + \frac{2}{3}\varepsilon_y)^{\chi} \tag{4.20}$$

The point resistance is then calculated as follow:

$$q'_c = \sigma'_o N_\sigma \tag{4.21}$$

The prediction of N_σ with ϕ' and ε_y is plotted in Figure 4.4 and Figure 4.5. The results show that (Elghaib 1989):

1) For a given friction angle ϕ', the point resistance decreases with the size of the plastic failure zone, $\frac{z_p}{R}$

2) The magnitude of N_σ can vary by a factor of 10 at a given friction angle, ϕ' depending on the size of the plastic zone (i.e., an increase in ε_y induces a decrease in N_σ).
3) The size of the plastic zone is uniquely determined by the yield strain, ε_y (measured from a drained triaxial shear test at constant σ').
4) For a given yield strain, ε_y, the point resistance, N_σ changes by a factor of 4 when ϕ' varies in the range of practical interest (30° to 45°).

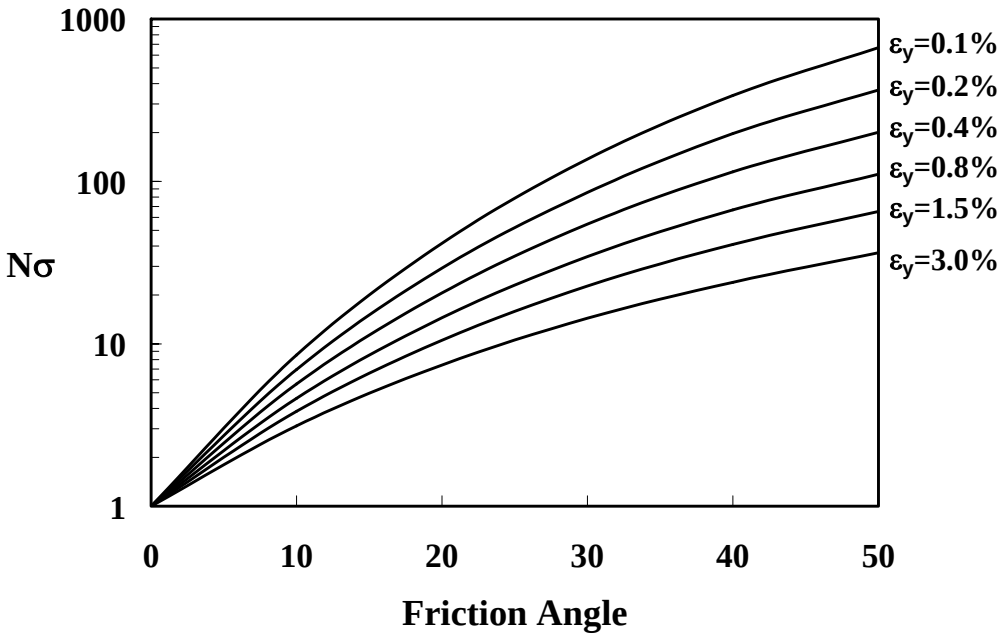

Figure 4.4 Point Resistance Factor versus Friction Angle (Reproduced after Elghaib 1989)

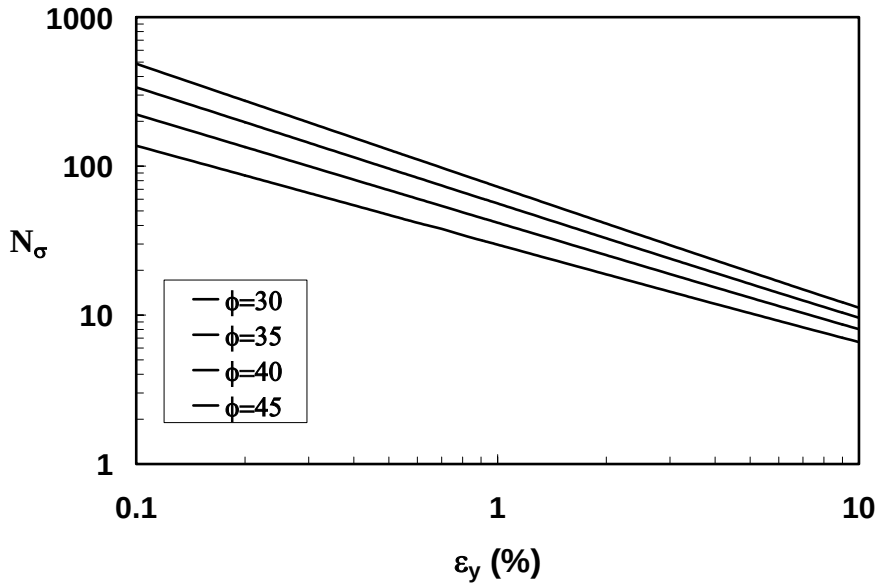

Figure 4.5 Point Resistance Factor versus Axial Yield Strain (Reproduced after Elghaib 1989)

Cemented soils exhibit a component of shear strength due to cohesion. Cohesion is usually defined by a cohesion intercept, c', in the Mohr-Coulomb failure criterion:

$$\tau = c' + \sigma' \tan \phi' \tag{4.22}$$

By equating Mohr-Coulomb failure criteria and extended von Mises in triaxial space, a modified failure criterion can be written:

$$S_1 = \sqrt{3}k(\sigma' + c' \cot \phi') \tag{4.23}$$

The equilibrium equation in the plastic zone for the simple pile centerline then becomes

$$\frac{d\sigma'}{dz} = -\frac{4\sin\phi'}{3(1+\sin\phi')}\frac{6}{(2+(z/z_p)^2)z}(\sigma' + c'\cot\phi') \tag{4.24}$$

The integration of the above equation results in the calculation of the tip resistance as follow:

$$q_c^{'} = \sigma_o' N_\sigma + c' N_c \tag{4.25}$$

where $N_c = (N_\sigma - 1)\cot\phi'$

Alternatively, a complete two-dimensional strain field and stress field can be generated and calculated respectively. Jeng (1992) used the complete two-dimensional strain field to calculate tip resistance as well as side resistance of the penetrator. In his model for frictional material, a non associated flow rule was assumed such that there was no tendency to develop volumetric strains when yield is reached. The yield function and plastic potential functions for the frictional material are in the following equations:

Yield criterion: $$f = \sqrt{J_2} - \alpha I_1 - k \tag{4.26}$$

Plastic potential function: $$g = \sqrt{J_2} - k \tag{4.27}$$

where J_2 $(= 1/2 s_{ij} s_{ij})$ is the second invariant of deviatoric stress,

I_1 is the first invariant of the stress tensor, and

α, k are positive material parameters.

The α and k can be estimated from the cohesion, c', and the friction angle, ϕ_{TC}', measured in drained triaxial compression shear test. The material parameters used were the friction angle, ϕ', shear modulus, G, and cohesion, c'. Instead of using the shear modulus, the axial yield strain was used in his model. The axial yield strain is converted

to shear modulus ($\varepsilon_y = k/\sqrt{3}G$) so the direct comparison with Elghaib's method is possible.

The profile of total mean stress from both Elghaib's (1989) and Jeng's (1992) methods are compared as in Figure 4.6. The result shows excellent agreement between the numerical predictions (Jeng 1992) and the closed form solution (Elghaib 1989). A friction material with $\phi' = 40^\circ$ is compared with Elghaib's result (1989). The axial yield strain, ε_y, is 0.5 percent.

4.3.2.2 Nonlinearity and Compressibility

Elghaib (1989) extended an incompressible elastic-perfectly plastic solution to a compressible nonlinear elastic-perfectly plastic case. The complete derivation of compressible nonlinear elastic-perfectly plastic model is presented in Elghaib's work (1989).

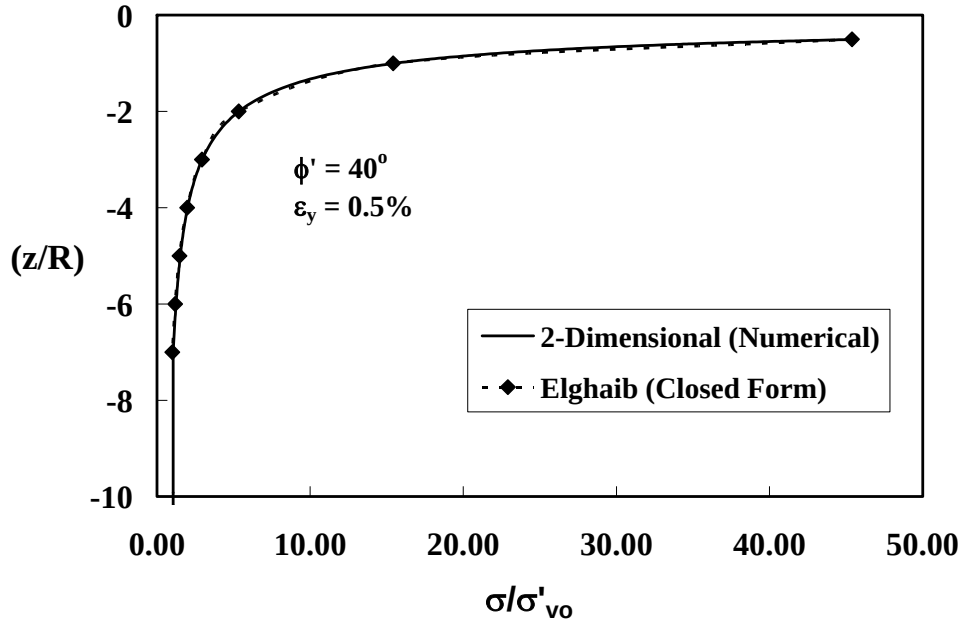

Figure 4.6 Profile of Mean Stress

The effect of nonlinearity was established through the transition of a bilinear model to a hyperbolic stress-strain relation before yielding. The introduction of non-linearity in the shear stress-strain relations generates changes in mean effective stress in ht elastic zone. Thus nonlinearity prior to failure significantly alters the predictions of the point resistance factor, N_σ . Elghaib (1989) presented the predictions of point resistance by estimating input parameters at three relative densities, Dr =45, 65 and 85 %. The model for sand behavior is hyperbolic stress-strain behavior requiring 7 input parameters to characterize the sand behavior. The predictions are evaluated by comparison with high quality laboratory data obtained in large scale calibration chamber tests. The determination of input parameters and prediction procedures are discussed extensively in Elghaib's work (1989). The results from the prediction are compared with Calibration Chamber Test (CC Test) data in Figure 4.7. As in Figure 4.7, for sand with relative density at 45 %, there is excellent agreement between the predictions and measured data for different confining pressures. As the relative density increases, the incompressible solutions underpredict the measured tip resistance. The reason for this is due to the neglected effect of dilation during the penetration of dense sand. Generally the prediction of tip resistance based on the incompressible assumption results in underprediction of the measurement. In order to have a better prediction at higher relative density, the effect of volume change should be incorporated into the centerline solution.

The prediction of point resistance using volume change properties of sand was based on spherical cavity expansion. Since the volume change in the plastic zone of a spherical cavity is equivalent to the expansion from a non-zero radius, the volume change in the plastic zone of a simple pile can be interpreted similarly as equivalent to the flow induced by an existing cavity included in a uniform flow (Elghaib 1989). Figure 4.7 shows the point resistance predicted at 3 different relative densities.

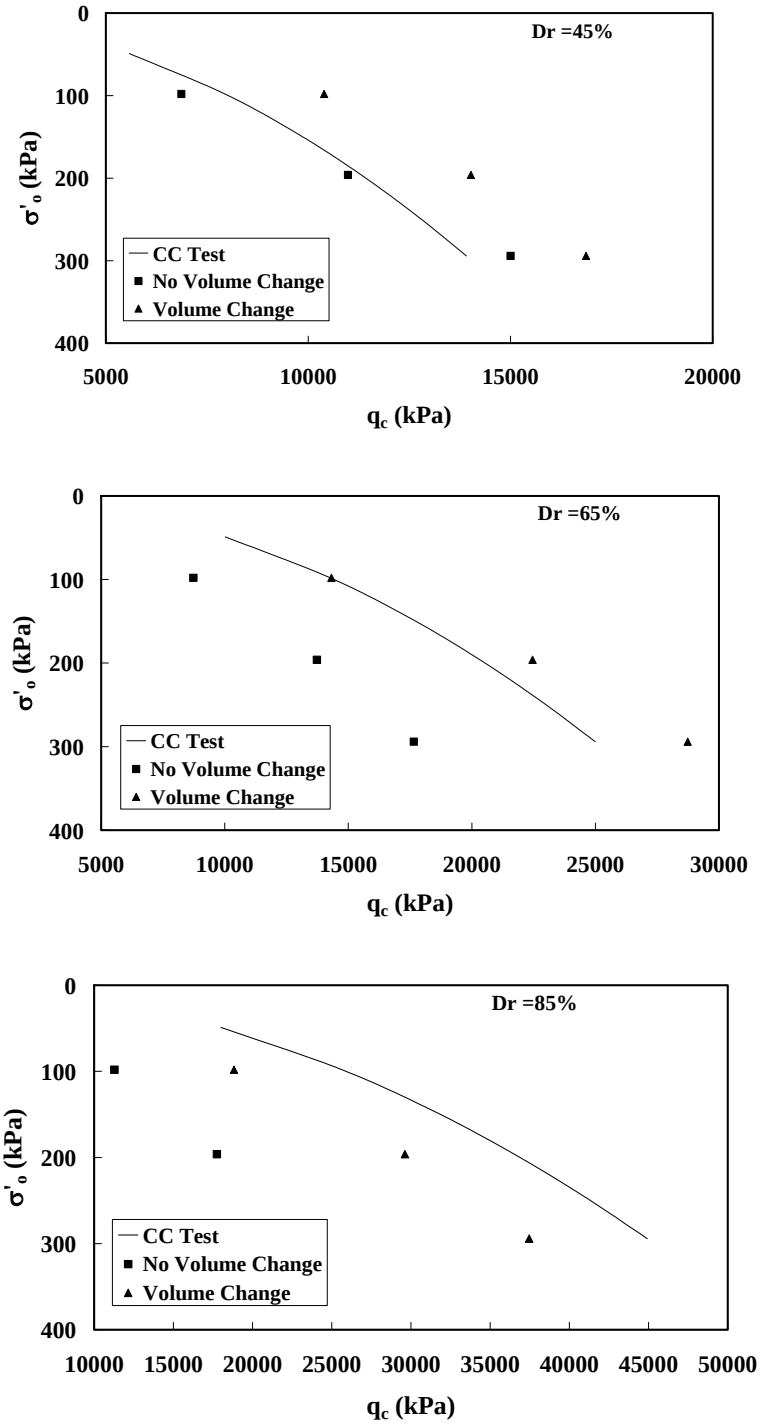

Figure 4.7 Comparisons among Incompressible and Compressible Predictions and Calibration Chamber Test Result (Reproduced after Elghaib 1989)

Overall the prediction based on including the volume change capability gives better agreement with the test data.

The prediction of the drained point resistance is a long and difficult process since the model needs 16 parameters to account for volume change during shear in the drained condition. However the complication of model parameter determination and calculation procedures are simplified by an equivalent axial strain, ε_y^*. The equivalent axial strain is introduced such that the use of Equation 4.12 is possible as in the following:

$$\left(\frac{z_p}{R}\right) = \sqrt{\frac{1}{4\varepsilon_y^*}} \tag{4.28}$$

The value of the equivalent axial strain depends on the nonlinearity of soil and the volume change of soil. It is a material property which can be computed given the soil parameters. This parameter is very difficult to obtain since it depends on a large number of parameters. However, backfiguring of the value, ε_y^* is possible from the calibration of chamber tests. In this case, the point resistance factor, N_σ, and shear strength parameters are known a priori from the calibration chamber tests (CC Test). It means that using Equation 4.20, ε_y^* can be back calculated with a known fiction angle, ϕ' and with measured tip resistance, q_c'.

In the back calculation process of ε_y^*, several observations were made by Elghaib (1989):

1) A unique $\varepsilon_y^* - N_\sigma$ curve can be defined irrespective of the initial relative density of the specimen.
2) The curve seems also to be independent of the initial mean effective stress.
3) The $\varepsilon_y^* - N_\sigma$ curve is also applicable to over consolidated sands due to the fact that the failure envelope parameters are independent of the OCR and appear to be a function of relative density only (Baldi et al. 1985).

A straight line relationship between ε_y^* and N_σ in a log-log space can be defined in the following equation:

$$\varepsilon_y^* = a(N_\sigma)^b \tag{4.29}$$

The parameters a and b are found to be 67.519 and -1.109 respectively for most sands. This procedure of backfiguring ε_y^* is verified by determining the friction angle which is eventually compared with the measured friction angle. For most sand, the difference between the friction angle calculated and measured are within $\pm 2^\circ$.

4.3.2.3 Calibration Chamber Test (CC Test)

Recent work in large calibration chamber testing has provided numerous correlations between cone penetration resistance and relative density for clean sand. The calibration chamber testing has shown that the cone resistance is controlled by sand density and in situ vertical stress.

Base on extensive calibration testing on Ticino sand, Baldi et al. (1985) recommended the following formula to estimate relative the density with a given tip resistance or the tip resistance with a given relative density.

$$D_r = \frac{1}{C_2} \ln\left(\frac{q_c}{C_o(\sigma')^{C_1}} \right) \tag{4.30}$$

where C_0, C_1, C_2 = soil constants,

σ' = effective mean or vertical stress in kPa, and

q_c = cone penetration resistance in kPa.

To estimate the relative density of a given sand from the CPT requires an estimate of the horizontal effective stress. For moderately compressible, normally consolidated unaged and uncemented silica sands, the effective vertical stress, σ_v', can be used.

Equation 4.30 can be used to generate curves of cone penetration resistance versus effective stress. The generated tip resistance curves are then compared with calculated tip resistance using the centerline solution as in Figure 4.8. In the calculation tip resistance, the equivalent yield strain was calculated using Equations 4.29 and 4.30 as a material parameter in the centerline solution. The experimental soil parameters, C_0, C_1, and C_2 are 157, 0.55, and 2.41 respectively for sand. The friction angles for each relative density are tabulated in Table 4.1.

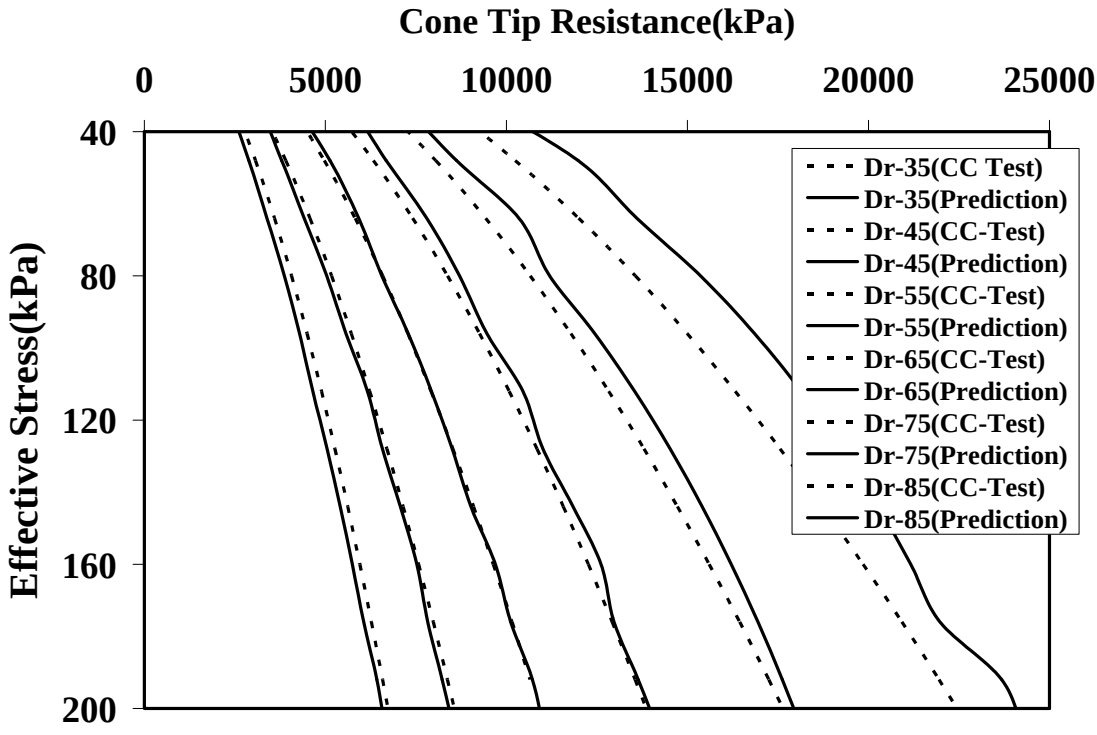

Figure 4.8 Comparisons between Measured and Calculated Cone Tip Resistance

Table 4.1 Typical Friction Angle for Sand (Elghaib 1989)

Dr	ϕ'	α
35	37	3
45	38.2	4
55	39.3	5.5
65	40.2	6.5
75	41.7	7.5
85	42.9	8

4.4 Liquefaction Potential in Unsaturated Soil

In this section, a simple method to calculate the tip resistance in an unsaturated media is presented. The analytical solution developed by Elghaib (1989) was used to predict tip resistance since the Elghaib's solution gives more flexibility over the numerical analysis of two dimensional stress fields.

Before the presentation of the prediction of tip resistance in unsaturated soil, the assumption is made that soil behavior is the same as that of saturated soil so that the same soil parameters, ε_y^* and ϕ', determined in the previous section can be used without using a complicated soil model. In the prediction of cone tip resistance in unsaturated soils, the shear strength equation presented in Chapter II is used to characterize the increase in cohesion with suction. The shear strength proposed by Lytton (1995) is following:

$$\tau = c' + \left[(\sigma - u_a) + f\theta(u_a - u_w)\right]\tan\phi' \tag{4.31}$$

The increase in cohesion due to the existence of matric suction can be written as follow:

$$c = c' + f\theta(u_a - u_w)\tan\phi' \tag{4.32}$$

The unsaturated shear strength function, f, in sand can be unity at low matric suction. Hence, an increase of cohesion is a function of volumetric water content with a known matric suction and friction angle.

To obtain the volumetric water content of sand, filter paper suction was conducted on sand samples obtained from the Riverside Campus of Texas A&M University. The same sieving procedure as described in Chapter III was performed to get clean sand out of the silty sand. Figure 4.9 shows the plot of volumetric water content against matric suction. The volumetric water content and matric suction relationship can be represented by Gardner's equation as follow:

$$\theta = \frac{n}{1 + a|h|^{b}} \tag{4.33}$$

where θ = volumetric water content,

n = porosity,

h = matric suction, and

a, b = Gardner water content coefficient.

Gardner water content coefficients, a and b, were found to be 0.022 and 0.96 respectively. Volumetric water content based on Gardner's equation and water content coefficients will be different with different sand samples. However, the difference in the volumetric water content will be small resulting in small differences in cohesion increases in sand sample. Thus, for each suction level, the calculation of the volumetric water content using a and b parameters determined in this study is acceptable.

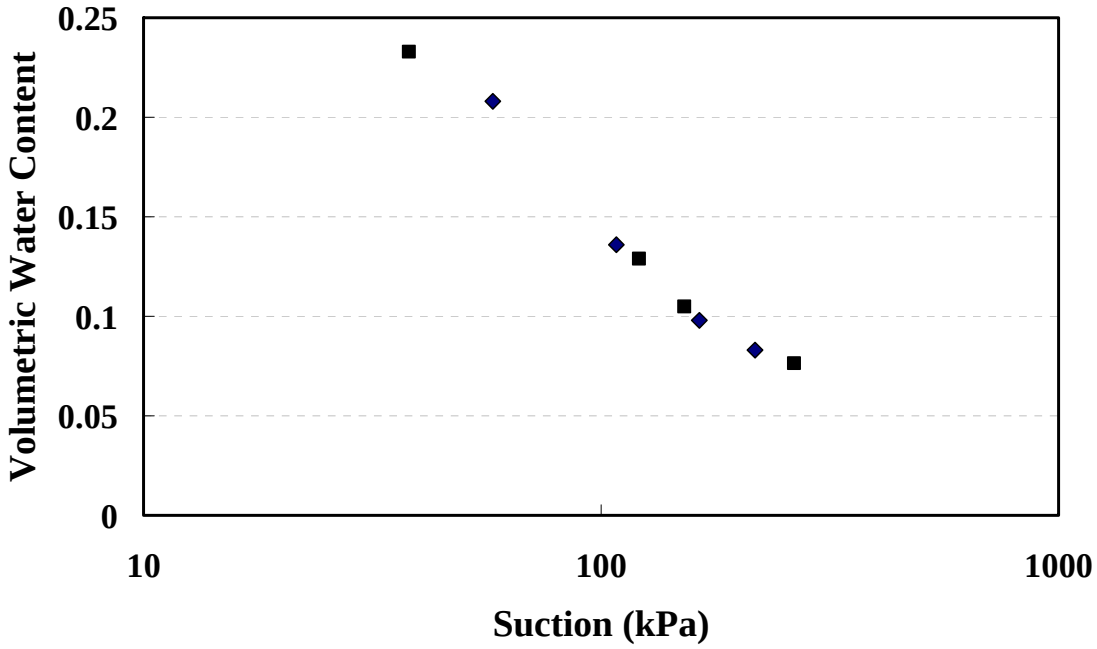

Figure 4.9 Volumetric Water Content and Matric Suction with Sand Sample

Once cohesion, the equivalent yield strain, and internal friction are known, N_{σ} can be calculated based on the centerline solution.

The above method will be used to calculate the point resistance in a hypothetical soil condition as presented as in Figure 4.10 (A 30m thick profile of clean sand with the ground water table at a depth of approximately 25m). The profile is assumed to have constant suctions above the water table and constant relative densities with depth. The two matric suction levels assumed are 40 and 80 kPa. The relative densities considered are from 35% to 75 %. For each relative density, the cyclic resistance ratio can be calculated using Equations presented previously and can be plotted against assumed peak horizontal acceleration (0.2g and 0.3g).

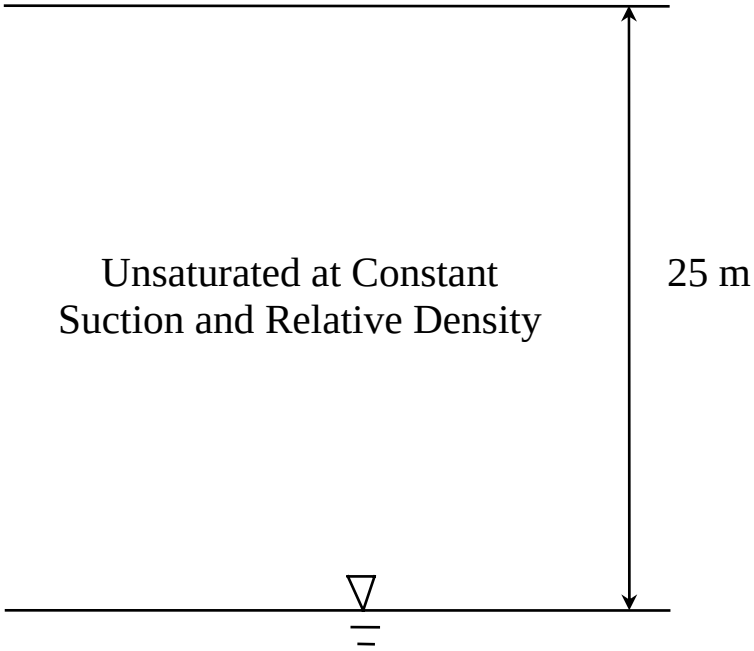

Figure 4.10 Hypothetical Soil Condition

Figure 4.11 shows that for a saturated soil sample, liquefaction will occur at low relative density. When the sand sample is unsaturated, the sand sample is still susceptible to liquefaction at suctions below 100 kPa.

Based on the result of this study, unsaturated soil can liquefy at low relative density and low suction level. However this result is subject to systematic error on the calculation of cone tip resistance since the soil model used in the centerline solution is not for an unsaturated soil model. For more accurate calculation of cone tip resistance, a soil model for unsaturated soil is necessary.

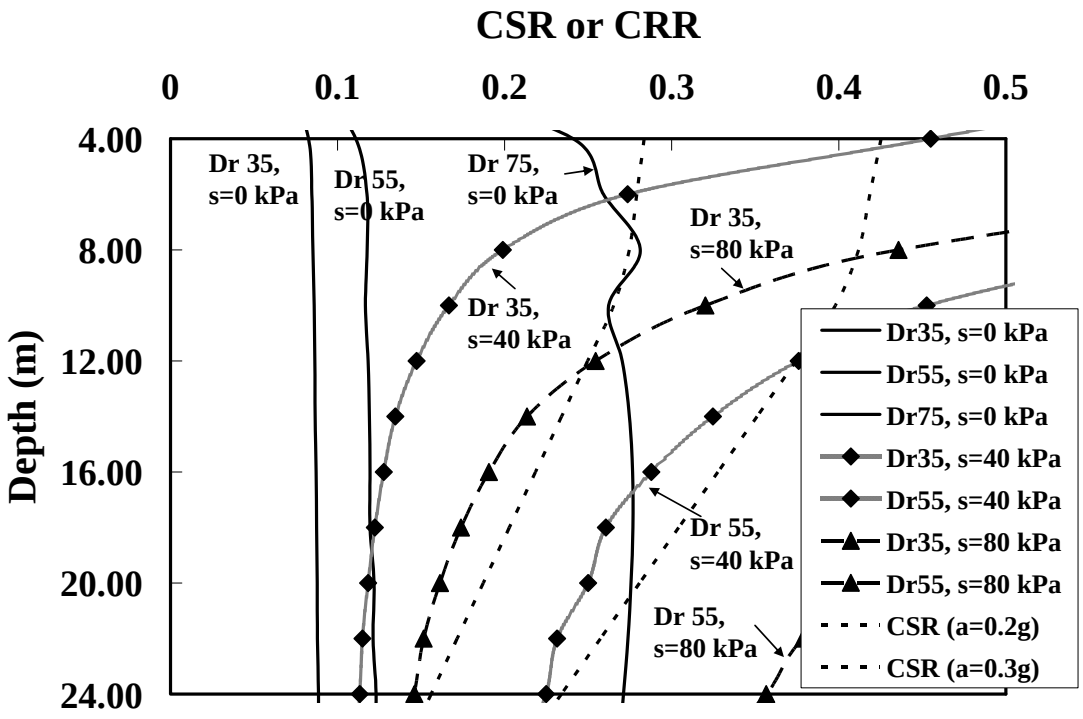

Figure 4.11 Liquefaction Potential of Unsaturated Clean Sand

CHAPTER V
CONSTITUTIVE MODELING OF UNSATURATED SOIL AND PSEUDO STRAIN

This chapter provides a brief review of constitutive modeling for unsaturated soils, with particular emphasis on the elasto-plastic model of Alonso, Gens and Josa (1990). The model is formulated within the framework of hardening plasticity, and is able to represent many of the fundamental features of the behavior of an unsaturated soil, which had been treated separately by previous empirical models. The basic framework of the model is an extension of the classical Modified Cam Clay (MCC).

This chapter also includes the physics involving the mechanism of energy dissipation. Two major energy dissipations are reviewed. The calculation of strain energy from the tests is included in this chapter. Lastly, the concept of pseudo strain is introduced to remove viscous energy dissipation exerted by the action of water in the soil.

5.1 Elasto-Plastic Model of Alonso, Gens and Josa

5.1.1 Isotropic Stress States

Elasto-plastic models have been developed recently to offer a general framework able to represent the mechanical behavior of unsaturated soils. The first development of the formulation of a constitutive model for unsaturated soil, which made use of the traditional framework of elasto-plasticity, was due to Alonso, Gens and Josa (1990). The model is described in terms of three stress parameters: the net mean stress, p, the matric suction, s, and the deviatoric stress, q, whereas only two strain parameters are considered: the increment of volumetric strain, $d\varepsilon_{v,}$ and the increment of deviatoric strain, $d\varepsilon_q$.

In order to completely define the elasto-plastic stress-strain relationships, four elements have to be given: an elastic law, a yield locus, a hardening law, and a plastic flow rule. In this section, a description of the model for isotropic stress states is given.

The yield locus in the (p, s) plane for isotropic stress states and the hardening law are both linked to the form of behavior assumed during isotropic loading to virgin states. The model assumes that whenever an unsaturated soil subject to an isotropic stress state behaves plastically, the soil state must fall on an isotropic normal compression surface in (v, p, s) space. Thus, in full correspondence with the behavior of saturated soil the specific volume, $v = 1 + e$, will be given by:

$$v = N(s) - \lambda(s) \ln \frac{p_o}{p^c} \tag{5.1}$$

where p^c is a reference stress for which $v = N(s)$, $\lambda(s)$ is a stiffness parameter for the change in net mean stress for the virgin states of the soil. Both $N(s)$ and $\lambda(s)$ are suction dependent parameters. Alonso, Gens and Josa assume that $\lambda(s)$ decreases with increasing suction according to the following equation:

$$\lambda(s) = \lambda(0)[(1-r)\exp(-\beta s) + r] \tag{5.2}$$

where $\lambda(0)$ is the slope of the normal compression line, r is a constant related to the maximum stiffness of the soil (for infinite suction), $r = \lambda(s \to \infty)/\lambda(0)$, and β is a parameter which controls the rate of increase of soil stiffness with the suction. Figure 5.1 shows a schematic representation of a family of normal compression lines represented by Equations 5.1 and 5.2. However, for the sake of simplicity, the model assumes that the slope, κ, of the isotropic-rebound is not suction dependent.

On the unloading and reloading path, the soil is assumed to behave elastically yielding the following equation:

$$dv_p = -k \frac{dp}{p} \tag{5.3}$$

where κ is an elastic constant.

Figure 5.2 shows two different unloading/wetting stress paths to illustrate the basic concepts of the model's framework for an unsaturated soil under isotropic stress states. The saturated preconsolidation stress is labeled p_o^* and corresponds to point 3 with specific volume, v_3. The yield stress at a higher suction is denoted as p_o and corresponds to point 1 with specific volume, v_1. The unsaturated soil sample, initially at point 1, follows the path $1 \rightarrow 2$, where matric suction, s, is kept constant and the net mean stress , p, is decreased to a value equal to p_o^*. The soil experiences an elastic rebound following the isotropic-rebound line with slope κ, as depicted in Figure 5.2. Next, the sample is subjected to a wetting process $2 \rightarrow 3$ until reaching full saturation, by decreasing matric suction, s, and keeping the net mean stress, p_o^*. Upon wetting a reversal swelling is experienced by the soil as in Figure 5.2 (a) and (b). The elastic swelling occurring along such a path (due to reduction of p along path $1 \rightarrow 2$ and the reduction of s along path $2 \rightarrow 3$ is given by the following equation:

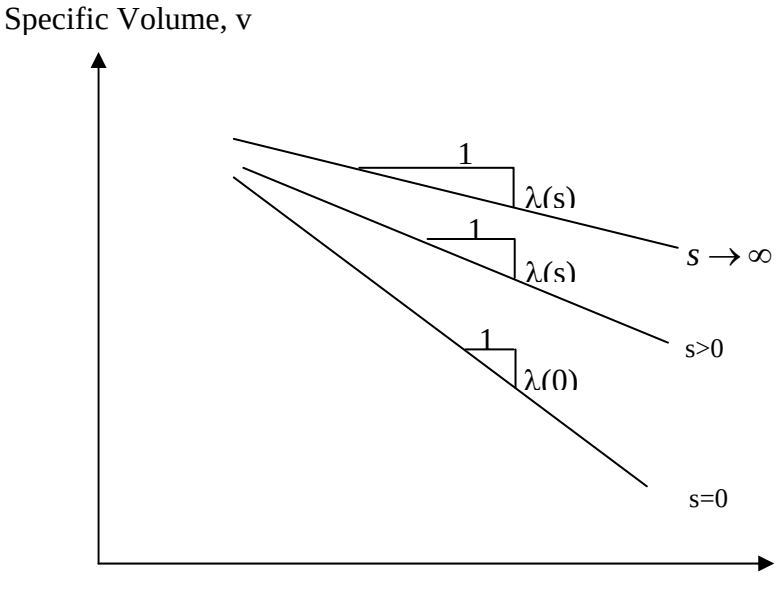

Figure 5.1 Schematic Representation of Normal Compression Line (Alonso et al. 1990)

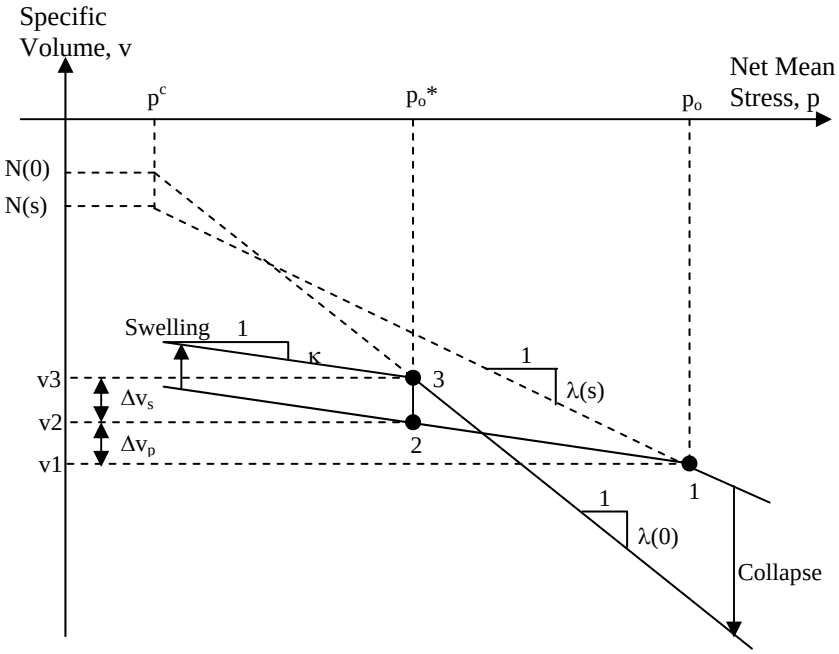

a)

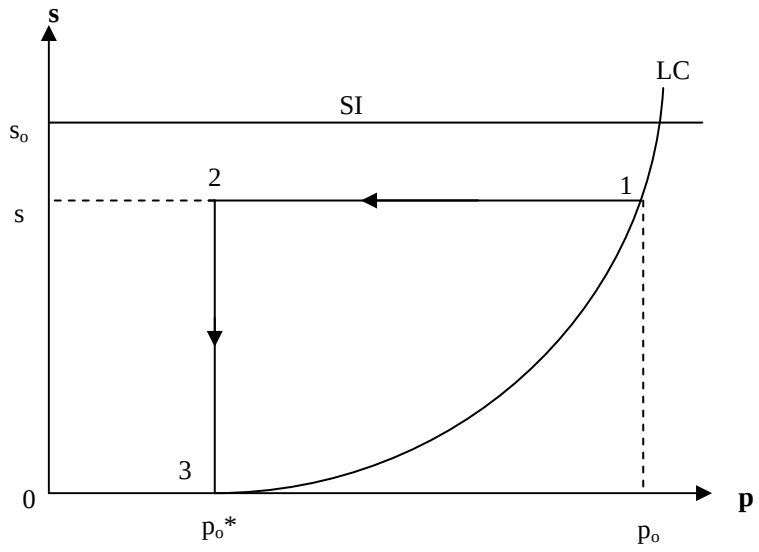

b)

Figure 5.2 Isotropic Stress Response: a) Compression Curves in the (v, ln p) plane; b) Stress Path and Yield Curves in the (p, s) plane (Alonso et al. 1990)

$$v_3 - v_1 = \Delta v_p + \Delta v_s \tag{5.4}$$

The suction unloading (wetting) from 2 to 3 occurs in the elastic domain. With this condition, a reversal swelling Δv_s takes place and is expressed as follow:

$$dv_s = -k_s \frac{ds}{(s + p_{atm})} \tag{5.5}$$

where κ_s denotes the elastic volumetric soil stiffness for changes in matric suction and p_{atm} denotes the reference atmospheric pressure (101 kPa), included as a reference pressure. By integrating Equation 5.3 and 5.5 and accounting for Equation 5.1, Equation 5.4 becomes:

$$v_3 - v_1 = k \ln\left(\frac{p_o}{p_o^*}\right) + k_s \ln\left(\frac{s + p_{atm}}{p_{atm}}\right) \tag{5.6}$$

Another form of the Equation 5.6 is also possible:

$$N(s) - (\lambda(s) - k)\ln\left(\frac{p_o}{p^c}\right) + k_s \ln\left(\frac{s + p_{atm}}{p_{atm}}\right) = N(0) - (\lambda(0) - k)\ln\left(\frac{p_o^*}{p^c}\right) \tag{5.7}$$

The authors postulated the existence of a value of the reference pressure p^c at which one may move from a generic unsaturated normal compression line to the saturated one through a stress path which involves only elastic swelling due to a change in suction. In other words, they assume that it is possible to define a value of p^c at which the following equation holds:

$$\Delta v(p^c)\Big|_s^0 = N(0) - N(s) = k_s \ln\left(\frac{s + p_{atm}}{p_{atm}}\right) \tag{5.8}$$

The above equation says that the yield curve is a vertical straight line for $p_o^* = p^c$. Equation 5.8 is used in Equation 5.7 and the following relation is obtained.

$$p_o = p^c \left\{\frac{p_o^*}{p^c}\right\}^{\frac{\lambda(0)-k}{\lambda(s)-k}} \tag{5.9}$$

Equation 5.9 describes the spatial location of the family of yield curves, called Loading –Collapse (LC) yield curves in the (p, s) plane. A qualitative representation of such a family of yield curves is shown in Figure 5.3, where the expansion of the yield curves with an increasing value of p_o^* is evident. Figure 5.3 also illustrates the major assumption implicitly made in the model that there exists a value, p^c, for which yield curve is a vertical straight line.

As one may expect, an increase in matric suction, s, may also result in irrecoverable strain in the soil sample. As in figure 5.2 (b), the value of matric suction, s_o, represents the maximum past matric suction experienced by the soil, and bounds the transition from the elastic region ($s < s_o$) to the virgin, elasto-plastic zone ($s > s_o$). This yield locus is the suction-increase, SI yield locus. Both LC and SI yield curves enclose an elastic region in (p, s) plane.

The elastic response of the soil stress paths taking place within the elastic region at a constant net mean stress, p, follows a drying-wetting line with a slope k_s with matric suction beyond the SI curve, the soil experiences an elasto-plastic volumetric compression with a slope λ_s, which represents the volumetric soil stiffness for changes in matric suction at constant net mean stress, p. According to the authors, some

dependence of λ_s and k_s on the net mean stress may be suspected but, for simplicity, they will be taken as constant.

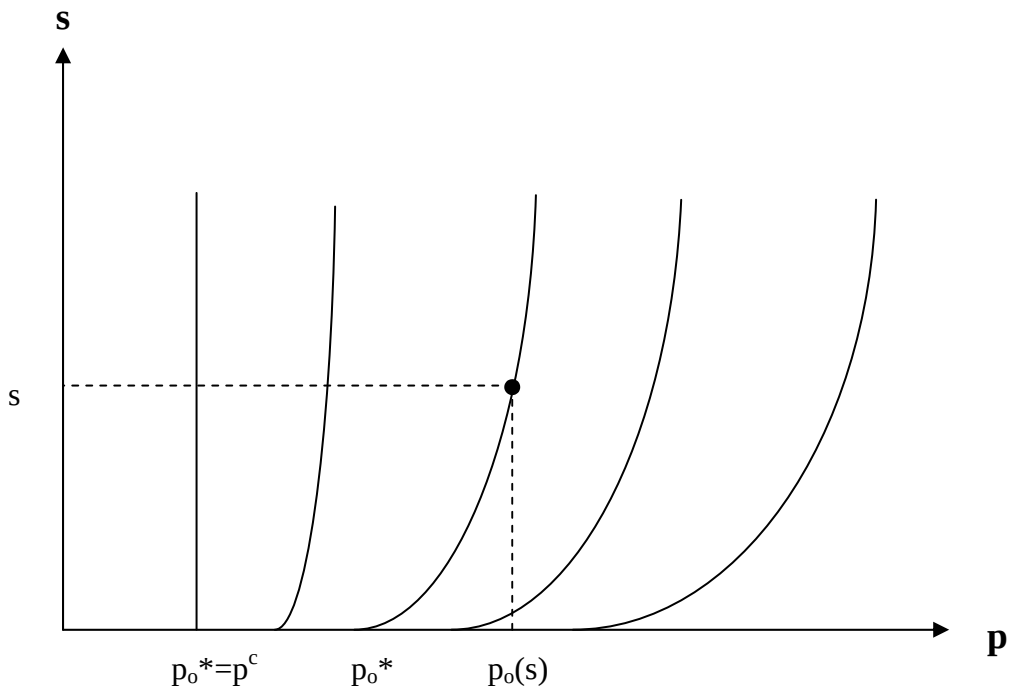

Figure 5.3 Schematic Representation of the Family of LC Yield Curves (Alonso et al. 1990)

Along the virgin line ($s > s_o$), a change in specific volume, dv, as a result of a suction increase, can be written as follow:

$$dv = -\lambda_s \frac{ds}{(s + p_{atm})} \tag{5.10}$$

The change in specific volume, dv, due to a change in suction, within the region bounded by the LC and SI loci, is expressed in Equation 5.5.

5.1.2 Hardening Laws

In the elasto-plastic models, the volumetric strain increment, $d\varepsilon_v = d\varepsilon_1 + 2d\varepsilon_3$ due to either changes in net mean stress, p, or matric suction, s, can be divided into total elastic volumetric and plastic volumetric strain increment, $d\varepsilon_v^e$ and $d\varepsilon_v^p$. Thus the following equation can be written.

$$d\varepsilon_v = d\varepsilon_v^e + d\varepsilon_v^p \tag{5.11}$$

The authors furthermore subdivide the elastic and plastic volumetric strains into more components.

$$d\varepsilon_v^e = d\varepsilon_{vp}^e + d\varepsilon_{vs}^e \tag{5.12}$$

$$d\varepsilon_v^p = d\varepsilon_{vp}^p + d\varepsilon_{vs}^p \tag{5.13}$$

where

$d\varepsilon_{vp}^e$ = elastic volumetric strain increment due to a change in net mean stress, p,

$d\varepsilon_{vs}^e$ = elastic volumetric strain increment due to a change in matric suction, s,

$d\varepsilon_{vp}^p$ = plastic volumetric strain increment due to a change in net mean stress, p, and

$d\varepsilon_{vs}^p$ = plastic volumetric strain increment due to a change in matric suction, s.

Also possible are expressions for the total volumetric strain increments due to a change in net mean stress and a change in matric suction. Thus the following equations can be written.

$$d\varepsilon_{vp}^{tot} = d\varepsilon_{vp}^e + d\varepsilon_{vp}^p \tag{5.14}$$

$$d\varepsilon_{vs}^{tot} = d\varepsilon_{vs}^e + d\varepsilon_{vs}^p \tag{5.15}$$

An increase of p in the elastic region bounded by LC and SI yield curves will induce a compressive (positive) volumetric strain given by:

$$d\varepsilon_{vp}^{e} = -\frac{dv}{v} = \frac{k}{v}\frac{dp}{p} \tag{5.16}$$

Once the net mean stress p reaches the yield value p_o, the total volumetric strain increment, for any further increase in p along a specific value of matric suction, may be computed as:

$$d\varepsilon_{vp}^{tot} = \frac{\lambda(s)}{v}\frac{dp_o}{dp_o} \tag{5.17}$$

Therefore, the plastic component of the volumetric strain increment due to a change in net mean stress at a specific value of matric suction can be expressed as:

$$d\varepsilon_{vp}^{p} = \frac{\lambda(s)-k}{v}\frac{dp_o}{p_o} \tag{5.18}$$

An increase of the matric suction within the elastic region also results in a compressive volumetric strain increment.

$$d\varepsilon_{vs}^{e} = \frac{k_s}{v}\frac{ds}{s+p_{atm}} \tag{5.19}$$

Moreover, the matric suction beyond the yield value, s_o at a specific value of net mean stress will induce a total volumetric strain. Thus, the total and plastic volumetric strain due to an increase of matric suction can be given as:

$$d\varepsilon_{vs}^{tot} = \frac{\lambda_s}{v}\frac{ds_o}{(s_o + p_{atm})} \tag{5.20}$$

$$d\varepsilon_{vs}^{p} = \frac{(\lambda_s - k_s)}{v}\frac{ds_o}{(s_o + p_{atm})} \tag{5.21}$$

According to authors' assumption, the hardening associated with the expansion of the both LC and SI yield loci depend exclusively on the plastic volumetric strain. Then the proposed hardening law for isotropic loading conditions can be expressed as:

$$\text{LC yield curve}: \frac{dp_o}{p_o} = \frac{v}{(\lambda(0) - k)} d\varepsilon_v^p \tag{5.22}$$

$$\text{SI yield curve}: \frac{ds_o}{s_o + p_{atm}} = \frac{v}{(\lambda_s - k_s)} d\varepsilon_v^p \tag{5.23}$$

5.1.3 Anisotropic Stress States

The previous two sections described the model of Alonso, Gens, and Josa (1990) as applied to isotropic stress states. The model is extended to triaxial stress states by the authors introducing in the model a third stress parameter, the deviatoric stress, q, and a second strain parameter, the increment of deviatoric strain $d\varepsilon_q$. These two parameters are defined for triaxial stress states as:

$$q = \sigma_1 - \sigma_3 \tag{5.24}$$

$$d\varepsilon_q = \frac{2}{3}(d\varepsilon_1 - d\varepsilon_3) \tag{5.25}$$

In order to extend the model to a shearing stage (Triaxial Test), three new elements have to be introduced: an incremental link between the new strain variable, $d\varepsilon_q$, and the stress increments in the elastic domain, and the extension of the yield locus for isotropic stress states defined in the (p, s) plane to the three-dimensional stress state

space (q, p, s), and the definition of a flow rule for predicting plastic components of deviatoric strain.

When suction is equal to zero (fully saturated condition), the model is assumed to coincide with the Modified Cam-Clay (MCC) model (Roscoe and Burland 1968). Therefore at zero suction the yield locus in the (q, p) plane coincides with the MCC elliptical curve. This elliptical shape of the yield is retained also in the constant suction planes as in Figure 5.4 (a). As in the MCC case, the complete definition of the elliptical yield locus in each constant suction plane is obtained by specifying the value of the isotropic stress and the critical state line relating q and p at ultimate critical states at a given value of suction. Regardless of the value of suction, the slope, M, of critical state lines in the (q, p) plane is assumed to be constant.

The effect of matric suction is represented by an increase in the apparent cohesion of the soil. Figure 5.4 (a) shows the intercept with the q axis is assumed to be equal to zero at zero suction and then increases linearly with the suction. This assumption is analogous to the extension of the shear strength theory proposed for an unsaturated soil in the (τ , $\sigma - u_a$) plane. This is illustrated schematically in Figure 5.5. Critical state line (CSL) projected horizontally onto the (q, p) plane, as shown in Figure 5.5 (a), and lines of the Mohr-Coulomb failure envelope projected onto the (τ , $\sigma - u_a$) plane, as shown in Figure 5.5 (b), indicate an increase in the apparent cohesion of the soil with matric suction. The analytical expression of such a critical state line in the (q, p) plane at a given suction is given by:

$$q = Mp + Mks = Mp + Mp_s \tag{5.26}$$

where k is the parameter indicating the rate of increase in apparent cohesion with matric suction, s.

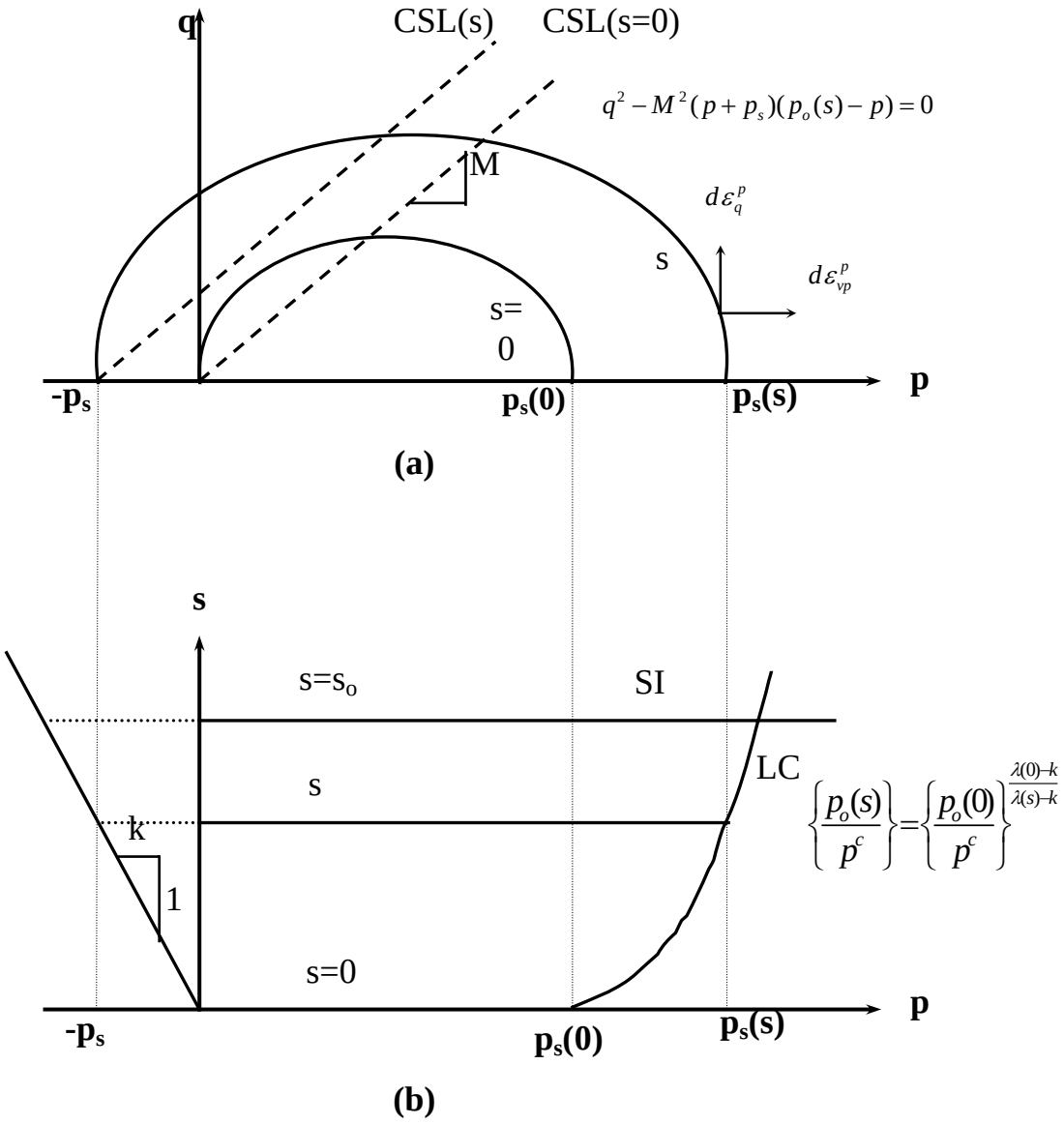

Figure 5.4 Yield Surface: a) Yield Loci Induced by Shear; b) Yield Loci Induced by Isotropic Loading and Wetting /Drying (Hoyos 1998)

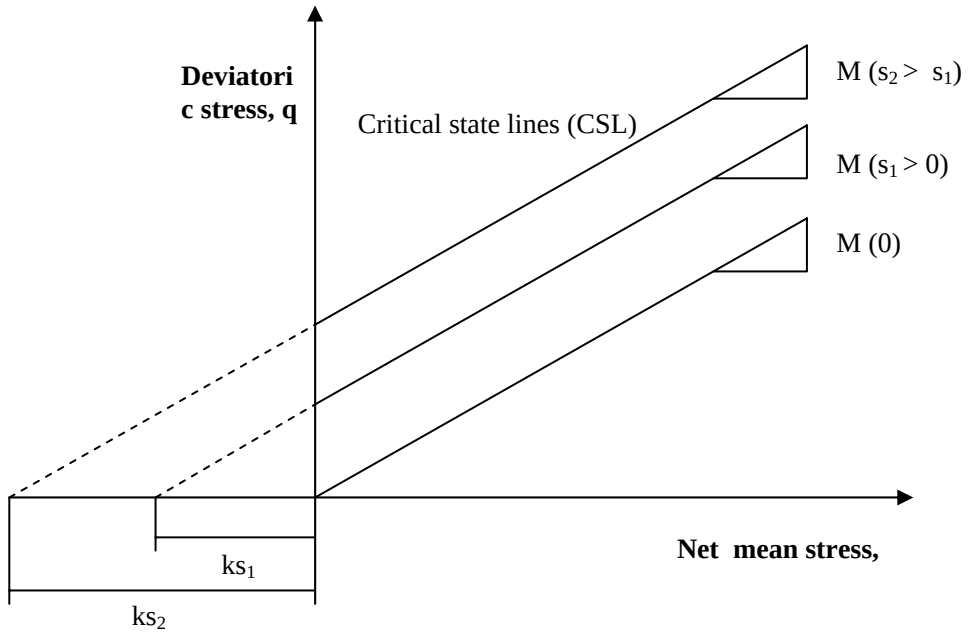

a)

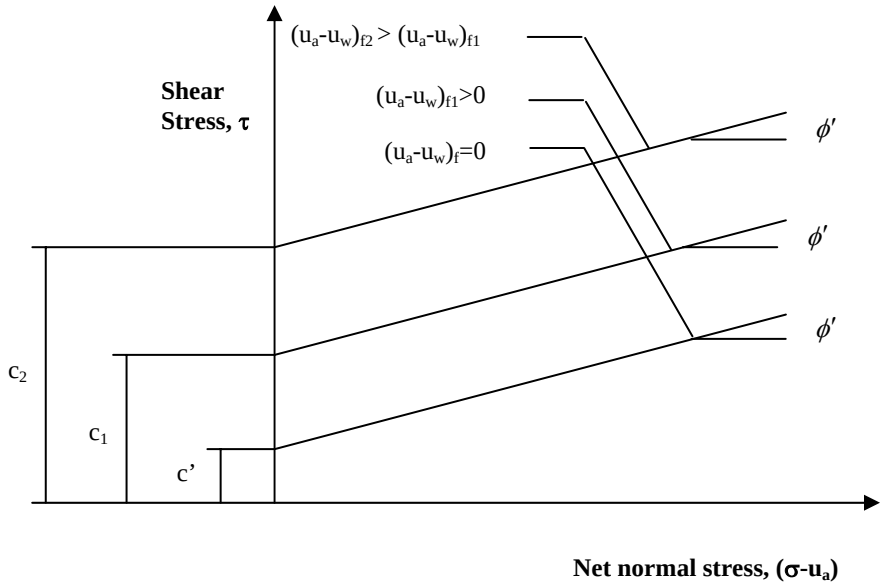

b)

Figure 5.5 Model's Framework in (p, q) Plane Viewed as an Extension of the Shear Strength Theory Proposed for an Unsaturated Soil: a) Critical States Lines Projected Horizontally onto the (p, q) Plane; b) Contour of Lines of the Extended Mohr-Coulomb Failure Envelope Projected Horizontally onto the (τ, σ-u_a) Plane (Hoyos 1998)

The aspect ratio of the elliptical yield loci in the constant-suction plane is assumed not to vary with suction and it is fixed by the valued of the parameter M. The equation of the yield locus in the (q, p, s) space is therefore given by:

$$F_1 = q^2 - M^2(p + p_s)(p_o - p) = 0 \tag{5.27}$$

A complete three-dimensional view of the yield loci in (q, p, s) stress space is depicted in Figure 5.6. Figure 5.6 enables several important features of the constitutive behavior of an unsaturated soil to be modeled.

The suction-increase, SI, yield locus rises vertically. No explicit dependence on q is postulated (Alonso et al. 1990). Therefore, the expression for the suction-increase, SI, yield locus can be written as:

$$F_2 = s - s_o = 0 \tag{5.28}$$

5.1.4 Flow rule

The shear strain increment associated with the application of deviatoric stress can be divided into to elastic shear stain and plastic shear strain.

$$d\varepsilon_q^{tot} = d\varepsilon_q^e + d\varepsilon_q^p \tag{5.29}$$

As far as the first point is concerned, the elastic increment of deviatoric strain, $d\varepsilon_q$ is related to the increment of deviatoric stress, dq through the shear modulus, G:

$$d\varepsilon_q^e = \frac{1}{3G} dq \tag{5.30}$$

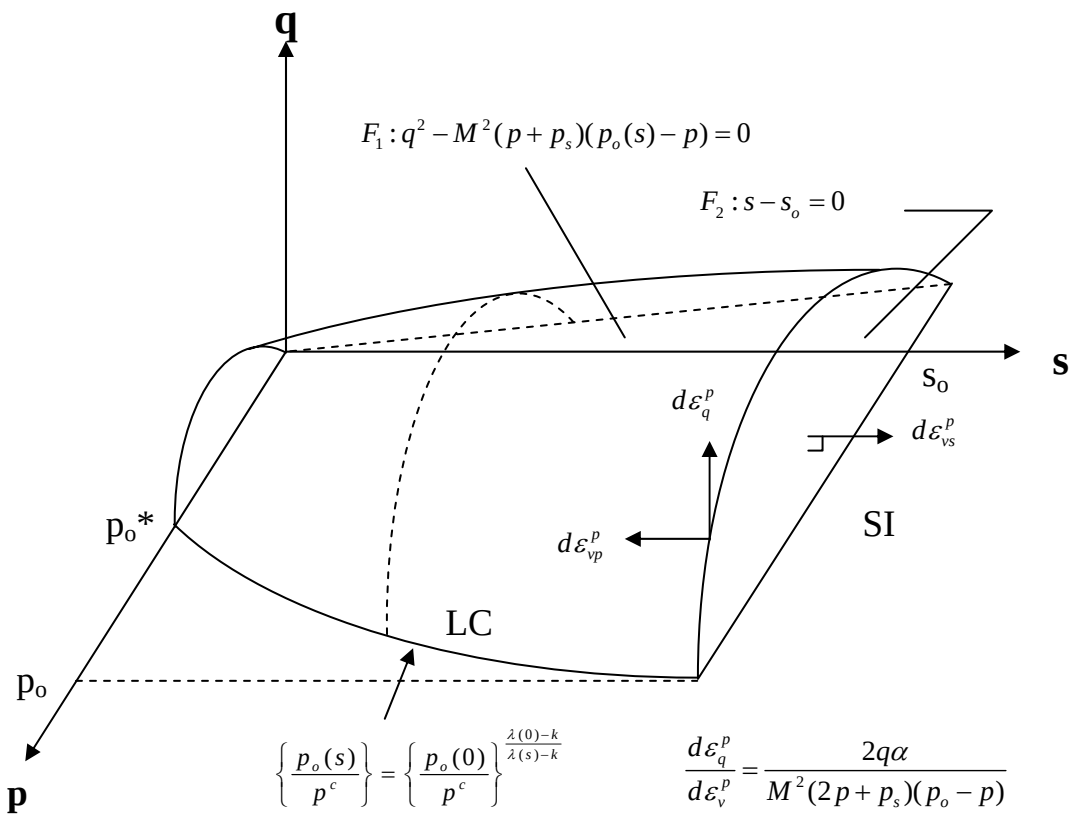

Figure 5.6 Three Dimensional View of the Yield Loci (Modified from Hoyos 1998)

Alonso, Gens, and Josa adopted a non-associated flow rule. They argued for a non-associated flow rule in order to get better predictions of the value of K_o along an oedometric stress path. The plastic potential is given by:

$$G = \alpha q^2 - M^2(p + p_s)(p_o - p) = 0 \tag{5.31}$$

The value of α is chosen in such way that the flow rule predicts zero lateral strain for stress states corresponding to Jaky's K_o values and is written as:

$$\alpha = \frac{M(M-9)(M-3)}{9(6-M)}\left\{\frac{1}{1-\frac{k}{\lambda(0)}}\right\} \tag{5.32}$$

The proposed flow rule is of the form:

$$\frac{d\varepsilon_q^p}{d\varepsilon_v^p} = \frac{2q\alpha}{M^2(2p+p_s)(p_o-p)} \tag{5.33}$$

As mentioned previously, the suction increase, SI, rises vertically. Therefore, the plastic volumetric strain increments associated with the SI are calculated using an associated flow rule.

5.2 Parameters for the Model

The application of the models proposed by Alonso et al. (1990) requires the specification of initial state parameters such as initial stress stated and specific volume as well as material parameters. This information is summarized in Table 5.1. The determination of material parameters require a series of suction-controlled tests using the axis-translation technique which is described in Chapter II. A detailed procedure in determining material parameters is presented with test results in Chapter VII.

Depending on the dimension of the problem (i.e. isotropic, triaxial case), the number of model's parameter will be different. Following parameters are tabulated depending in the different dimension of problem.

Table 5.1 List of Model Parameters

Isotropic Stress States for change in net mean stress, p	
$\lambda(0)$	Compressibility coefficient for change in p along virgin loading at saturated condition
κ	Compressibility for change in p along elastic stress paths
β	Parameter controls the rate of increase in stiffness with suction
r	Parameter defining the maximum soil stiffness, i.e., $r = \lambda(s \to \infty) / \lambda(0)$
p^c	Reference stress state parameter
Isotropic Stress States for change in matric suction	
λ_s	Compressibility coefficient for change in suction under virgin condition
κ_s	Compressibility coefficient for change in suction within elastic region
Triaxial Stress States	
K	Elastic bulk modulus
M	Slope of critical state line
k	Parameter which controls the increase in cohesion with suction
Initial stress state and volumetric state condition	
p_{ini}	Initial net mean stress
q_{ini}	Initial deviatoric stress
s_{ini}	Initial matric suction
v_{ini}	Initial specific volume

5.3 Mechanism of Energy Dissipation

This section will review mechanisms of energy dissipation in soils. The purpose of this section is to provide better physical insight into the energy imparted to the soil and the dissipation mechanisms. Two major dissipation mechanisms are presented although other energy dissipations are possible. When cyclic loading is applied to the soil, a part of their energy dissipates. Normally, in cohesionless soils, the dominant

mechanism of dissipation is due to friction. This can occur when a grain slips over another grain. In saturated soil or unsaturated soil, a part of the energy can also be dissipated through viscous drag of the pore fluids moving relative to the soil skeleton. There can be other dissipation mechanisms, but their effects are negligible or considered as frictional. That part of energy that is not dissipated is stored energy.

5.3.1 Frictional Dissipation Mechanism

The frictional dissipation plays a major role in relation to liquefaction. This is because the liquefaction requires some deformations of soil mass invoking the slippage mechanism among particles. Physics of dissipation by friction is explained by the interaction of two spheres under the action of normal and shear forces. As an illustration, the contact forces and corresponding stresses between two spheres are shown in Figures 5.7, 5.8, and 5.9. As in Figures 5.7 and 5.8, with an increase of tangential force T, there is a proportional increase in the lateral displacement between the centers of the spheres. Figure 5.9 shows the variation of the normal stress across the contact area, which is a function of both the applied normal force and the elastic properties of the spheres. The progression of lateral displacement starts as the tangential force increases from 0 to fn. The complete sliding across the entire contact area will occur when the tangential force, T, reaches fN . The sliding starts at the outer radius of a contact area and progresses inward forming an annulus of slippage as in Figure 5.9. A series of experimental evidence confirm this theoretical behavior (e.g., Deresiewicz 1974).

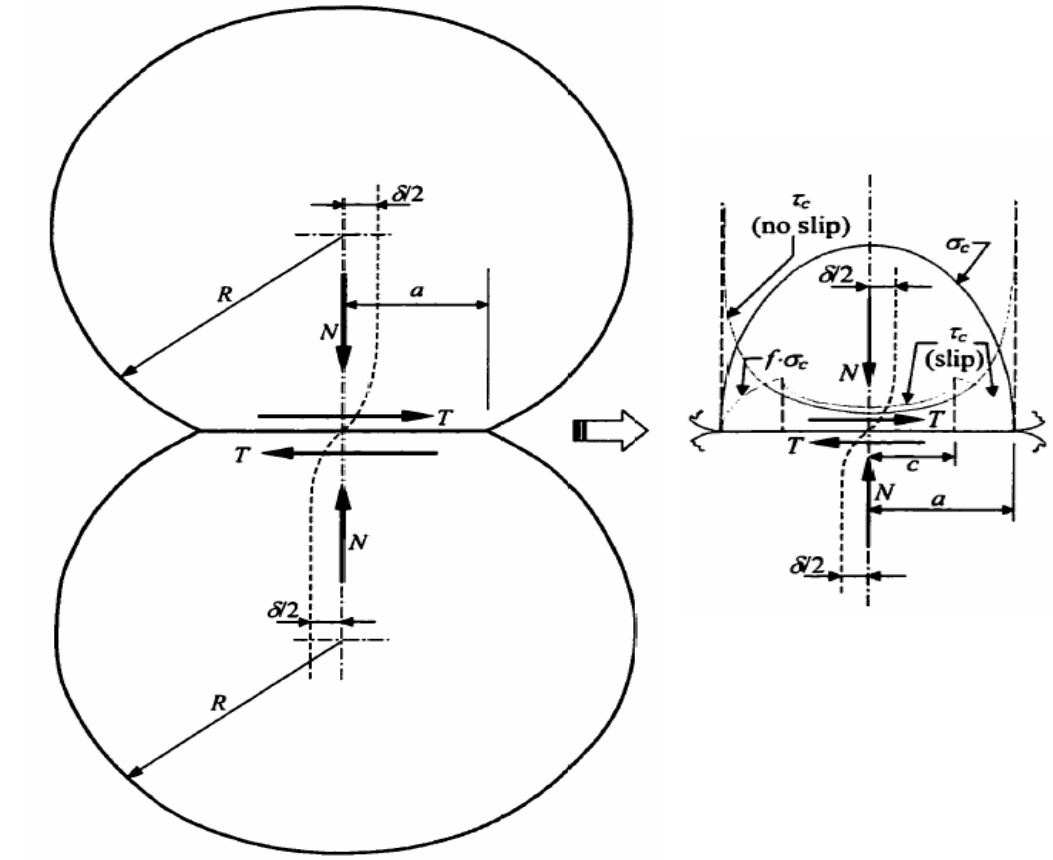

R = radius of spheres
N = normal force
T = tangential force
δ = lateral displacement of spheres
f = coefficient of friction between the spheres
σ_c = normal stress between the spheres
τ_c = shear stress between the spheres
a = radius of the contact area
c = radius of the non-slip contact area

Figure 5.7 Contacts of Two Spheres with Normal and Shear Forces (Green 2001)

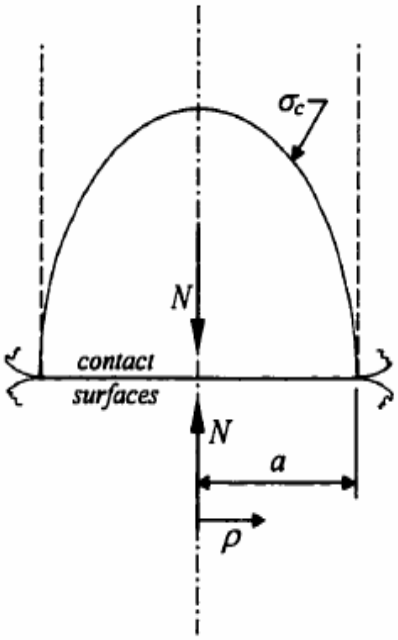

$$a = \left[\frac{3(1-\nu^2)RN}{4E}\right]^{1/3}$$

$$\sigma_c = \frac{3N}{2\pi a^3}\left(a^2-\rho\right)^{0.5}$$

R = radius of spheres
N = normal force
a = radius of the contact area
ν = Poisson's ratio

σ_c = normal stress between the spheres
ρ = distance from the center of the contact area
E = Young's modulus

Figure 5.8 Normal Stresses Acting across Spheres (Green 2001)

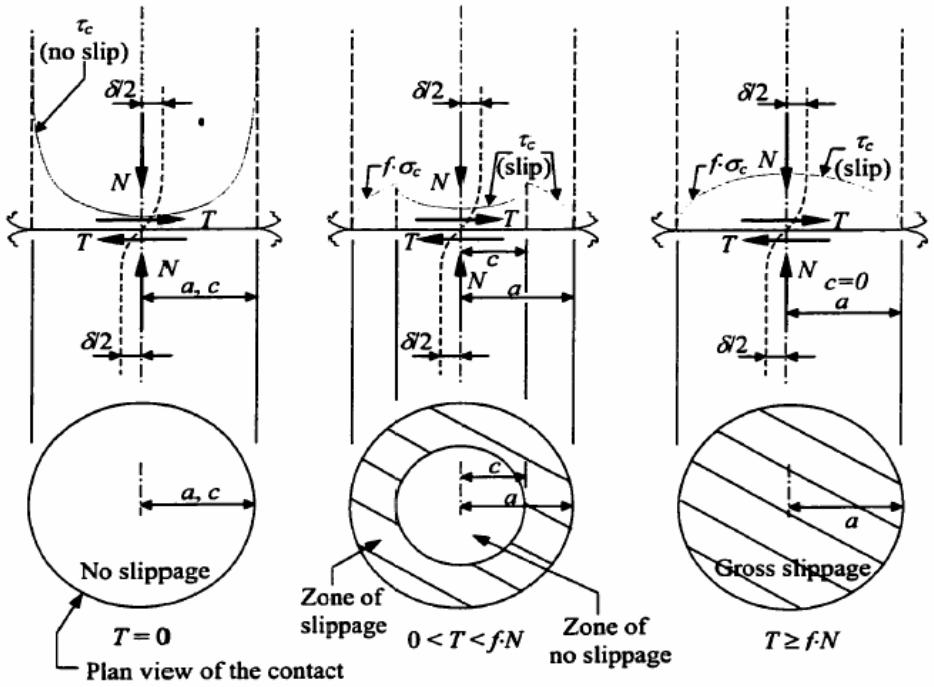

$$\left(\frac{c}{a}\right)^3 = 1 - \frac{T}{f \cdot N} \qquad \delta = \frac{3(2-\nu)(1-\nu) f N}{4 E a} \cdot \left[1 - \left(1 - \frac{T}{f N}\right)^{2/3}\right]$$

R = radius of spheres
N = normal force
T = tangential force
δ = lateral displacement of spheres
f = coefficient of friction of the spheres
E = Young's modulus
σ_c = normal stress between the spheres
τ_c = shear stress between the spheres
a = radius of the contact area
c = radius of the non-slip contact area
ν = Poisson's ratio

Figure 5.9 Relative Slippage of the Spheres (Green 2001)

5.3.2 Viscous Dissipation Mechanism

This portion of dissipation is due to viscous drag of the relative movement of a fluid and a solid. The theory by Biot (1956) may be used for the theoretical evaluation of energy dissipation by the viscous mechanism in soils. Hall (1962) and Hall and Richard (1963) outlined the results of a laboratory study examining the influence of various parameters on the total energy dissipated in granular materials, including the viscosity of the pore fluids. Comparison of saturated and dried samples can distinguish the relative contributions from friction and viscous drag.

Hall(1962) and Hall and Richard(1963) performed a series of resonant column tests. In their study, the specimens were excited at their first mode of vibration and then set in free vibration. The decay in the rotational amplitudes is energy dissipation. By comparing the rotational amplitude decay in saturated soil and dry soil, the relative contributions of the viscous and frictional energy dissipation can be examined. From the results of their study, the logarithmic decrement for the saturated specimens shows less vibration with rotational amplitude than the dry specimens. The portion of energy dissipated by viscous mechanisms increases as the amplitude of the rotations decreases (Hall 1962).

5.4 Computing Dissipated Energy from Laboratory Tests

In this section, the computation of dissipated energy for arbitrary load paths in laboratory test results will be outlined. The calculation of dissipated energy starts with general expression for incremental work per unit volume of material in the element and is in the following equation:

$$dW = \sigma_{ij} d\varepsilon_{ij} \tag{5.34}$$

Expanding this equation and assuming a symmetric stress and strain tensor results in the following:

$$dW = \sigma_{11} d\varepsilon_{11} + \sigma_{22} d\varepsilon_{22} + \sigma_{33} d\varepsilon_{33} + 2\sigma_{12} d\varepsilon_{12} + 2\sigma_{13} d\varepsilon_{13} + 2\sigma_{23} d\varepsilon_{23} \quad (5.35)$$

For an arbitrary load path, the cumulative energy dissipated per unit volume of material can be computed by integrating equation 5.34 or 5.35.

$$\Delta W = \int dW \quad (5.36)$$

In the cyclic triaxial test, the following boundary conditions are applied:

$$\sigma_{12} = \sigma_{21} = \sigma_{32} = \sigma_{23} = \sigma_{13} = \sigma_{31} = 0$$

Applying the above boundary conditions into equation 5.35, yields the following equation:

$$dW = \sigma_1 d\varepsilon_a + 2\sigma_3 d\varepsilon_h \quad (5.37)$$

where $d\varepsilon_a$ = increment in axial strain and

$d\varepsilon_h$ = increment in lateral strain

This expression can be further simplified using deviatoric stress and Poisson's ratio:

$$\sigma_d = \sigma_1 - \sigma_3 \quad (5.38\ a)$$

$$\nu = -\frac{\varepsilon_h}{\varepsilon_a} \quad (5.38\ b)$$

Substituting these expressions into equation 5.37 yields:

$$dW = \sigma_d d\varepsilon_a + \sigma_3 (1 - 2\nu) d\varepsilon_a \quad (5.39)$$

For a saturated undrained test, $\nu = 0.5$, then above equation reduces to:

$$dW = \sigma_d d\varepsilon_a \tag{5.40}$$

Using the trapezoidal rule to integrate, the dissipated energy per unit volume of material is follow:

$$\Delta W = \frac{1}{2}\left[\sum_{i=1}^{n-1}(\sigma_{d,i+1}+\sigma_{d,i})(\varepsilon_{a,i+1}-\varepsilon_{a,i})+(\sigma_{3,i+1}+\sigma_{3,i})(1-2\nu_i)(\varepsilon_{a,i+1}-\varepsilon_{a,i})\right] \tag{5.41}$$

Where, ΔW = dissipated energy per unit volume of material,

i = subscript representing ith increment in stress, strain and poisson's ratio, and

n = total number of increment.

5.5 Pseudo Strain

The development of the theory behind pseudo strain concept is presented in Schapery (1984). More recently Lee and Kim (1998), Cleveland (2001), and Si (2001) used the pseudo strain to analyze tests on asphalt. The above authors applied the elastic-viscoelastic correspondence principle of Schapery (1984) to the linear elastic equation. The solution results in stresses and strains that are not physical quantities but rather pseudo variables.

In the uniaxial condition, with a linear viscoelastic material, a stress can be calculated in the form of convolution integrals expressed as follow:

$$\sigma(t) = \int_0^t E(t-\tau)\frac{\partial\varepsilon(\tau)}{\partial\tau}d\tau \tag{5.42}$$

where $\sigma(t)$ = calculated linear viscoelastic stress,

t = present time,

τ = loading time history at which strain is measured,

$E(t-\tau)$ = Relaxation modulus at the time $t-\tau$, and

$\varepsilon(\tau)$ = measured strain at a previous time τ .

According to Schapery's extended correspondence principle, the uniaxial pseudo strain is defined as follow:

$$\varepsilon^R = \frac{1}{E_R}\int_0^t E(t-\tau)\frac{\partial\varepsilon(\tau)}{\partial\tau}d\tau \tag{5.43}$$

Where, ε^R = pseudo strain and

E_R = Reference modulus

With the definition of pseudo strain in Equation 5.42, Equation 5.43 can be rewritten as follows:

$$\sigma = E_R\varepsilon_R \tag{5.44}$$

Equation 5.44 is similar in form to the linear elastic stress-strain relationship. However it uses a reference modulus and a calculated pseudo strain. Figure 5.10 shows the relationship for a viscoelastic material in the pseudo strain domain, which has been undamaged. The undamaged material is illustrated by the linear elastic response in the pseudo strain domain.

In general, for a non-linear viscous material, which is more common in geological material, the plot of the measured stress versus the pseudo stain is a hysteresis loop as shown in Figure 5.11. There will be a hysteresis loop. This hysteresis loop so called pseudo hysteresis loop. The area within the pseudo hysteresis loop is the dissipated pseudo strain energy. The dissipated pseudo strain energy is the energy dissipated mostly due to friction, plastic behavior, and non-linearity since the time dependent viscoelastic behavior has already been eliminated by using pseudo strain.

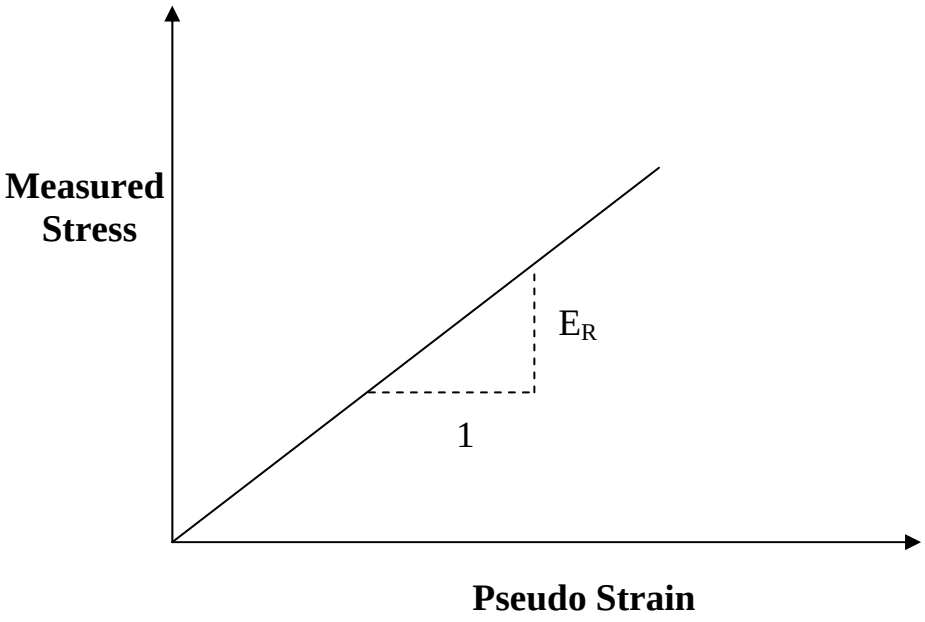

Figure 5.10 Undamaged Linear Viscoelastic Materials

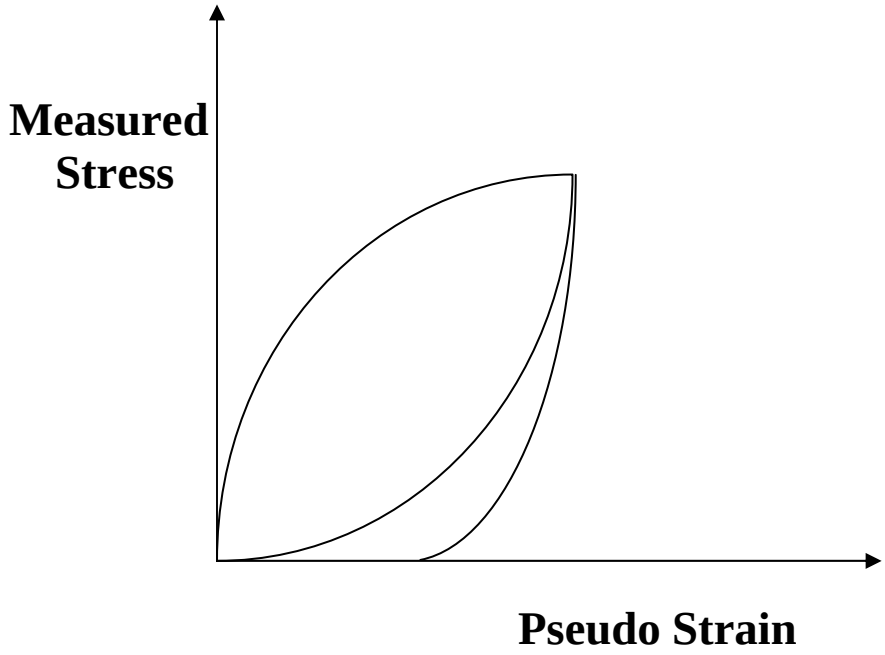

Figure 5.11 Stress versus Pseudo Strain Response of Nonlinear Viscous Materials

CHAPTER VI
LABORATORY APPARATUS

Geotechnical laboratory testing of unsaturated soils requires special modifications of the conventional testing apparatuses. The most significant modification is the use of the axis translation technique to control suction. This is accommodation of the independent measurement or control of the pore-air and pore water pressure in the unsaturated soil samples.

This chapter discusses the implementation of a servo-controlled, computer driven triaxial testing apparatus to test unsaturated soils under varying matric suction conditions. The discussion includes several components in testing equipment: computer control of the equipment, computer controlled data acquisition, triaxial cell, four axis actuators, and the control used in controlling the test environment. The purpose of this chapter is to familiarize the reader with the details of the equipment developed for making measurements and to give insight into the testing potential of the equipment. The original development of the testing device was presented by Brarfknecht (2001).

6.1 Testing Control and Data Acquisition Equipment

The triaxial testing for this study was performed on an automated triaxial testing system developed by Dr Jayson E. Barfknecht. This uses closed-loop feed back systems to control the loadings.

In the control equipment, a Pentium computer is utilized. A computer program written in LabVIEW provides the control. Simply comparing voltage values returned to the computer via an analog to digital board provides the control. Based on what target value is within the computer program a return voltage is sent to change a load or fluid pressure to the triaxial cell. The axis actuator responds by either increasing or decreasing the load or fluid pressure to the triaxial cell. This process is continuous during the test.

In the computer controlled data acquisition, another Pentium computer records the voltage output of transducers within the system. This voltage is logged into a Hewlett

Packard data acquisition unit. Some of these voltages are used to control the loads and applied pressure. To maintain the same voltages from each transducer, the signals are split at a junction box. Figure 6.1 shows a diagram interaction of the data acquisition, the computer providing the control, and the signals being sent to the axis actuators.

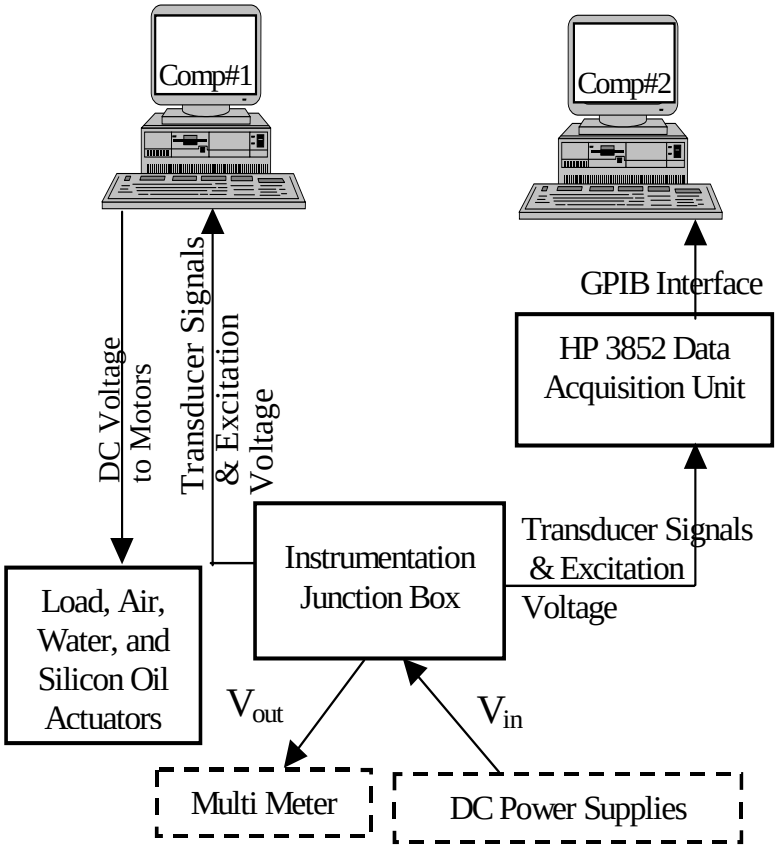

Figure 6.1 Testing Equipment Interaction (Barfknecht 2001)

6.2 Unsaturated Soil Triaxial Path Cell

A layout of the triaxial cell is shown in Figure 6.2. The basic function of a triaxial cell is to hold the specimen and apply stresses and/or strains in a controlled

manner. In this research, four variables that need to be controlled when testing unsaturated soils are the axial and confining stresses and pore-air and pore-water pressures.

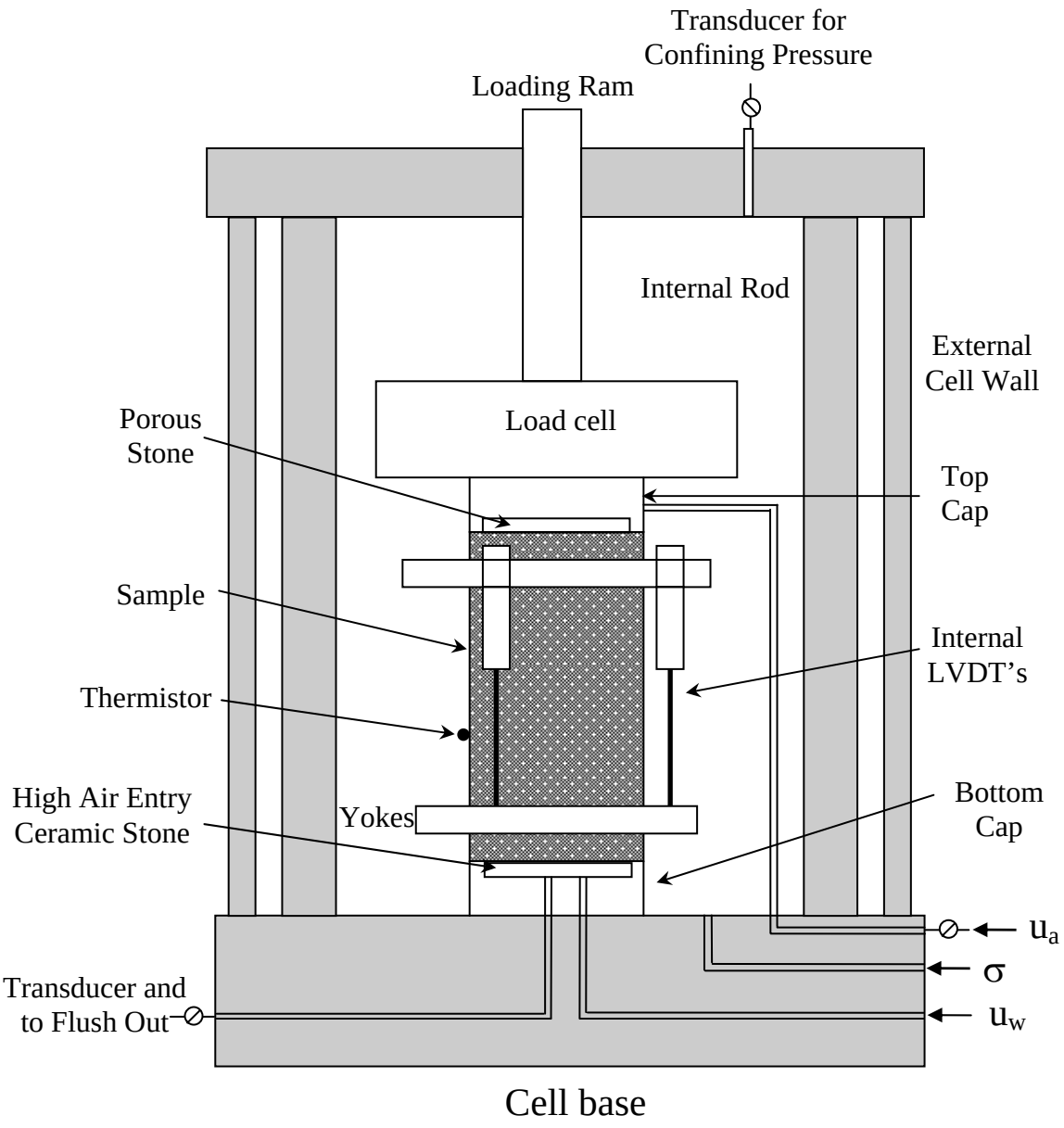

Figure 6.2 Stress Path Cell Layout (Barfknecht 2001)

The custom designed stainless steel cell manufactured by Geotechnical Consulting and Testing Services rests between two steel plates, which comprised the load frame. The cell has a confining pressure capacity of 7,000 kPa. The overall dimensions of the cell are 11-inch in the outside base diameter, 20.25-inch in height, and 0.5-inch in thickness. The internal space is 6.5-inches in diameter and 14-inch in height. Inside the cell, six internal rods are connected to bottom and top of cell. Therefore, sensitive internal electronic devices can be installed on the specimen. The top of the cell contains a 1.25-inch diameter opening with a graphite fiber reinforced seal that allows for the 12-inch long load shaft to move and apply pressure to the top of soil specimens. A load cell is attached to the bottom of the load shaft inside the cell to eliminate friction from the load shaft. The connection between the load cell and the load shaft is made by threading the end of the load shaft to match the threads in the load cell. A bottom plate is then bolted to the load cell, which allows the top-loading cap to be connected to the load cell through a threaded connection.

This triaxial cell can be viewed as a conventional cell for saturated soils, which has been modified in order to accommodate for the testing of unsaturated soils. Modifications are additional pore pressure connectors, electronic feed through lines through the base and top, and interchangeable platens.

The top cap is dedicated to the application and measurement of pore air pressure, through a coarse-porous stone linking the top of the sample to a controlled, continuous air phase. The low attraction (or low air entry value) of the porous stone prevents water from entering the pore-air pressure system. Therefore, continuity between the air in the voids of the sample and the controlling system is ensured. This kind of interface between a soil sample and the air phase has now become standard in testing unsaturated soils, and cause little problems, because the air pressure is usually kept well above the water pressure to apply suction and helps water not to enter the porous stone.

Also located in the top of the cell is an external port. This port allows for the air within the cell to be expelled as the cell fills with the confining fluids. Once the cell is

full, a pressure transducer is attached to the port to measure the confining pressure of the cell.

The bottom of the cell, which rests on the bottom plate of the load frame, is dedicated to the pore-water pressure control and suction control. Four ports are located in the base of the cell. One port is used for the pore air and is attached via internal tubing to the top cap. Another port is dedicated to the confining fluids. Two ports are used for the pore-water pressure. One port for the pore-water fluid is used to force water into the base, which leads to one side of the bottom cap. The bottom cap has grooves in the bottom to prevent air bubbles from becoming trapped as in Figure 6.3. The other side of the bottom cap leads the other port. This port is to flush out air bubbles that accumulate beneath the bottom stone.

The axis translation technique, developed by Hilf (1956) can be summarized as a shift of the pore-air and pore water pressure, keeping their difference constant. The interface between the pore-water pressure measuring system and the soil sample is critical to prevent air bubbles to penetrate the measuring system, as air is kept at a higher pressure than water. A high air entry disk is used for this purpose.

The pore water pressure is controlled or measured through a saturated high air entry ceramic disk. The high air entry ceramic disk is very fine porous filter, which allows the passage of water but prevents the passage of air. The air entry value is the maximum difference between air and water pressure. The matric suction in the soil specimen must not exceed the air entry value of the ceramic disk otherwise air flows through the disk. In this study, the ceramic disk with high air entry value of 15 bar is used. Originally the testing equipment was designed to test high-pressure range. This disk has to be sealed in the bottom cap, using epoxy resin in order to prevent the passage of air and water around its circumference.

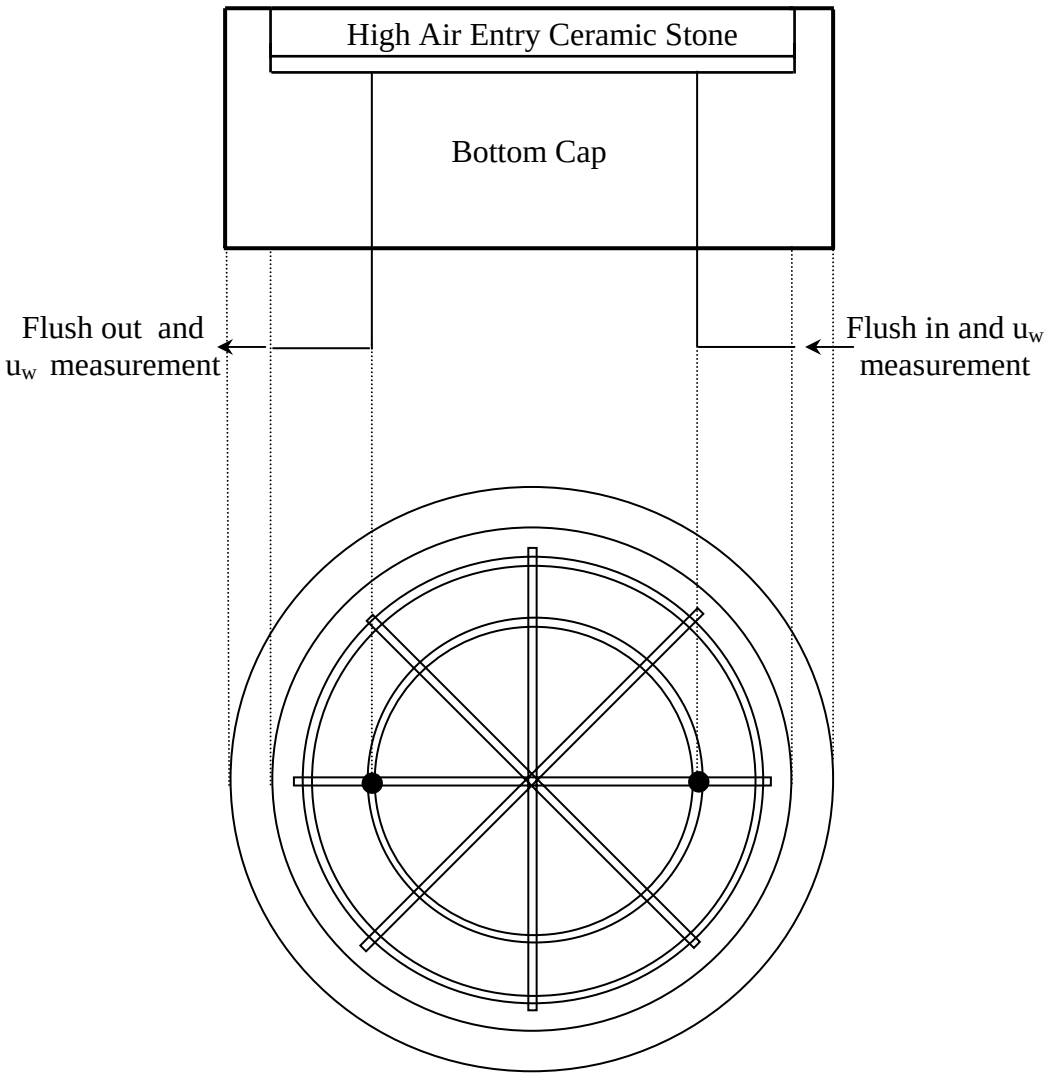

Figure 6.3 Layout of Bottom Cap and Grooves

For both the top cap and the bottom of the cell, the electrical feed-through lines are designed so that internal instruments can send analog signals to the computer. A total of 32 lines have been machined, 12 through the top of the cell, 20 through the base. 20 feed-through connectors allow for LVDT's to be placed onto the sample to monitor axial deformations. Twelve feed-through connectors are used to monitor and control axial load and temperature inside the cell.

A non- conductive fluid must be employed to apply the confining pressure around the specimen in order to allow for internal instrumentation to work properly. The fluid chosen is a high-viscosity Dow Corning silicon oil. The reason for high viscosity is to reduce leakage during tests. Its average kinematic viscosity is 200 centistokes.

6.3 Internal Instrumentation

In order to increase the accuracy of measurements, direct internal (i.e. inside the triaxial cell) measurements are needed to avoid errors due to the equipment itself. Four different measurements are placed inside the cell. All these instruments are suitable to work in a pressurized environment.

6.3.1 Axial Load

The loading cell with a 5,000 lbs capacity is used to measure the axial load applied to the sample. Previously, a 20,000 lbs capacity load cell was used by Barfknecht (2001). However, this load cell capacity is too high to measure the axial load applied to the sample at low net confining pressures (50 to 200 kPa) and low suction levels (40 and 80 kPa). The new load cell (model SWP-5K) was purchased from Transducer Techniques. For the calibration of load cell, Instron Testing Machine was used. The calibration factor for the load cell in the soil testing system is 2348.46 lbs/mV/V with an R-squared value of 0.99966. The calibration curve for the new load cell is in Appendix A.

6.3.2 Axial Deformation

The axial deformation of the sample is measured by three AC/AC type LVDT's manufactured by Lucas Control Systems. These LVDT's are mounted to specimens vertically by means of two yokes (Figure 6.2). The yokes are machined from aluminum and allows for the transducers to be spaced 120^{o} apart around the circumference of the specimen. The transducer's lightweight and small size makes them suitable for the axial deformation of the sample to be monitored with minimal sample disturbance. The range

of operation for the transducers is +/- 0.25 in. Three signal conditioning units are needed to convert an input DC voltage to a LVDT AC excitation voltage with a frequency of 10 kHz. With this type of configuration the manufacturer guarantees the linearity to be 0.09% across the full range. This equates to a strain of 1.92x10-4 in/in for a gauge length of 2.340 inches. The calibration of the internal LVDT's was done by Jayson Barfknecht (2001). The calibration factors for the three internal LVDT's are given in Table 6.1. Additional sample deformation is measured with a DC/DC type LVDT placed outside the cell and will be described in the external instrument section. Also available is non-contacting sensor to measure radial deformation. However, the use of this is prohibited due to difficulty of receiving light from target surfaces.

Table 6.1 Calibration Factors for Internal LVDT's (Barfknecht 2001)

Description	Calibration Factor (in/V)	R-squared
LVDT 1	0.026983	0.999957
LVDT 2	0.028150	0.999986
LVDT 3	0.028391	0.999998

6.3.3 Temperature

A Thermistor purchased from YSI (YSI 44015 Precision Thermistor) is used to measure the temperature inside the cell. It basically consists of a resistor, which has resistance proportional to temperature. As the temperature was changed in the cell, the measurement of the voltage in the resistor, compared to the input voltage, will be indicative of the temperature inside triaxial cell.

6.4 External Instrumentation

The external instrumentation consists of three pressure transducers, 3 LVDT's to measure volume change of three fluids, and LVDT to measure axial deformations.

6.4.1 Pressure Transducers

The measurement of pressure is accomplished by means of pressure transducers. They are mounted in an adapter connected to the fluids tubing. The high accuracy pressure transducers that were purchased (Data Instruments model AB/HP) are made of 316 L stainless steel. The transducers have a measuring range of 0-100 psi. The calibration factors for the three transducers are in Table 6.2. The calibration curves for the three transducers can be found in Appendix A.

Table 6.2 Calibration Factors for Pressure Transducers

Transducers	Calibration Factor ((psi/mV)/V)	R-squared
Pore-Air	5.002471	0.999994
Pore-Water	5.020163	0.999993
Silicon Oil	5.010303	0.999988

6.4.2 Axial Deformation and Fluid Volume

The three LVDT's have a measuring range of 8, 10, 12 inches. Each LVDT (purchased from RDP)is attached to an actuator piston to measure the displacement of the piston. The purpose of the LVDT's is to measure the volume change of each fluid phase and serve as an independent measurement of total volume change of the specimens. Although three internal LVDT's are available to measure axial deformation of specimens, another LVDT is necessary to measure large deformation of the samples. In order to provide this measurement a DC/DC type LVDT is placed outside the cell. The calibration factor for 4 LVDT's summarized in Table 6.3.

Table 6.3 External LVDT Calibration Factors (Barfknecht 2001)

LVDT	LVDT Stroke Length (in)	Calibration Factor (in/V)	R-squared
Pore-Air Actuator	12	0.58533	0.999985
Pore-Water Actuator	8	0.38279	0.999997
Silicon Oil Actuator	10	0.57798	0.999987
External LVDT	2	0.09817	0.999961

A reaction arm attached to the loading shaft allows for the measurement of the displacement made. The external LVDT is mounted off to the side of the cell near the top by using a post that is threaded into an existing hole in the top of the cell. Figure 6.4 shows the arrangement for measuring large axial strain in more detail.

6.5 Temperature Control

In order to keep surface tension of fluids constant, the temperature of the cell is essential. Temperature control requires a good isolation from the room temperature. Therefore, an environmental chamber was built around the triaxial cell and its frame. The internal temperature of the cell is controlled from an external heat source. Two heat lamps are used to produce an external heat source. An independent control device controls the temperature of an environment chamber at 25^{o}C. When the temperature within the chamber drops below 25^{o}C, the heat lamp is turned on and the temperature rises. Also, 18-inch fans within the chamber continuously circulate the air. Figure 6.5 show the picture of the environmental chamber to control temperature.

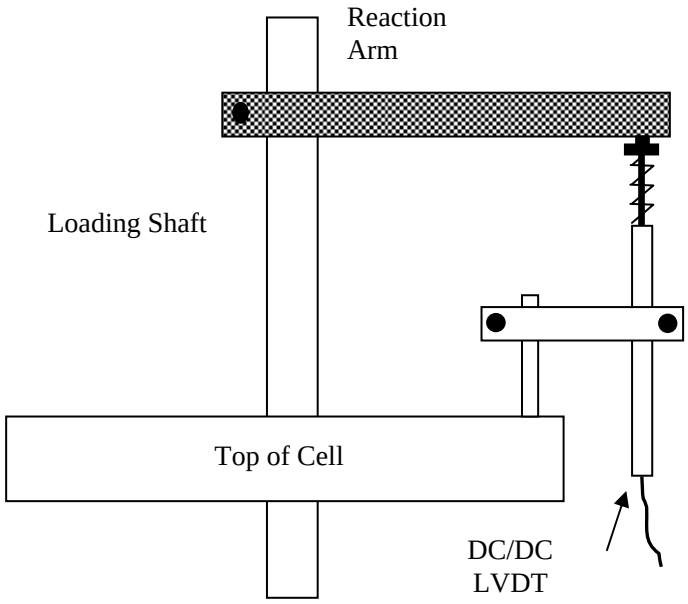

Figure 6.4 External Strain Measurement (Barfknecht 2001)

Figure 6.5 Photograph of Environment Chamber

6.6 Pore-Water, Pore-Air, Cell Fluid, and Axial Load Servo Control

The triaxial testing equipment actually consists of three pressure or volume servo-controls and one axial load or deformation servo control. Servo-controls (axis actuators) are needed to control the applied pressures and load to the soil sample independently. Three servo-controllers for the fluids are digital pressure-volume controllers (DPVC) and consist of an electric motor, hydraulic cylinder, ball screw actuator, and LVDT. The electric motor is attached to the ball screw actuator through a bevel gear interface. The rotation of the electric motor is turned into an axial translation of the pressuring piston by the ball screw actuator that pulls or pushes the piston inside the cylinder, thereby decreasing or increasing the fluid pressure. This mechanism constitutes an closed-loop system. The feedback can be ensured by any electrical sensing device which measures the response of the system. Depending on the instrument used as the feedback signal, one can control pressure and measure volume change or control volume change and measure pressure. This is the basic of principle of a DPVC as in Figure 6.6.

The LVDT is attached to the ball screw actuator by a special link. The LVDT records the movement of the piston. By knowing the internal area of the piston the volume change within the cylinder can be determined.

Each fluid phase has a different compressibility. Therefore, each one had to be sized independently. The pore-water axis actuator piston was sized so that a soil sample could be fully saturated. In order to supply the water actuator with de-aired water, a Nold Deaerator was attached to the system. A three-way valve controls the direction of the water flow. Figure 6.7 illustrates the layout of the water actuator.

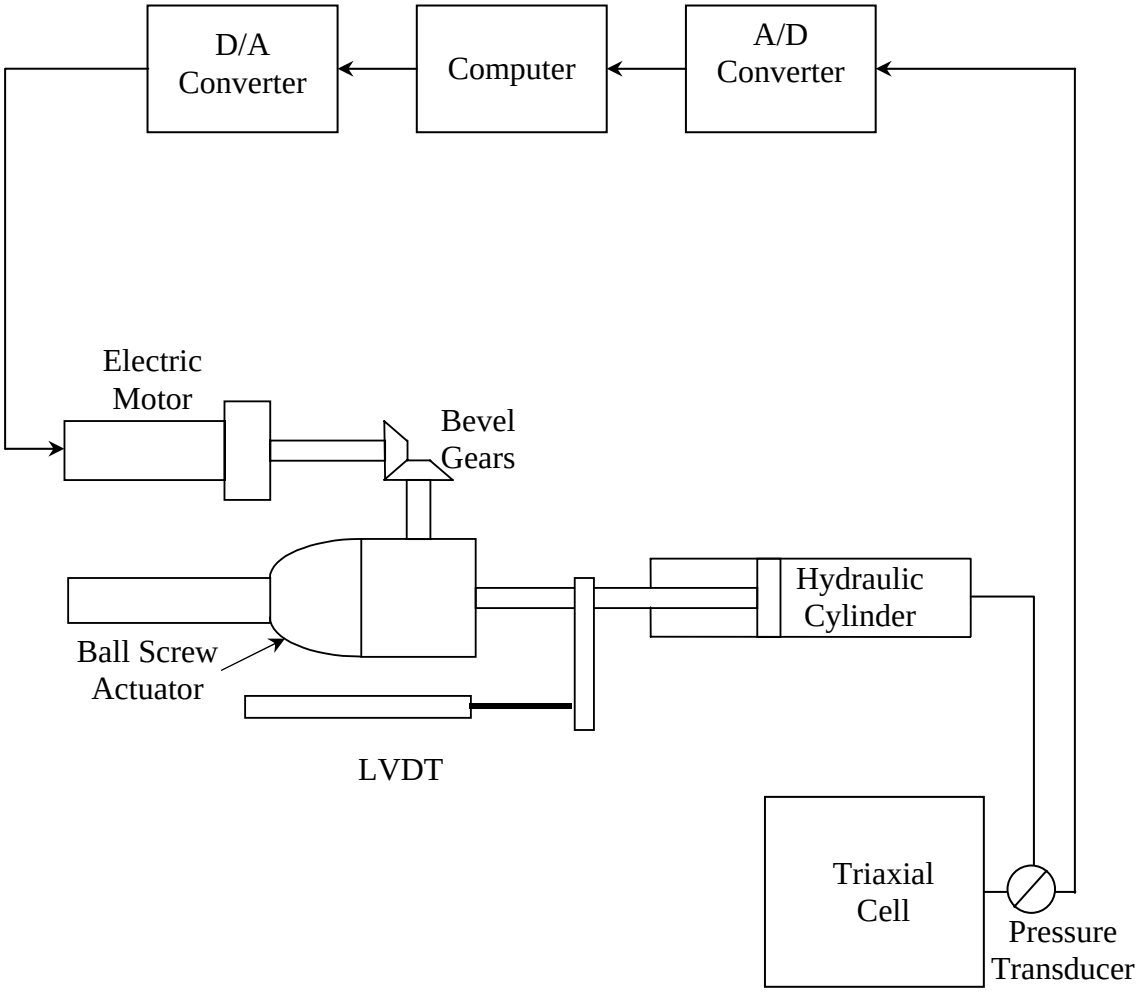

Figure 6.6 Fluid Axis Actuator Components and Closed-Loop Servo-Control

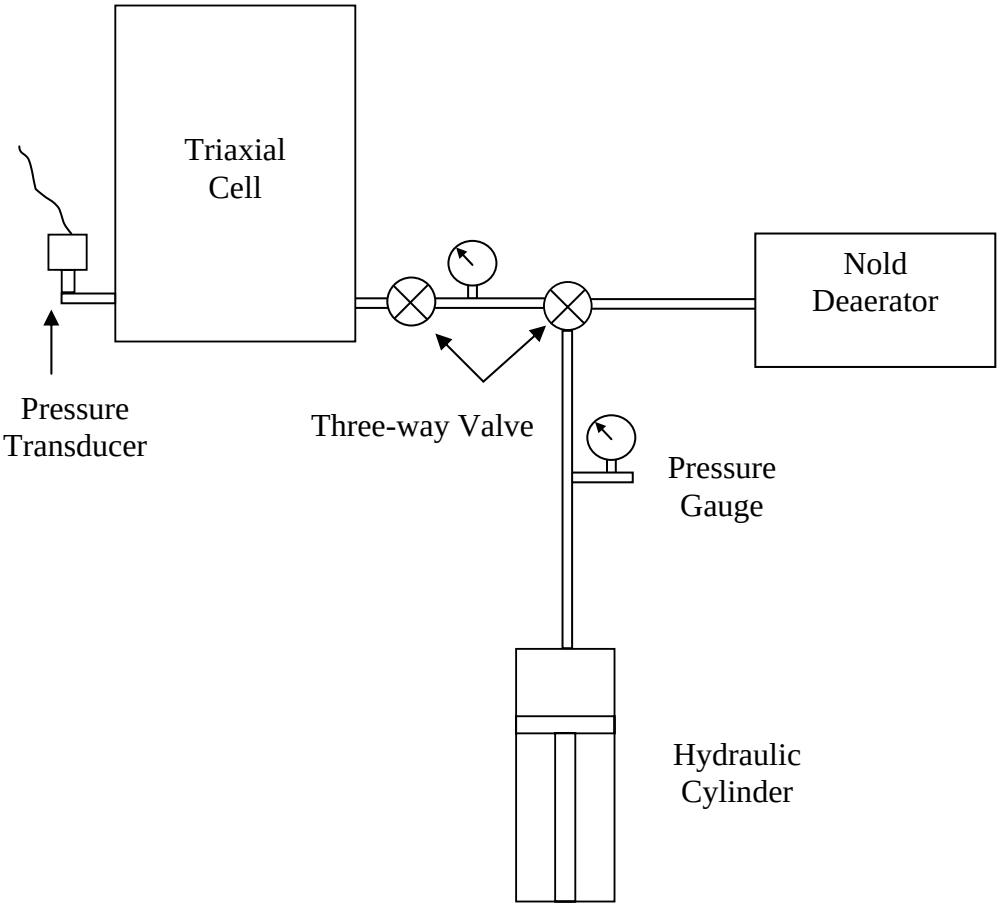

Figure 6.7 Pore-Water Axis Actuator Piping Layout (Barfknecht 2001)

The silicon oil actuator piston was sized such that the compressibility of the oil could achieve the maximum cell pressure of 7000 kPa. By taking account of the instrumentation, internal rod, load cell, soil sample, and load shaft a cylinder with a volume of 22.7 in^3 was selected and used. Figure 6.8 shows the layout of the silicon oil actuator.

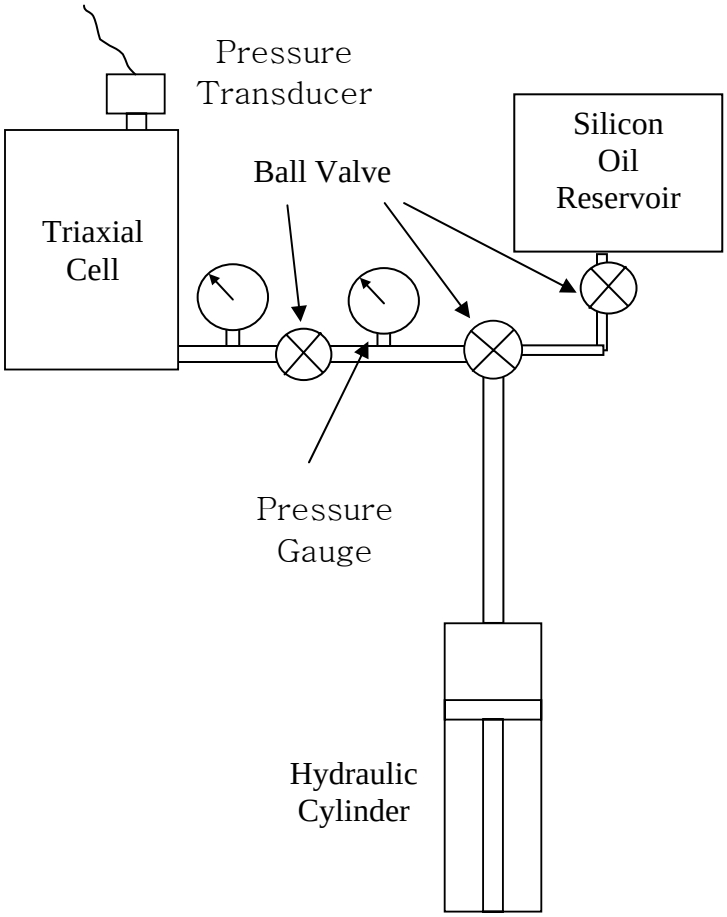

Figure 6.8 Silicon Oil Axis Actuator Piping Layout (Barfknecht 2001)

For the pore-air actuator, an external gas cylinder filled with nitrogen gas is linked to the pore-air actuator. This is necessary since air is much more compressible than water and silicon oil. By using the compressed air cylinder, the pressure within the sample can be brought close to the desired pressure. The pore-air actuator is then used to maintain the pressure to achieve the desired level of matric suction during the test. Figure 6.9 shows the layout of the pore-air actuator system.

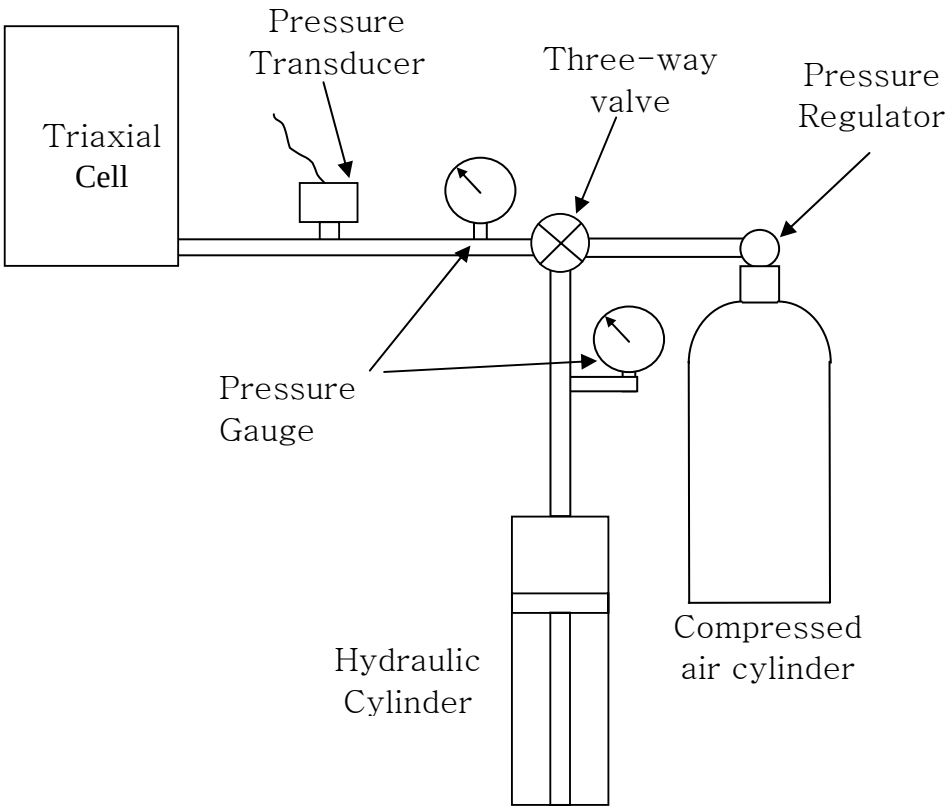

Figure 6.9 Pore-Air Axis Actuator Piping Layout (Barfknecht 2001)

In order to control axial load or displacement, a force or displacement is applied directly to the soil sample. There is no need for a hydraulic cylinder to pressurize a given fluid. The feedback signal can come from the load cell (for stress-controlled tests) or from the LVDT connected to the loading ram (for strain-controlled tests).

The axial load actuator is composed of a ball screw actuator and an electric motor. The electric motor is connected to the ball screw actuator in order to transform the rotation to a translation. This translation motion forces the load shaft either up or down depending on the desired level of stress on the specimen. In order to ensure that no moment is translated to the specimen, a steel ball is placed between the end of the ball screw actuator and the load shaft.

The electric motor (servomotor) and ball screw actuator are fixed to the triaxial loading frame, a 100,000 lbs capacity frame, consisting of two horizontal steel plates, the triaxial cell being supported by the lower one, the electric motor and ball screw actuator being fixed to the top one. Figure 6.10 shows a diagram of the axial load actuator and the linkage between the actuator and the load shaft.

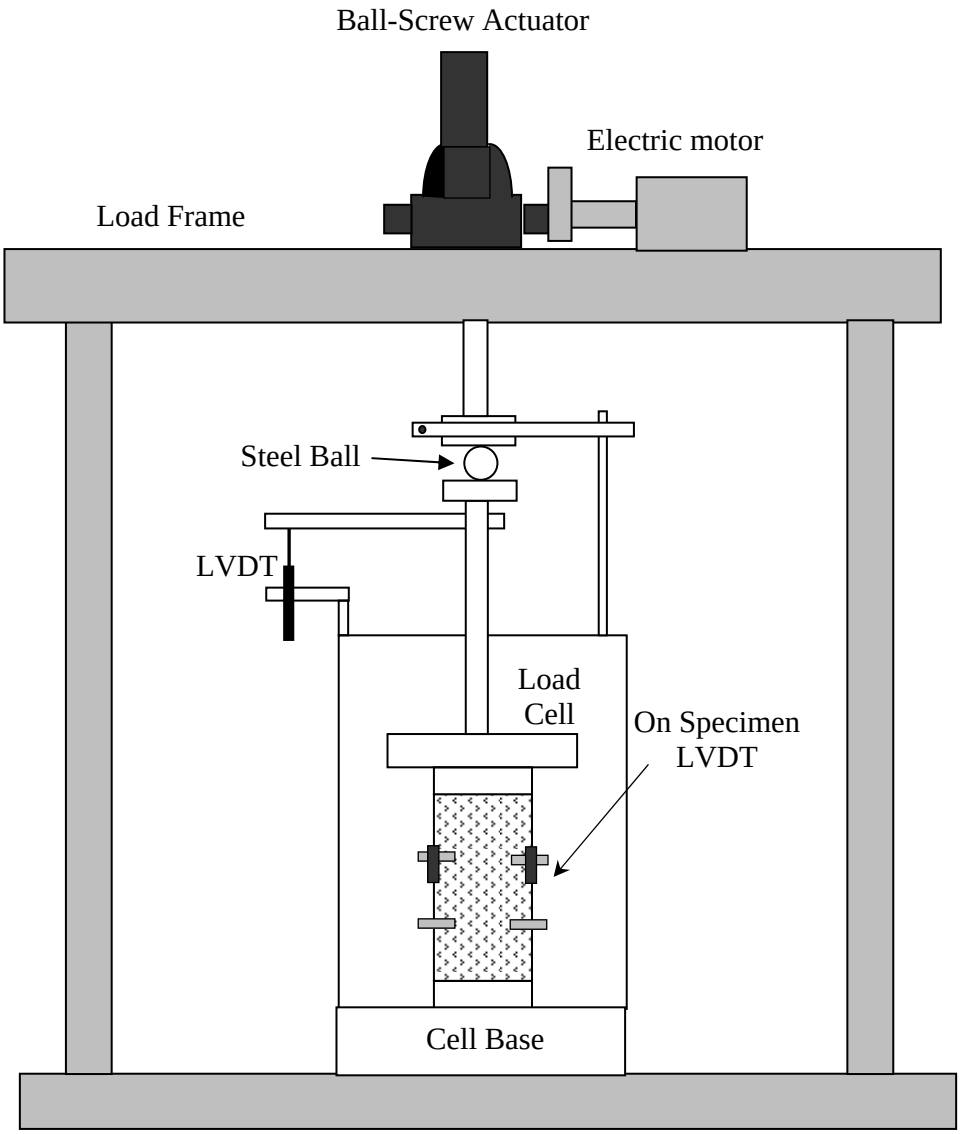

Figure 6.10 Axial Load Axis Actuator (Barfknecht 2001)

6.7 Measurement of Total Volume Change of Specimen

The measurement of total volume change for an unsaturated soil specimen is much more complicated than for a saturated soil specimen. In the case of a saturated soil, the total volume change is equal to the water volume change and can easily be measured by a volume change gauge. In an unsaturated soil, the total volume change is equal to the sum of water-phase and air-phase volume changes if the soil particles can assumed to be incompressible.

Geiser et al. (2000) summarized the existing methods of volume measurement for unsaturated soils and classified them into three categories. They are 1) cell fluid measurement, 2) direct air and water volume change measurement and 3) direct measurement on the specimen.

In the original development of the unsaturated stress path cell, direct measurement on the specimen was available using fiber optic censors. However the use of these was limited due to this research, the total volume change is measured indirectly from the flow of oil filled in the cell. The volume change is determined by recording the motion of the piston using an LVDT attached to the piston and multiplying this change in length by the area of the piston.

CHAPTER VII
EXPERIMENTAL PROGRAM AND NUMERICAL ANALYSIS

This chapter begins with a description of the types of soil used in this investigation, the procedure for sample preparation, and the test set up for triaxial tests. It is followed by the procedure followed to conduct suction controlled drained tests on recompacted silty sand specimens. The next presentation in this chapter is the results of the triaxial tests. The test results are used to determine model parameters for the critical state model for unsaturated soil used in this research. The model and test results are compared to validate the critical state based model proposed by Alonso et al. (1990). A brief review of the calculation of cone tip resistance using the unsaturated soil model is presented. The method of analysis of the liquefaction process of unsaturated silty sand is presented thereafter. The last part of this chapter presents undrained cyclic triaxial test results and the calculation of dissipated pseudo-strain energy of the unsaturated soil samples.

7.1 Soil Testing

7.1.1 Index Testing

An index testing program was performed on fine-grained sand from the Texas A&M University Riverside Campus. Previously, Briaud and Gibbens (1994) and Tand (2000) have documented the soil properties of the sand at various depths. Soils taken for the test was classified as silty sand. Additional tests were conducted by Barfknecht (2001) to validate these test data.

Tand (2000) and Briaud and Gibbens (1994) both documented the dry density and in-situ moisture content of the samples taken during two different times of the year within a depth of 2 to 4 feet from the surface. Tand (2000) reported an average moisture content of 15 % with a dry density ranging from 1600 to 1700 kg/m^3. Records of Briaud and Gibbens (1994) show dry density range of 1450 to 1550 kg/m^3 and an average moisture content of 5 %. The former data were collected in January, 2000, which is a

wet season for Bryan/College Station. The latter data were collected in the summer of 1994, which is a dry season.

Due to spatial variation of soil samples in the field, more laboratory tests were conducted. Tests included grain size distribution, specific gravity, liquid limit test, and plastic limit test according to ASTM standards. The index properties of the soil are summarized in Table 7.1 and the sieve and hydrometer analysis results are in Figure 7. 1.

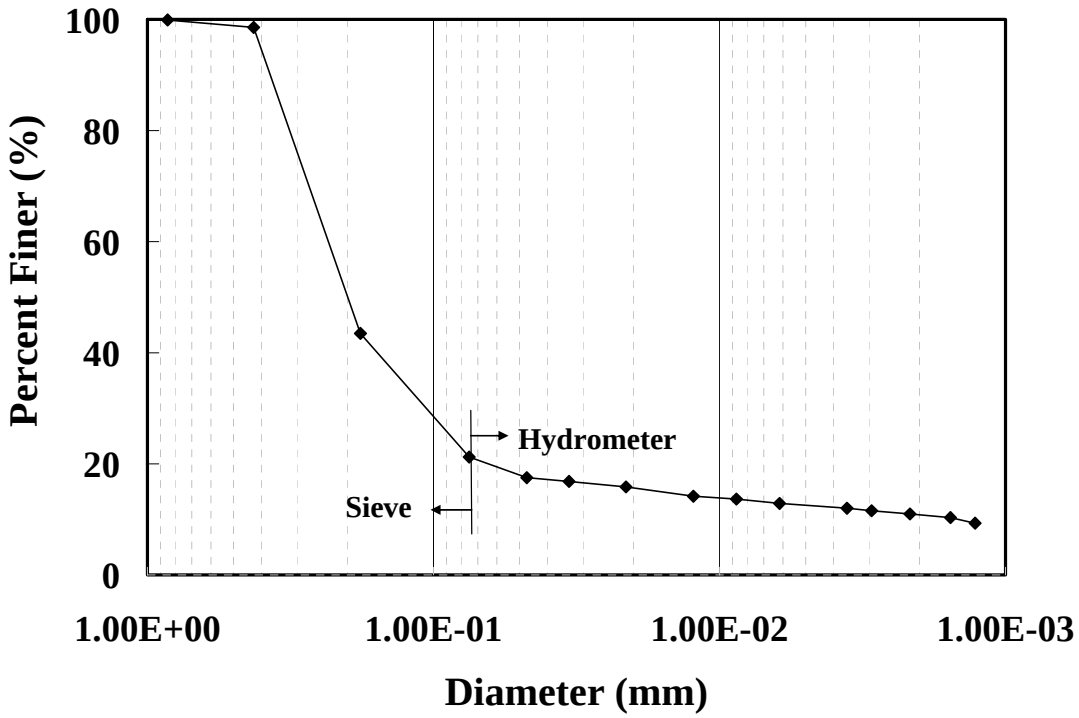

Figure 7. 1 Particle Size Distribution

Table 7.1 Index Properties of Soils from the Riverside Campus

USCS Classification symbol	SM
Median Grain Size (mm)	0.2
Coefficient of Uniformity, C_c	2.15
Coefficient of Curvature, C_u	4
Specific Gravity, G_s	2.66
Liquid Limit	21
Plastic Limit	16

7.2 Sample Preparation and Compaction

Once the material was classified, a method had to be developed to produce a specimen that could be duplicated. The duplication was in terms of moisture content and dry density. This duplication was important to eliminate any adverse effects the properties of the samples might have from test to test.

In the beginning, the soil was oven-dried to a temperature of 125^{o}C and then was cooled down. At least one day prior to testing, the required quantity of water was added slowly to the dry soil and mixed thoroughly in a mechanical mixer. Thereafter, the soil was stored and sealed inside a double plastic bag for at least 24 hours so that the water could be distributed evenly throughout the soil. The target water content for the samples with the full equalization process was 12 % and with less equalization time was 13 % and 14%. Triaxial specimens of 3 inches in diameter and 6 inches in height were prepared by moist tamping in multiple layers. Specimen was not compacted directly on the base pedestal of the triaxial cell. Disturbance is unavoidable during transportation to the triaxial cell. The compaction apparatus consisted of a supporting frame and a sliding hammer as in Figure 7.2. The desired dry density of the soil specimen was achieved by controlling the thickness of the soil for a given mass of soil.

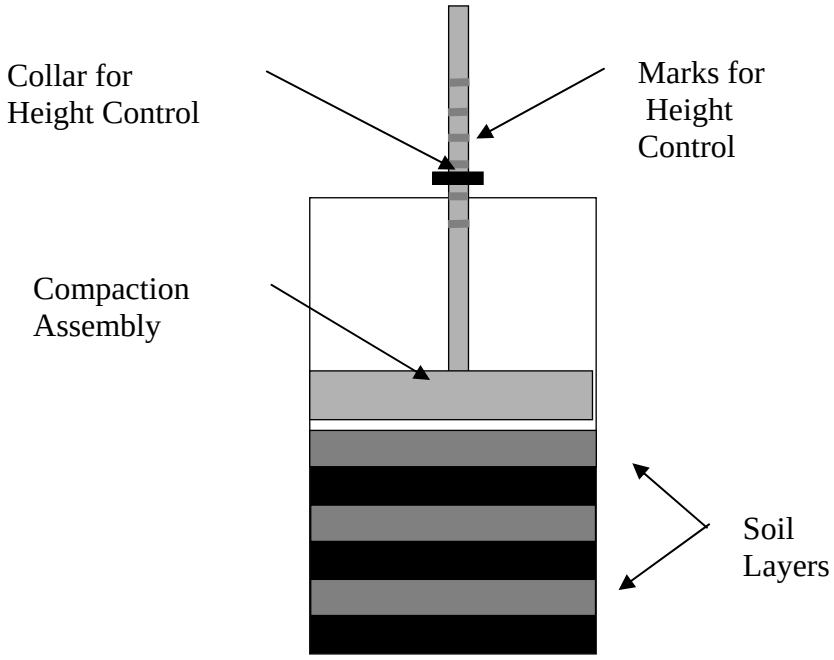

a)

b)

Figure 7.2 Schematic of the Compaction Process (a) and Compaction Mold (b)

The undercompaction method proposed by Ladd (1978) was adopted to prepare a uniform specimen. The bottom layer should be under-compacted and the top layers should be over-compacted in order to achieve a more uniform specimen.

In this study, the intention was to reproduce unsaturated soil specimens with a low value of isotropic yield stress, so that, subsequently, it was relatively easy to reconsolidate the soil to a virgin state for calibration of the elasto-plastic model parameters (Alonso et al. 1990 and Wheeler and Sivakumar 1995). The average target dry density was 1400 kg/m^3. The water content of the soil was determined by equalizing unsaturated soil specimens at 40 and 80 kPa. After equalization of the unsaturated soil specimens, the water content of soil specimens was measured for each suction level. In the subsequent tests, each sample was compacted at the desired water content for each suction level (13 % for 80 kPa and 14% for 40 kPa of suction) in order to reach equalization rapidly.

Specimens with chemicals were prepared in the same manner prior to all testing. The two chemicals used in this study were acetone for organic chemicals and sodium chloride (NaCl) for inorganic chemicals. The target concentration of sodium chloride was 20% (g/100g solution). The appropriate weight of sodium chloride was dissolved into the amount of distilled water needed to achieve the initial target water content. The solution was added to the soil and thoroughly mixed. The target concentration for acetone was 10% (g/1000g solution). The water and acetone are mixed together and added to the dry soil.

All the samples are labeled in the following convention: The first letter “S” and number indicates initial suction level applied. The second letter “I” or “M” indicates isotropic or monotonic tests. The last letter indicates the chemicals in the water. D indicates distilled water, N indicates sodium chloride in the water, and A indicates acetone added in the water. Therefore, for example, S40ID is sample with initial suction level of 40 kPa, isotropic test, and no chemicals in the water.

Filter paper suction tests are performed after compaction of the soil samples. The use of the Van't Hoff's Equation in Chapter II enables us to check with the osmotic suction measurement by filter paper suction tests as in Table 7.2.

Table 7.2 Filter Paper Suction Tests after Compaction (Units: pF)

	S80ID	S40ID	S80IN	S40IN	S80IA	S40IA
Water Content	12.9%	14%	13.1%	14.2%	13.2%	14.3%
Matric Suction	2.73	2.42	2.77	2.22	2.71	2.28
Osmotic Suction	2.49	2.63	4.83	4.89	2.74	2.64
Total Suction	2.93	2.84	4.83	4.89	2.98	2.87
Osmotic Suction By Van't Hoff Eq.			5.0	5.0	1.638	1.638

7.3 Test Set Up

Before each unsaturated test, the high air entry ceramic disk was saturated in order to minimize the amount of air bubbles trapped inside the disk and in the water reservoir beneath the disk. The procedure recommended by Fredlund and Rahardjo (1993) was adopted to saturate the high air entry disk. Additionally, the ceramic disk was kept under the water reservoir above the disk. Before setting up the specimen, any excess water left on the high air entry disk was removed with a dry tissue. The specimen for unsaturated tests was compacted in the compaction mold. After the sample was compacted, a latex membrane was placed on the specimen. Subsequently, the specimen was loaded on the triaxial stress path cell and the membrane was sealed to the top cap and the base pedestal by O-rings. In addition to sealing the membrane, the on-specimen strain yoke was mounted on the membrane. Then, the on-specimen LVDT's were attached.

After setting the on-specimen LVDT's, a bi-axis measuring telescope is used to measure the height and diameter of the specimen as well as the gauge length for the on-specimen strain yoke. The bi-axis telescope uses a vernier scale to measure the dimensions to 0.001 inches in two planes (x-y). In order to ensure that the telescope does not move during the measurement, the support is clamped to the table. The diameter of the sample is measured at the bottom, middle, and top of the specimen. The thickness of membrane was subtracted thereafter. The gauge length for the on-specimen strain yoke is measured in three locations in order to obtain an average length.

After the test, the sample is measured again. The gauge length is measured first in three locations and then removed. After the removal of the yoke, the specimen dimensions are measured again. This time, the diameter is measured in 13 locations in order to provide a profile of the final deformed shape. The largest diameter is used in calculating the corrected area for the specimen during the test so that the stress at that point in time can be calculated.

Once the specimen measurement and measurements of the gauge length are complete, the metal cell wall is placed in position. Subsequently, the cell is filled with the silicon oil. The time to fill the cell is 1 hour due to the high viscosity (200 cSt) and small pipe diameter. As mentioned before, in this study, the equalization stage is shortened for most tests due to the high air entry ceramic disk and leakage of cell fluid. Thus, once the cell is filled, an initial net cell pressure of 50 kPa is applied. Quickly, the pore air and pore water pressure are raised to desired suction value (40 or 80 kPa). In this study, the water pressure was raised to 200 kPa. Therefore, the air pressure was raised to 240 or 280 kPa and the initial confining pressure was raised to 290 kPa or 330kPa to reach a net confining pressure of 50 kPa. The specimen is left under these conditions until the specimen equalizes at constant suction and the temperature stabilizes at 25 ^{o}C. To standardize the procedure, all specimens were left for 1 day under cell pressure, air pressure, and water pressure. During this period, the volume change of the specimens was monitored by the on-specimen LVDT's and oil actuator LVDT.

7.4 Monotonic Triaxial Testing Procedure

A typical drained stress or strain/suction controlled test follows three main steps and is summarized as follows. Once the complete triaxial testing device has been fully assembled, the unsaturated soil specimen is subjected to an initial hydrostatic stress state, σ-u_a and u_a-u_w. Equalization is then allowed in the pore-water (Stage 1: equalization stage). Once no further water volume change is detected from the sample, the sample is considered to be equalized with the applied stresses. For further isotropic loading (Stage 2: ramped consolidation) and shear loading (Stage 3: shearing), the sample is loaded at a constant stain or stress rate. Any excess in the pore-air and pore water pressures, caused by the applied load, are then dissipated by allowing the pore fluids to flow in or out of the soil specimen. This 3-stage process is depicted in Figure 7.3.

As mentioned previously, in this study, the equalization process was shortened by compacting samples at the desired suction levels. In case of shearing, the deviatoric stress is applied until it is apparent that the stress has reached a peak value. (20 % of axial strain).

7.5 Experimental Results and Model Parameter Determination

In this section, the experimental results of two series of triaxial tests conducted on the loosely compacted soil specimens are presented. The triaxial tests include:

1) 6 drained isotropic compression tests.
2) 17 drained (constant suction) monotonic triaxial tests.

All specimens were compacted at a dry density of 1400 kg/m^3 and at a water content 13% and 14% except for two samples. These two samples, which were used for the equalization tests, were compacted at dry a density of 1400 kg/m^3 and at water content of 12%.

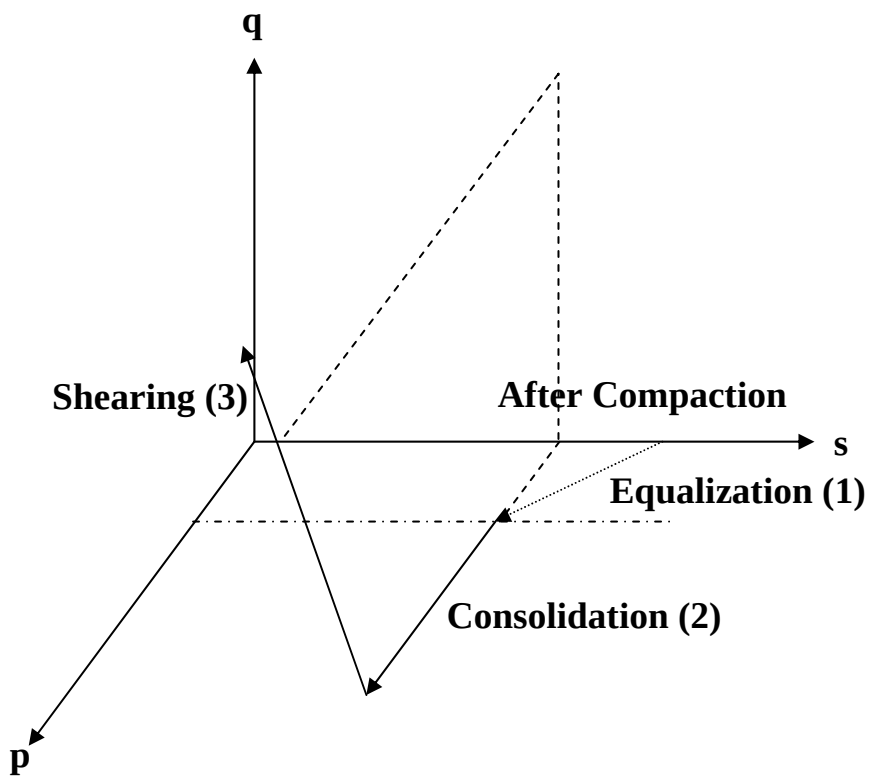

Figure 7.3 Typical Multistage Stress Path in Unsaturated Soil Testing

7.5.1 Equalization

The purpose of the equalization stage is to enable the pore water pressure within the sample to equal the back pressure value. During equalization, the matric suction within the sample will be down or up from the desired valued. In this study, the equalization stage was conducted to determine the water content of each suction level to be tested so that during the compaction process, the specimen can be compacted at the desired suction level. The specimens were compacted at 12 % water content and 1400 kg/m^3 of dry density. Figure 7.4 shows the change in specific volume, v = 1+e, with time t, during the equalization stage. Each test started with an immediate reduction in specific volume corresponding to a rapid increment of net mean stress from zero to 50 kPa. For both cases, the initial compression was followed by an increase in specific volume. For

both test with an applied suction s = 40 kPa and s = 80 kPa, there were reductions in specific volume (collapse) during the later part of the equalization. The amount of collapse for a suction of s=80 kPa was smaller than that for s = 40 kPa. The equalization was completed within 2 to 5 days. During equalization, the total volume change of the specimen was monitored by the flow of the cell fluid, the flow of the water, and the inside LVDT's. Specimens compacted at 13% and 14% show similar behavior as in the case of samples compacted at 12 % water content. However, there were no signs of collapsible behavior and equalization time was shortened.

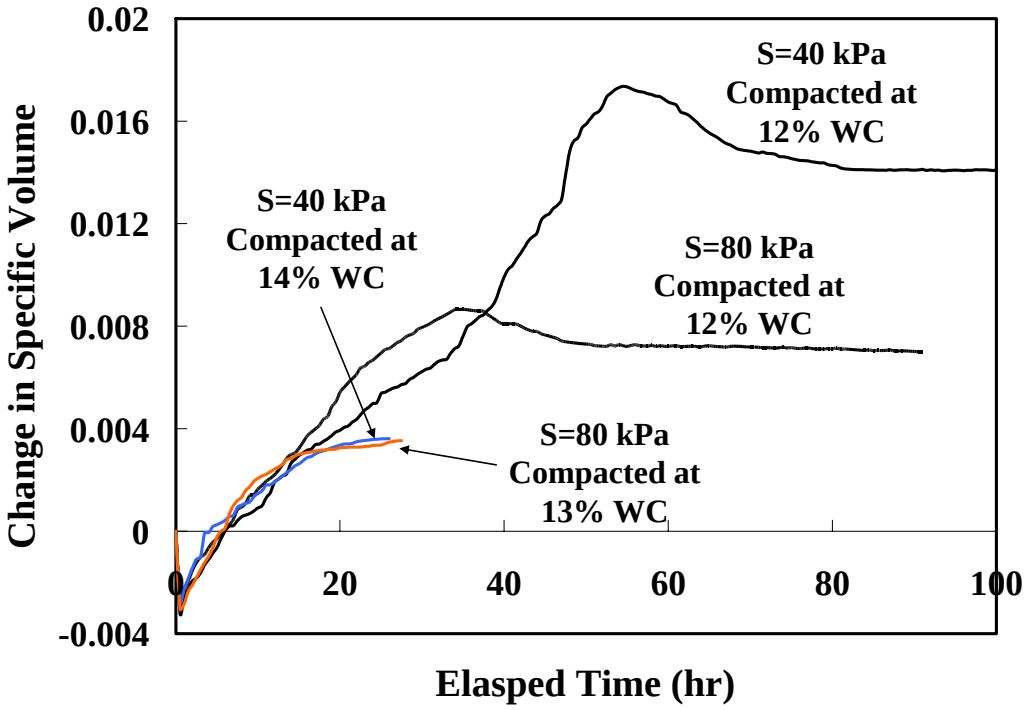

Figure 7.4 Equalization Process

7.5.2 Isotropic Compression

Once the specimen was equalized at the specified initial suction, it was isotropically compressed to the required net mean stress at constant suction. A total of 6 drained isotropic compression tests were conducted in the triaxial test device to experimentally characterize the behavior of unsaturated soil under isotropic loading conditions. While maintaining the suction constant, the cell pressure was raised to the required target value. Ramped consolidation was preferable to conventional step-loading consolidation in order to limit the excess pressure generated in the soil sample to a low value.

A problem associated with the generation of high excess pore water pressure in unsaturated soil may occur as depicted in Figure 7.5. Wheeler and Sivakumar (1995) illustrated that for an unsaturated soil sample subjected to a step increment of total stress, the stress path would be $A \rightarrow B \rightarrow C$ instead of being $A \rightarrow D$. Despite the adverse effect of step loading consolidation, in this research, control on the rate of ramped compression is limited due to lack of control on the slow rate of compression and the small amount of leakage of the pressurized confining fluid.

The leakage rate was determined on the test set up with a stainless steel dummy specimen being 3 inches in diameter and 6 inches in height and under the same pore air, water, and net confining stress conditions. Instead of controlling the rate of compression, an increment of 10 kPa of compression was applied followed by 3 hours of a time lapse before the next 10 kPa application of compression. The reason behind using 3 hours of a time lapse was based on the previous test results by Hoyos (1998) and Fai (2001). Hoyos (1998) used 10 kPa/h stress rate on the silty sand and Fai (2001) used a 3 kPa/h stress increase rate on decomposed volcanic soil and decomposed granite soils. All three soil samples were finer than the soil used in this research. Once the net mean stress reaches 100 kPa, an additional 100 kPa of confining stress is applied to reach 200 kPa of net confining stress. Thereafter, a time lapse of 40 hours was left between the final step-loading compression and the beginning of shearing, to allow full dissipation of excess pore-water pressure throughout the specimen.

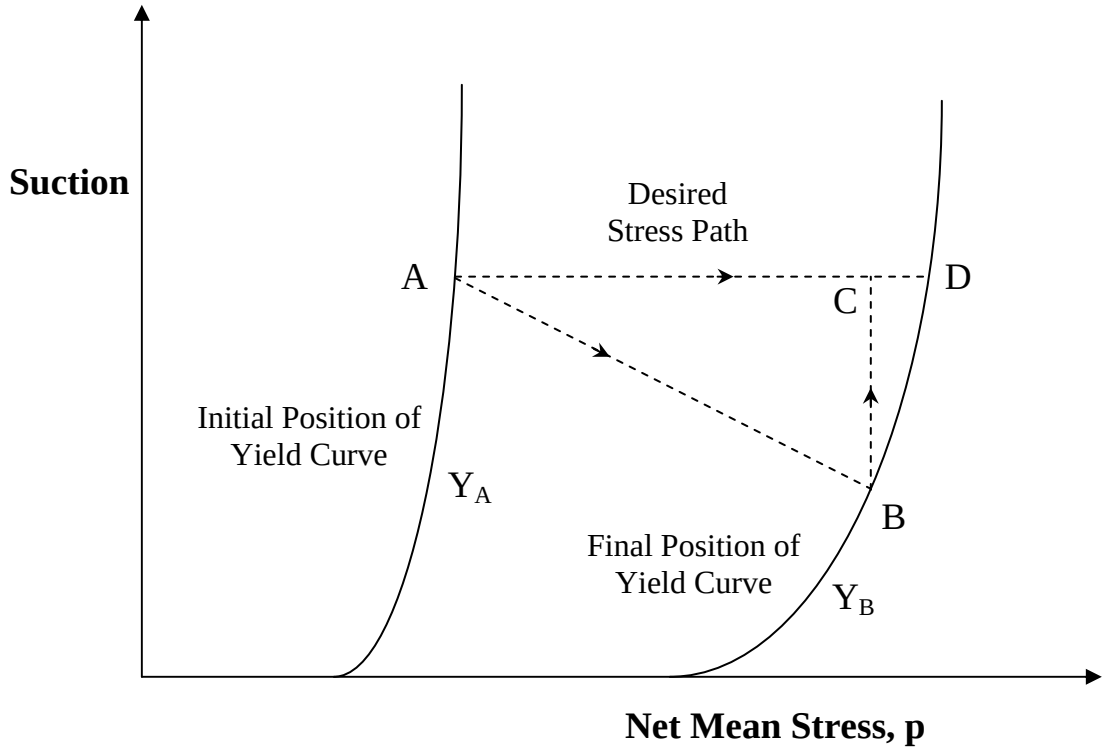

Figure 7.5 Stress Path for Isotropic Consolidation by Step-Increment of Cell Pressure

By reducing the net mean stress from 200 kPa to a 100 kPa, unloading tests were performed on samples compacted at 12 % water content. The suction was held constant during this reduction of net mean stress. A period of 24 hours was allowed to elapse after the sample reached 100 kPa of net confining stress to ensure equalization of pore water pressure.

The isotropic compression curves of the unsaturated specimens at suctions of 40 and 80 kPa are shown in Figures 7.6, 7.7, 7.8, 7.9, 7.10, and 7.11. It can be seen that there is no clear yield point on each isotropic compression curve. This suggests that the entire ramped consolidation process took place under virgin conditions and no adverse effect of step loading consolidation was observed.

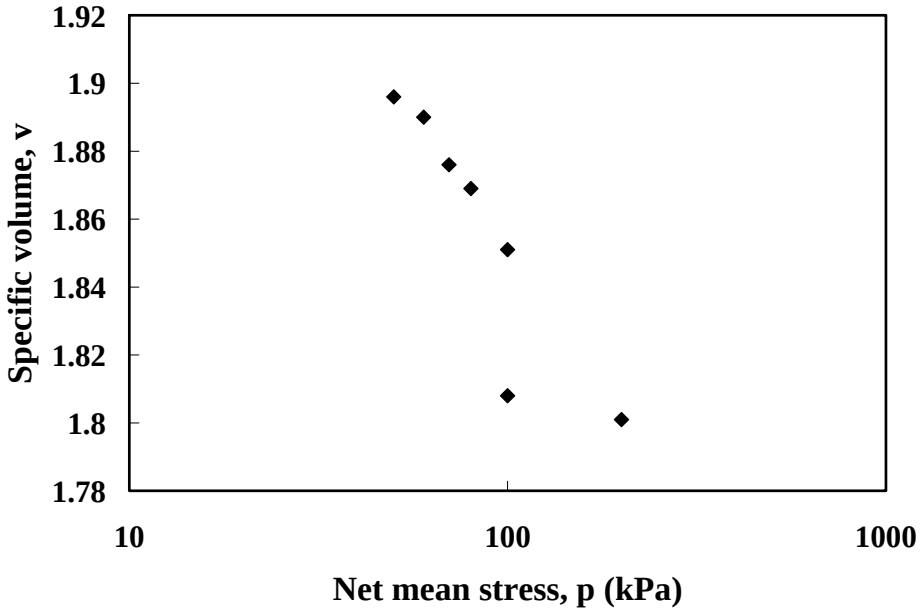

a)

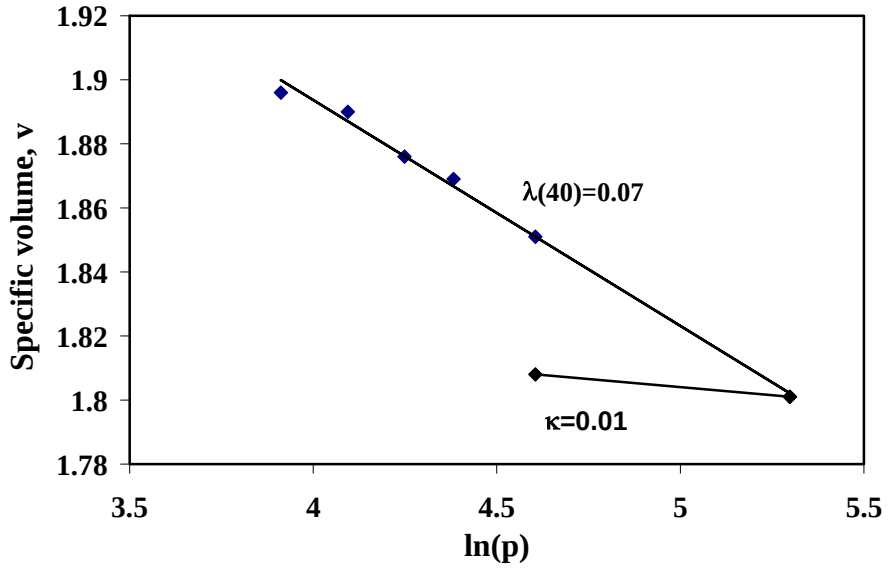

b)

Figure 7.6 Isotropic Compression Curves for s = 40 kPa with Equalization Process: a) p on Logarithmic Scale with Base 10; b) p on Logarithmic Scale with Natural Base.

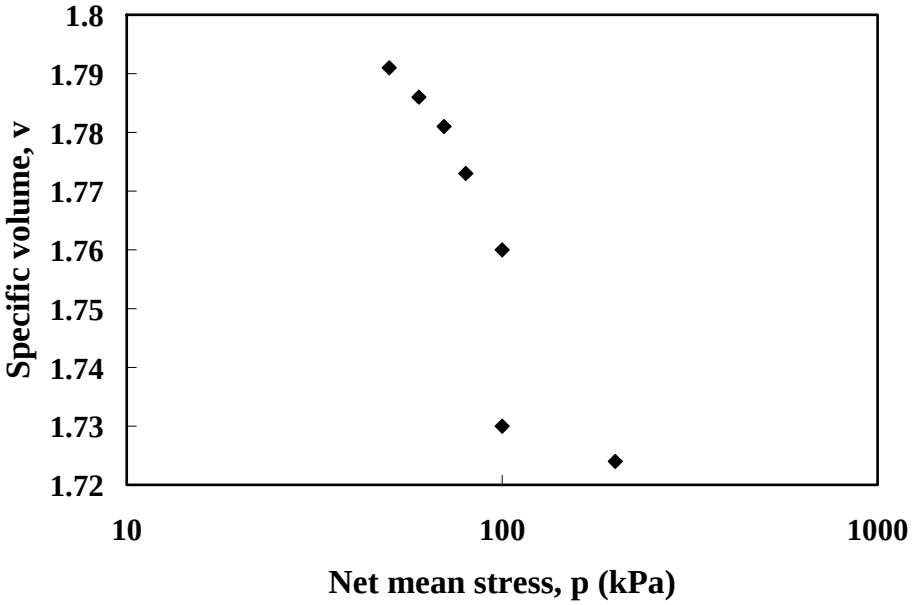

a)

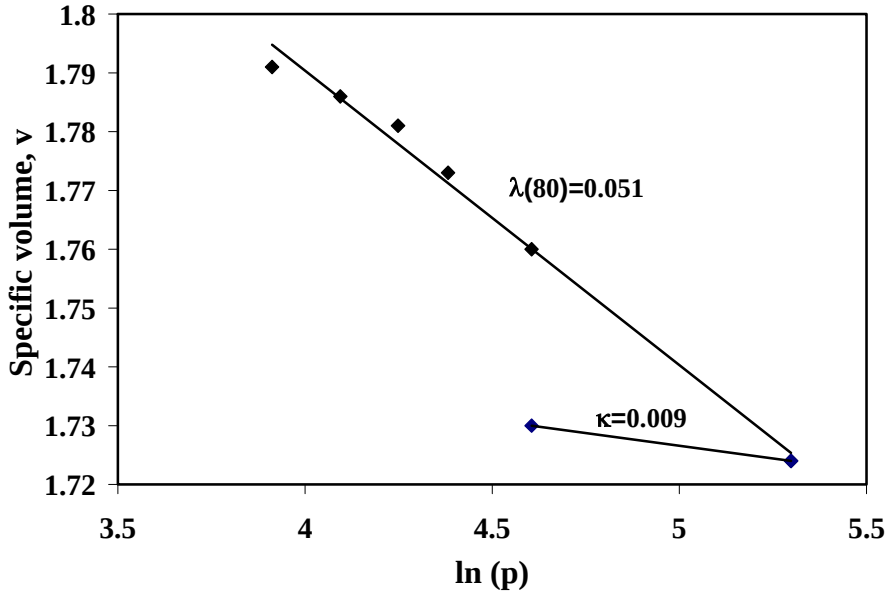

b)

Figure 7.7 Isotropic Compression Curves for s = 80 kPa with Equalization Process: a) p on Logarithmic Scale with Base 10; b) p on Logarithmic Scale with Natural Base.

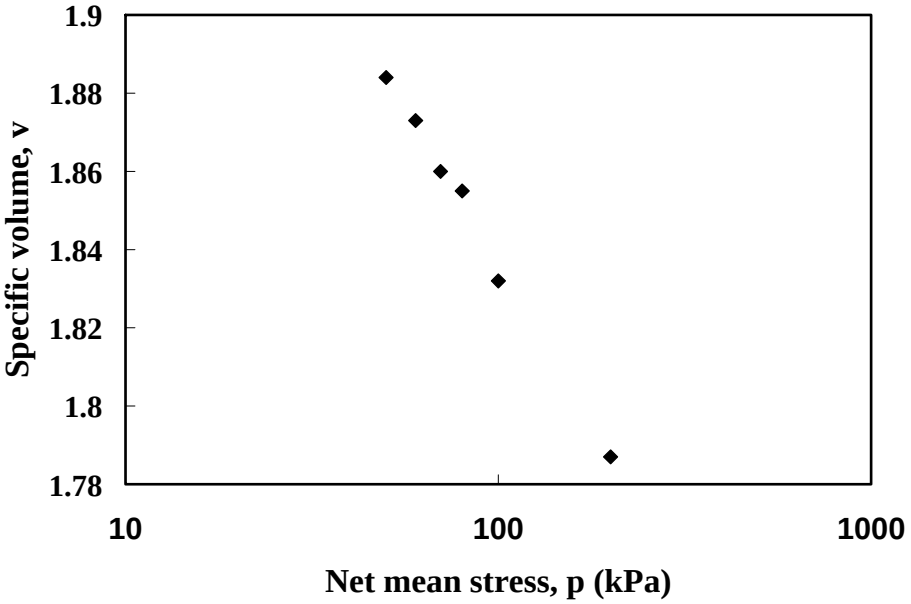

a)

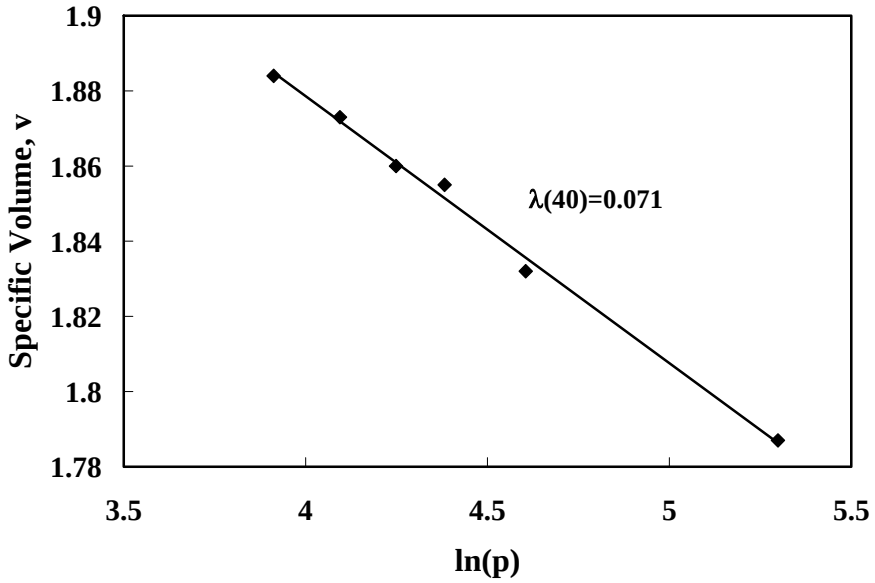

b)

Figure 7.8 Isotropic Compression Curves for s = 40 kPa with Short Equalization Process: a) p on Logarithmic Scale with Base 10; b) p on Logarithmic Scale with Natural Base.

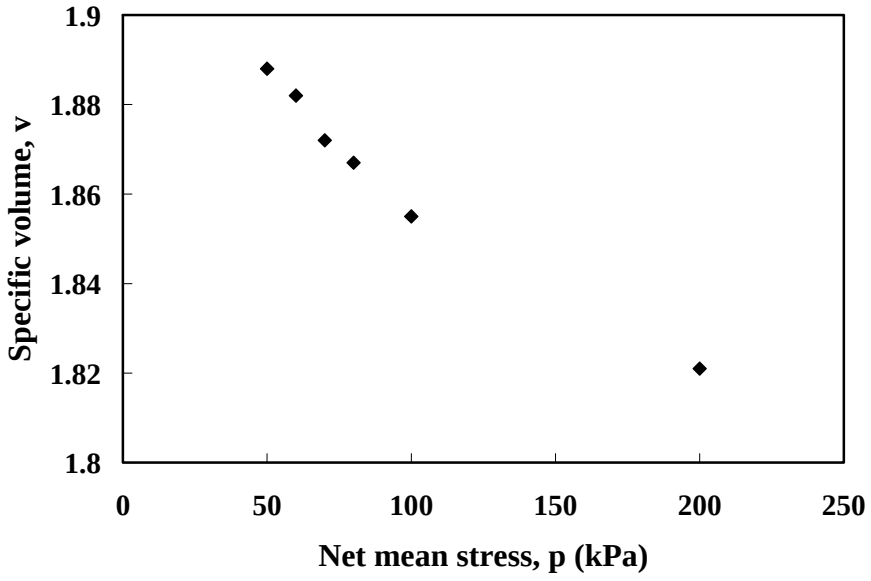

a)

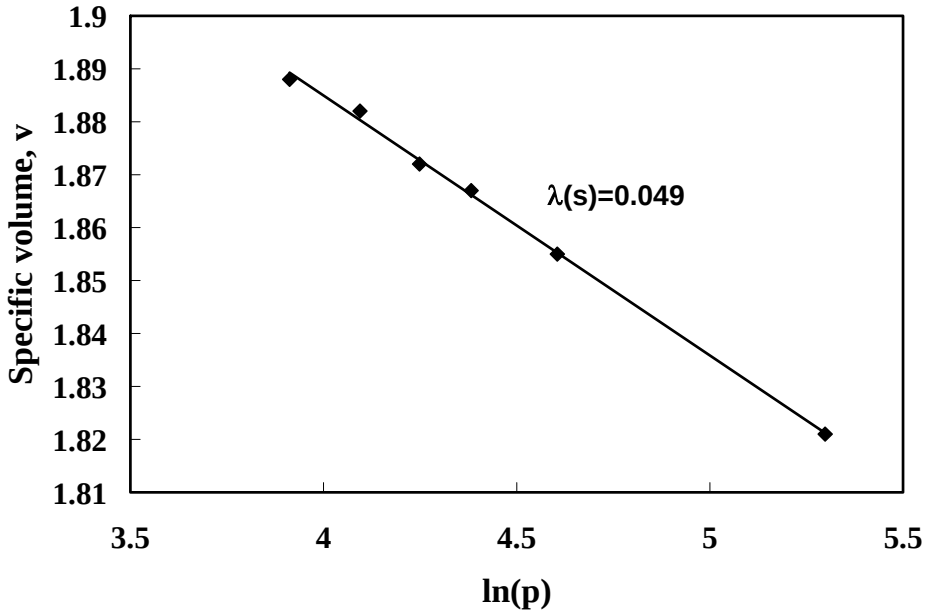

b)

Figure 7.9 Isotropic Compression Curves for s = 80 kPa with Short Equalization Process: a) p on Logarithmic Scale with Base 10; b) p on Logarithmic Scale with Natural Base.

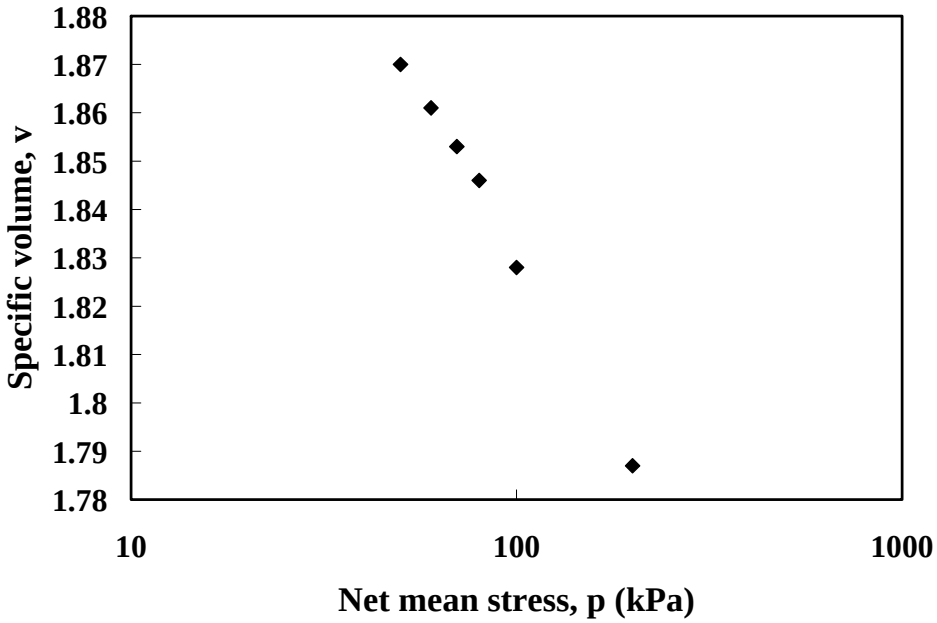

a)

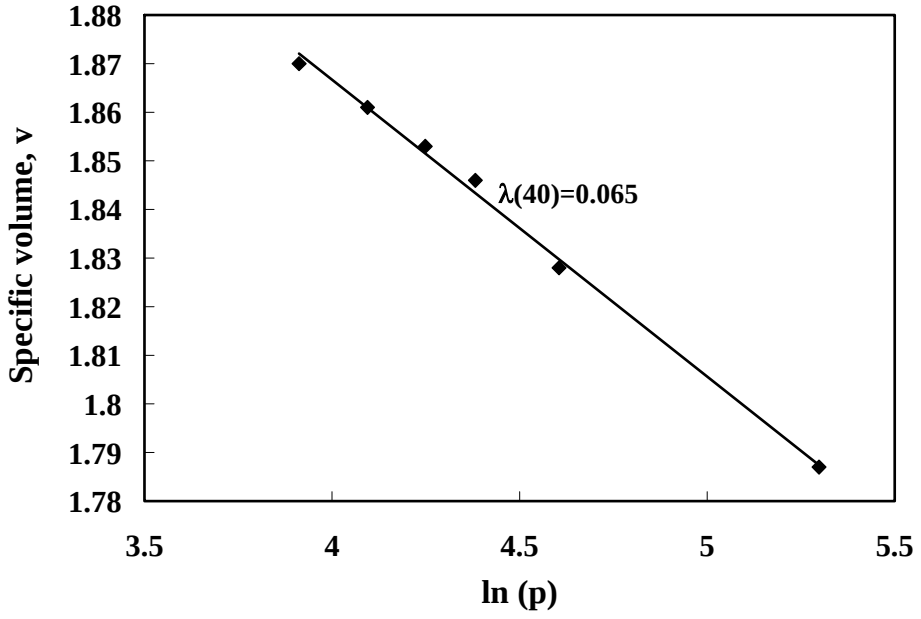

b)

Figure 7.10 Isotropic Compression Curves for s = 40 kPa with Salt: a) p on Logarithmic Scale with Base 10; b) p on Logarithmic Scale with Natural Base.

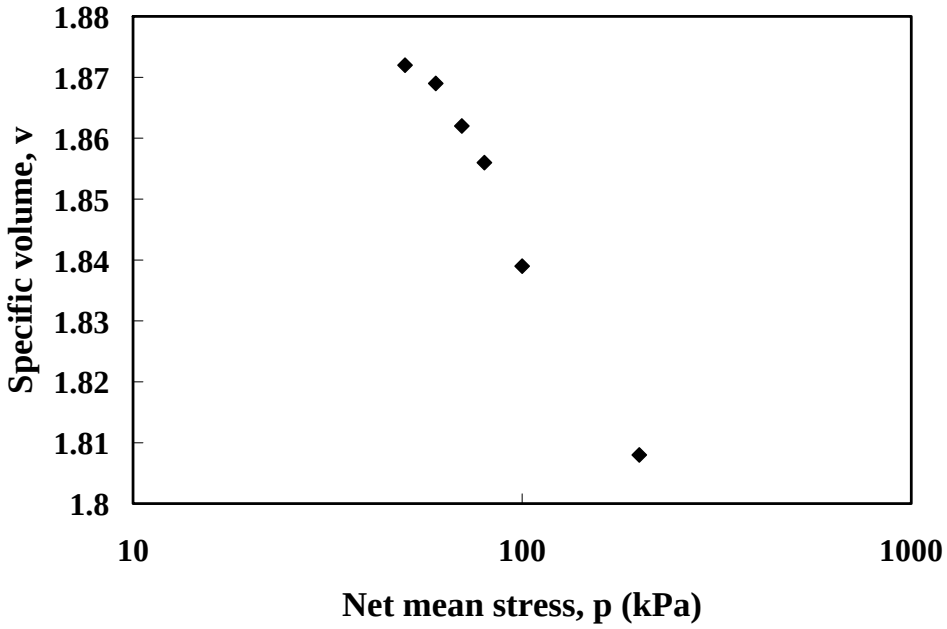

a)

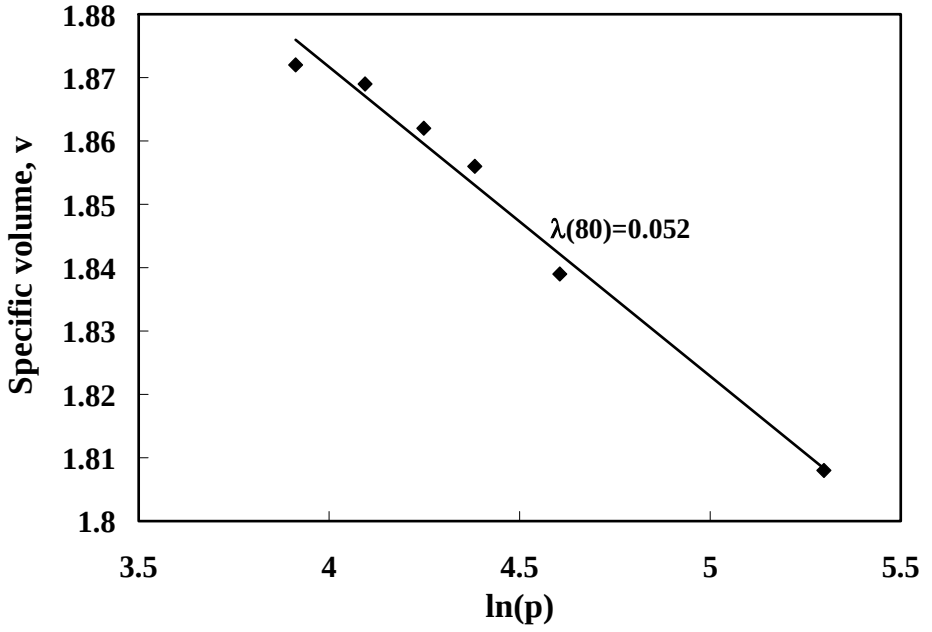

b)

Figure 7.11 Isotropic Compression Curves for s = 80 kPa with Salt: a) p on Logarithmic Scale with Base 10; b) p on Logarithmic Scale with Natural Base.

Further inspection of the data from the figure reveals that the isotropic normal compression hyperline can be represented by the following equation:

$$v = N(s)-\lambda(s)\ln(p/p_{atm}) \qquad (7.1)$$

where $\lambda(s)$ is the gradient of the isotropic normal compression hyperline (Wheeler & Sivakumar, 1995) and N(s) is the specific volume at p_{atm}.

The isotropic normal compression hyperline describes a locus of isotropic compression states in a three dimensional space of (p, s, v). The gradients of the isotropic normal compression hyperline, $\lambda(s)$, are found to be a function of suction and are shown in the above figures. The variation of the stiffness parameter, $\lambda(s)$, is consistent with the proposals from Alonso et al. (1990), who suggested a monotonic decrease in $\lambda(s)$ with increasing matric suction, s, so that the isotropic normal compression lines for different values of matric suction, s, diverge with increasing p, as observed in the Figure 7.6 to 7.11. The best-fit values of the stiffness parameter $\lambda(s)$ were found to be $\lambda(40)=0.071$, $\lambda(80)=0.05$ for specimens with distilled water and $\lambda(40)=0.065$, $\lambda(80)=0.052$ for samples with sodium chloride. The influence of sodium chloride seems to be very small. At a suction of 40 kPa, the slope of the normal compression line for samples with sodium chloride is less. On the other hand, at 80 kPa of suction, there isn't much difference in the slope of the normal compression line between the two samples. Isotropic unloading tests were also conducted on unsaturated samples at suctions of 40 and 80 kPa. The gradient of unloading lines is 0.009 for both suction levels. For each value of matric suction, there was relatively little scatter in the value of the stiffness parameter, $\lambda(s)$, reflecting the accuracy achieved in measuring the change in specific volume, v=1+e.

7.5.3 Choice of Parameter $\lambda(0)$, r, and β

The parameter, $\lambda(0)$, is the slope of the normal compression line for a value of suction equal to zero, corresponding to saturated conditions for the soil. The parameter, r, represents the ratio between the slope of the normal compression line for suction tending to infinity, $\lambda(\infty)$, and the slope of the normal compression line for suction equal to zero. The parameter β controls the exponential rate of variation of the slope of the normal compression lines with suction.

The experimental value of the slope $\lambda(s)$ of normal compression lines of samples without salt at constant suction were $\lambda(40) = 0.071$ and $\lambda(80) = 0.049$. The Equation 5.2 in Chapter V suggests that three values of $\lambda(s)$ are needed to get three unknowns, r, β, and $\lambda(0)$. In this research, only two values of the slope of normal compression lines are available. This leads to an estimation of the three unknowns by trial and error so that the calculated value of stiffness, $\lambda(s)$, is close to the experimental values. The three unknowns for samples with pure water were found to be: $\lambda(0) = 0.11$, $\beta = 18.1$ Mpa^{-1}, and r = 0.29. The calculated values of stiffness were $\lambda(40) = 0.069$ and $\lambda(80)$ =0.05.

The same procedure was used to determine the three unknowns for the sample with salt. The experimental value of the slope $\lambda(s)$ at constant suction were $\lambda(40) = 0.065$ and $\lambda(80) = 0.052$. The three unknowns were found to be: $\lambda(0) = 0.1$, $\beta = 18.7$ Mpa^{-1}, and r =0.33. The calculated values of the slopes were $\lambda(40) = 0.065$ and $\lambda(80) = 0.048$. The selection of a value less than 1 for the parameter, r, is due to the decrease in $\lambda(s)$ with increasing suction according to Wheeler et al. (2002).

7.5.4 Choice of Parameter p^c

One of the most difficult tasks in selecting values of the Barcelona Basic Model (BBM) parameters is identifying a value for p^c. Most authors who have attempted the BBM model, have selected a value for p^c by inspecting the experimental data on the shape of the yield curve. However this method leads to inaccuracy in values of p^c (Wheeler et al. 2002).

Wheeler et al. (2002) presented a simple method of identifying a value for p^c. They used the isotropic normal compression lines for different values of suction. These normal compression lines are reasonably simple to identify experimentally.

In their method, the experimental isotropic normal compression line should be plotted as values of $v + k_s \ln((s + p_{atm}) / p_{atm})$ against the net mean stress in logarithmic scale as in Figure 7.12. When the experimental data from the isotropic consolidation tests are plotted in this way and then extrapolated, the lines should all intersect at a single value of p, and this gives the value of the parameter p^c. Figures 7.12 a) and b) show the forms of graphical construction required for simulations where r<1 and r>1, respectively.

Figures 7.13 and 7.14 shows the experimental isotropic normal compression line plotted in $v + k_s \ln((s + p_{atm}) / p_{atm})$ and ln(p) axis. The extrapolation of the normal compression lines enables us to determine p^c at 41 kPa for the specimens with pure water, and 38 kPa for the specimens with sodium chloride.

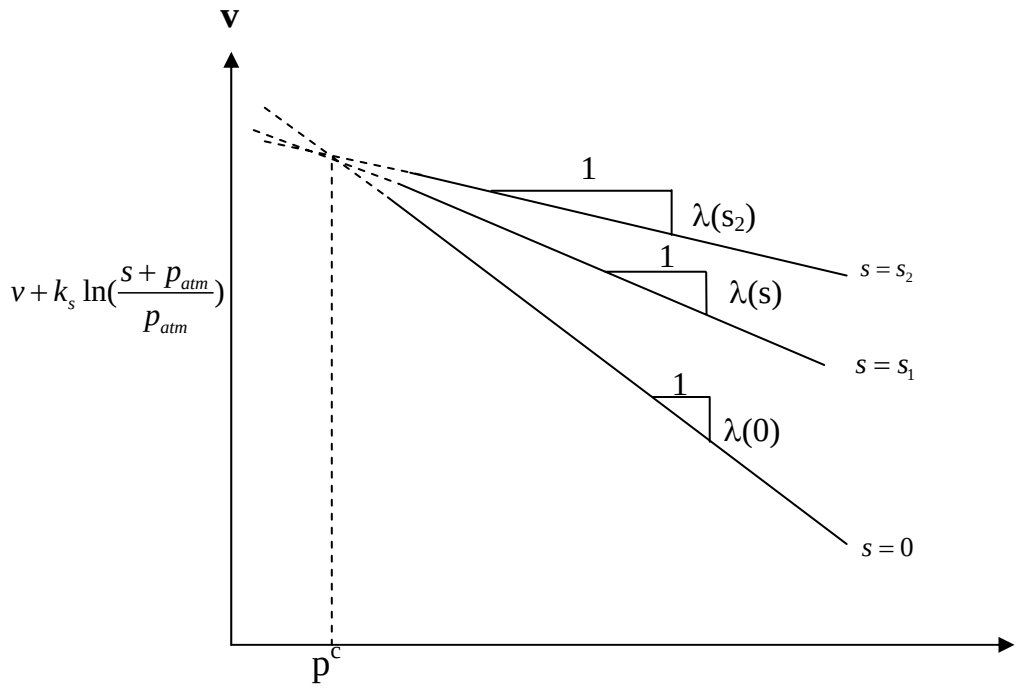

a)

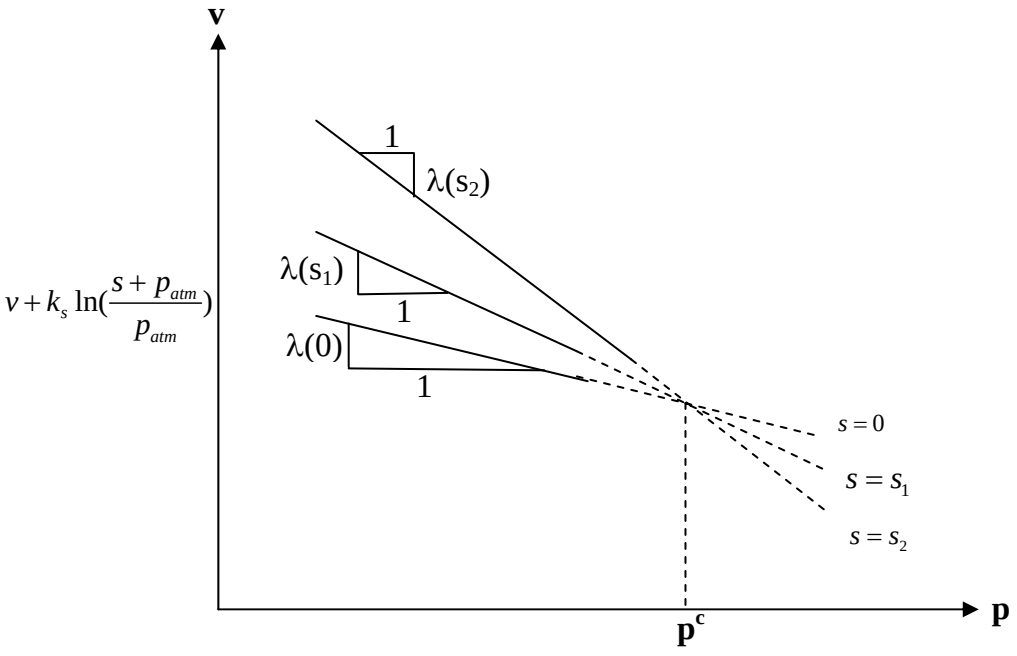

b)

Figure 7.12 Graphical Representation of Determining a Value for p^c (Wheeler et al. 2002): a) if r < 1; b) if r > 1

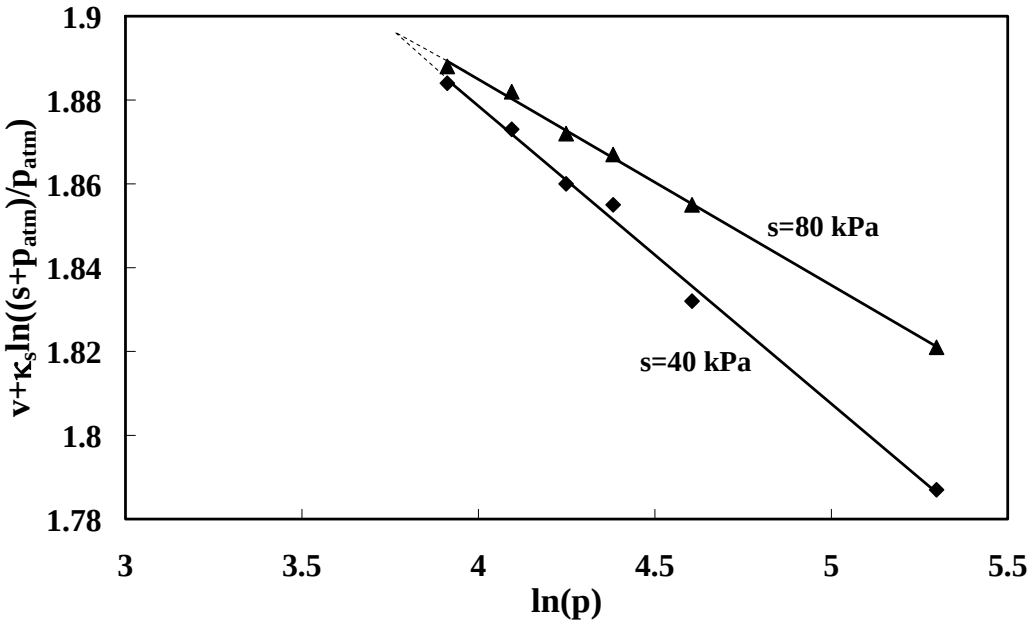

Figure 7.13 Determination of p^c on Samples with Distilled Water

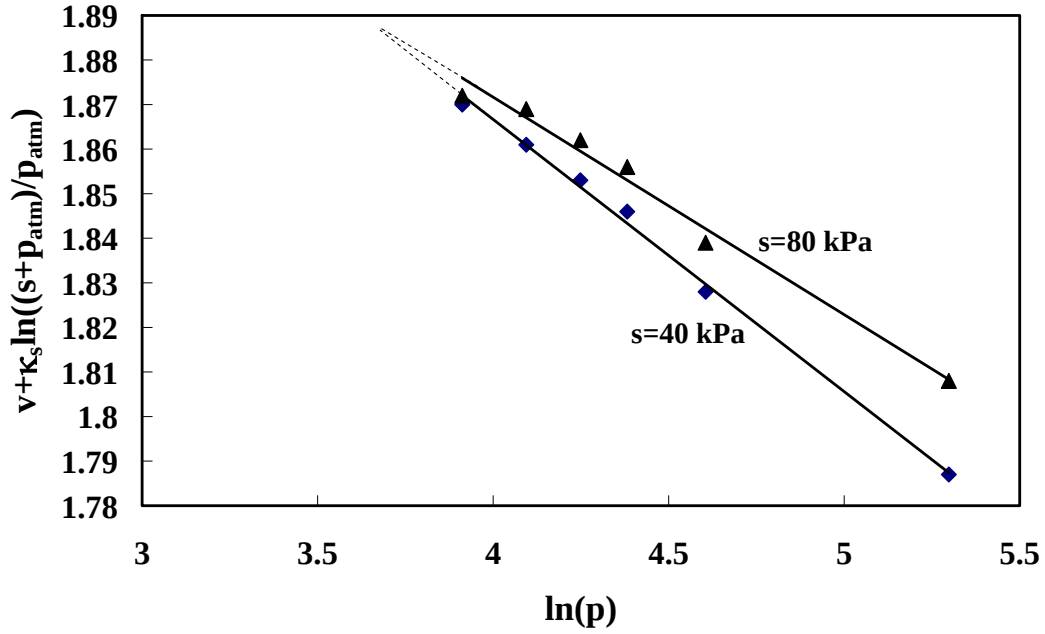

Figure 7.14 Determination of p^c on Samples with Salt Water

7.5.5 Relaxation Modulus

Prior to starting the monotonic tests after the specimens had been consolidated, relaxation tests were conducted at very small strain range so that soil cannot experience damage or plastic strain. This was accomplished by increasing the strain at a constant rate and then allowing the sample to relax without any further movement in the loading actuator. The measurement of strain was accomplished with the on-specimen LVDT's. Once a sufficient number of data points were taken to define the relaxation modulus, the load is decreased back to zero. Figure 7.15 shows the actual axial strain pattern of a soil sample for the determination of the relaxation modulus. By dividing the applied stress on the specimen during the constant strain, the relaxation modulus for the sample can be determined. Figure 7.16 shows that the relaxation modulus has the form of a power law (see Equation 5.46). Tables 7.3 and 7.4 summarize the relaxation modulus for all the samples tested.

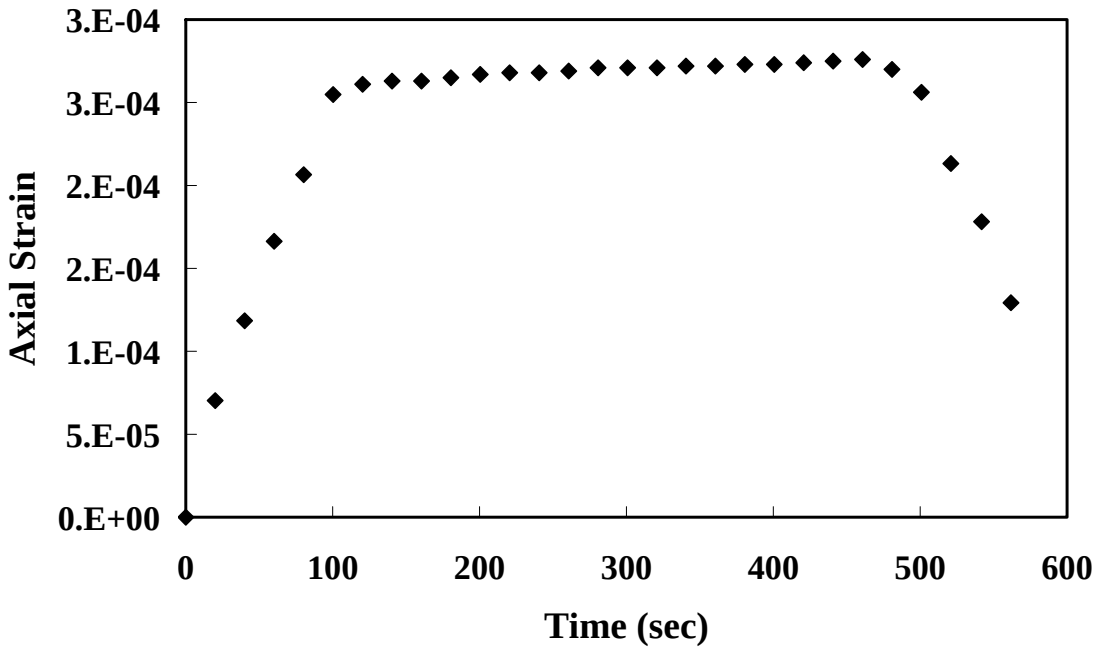

Figure 7.15 Strain Pattern Applied to Soil Specimen with s= 40 kPa and p=100 kPa

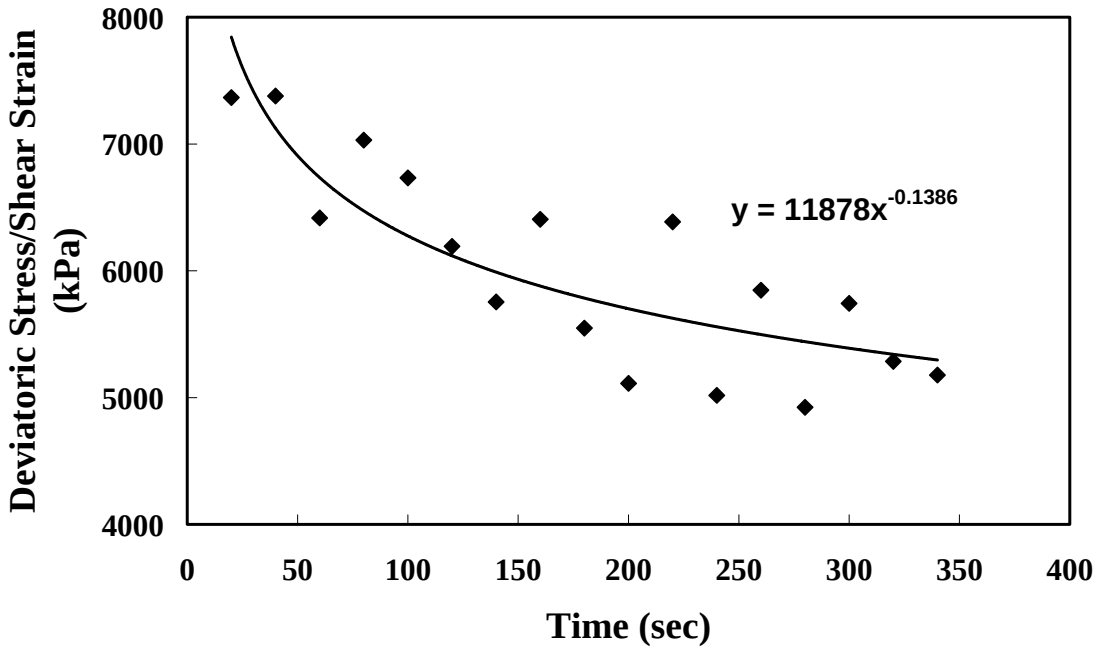

Figure 7.16 Relaxation Modulus for Soil Specimen with s=40 kPa and p=100 kPa

Table 7.3 Relaxation Modulus for Samples with Distilled Water

	S=40 kPa			S=80 kPa		
	P=50	P=100	P=250	P=50	P=100	P=250
G_0 (kPa)	9912	11878	23547	13021	16122	24585
M	0.1	0.14	0.14	0.09	0.13	0.06

Table 7.4 Relaxation Modulus for Samples with Salt Water

	S=40 kPa			S=80 kPa		
	P=50	P=100	P=250	P=50	P=100	P=250
G_0 (kPa)	9738	13278	24574	11373	15342	22581
M	0.09	0.13	0.08	0.11	0.06	0.12

7.5.6 Shear Loading

After isotropic consolidation and relaxation tests, the specimen was sheared under drained conditions for both the pore air and pore water phase. All tests were strain-controlled at a constant rate of displacement. The choice of strain rate is based primarily on the coefficient of consolidation and the permeability properties of the high entry disk (Ho and Fredlund 1982). For many soils, the permeability of the high-air-entry disk with respect to the water phase will control the rate of strain. Suggested typical strain rates for low plasticity soils are in the order of 0.001% to 0.004% strain per minute.

In this research, an adequate strain rate was sought by conducting a series of suction controlled shear tests at different strain rates. Figure 7.17 shows the shear stress-axial strain response from a series of consolidated drained triaxial tests at different rates of strain rate on 3 different specimens. Based on the results shown in Figure 7.17, a strain rate of 0.5%/hr was selected in this study to provide adequate equalization of excess pore-air and pore water pressures. Once the strain rate was determined, a series of 17 drained (constant-suction) monotonic triaxial tests were conducted to experimentally study the mechanical behavior of an unsaturated soil. All samples were sheared until 20 % of axial strain, ε_a.

Figures 7.18 to 7.23 show the results of the tests obtained at matric suctions of 40 kPa and 80 kPa, respectively. The matric suction exerted a noticeable influence on the shear resistance of the soil specimens. The deviator stress increased with the applied net mean stress. Similar behavior is observed in the tested conducted on samples with chemicals in the samples. When salts are present in the samples, there are slight increases in the stress-strain responses. However, the increase in the stress-strain response is very small. When acetone is added to samples, the stress-strain response is almost the same as that of a soil sample without any chemicals.

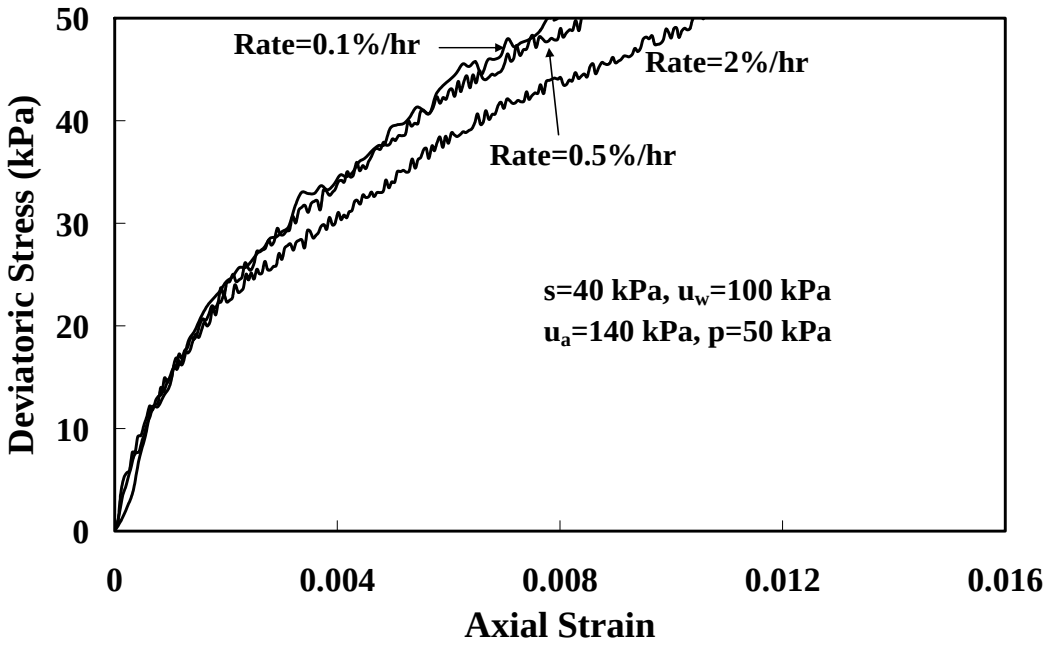

Figure 7.17 Selection of Strain Rate

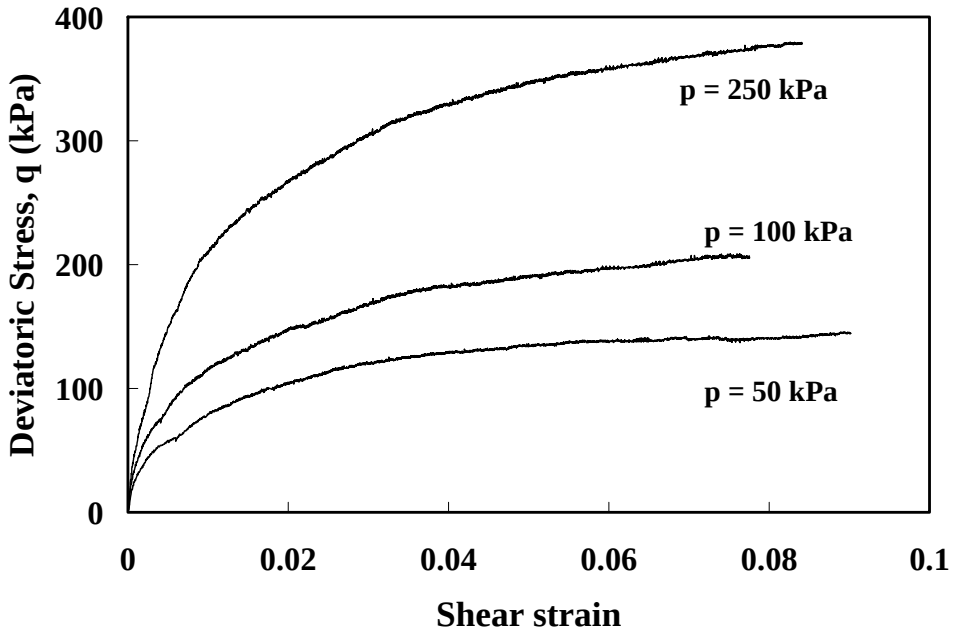

Figure 7.18 Experimental Stress Strain Response with Constant Suction (S40MD)

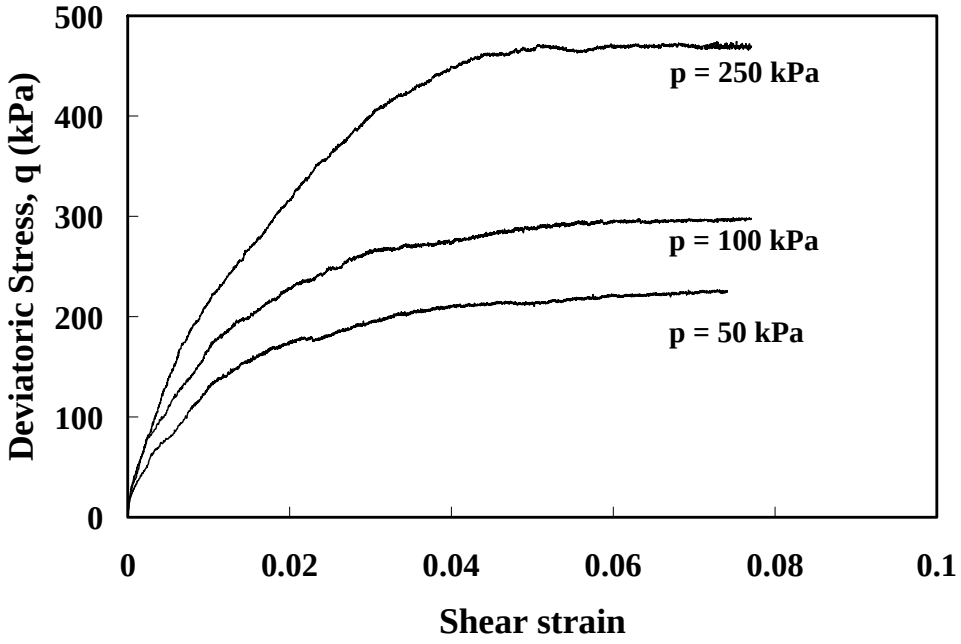

Figure 7.19 Experimental Stress Strain Response with Constant Suction (S80MD)

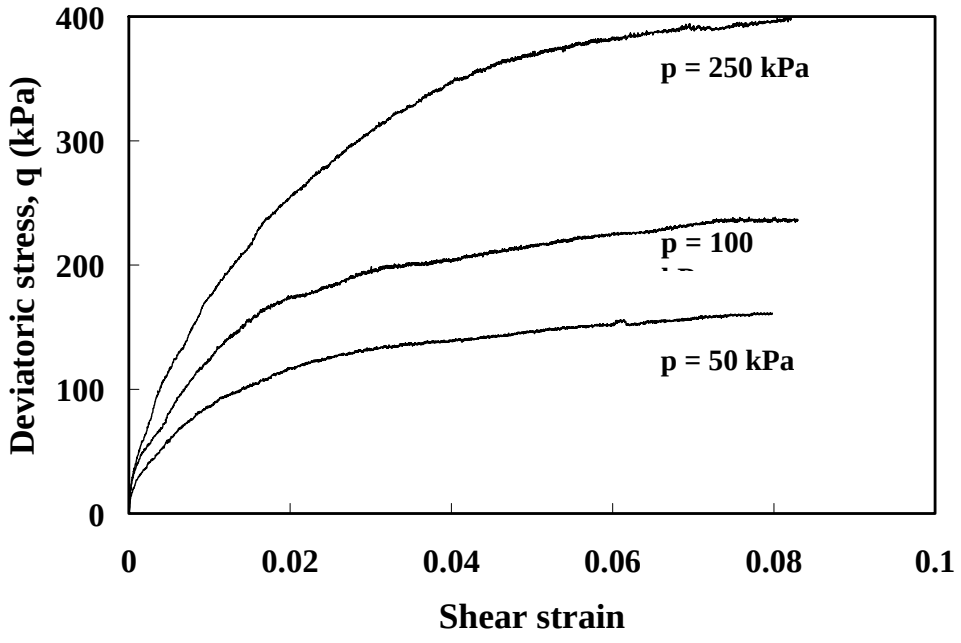

Figure 7.20 Experimental Stress Strain Response with Constant Suction (S40MN)

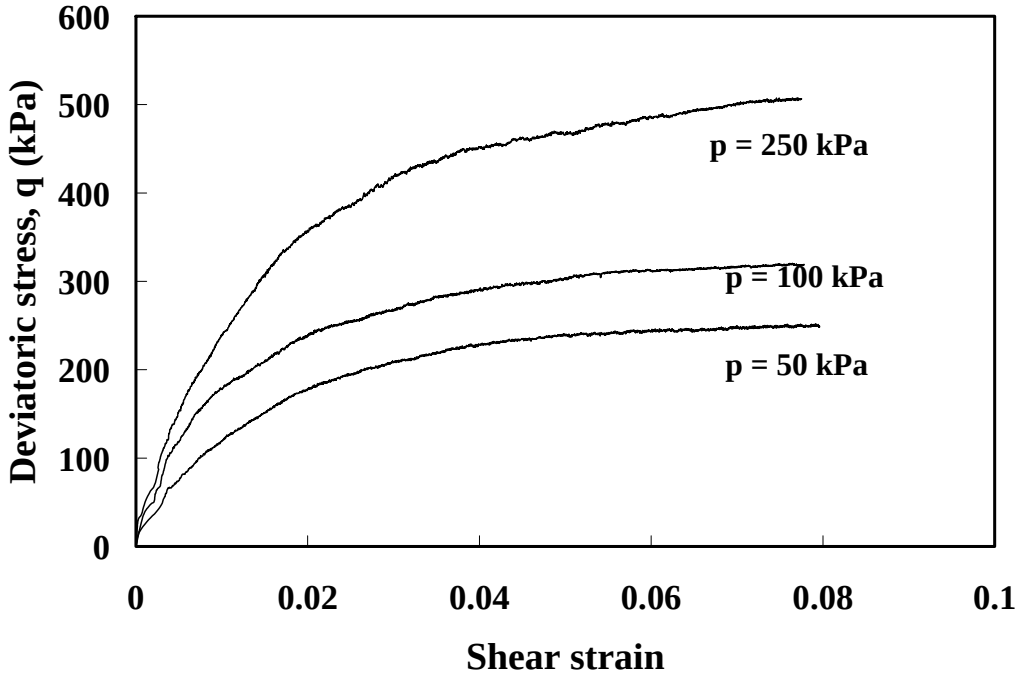

Figure 7.21 Experimental Stress Strain Response with Constant Suction (S80MN)

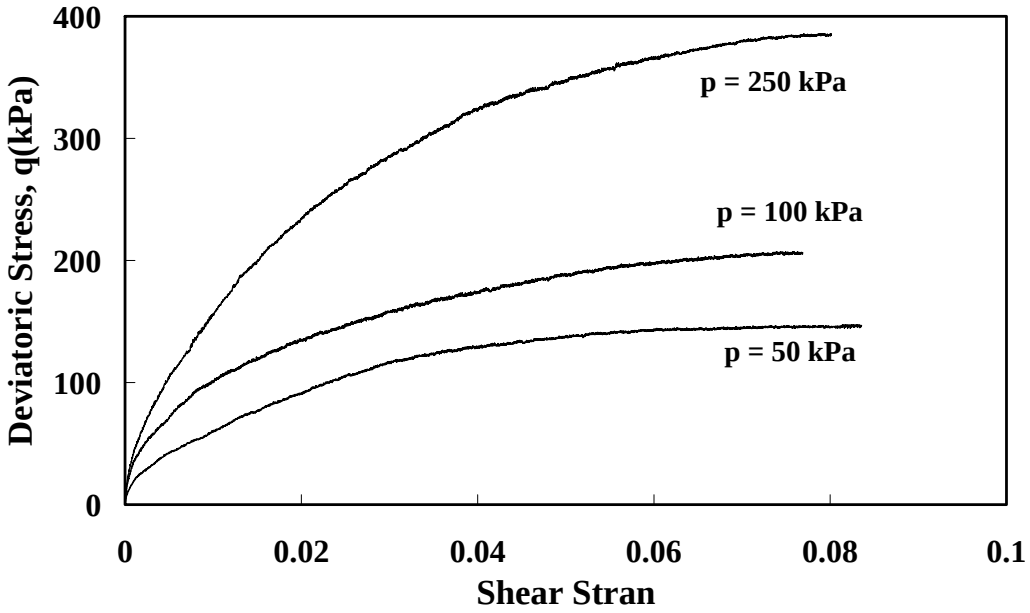

Figure 7.22 Experimental Stress Strain Response with Constant Suction (S40MA)

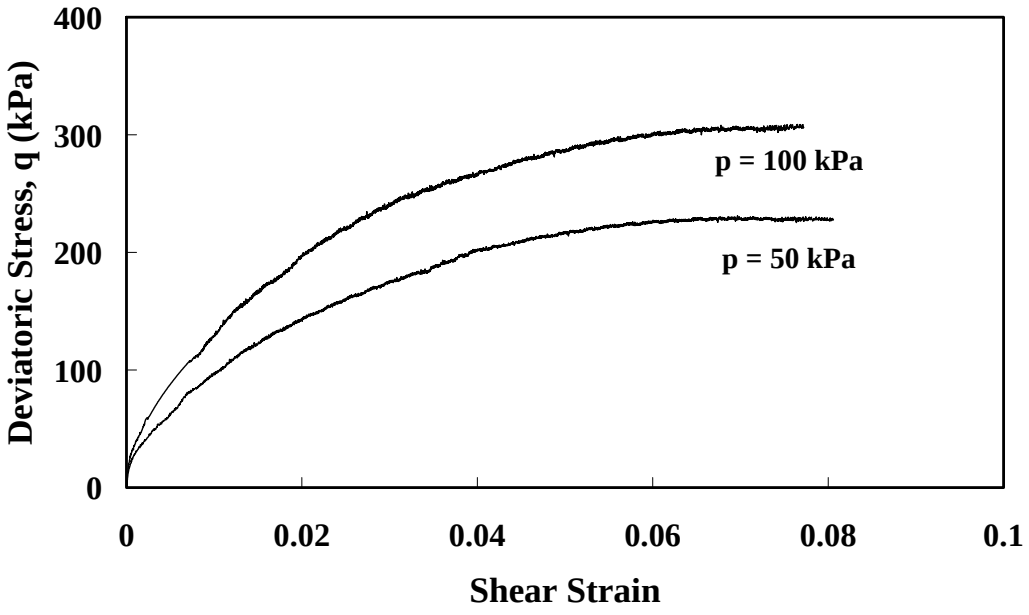

Figure 7.23 Experimental Stress Strain Response with Constant Suction (S80MA)

As in Figures 7.24 to 29, only contractive volumetric behavior is observed for all of the specimens and the amount of contraction decreases with the applied net mean stress. The trend of the volumetric changes in shearing phases for this soil was different from the trend in conventional triaxial tests on saturated specimens. This is probably because the higher net mean stresses have reduced the pore spaces significantly during the isotropic compression which preceded the shear loading stage.

As in the case of shear resistance, matric suction exerted influence on the volume change during the shear phase. Also samples with sodium chloride showed stiffer volumetric response than samples with distilled water and with acetone did.

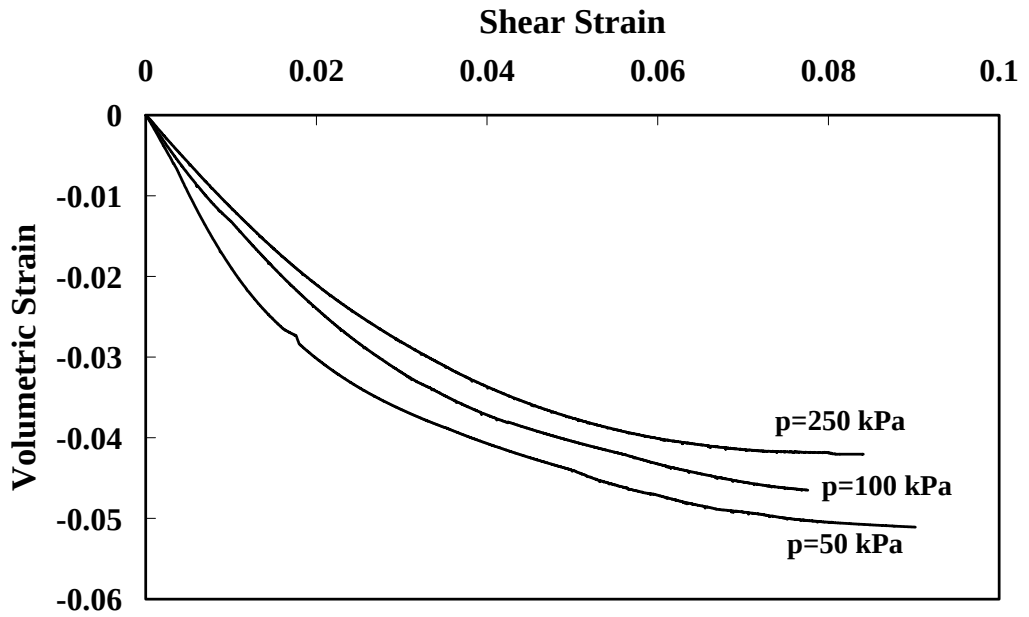

Figure 7.24 Volumetric and Shear Strain Relationships (S40MD)

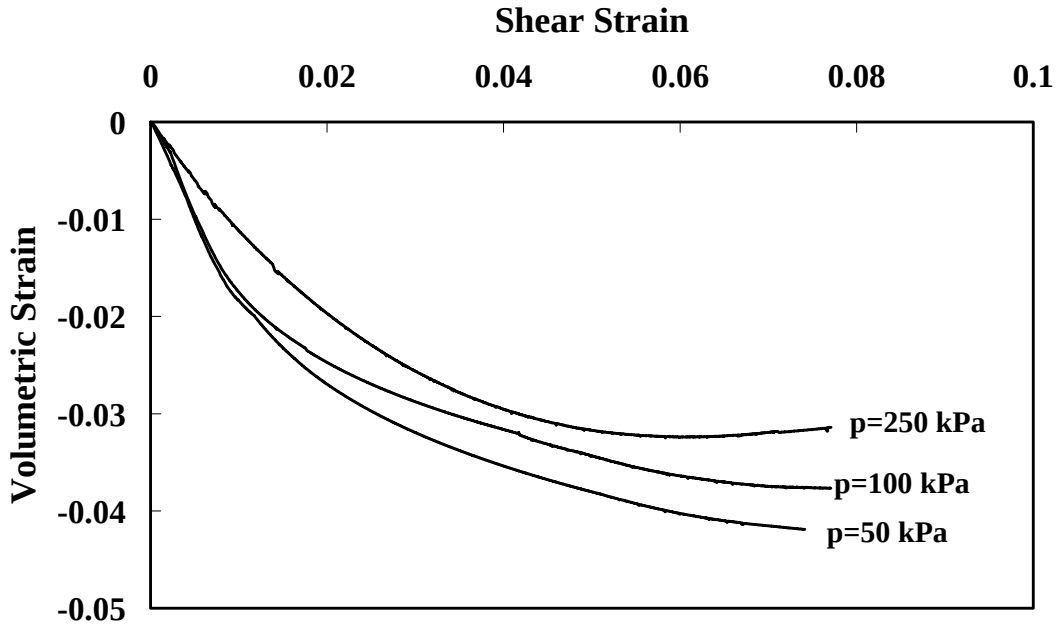

Figure 7.25 Volumetric and Shear Strain Relationships (S80MD)

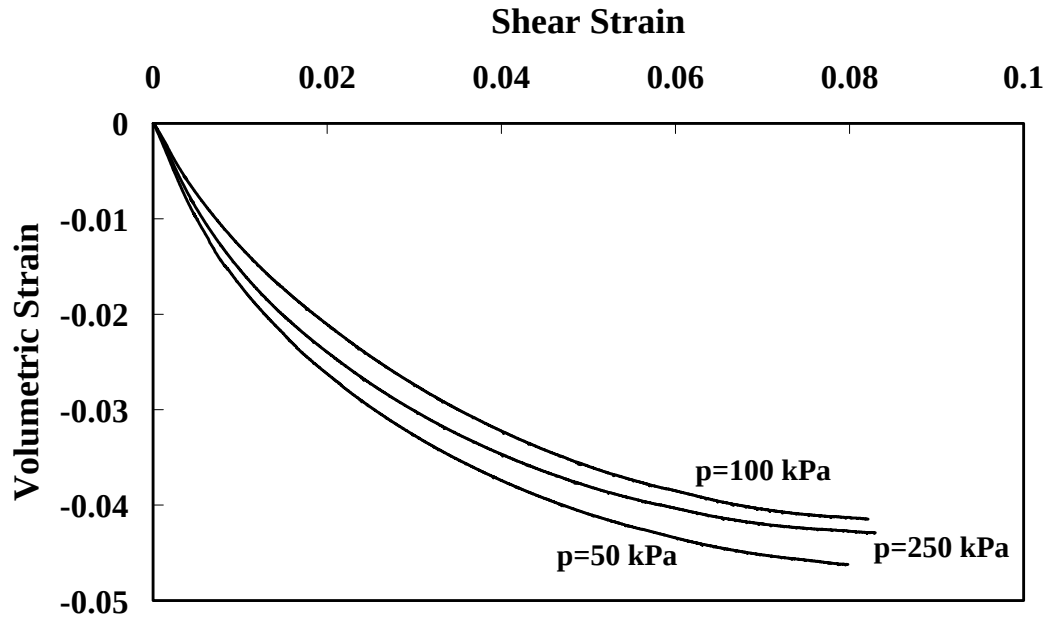

Figure 7.26 Volumetric and Shear Strain Relationships (S40MN)

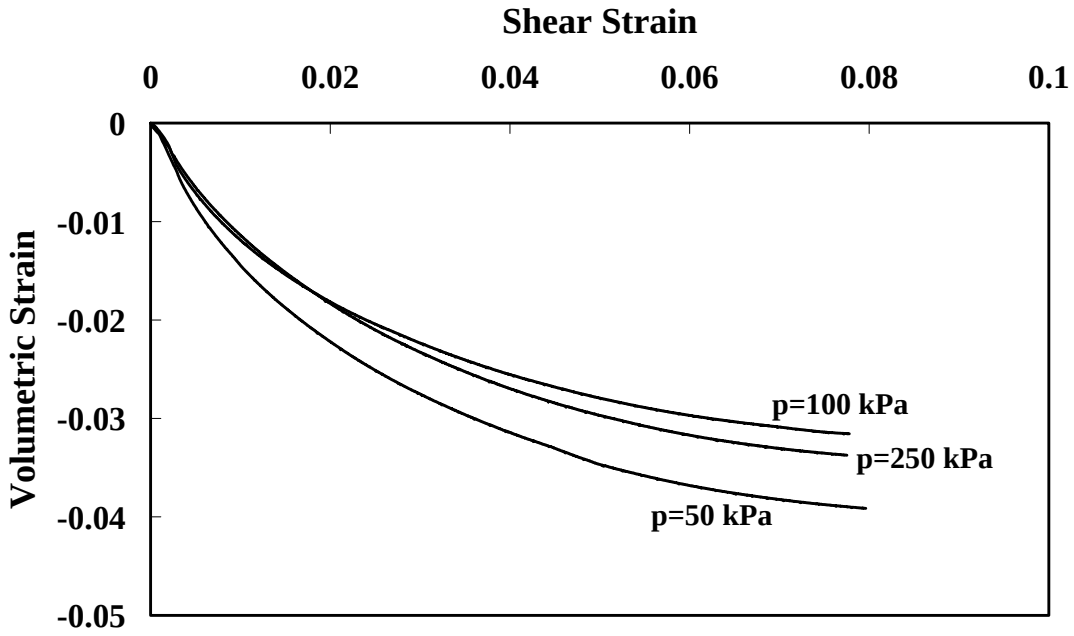

Figure 7.27 Volumetric and Shear Strain Relationships (S80MN)

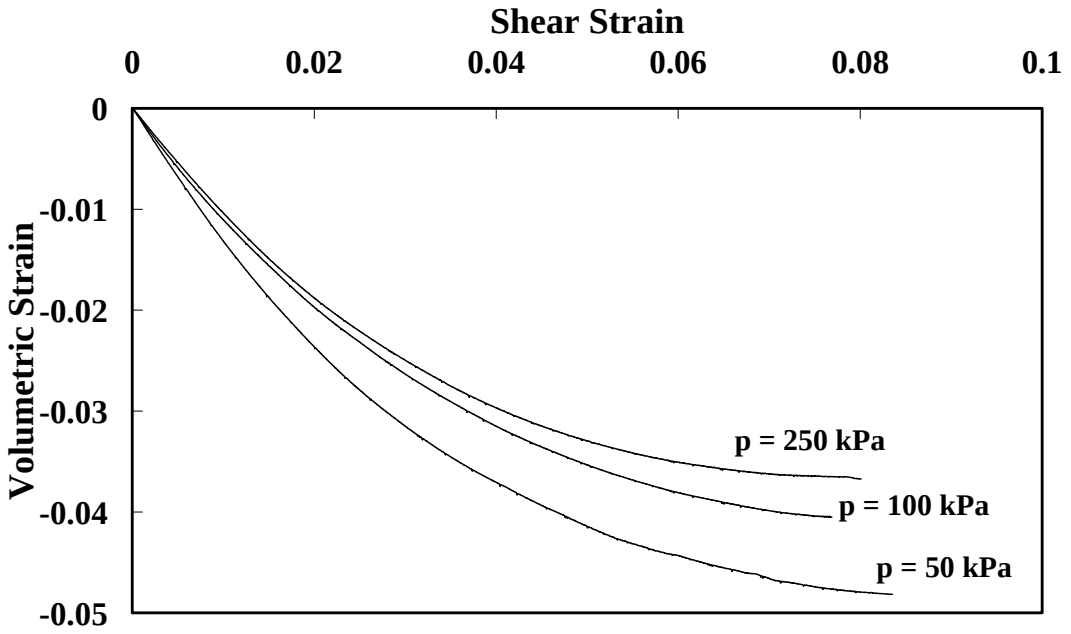

Figure 7.28 Volumetric and Shear Strain Relationships (S40MA)

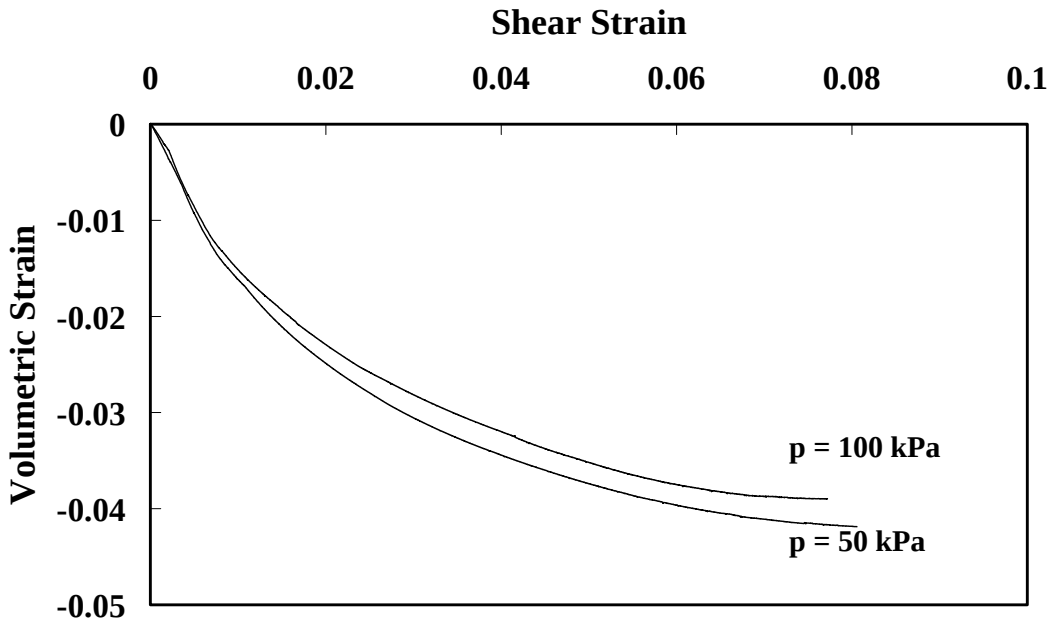

Figure 7.29 Volumetric and Shear Strain Relationships (S80MA)

As is seen from the test result, the effect of the presence of sodium chloride on stress strain response is small. This is due to somewhat larger particle size. From the particle model analysis of sand and silty size particle, the increase of equivalent effective stress is very small with the increase of surface tension due to the dissolved salt. Hence, the effect of surface tension effect is very small on relatively larger particle size. If clay soil samples are used, the test results will be different.

The presence of acetone on the stress strain response is negligible despite a rapid drop of surface tension due to the presence of a small amount of acetone. The reason for this is two fold. One is the particle size. The use of sand and silt size soil sample results in a small decrease of equivalent effective stress. Hence a relatively small change of resistance at particle contact is expected. The other is the very volatile nature of acetone. During the mixing of the soil samples and compaction procedure, a large amount of acetone actually evaporated.

7.5.7 Choice of Parameter M and k

The slope of the critical state lines in each constant suction plane, M, and the parameter controlling the cohesion increase with suction, k, defined in the following Equation 7.2 were chosen according to triaxial test data presented in Figures 7.18 to 7.21.

$$q = Mp + Mks \tag{7.2}$$

Within the range of stresses applied (s=40 kPa to 80 kPa, and p=50 kPa to 250 kPa), M=1.32, k=1.41 for samples with distilled water and M=1.32, k=1.58 for the samples with sodium chloride fits all of the experimental values of deviatoric stress. In this research, the constant suction drained triaxial tests were continued until samples experienced 8% shear strain (20% axial strain). Thus the incipient critical state condition was reached at approximately 8 % of the total shear strain. However, the true critical condition may have been reached at shear strain levels larger than 8 %.

7.5.8 Pseudo Strain Analysis of Monotonic Test

Pseudo strain can be calculated from the relaxation modulus and input strain rate. Using the relaxation modulus with the input strain rate, the stress under triaxial loading can be calculated using the following equation:

$$\sigma(t) = \int_0^t G(t-\tau)\frac{d\varepsilon_q(\tau)}{d\tau}d\tau \tag{7.3}$$

where $\sigma(t)$ is the time dependent deviatoric stress, t is present time, τ is the time history at which strains were measured, $G(t-\tau)$ is the relaxation modulus of the material at loading time and $\varepsilon_q(\tau)$ is the measured shear strain at the previous time, τ.

A typical strain rate is in Figure 7.30. In this study the shear strain rate is chosen to be constant. Once the stress is calculated, the shear pseudo-strain can be calculated by dividing the calculated stress by a reference modulus, G_R. The strain rate in Figure 7.30 is $5.33*10^{-7}$ strain per second.

$$\varepsilon_{qR}(t) = \frac{1}{G_R}\int_0^t G(t-\tau)\frac{d\varepsilon_q(t)}{d\tau}d\tau \tag{7.4}$$

where G_R is the reference modulus.

The Equation 7.4 describes a straight line with a slope of G_R which is similar to the shear modulus in linear elastic materials. However, because the soil is a nonlinear material, a straight line cannot be obtained.

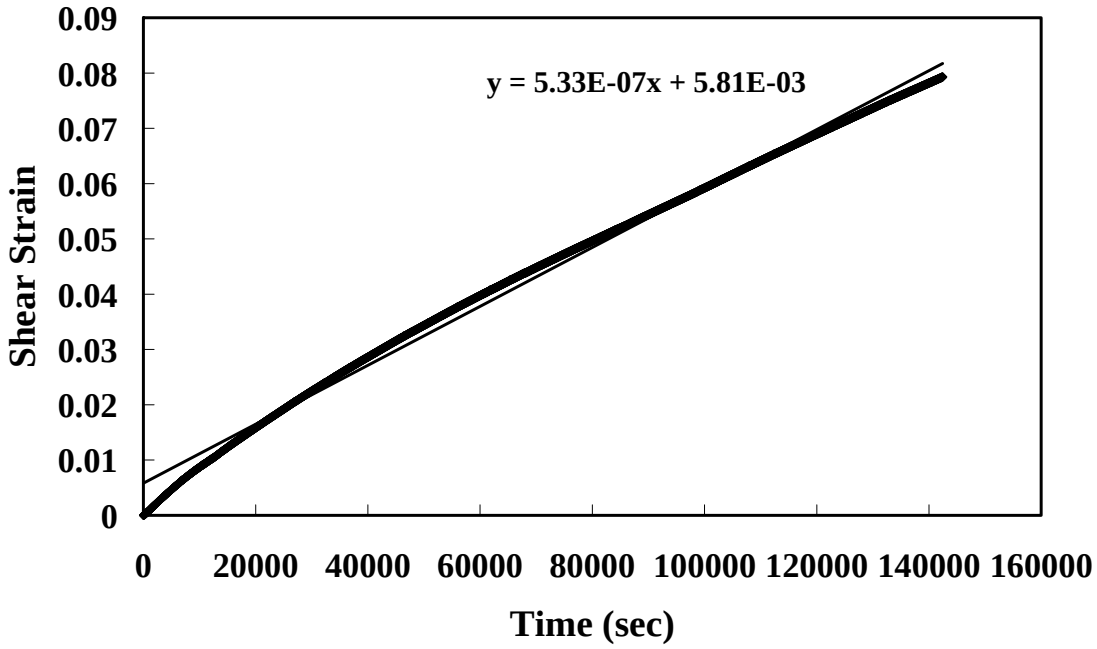

Figure 7.30 Shear Strain Rate on Soil Specimen with p=100 kPa (S40MD)

7.6 Comparison among Experimental Results, Pseudo Strain, and Model Prediction

Tables 7.5 and 7.6 summarize the experimental values of the model's parameters proposed by Alonso et al. (1990) obtained for the recompacted silty sand.

Experimental results obtained from drained suction controlled tests conducted on silty sand specimens validated the basic features of the elasto plastic critical state model proposed by Alonso et al. (1990). Figures 7.31 to 7.34 show the experimental and model predicted v-p responses of silty sand during the ramped consolidation stage of the test. The observed agreement is satisfactory. Figures 7.35, 7.36, 7.37, and 7.38 show the comparison between experimental and predicted stress-strain relationships from the drained tests conducted on silty sand specimens.

Table 7.5 Model's Parameters Proposed by Alonso et al. (1990) for Samples with Distilled Water

Parameter	Value	Units
$\lambda(0)$	0.11	
κ	0.009	
β	18.1	(MPa^{-1})
R	0.29	
p^c	0.041	(MPa)
M	1.32	
K	1.41	
$p_o(0)$	0.045	(MPa)
s_o	NA	(MPa)

Table 7.6 Model's Parameters Proposed by Alonso et al. (1990) for Samples with Salt Water

Parameter	Value	Units
$\lambda(0)$	0.10	
κ	0.009	
β	18.7	(MPa^{-1})
R	0.33	
p^c	0.038	(MPa)
M	1.32	
K	1.58	
$p_o(0)$	0.045	(MPa)
s_o	NA	(MPa)

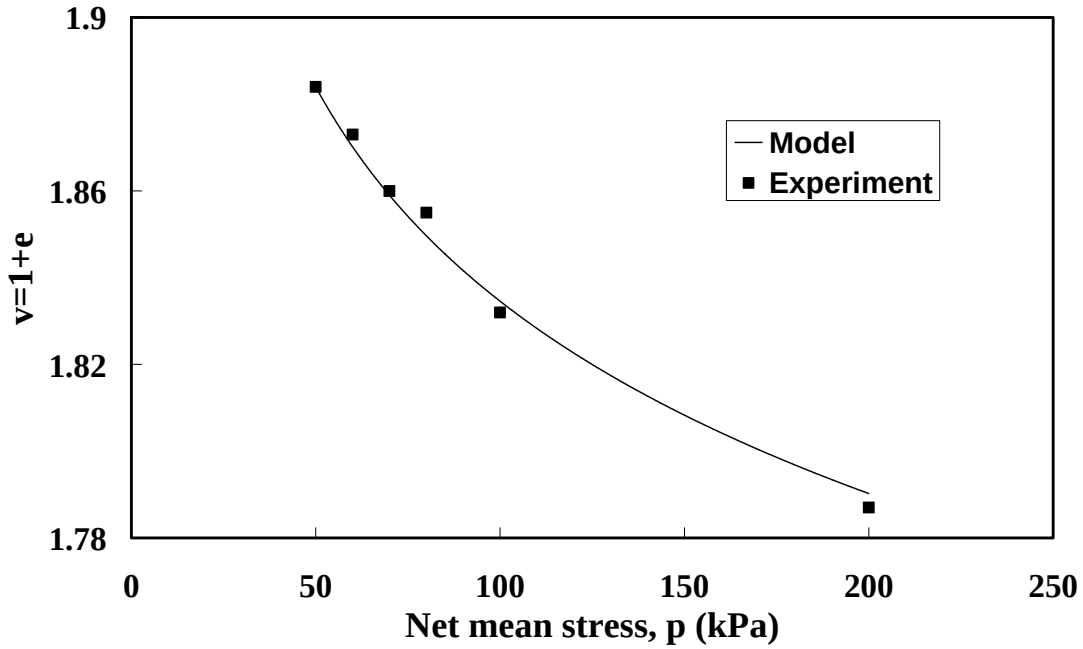

Figure 7.31 Experimental and Predicted v-p Response (S40ID)

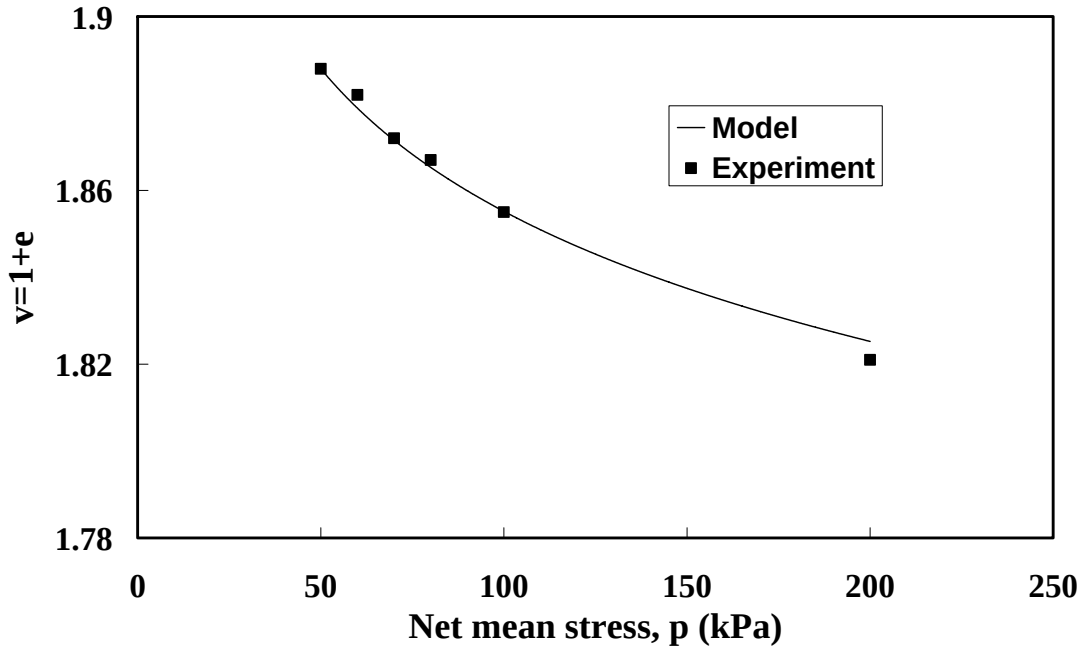

Figure 7.32 Experimental and Predicted v-p Response (S80ID)

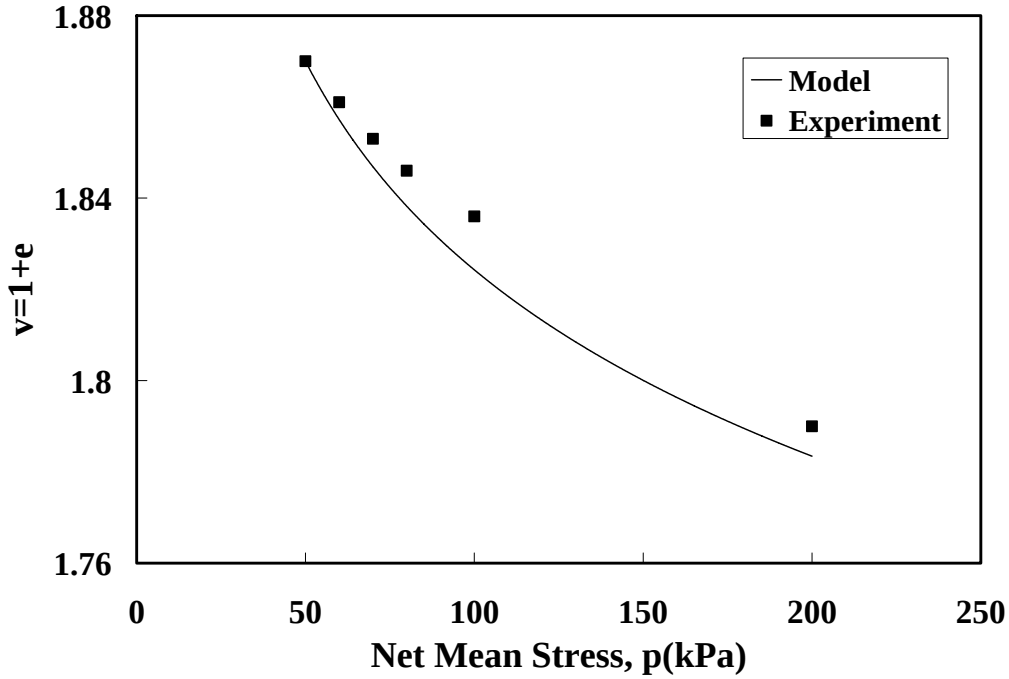

Figure 7.33 Experimental and Predicted v-p Response (S40IN)

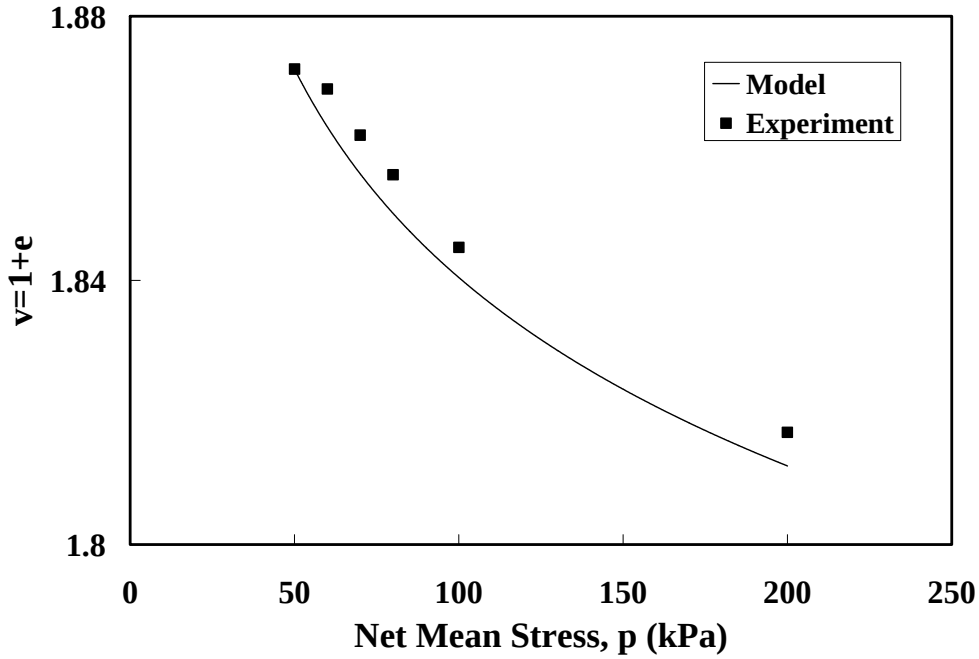

Figure 7.34 Experimental and Predicted v-p Response (S80IN)

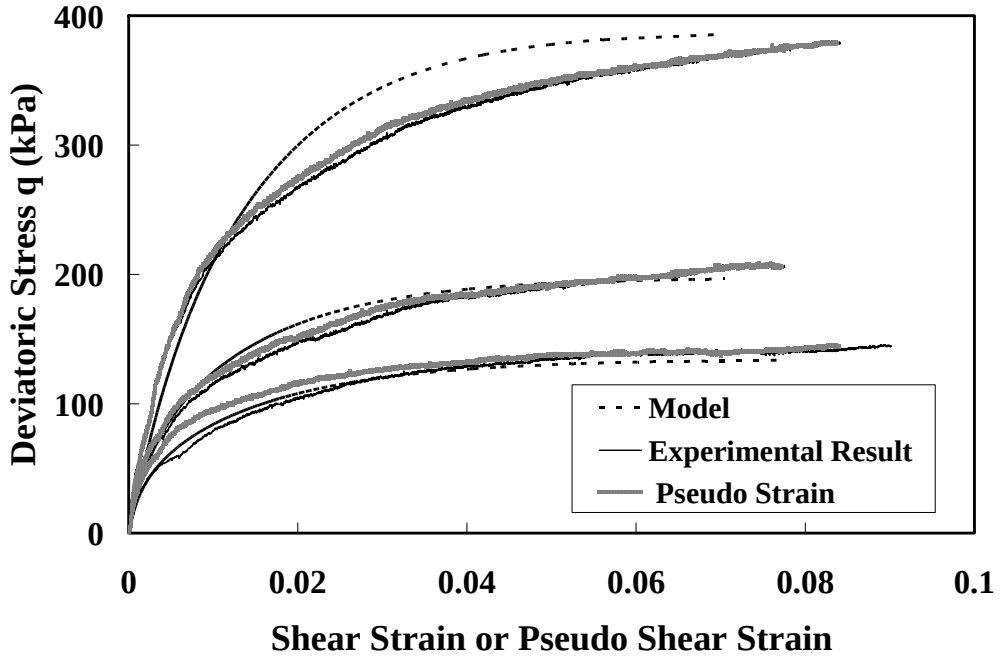

Figure 7.35 Experimental and Predicted Stress Strain Response (S40MD)

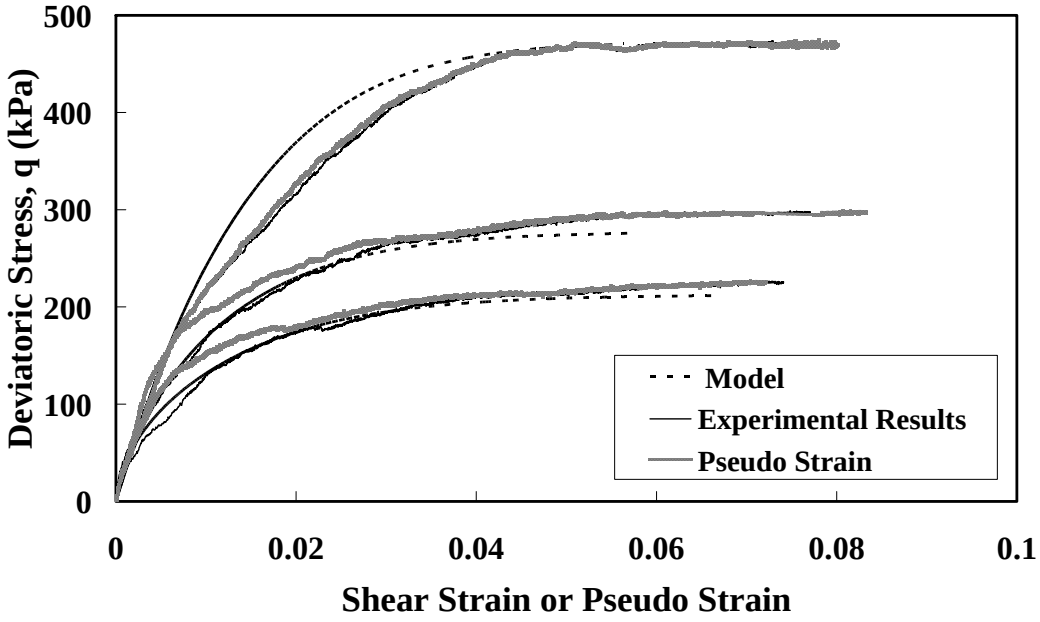

Figure 7.36 Experimental and Predicted Stress Strain Response (S80MD)

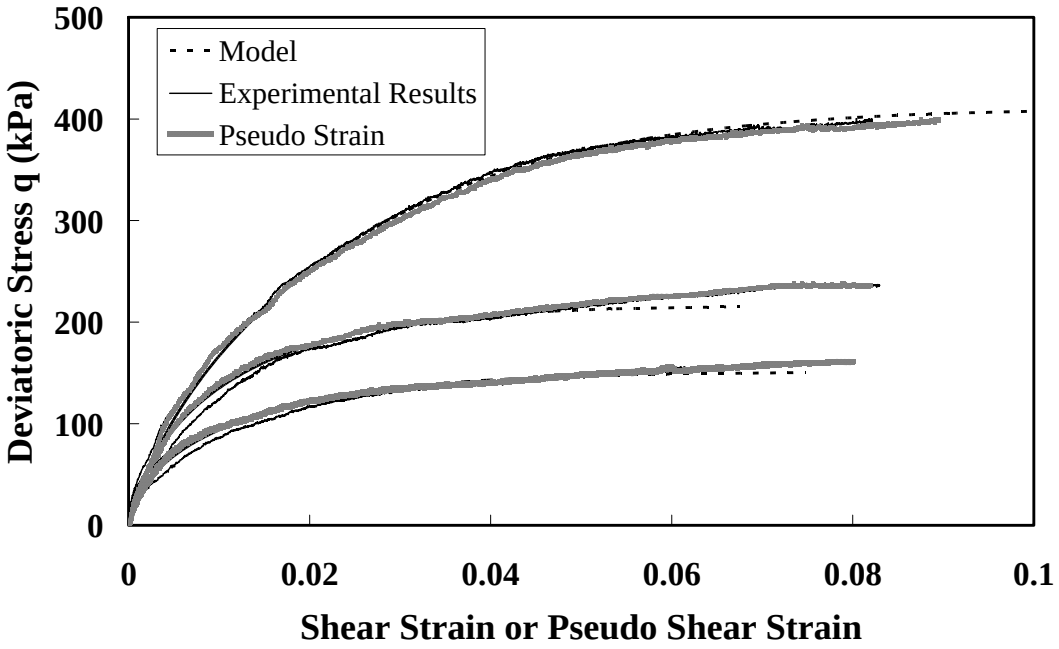

Figure 7.37 Experimental and Predicted Stress Strain Response (S40MN)

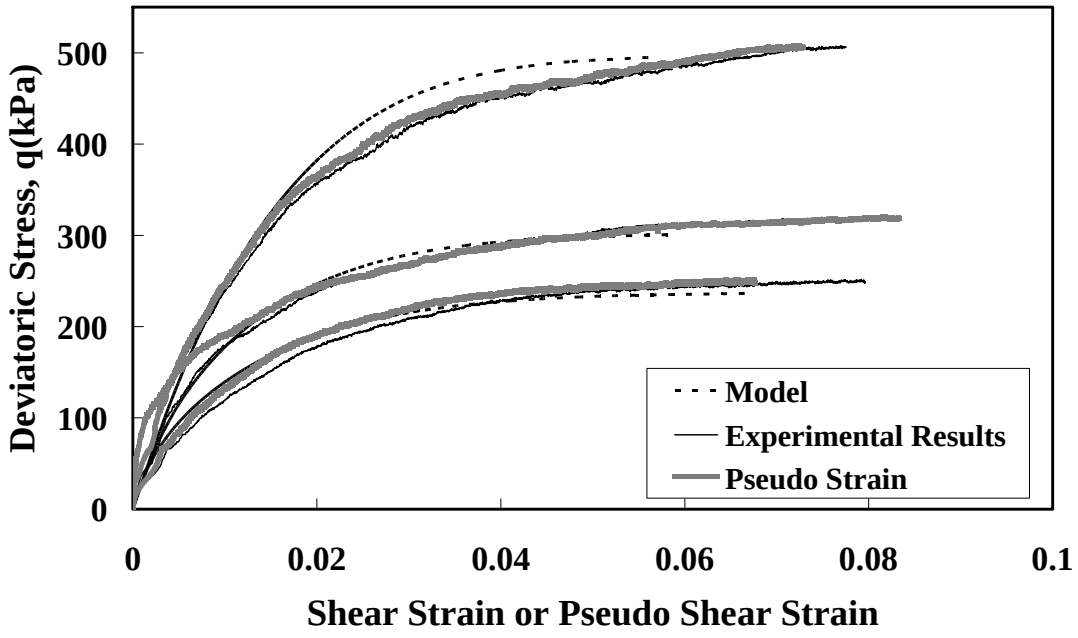

Figure 7.38 Experimental and Predicted Stress Strain Response (S80MN)

It is noted that the model gives reasonable predictions for the stress-strain relationship. The comparison of the experimental pseudo-strain curve and the predictions of the model give satisfactory results for some cases. However, unsatisfactory predictions are also observed. The discrepancy of prediction and pseudo strain tests may be due to the incorrect use of strain rate at the beginning of the test. In this research, constant shear strain rate was used to calculate pseudo strain. However, the correct strain rate is not constant as in Figure 7.30. Use of the exact strain rate at each time will give satisfactory predictions from the model.

7.7 Drained Analysis of the Centerline of a Simple Pile

The objective of the work presented in this section is to demonstrate the analysis of the problem of drained penetration using the critical state based elasto-plastic model. Due to high complexity of two dimensional analyses using strain path methods, only the centerline of a simple pile analysis is presented in this research. The procedure described in this section will be used to predict liquefaction potential in the unsaturated silty sand which was used in the unsaturated soil testing.

7.7.1 Undrained Analysis

Along the center line beneath the tip of a pile, soil elements are under a triaxial compression mode of shearing. Thus soil elements can be defined by two variables, volumetric and shear strains. The shear strain can be calculated based on the simple pile solution by:

$$\varepsilon_s(z) = \frac{R^2}{4z^2} \tag{7.5}$$

where R is the radius of the pile shaft and z is depth along centerline.
Mean effective stress and shear stress can be calculated using following equations:

$$S_1 = 3G(\dot{\varepsilon}_s - \dot{\varepsilon}_s^p) \tag{7.6}$$

$$\sigma' = K\left(\dot{\varepsilon}_v - \dot{\varepsilon}_v^p\right) \tag{7.7}$$

where G and K are shear and bulk moduli, respectively and $\dot{\varepsilon}_s^p$ and $\dot{\varepsilon}_v^p$ are the plastic component of the shear and volumetric strain increments (or rates), respectively. The mean total stress, σ, can be obtained from the equation of vertical equilibrium:

$$\frac{d\sigma}{dz} = -\frac{2}{\sqrt{3}}\left(\frac{1dS_1}{\sqrt{3}dz} + \frac{dS_3}{r}\right) \tag{7.8}$$

where S_3 is $\sqrt{3}\sigma_{rz}$.

Along the centerline, S_3=0 and r=0, however, $\frac{S_3}{r}$ exists and can be represented as follow:

$$\left(\frac{S_3}{r}\right) = \frac{3\sqrt{3}GR^2}{2z^3}\frac{1}{\left(1-2G\frac{\dot{\lambda}}{U}z\right)} \tag{7.9}$$

where $\dot{\lambda}$ is the plastic multiplier and U is the velocity of uniform flow.

The above analysis of the centerline solution is the undrained case. In this case, the effective and deviatoric components of stresses are calculated using Equations 7.6 and 7.7. The equilibrium equation in Equation 7.8 is used to calculate the pore water pressure increments.

7.7.2 Drained Analysis

For the drained analysis, soil elements are subjected to volume change. However, the volumetric stain fields in the strain path method are not known a priori. To get volumetric strain, an iterative procedure is necessary. Stress increments can be calculated from constitutive Equations 7.6 and 7.7. Due to the approximate nature of

strains in the strain path method, the stress calculated using the constitutive equation do not satisfy equilibrium. There will be stresses that are out-of-balance and these stresses can be used to perturbate new strain increments. The new strain increment at the next iteration i can be calculated as follows:

$$\dot{\varepsilon}_v^{(i)} = \dot{\varepsilon}_v^{(i-1)} + \dot{\Omega}_v^{(i)} \tag{7.10}$$

$$\dot{\varepsilon}_q^{(i)} = \dot{\varepsilon}_q^{(i-1)} + \dot{\Omega}_q^{(i)} \tag{7.11}$$

where $\dot{\Omega}_v^{(i)}$ and $\dot{\Omega}_q^{(i)}$ are perturbations around the solution at iteration (i-1).

The perturbation of strains can be calculated using the vertical equilibrium equation as in the following equation:

$$K\frac{d\dot{\Omega}_v^{(i)}}{dz} + 2G\frac{d\dot{\Omega}_q^{(i)}}{dz} = -\frac{d\dot{\sigma}'^{(i-1)}}{dz} - \frac{2}{3}\frac{d\dot{S}_1^{(i-1)}}{dz} - \frac{2}{\sqrt{3}}\left(\frac{S_3}{r}\right)^{(i-1)} \tag{7.12}$$

The right hand side of the equation is the out of balance term. In order to solve the above equation, the following relationship is assumed by Elghaib (1989).

$$\dot{\Omega}_v^{(i)} = 3\dot{\Omega}_q^{(i)} \tag{7.13}$$

The update of the strain increments can be achieved using Equations 7.12 and 7.13 until complete convergence.

The above procedure is applied to the Modified Cam Clay model. The input values for the soil parameters are of Boston Blue Clay which is used here as an example of a saturated soil. Figure 7.39 shows the undrained stress paths along the centerline of the simple pile. Results of the stress path for drained analysis are shown in Figure 7.40.

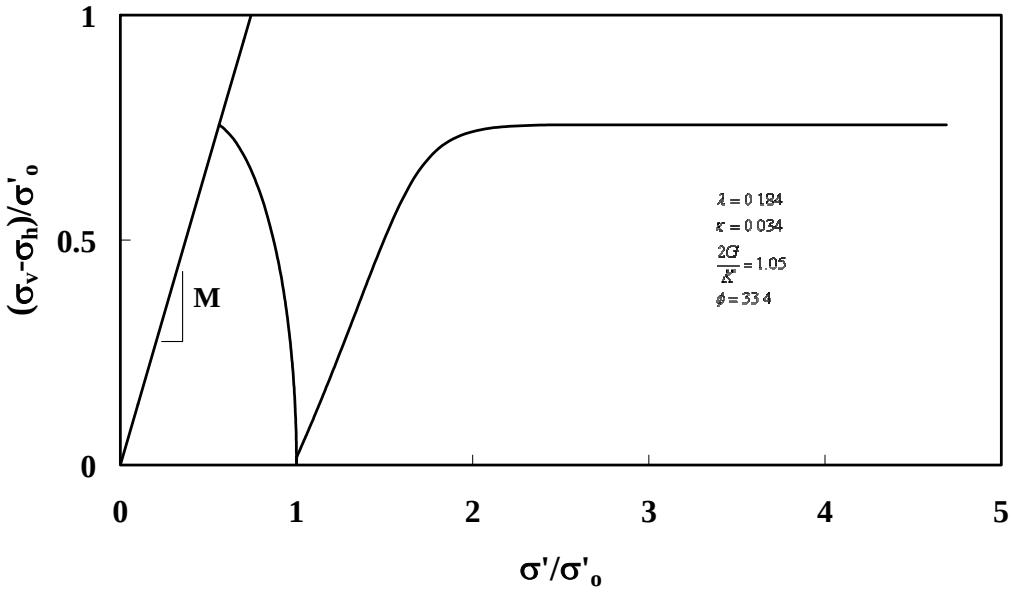

Figure 7.39 Total and Effective Stress Path Followed by a Soil Element along the Centerline

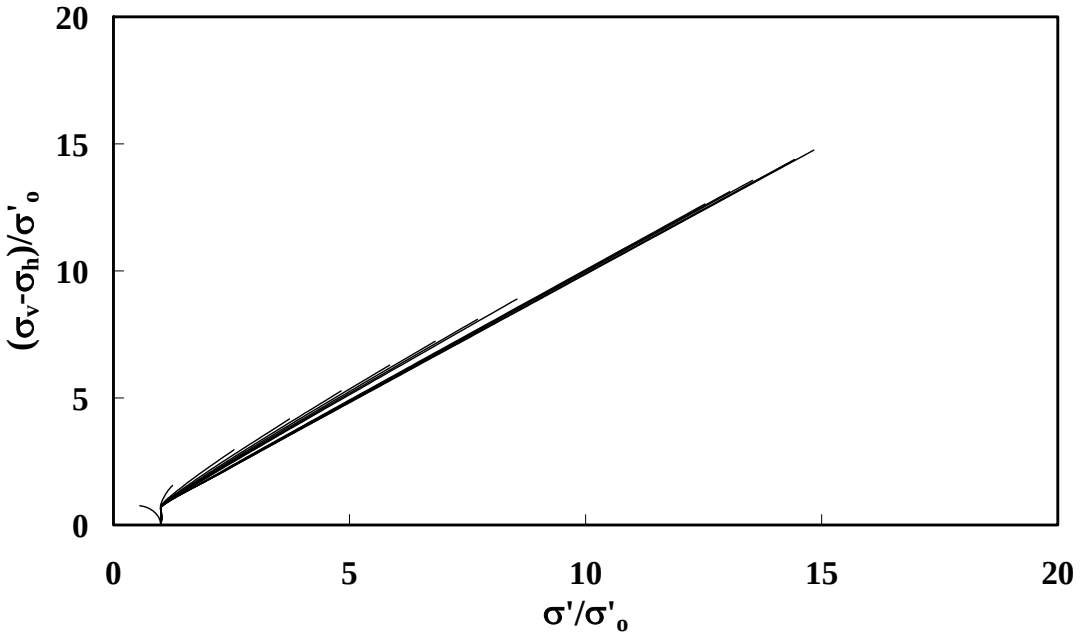

Figure 7.40 Drained Analysis with Modified Cam Clay

7.8 Liquefaction Potential Analysis using Unsaturated Soil Model

The application of the strain path method in unsaturated soil is highly tentative because of the difficulty in generating a strain field in unsaturated media. Unlike saturated conditions, there will be some degree of volumetric strain depending on the matric suction or degree of saturation of the soil during penetration. However in this work, it is assumed that volumetric strains vanish in the unsaturated soil as in the case of saturated soil. This condition leads to the generation of pore water pressure which reduces the magnitude of the matric suction. In order to remove the generation of pore water pressure, the drained penetration assumption should be made such that the value of the matric suction within the soil remains constant during the penetration. This assumption allows the same constitutive model employed for drained analyses in saturated soils to be used for unsaturated soils based on assumption that unsaturated soil at constant matric suction behaves qualitatively in the same way as saturated soil in drained conditions.

As in Chapter IV, a hypothetical soil condition is presented (see Figure 4.10). 40 kPa and 80 kPa suction levels are assumed throughout the soil layer above the water table. Unlike the previous case in Chapter IV, soil parameters of the elasto-plastic soil model were determined through the suction controlled drained tests. Isotropically consolidated soil condition is also assumed. The predicted tip resistance using the critical state model for unsaturated soil is then normalized using the following equations:

$$q_{c1N} = C_q (q_c / p_a) \tag{7.14 a}$$

$$C_Q = (p_a / \sigma'_{vo})^n \tag{7.14 b}$$

For the exponent value, n, 0.5 is used.

The normalized cone tip resistance versus CRR or CSR is plotted in Figure 7.41. The figure reveals that even in unsaturated soil conditions, soil can be liquefied without any corrections on normalized tip resistance. The normalized tip resistance is for clean sand with less than 5% of clay fraction. From the sieve and hydrometer test, the clay

fraction for silty sand is more than 10 %. Hence, the normalized penetration resistance for silty sands should be corrected to an equivalent clean sand value, $(q_{c1N})_{cs}$, as follow:

$$(q_{c1N})_{cs} = K_c q_{c1N} \tag{7.15}$$

where K_c is correction factor for grain characteristics.

In order to be able to determine, K_c, it is necessary to have data on the cone penetrometer sleeve resistance. In the present study, the prediction of stress along a pile shaft is limited due to the complexity of a complete analysis of the strain path method. The K_c value is between 1.0 and 3.4 depending on soil compositions. For cleans sand, K_c is 1.0. Soil with a K_c value larger than 3.4 is not likely to be liquefiable since the soil has too much fines. The calculated clean sand equivalent normalized cone resistance is plotted in Figure 7.41 assuming K_c = 2 and 3. Calculated tip resistance and hence the normalized tip resistance will be changed with different values of K_c since the soil will be different with different levels of K_c. However for the sake of simplicity, it is assumed that the normalized tip resistance does not change with increasing K_c. The clean sand base curves apply only to magnitude 7.5 earthquakes. To adjust the clean sand curves to magnitudes larger or smaller than 7.5, correction factors have to be applied. Factors may shift the normalized cone tip resistance down or up.

Figure 7.41 shows that with the clean sand equivalent normalized cone tip resistance in a saturated condition, the silty sand is susceptible to liquefaction. At unsaturated condition, the soil still shows the susceptibility to earthquake. When the correction factor for grain characteristics is considered, the silty sand shows increased resistance to liquefaction but is still susceptible to earthquake.

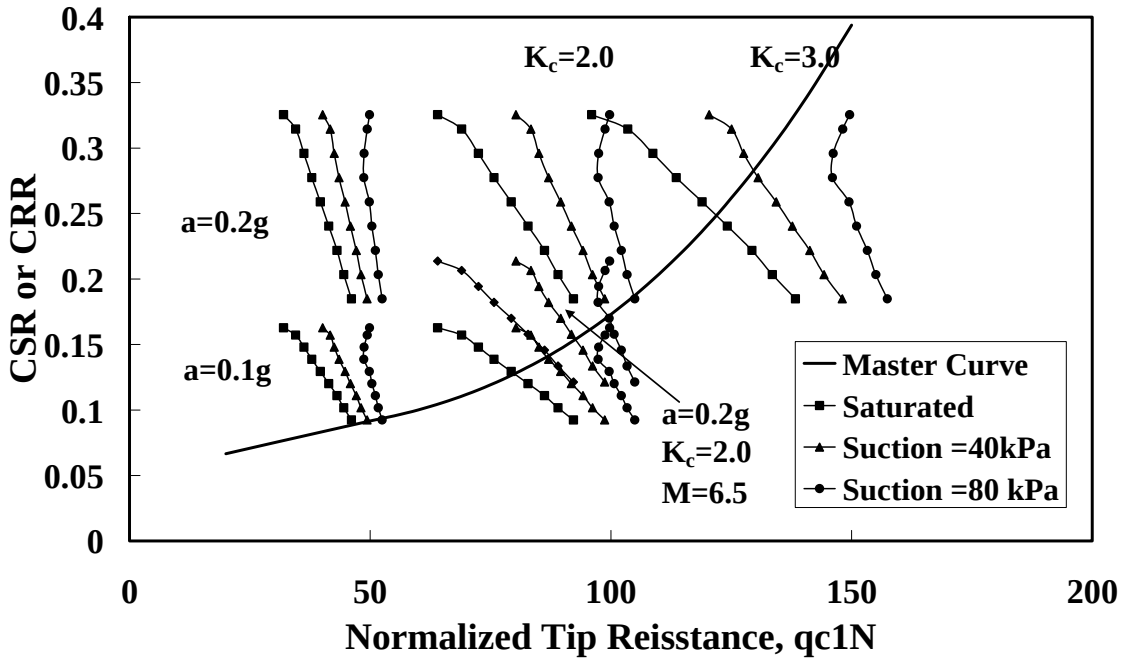

Figure 7.41 Liquefaction Potential of Unsaturated Silty Sand

So far, penetration resistance was calculated based on an artificial soil and suction profile due to the lack of good field cone penetration data. In general, good quality cone penetration data in silty materials along with good quality laboratory tests are almost non-existent. However, efforts have been made to search for the actual field cone penetration data with the occurrence of ground failure due to an earthquake in order to check that studies performed on the hypothetical soil condition is acceptable.

Significant occurrences of ground failure in the form of flow liquefaction, ground softening, and lateral spreading were documented by NSF-sponsored reconnaissance teams in several areas affected by the 1999 Chi-Chi earthquake (M_w = 7.6). Some of the field work was sponsored by the Pacific Earthquake Engineering Research (PEER) center and was performed by a large team of U.S. and Taiwan investigators who are listed on the web page (http://peer.berkeley.edu/lifelines/research_projects/3A02/). This work occurred primarily in three locations, Wufeng, Yuanlin and Nantou, Taiwan, where

significant ground failure occurred and shaking levels were high. Most of the boring data in the web page showed that the soil profile is not uniform except for one location at Nantou-NCREE/MAA Site.

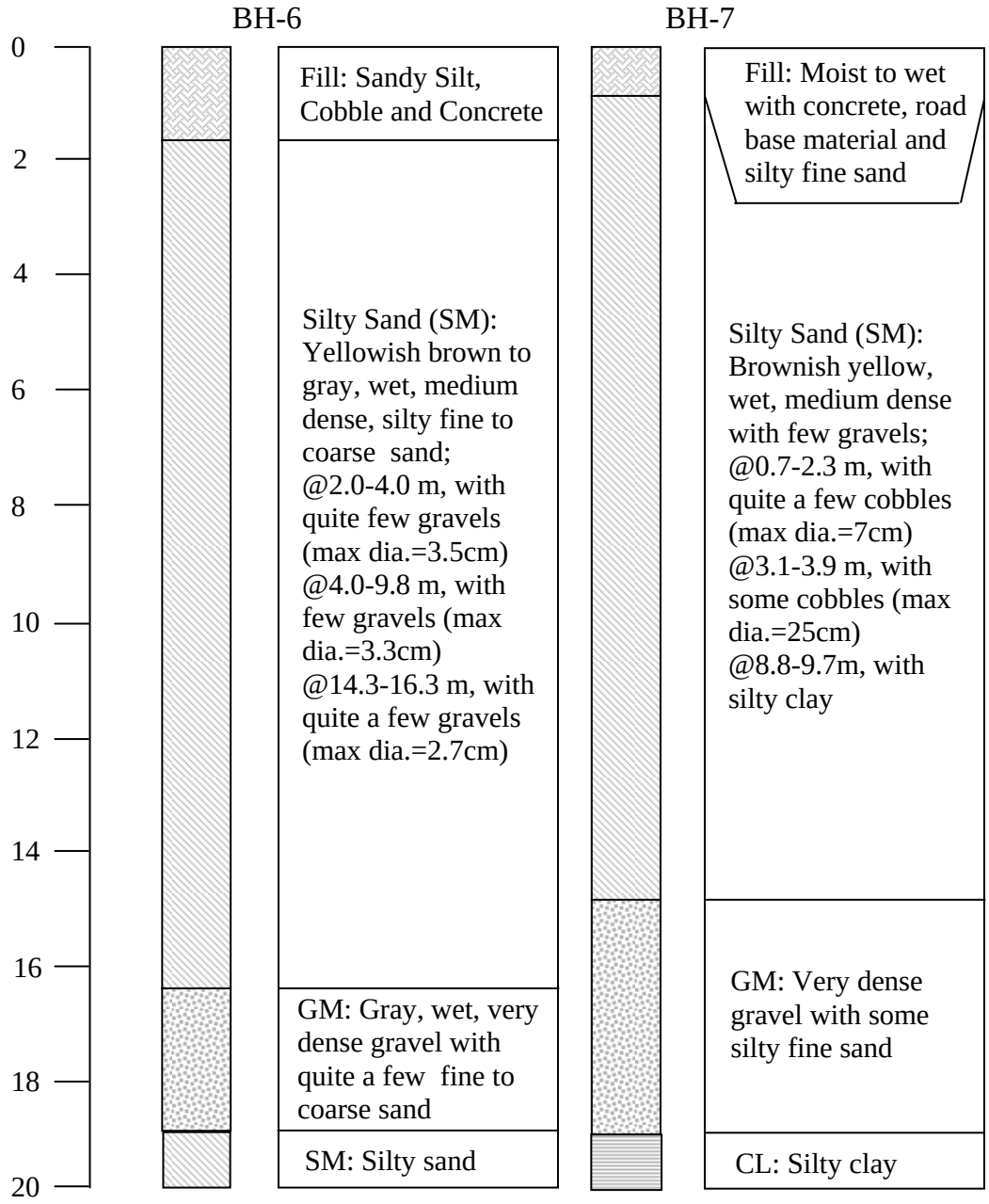

Figure 7.42 Subsurface Condition on Nantou-NCEER/MAA Site

Field investigations at this site were preformed by Moh and Associates. The description of two boring data logs (BH-6 and BH-7) for the location are shown in Figure 7.42. The layer of interest is comprised between 2 and 15 m and is constituted of silty sand having 10 to 40% fines (Passing the No. 200 Seive). Water content of the soil varies from 9.2 to 20%. Typical D_{50} ranges from 0.09 to 0.8 mm.

Penetration data are reported in Figure 7.43 along with the prediction from centerline analysis. The prediction of cone tip resistance needs exact material parameters. However for the sake of simplicity, the same soil material parameters determined through the triaxial monotonic tests on the Riverside Campus silty sand are used for the calculation of tip resistance except for the slope of the critical state line, M. The M value used was 1.52 and was chosen to give a reasonable prediction with the measured data. The comparisons between measured and predicted tip resistance showed excellent agreement from 4 meter to 10 meter depth. From about the depth of 10 m the calculated tip resistance showed overprediction. A lateral spreading type of failure was observed for this location.

The potential for triggering liquefaction in the site soils was evaluated using the assumed peak horizontal acceleration (0.1g and 0.2g). Since the magnitude of the earthquake was 7.6, no corrections were made to adjust cyclic stress ratio to equivalent cyclic stress ratio for M=7.5. The results of field CPT data were used to check the liquefaction potential of the site (Nauntou-NCEER/MAA-CPT8). The analyses of the CPT data are presented in Figure 7.44 and suggest that liquefaction occurred between the depth of 2 to 9 meter and 10 to 15 meter. The predicted cone tip resistance was also used to check liquefaction potential of the site. Instead of calculating side friction resistance from the 2-dimensional strain path method analysis, an average K_c value, 1 m above and below the depth of interest from the real CPT sounding, were used. The result of the predicted cone tip resistance show that liquefaction occurred between the depth of 4 to 8 meters. The analyses of the predicted CPT data suggest that even in unsaturated conditions, soil can be failed by earthquake loading.

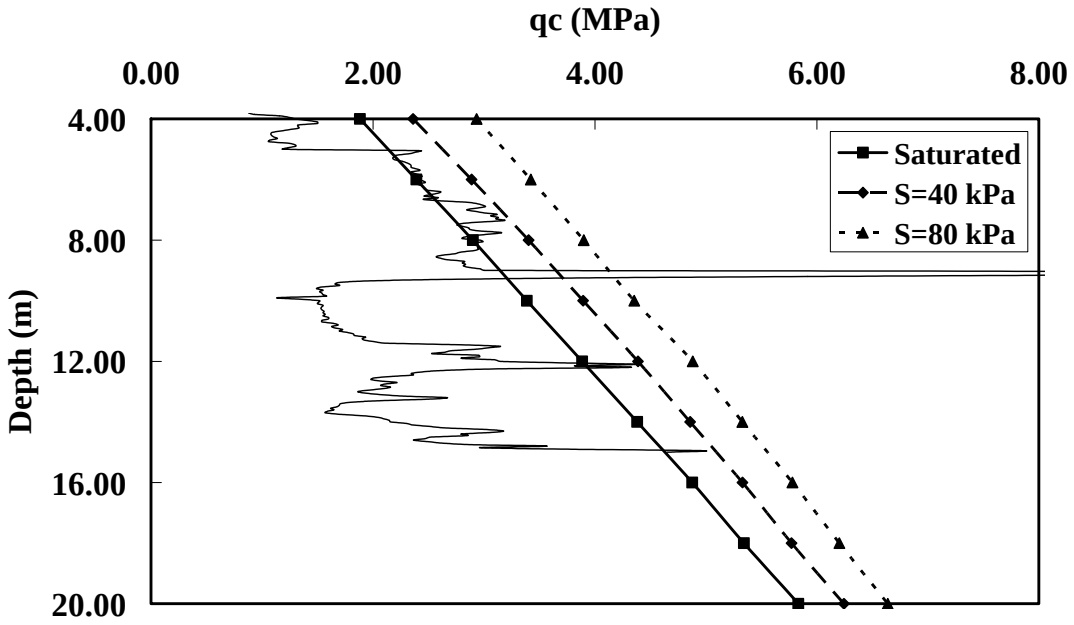

Figure 7.43 CPT Field Data and CPT Prediction (Nantou-NCEER/MAA Site)

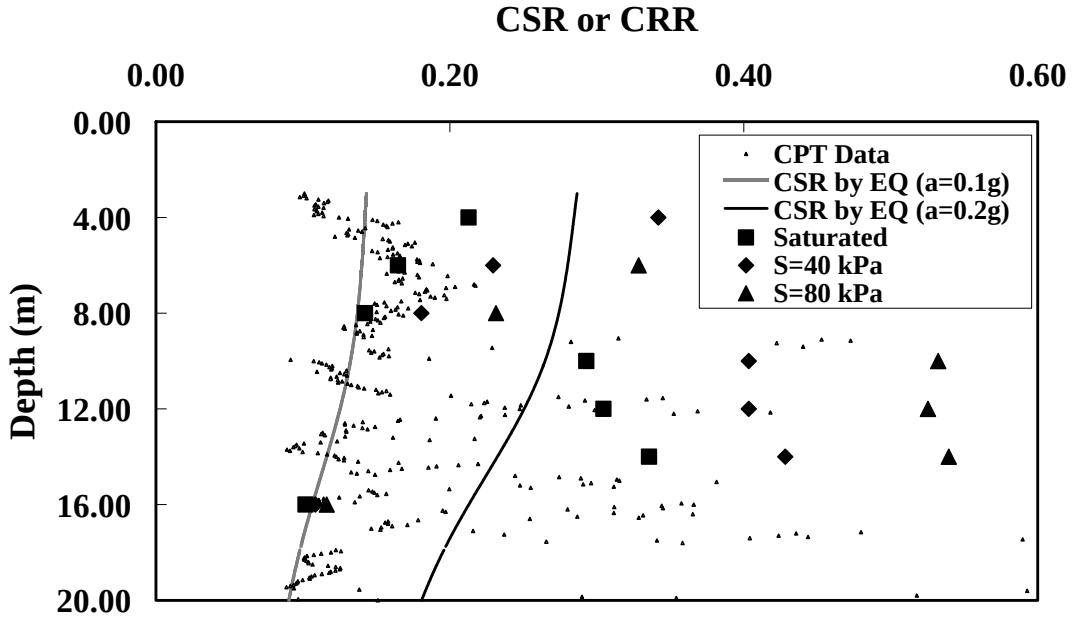

Figure 7.44 Liquefaction Potential of Silty Sand (Nantou-NCEER/MAA Site)

7.9 Cyclic Triaxial Tests

The original intention of the undrained cyclic triaxial tests was to observe the liquefaction potential of unsaturated silty sand. In order to do this, the cyclic triaxial test apparatus has the capability of following a standardized cyclic triaxial testing for the liquefaction study. The standard test practice for cyclic testing is controlling the peak deviator stress corresponding to the desired cyclic stress ratio, the period of the loading function (1 or 2 second), the shape of the loading function (sinusoidal), the number of cycles of loading (usually up to 200 cycles), and the limiting single amplitude axial strain at which the test will be terminated. However, the unsaturated stress path apparatus used in this research is far from the standard practice used in cyclic triaxial tests. Especially the control of the loading function and the generation of the loading function period can not be performed with out testing apparatus. The most rapid cycling of which the apparatus is capable is one cycle every minutes. Therefore, the cyclic triaxial tests data and their analyses in this study cannot be directly used in liquefaction potential analysis of soil. On the other hand, the analysis of test data presented in the following sections will give more insight into the analysis of liquefaction potential and can be beneficial in the liquefaction study.

This section deals with the calculation of dissipated pseudo strain energy. The step by step procedure leading to the calculation of dissipated pseudo strain energy is presented in detail along with testing method for the calculation of dissipated pseudo strain energy.

7.9.1 Sample Preparation and Testing Condition

The same silty sand is used in the undrained cyclic triaxial test. As in the case of drained suction controlled monotonic triaxial tests, all specimens were compacted at a dry density of 1400 kg/m^3 and at water content 13% and 14% in order to reach 80 kPa and 40 kPa initial suction conditions easily during the equalization process before the cyclic tests. A total of 8 samples were prepared for the tests: 4 samples with distilled water, 2 samples with sodium chloride, 2 samples with acetone. The target concentration

of sodium chloride was 12% (g/100g solution). The appropriate weight of sodium chloride was dissolved into the amount of distilled water needed to achieve the initial target water content. The solution was added to the soil and thoroughly mixed. The target concentration for acetone was 10% (g/1000g solution). The water and acetone are mixed together and added to the dry soil.

All the samples are labeled as the following convention: the first letter “S” and number indicates initial suction level before testing, the second letter “H” or “L” indicates level of stress level applied, and the last letter indicates the chemicals in the water. S40 indicates initial suction of 40 kPa. H indicates higher stress level applied and L indicates lower stress level. D indicates distilled water, N indicates sodium chloride in the water, and A indicates acetone added in the water. Therefore, for example, S40HD is sample with an initial suction level of 40 kPa, high stress level, and no chemicals in the water.

7.9.2 Testing Procedures

All specimens tested in cyclic triaxial tests were isotropically consolidated to a net mean stress of 120 kPa. Once consolidation was complete, the drainage lines were closed, and the specimen was loaded cyclically. The strain rate was set for 8 % /hr and 15 cycles of loading were applied to the soil sample. The original intention of the cyclic test was to see the effect of cyclic loading on unsaturated soil samples according to standardized cyclic triaxial test for liquefaction study. However, in this study, the controller for the unsaturated triaxial stress path is not capable of the loading rates used in standardized cyclic test.

As in the case of drained suction-controlled monotonic tests, at the beginning of the cyclic tests, a relaxation test is conducted on the isotropically consolidated soil samples. After enough data points have been taken to define the relaxation modulus, the load is decreased back to zero.

In the cyclic tests, the load is cycled to a predetermined target value or cyclic stress ratio. The cyclic stress ratio is the ratio of the applied shearing stress to the

effective confining stress. In an unsaturated soil cyclic test, the applied shearing stress on the plane of interest is taken to be one half of the applied deviatoric stress. Therefore the cyclic stress ratio is simply the ratio of the applied deviator stress to twice the initial net confining stress. The target cyclic stress ratio was 0.3 and 0.35. 0.35 indicates high stress level and 0.3 indicates low stress level in labeling the samples.

7.9.3 Cyclic Tests

7.9.3.1 Relaxation Modulus

After consolidation of the unsaturated silty sand specimen, the relaxation test is conducted. Figure 7.45 shows the actual trapezoidal strain of the silty sand specimen for the relaxation modulus. By dividing the applied stress on the silty sand sample by the constant strain, the relaxation modulus for the sample can be determined. The relaxation modulus has the power law form. Equation 7.15 shows the general power law form of the axial relaxation modulus:

$$E(t) = E_1(t-\tau)^{-m} \tag{7.16}$$

where E_1 is constant representing the initial relaxation modulus of the material and m is the slope of log stiffness versus log time curve.

As seen in Figure 7.46, E_1 and m are 16923 and 0.053 respectively. These values are used to determine the calculated axial pseudo strain. Table 7.7 presents E_1 and m for all samples tested.

Table 7.7 Relaxation Modulus for All Samples

	S40HD	S40LD	S80HD	S80LD	S40HN	S40LN	S40HA	S80HA
E_1 (kPa)	16923	27905	44309	39056	27399	22547	32502	38368
m	0.053	0.065	0.084	0.062	0.067	0.074	0.089	0.087

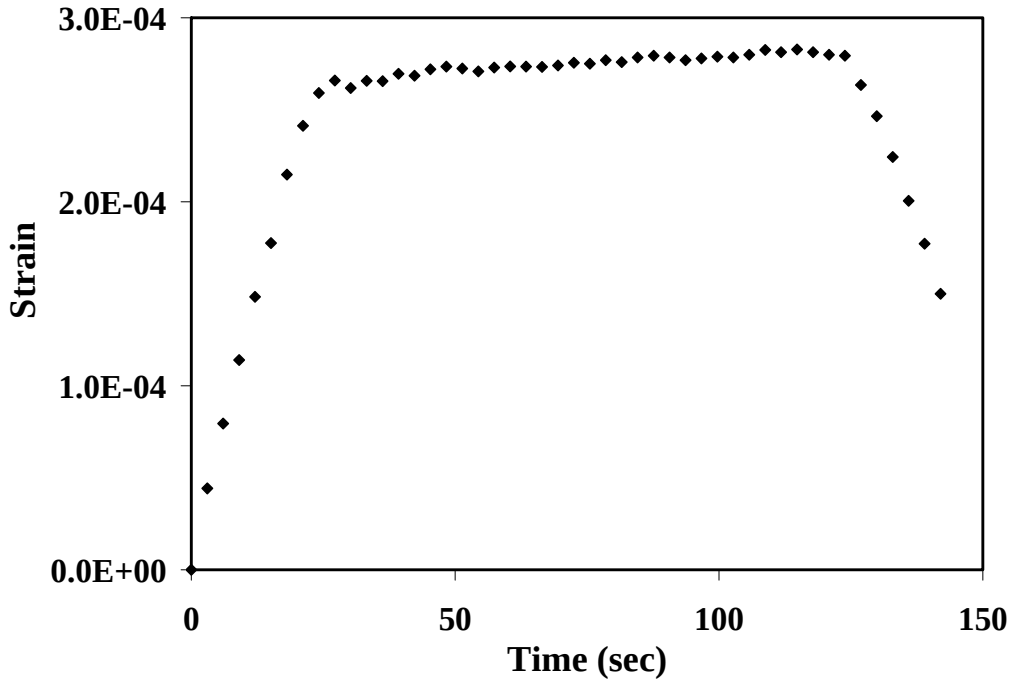

Figure 7. 45 Trapezoidal Strain Pattern (S40HD)

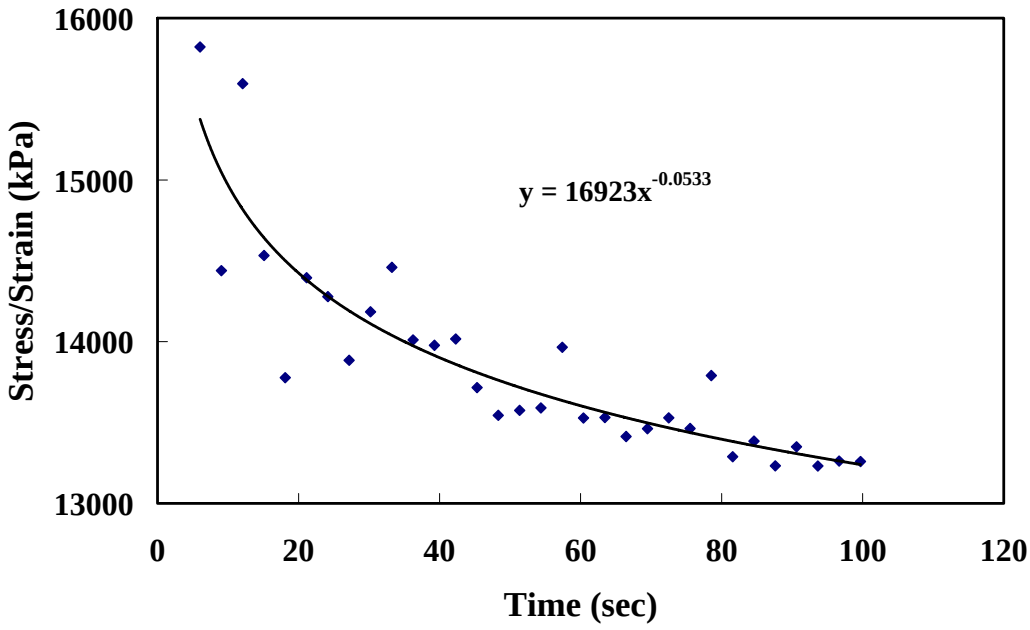

Figure 7.46 Relaxation Modulus (S40HD)

7.9.3.2 Pseudo Strain in Cyclic Tests and Dissipated Pseudo Strain Energy

Following the initial trapezoidal shape strain input relaxation test, the second part of the test is an undrained cyclic strain-controlled test. The strain rate for the tests were 8% per hour but varied from the first cycle to the next cycles due to slight variation of actual strain rate on the soil sample. The typical strain pattern with time is in Figure 7.47.

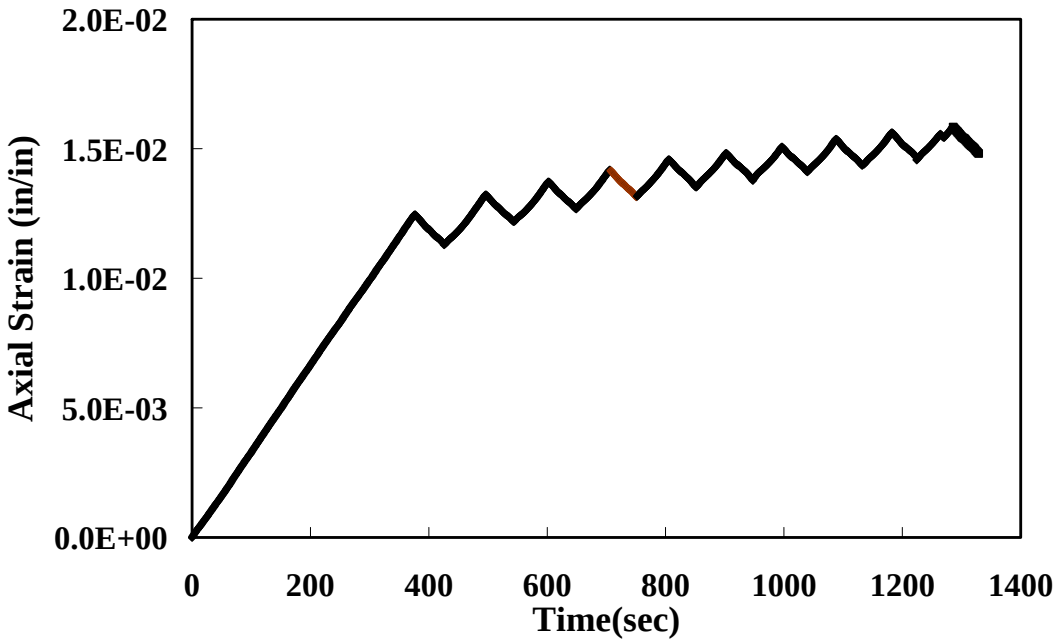

Figure 7.47 Strain Rate (S40HD)

Pseudo strain can be calculated from the relaxation modulus and strain rate. The limits on the integral are determined based on the loading and unloading time for each load cycle. Dividing the calculated linear viscoelastic stress by a reference modulus determines the calculated pseudo-strain as in Equation 5.42 in Chapter V. As a value of the reference modulus, normally unit value is selected as reference modulus. However, in this research E_1 is selected as the reference modulus. Figure 7.48 shows the stress

versus strain and pseudo strain for the one of the soil samples tested (S40HD). All of the test data for the cyclic tests can be found in Appendix B.

As seen in Figures 7.48, the area under the curve of each additional load cycle decreased. The stress versus strain or pseudo strain curves shows permanent strain. Due to this permanent strain, it is necessary to use correction factors to separate strain into a resilient pseudo strain and a plastic pseudo strain. The resilient pseudo strain line is drawn using following equation from the peak stress point back to the origin.

$$\varepsilon^R = \varepsilon^p \frac{\sigma_{peak} - \sigma}{\sigma_{peak}} \tag{7.17}$$

where ε^R is the calculated resilient axial pseudo-strain, ε^p is permanent axial pseudo strain for each loop, and σ_{peak} is peak stress for each load cycle.

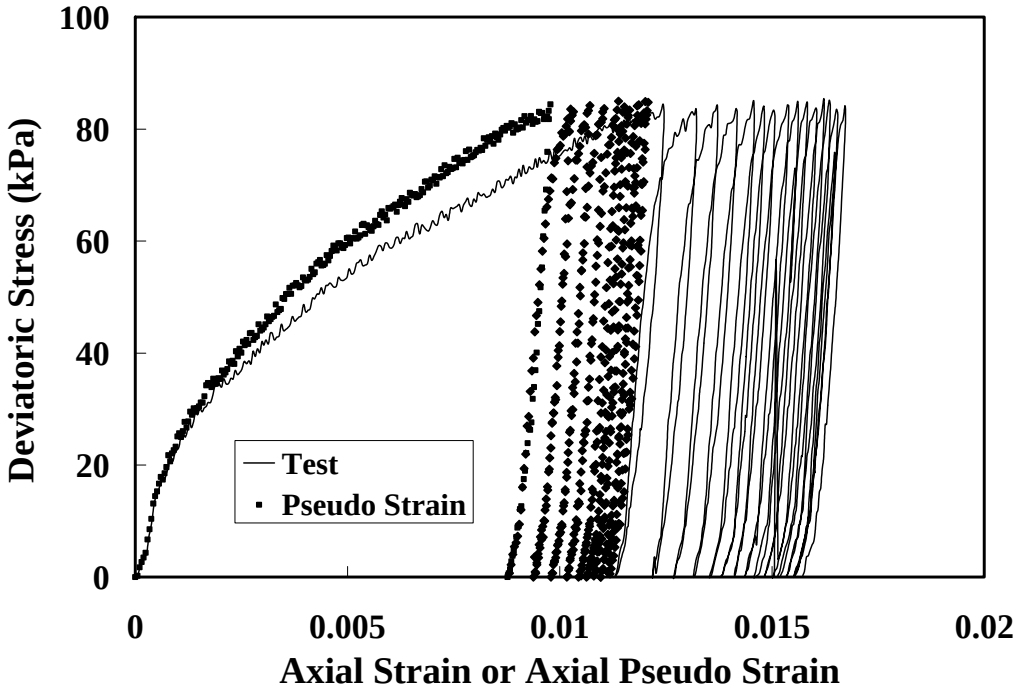

Figure 7.48 Stress versus Strain and Pseudo Strain (S40HD)

The resulting partition of the axial pseudo-strain is Figure 7.49. The unloading curve results in partitioning the total dissipated axial strain energy into two parts: a) a dissipated resilient axial pseudo strain energy due to non linear viscoelastic resistance and b) a dissipated plastic axial pseudo strain energy due to frictional resistance. The dissipated resilient axial pseudo strain energy is a measure of energy that is expended in stiffening the material or if strain softening, in reducing the stiffness of the material. The dissipated plastic axial pseudo strain energy is a part of the energy that is used in causing the permanent deformation of the material. The dissipated resilient axial strain is calculated by calculating area of the loop for each cycle in Figure 7.49. The dissipated plastic axial pseudo strain energy is determined by subtracting the dissipated resilient axial pseudo strain energy from the total axial pseudo strain energy.

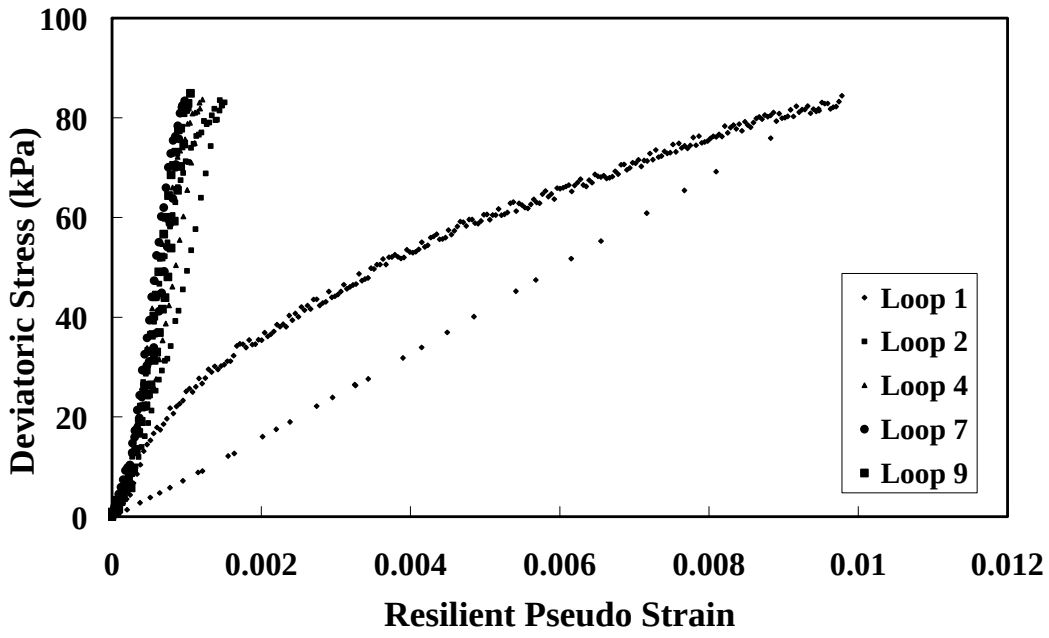

Figure 7.49 Stress versus Resilient Pseudo Strain (S40HD)

Unlike the undrained cyclic triaxial tests on saturated soil samples, volumetric strain is evident in unsaturated soil samples as in Figure 7.50. In the calculation of dissipated pseudo strain, radial strain has to be considered. The radial strain can be calculated from the volumetric and axial strain. The radial strain can be plotted against time to get the radial strain rate as in Figure 7.51. With the radial strain rate, the pseudo radial strain can be calculated. The same relaxation modulus equation used for pseudo axial strain is used in the integral. During cyclic loading, pore water pressure builds up, however the presentations of pore water generation are not available due to loss of data.

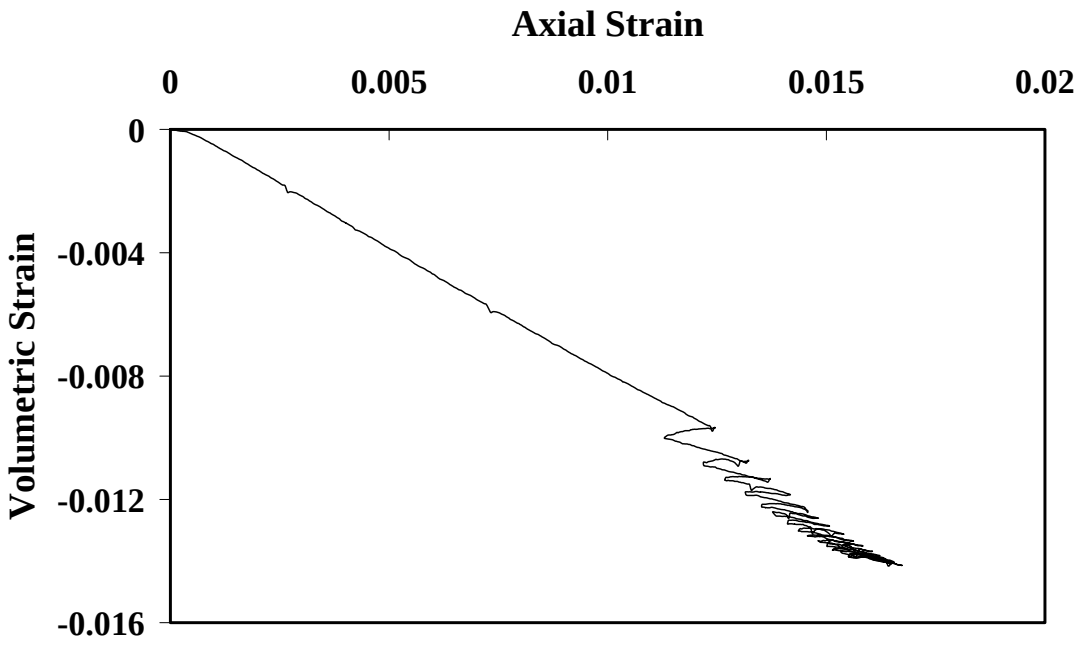

Figure 7.50 Axial Strain versus Volumetric Strain (S40HD)

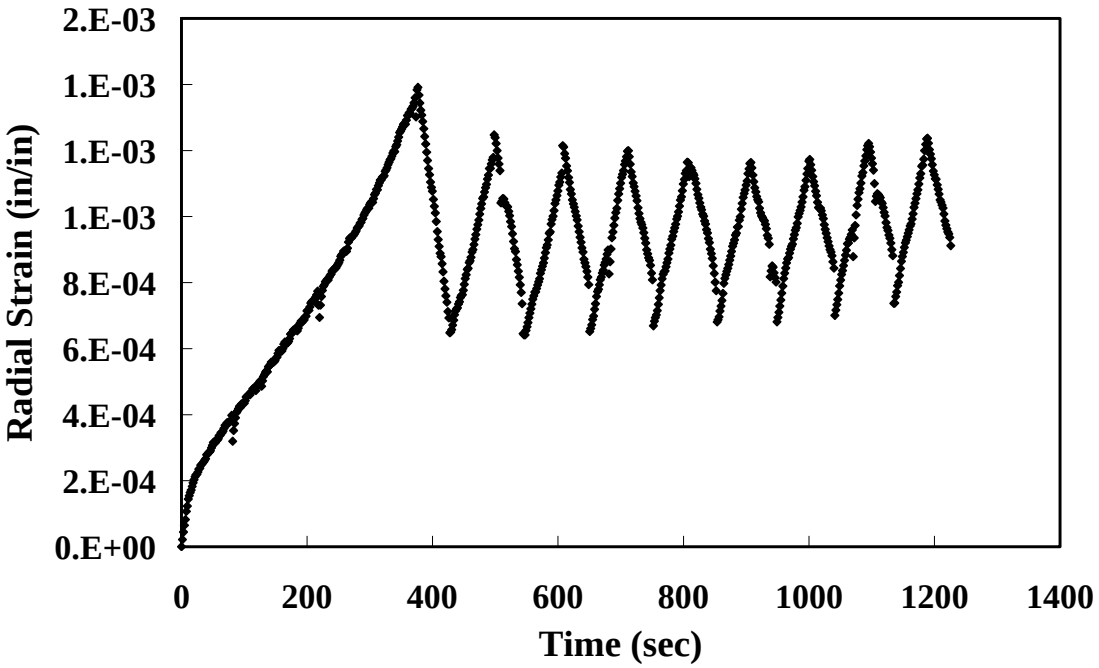

Figure 7.51 Radial Strain Pattern (S40HD)

The pseudo radial strain and pseudo axial strain allows us to calculate pseudo Poisson's ratio and hence total dissipated pseudo strain energy. The total dissipated pseudo strain energy can be calculated using Equation 5.41 in Chapter V. Table 7.8 summarizes the total dissipated pseudo strain energy for all samples.

As seen in Table 7.8, the total dissipated pseudo strain energy is higher at a lower suction value. This suggests that samples with lower suction show soft behavior. It seems that chemicals in the pore water do not affect soil behavior during cyclic loading since the difference between the dissipated pseudo strain energy for distilled water samples and for samples with chemicals in soil samples are small.

The strain rate applied during the test was 8% per hour which is very slow when compared to the standard cyclic tests for liquefaction study. When the loading rate is very fast as in the case of earthquake loading, the effect of matric suction is expected to be very small. This is because the meniscus is susceptible to breaking apart at fast loading condition. Thus during a much faster loading condition, the total dissipated

pseudo-strain energy will be larger due to larger strain. On the other hand, when slower loading rate is applied, it is also expected that the effect of matric suction is more evident than that of the current cyclic test result.

Table 7.8 Total Dissipated Pseudo Strain Energy for All Samples (units: kPa)

Samples	Loop1	Loop2	Loop5	Loop8	Loop10	Total
S40HD	1.353	0.262	0.054	0.032	0.02	1.99
S40LD	0.741	0.082	0.032	0.021	0.018	1.026
S80LD	0.59	0.1	0.034	0.02	0.014	0.954
S80HD	1.036	0.121	0.035	0.023	0.017	1.465
S40HA	1.326	0.232	0.057	0.026	0.022	2.122
S80HA	0.947	0.09	0.029	0.029	0.021	1.267
S40HN	1.311	0.212	0.039	0.024	0.023	1.884
S40LN	0.671	0.113	0.037	0.022	0.013	0.963

7.9.3.3 Dissipated Pseudo Strain Energy in Liquefaction Study

As it is mentioned previously, the undrained cyclic tests in this research can not be used to evaluate liquefaction potential in the standard way. However, the calculation of pseudo strain energy and testing methods for pseudo strain energy calculation can be very useful in the future liquefaction study.

As it is mentioned in the previous chapter, liquefaction potential evaluation needs two variables: Demand and Capacity. The computation of Demand imparted to soil based on the energy method can be found in many references in the literature (Gutenberg and Richter 1956, Davis and Berrill 1982, Berrill and Davis 1985, Law, Cao, and He 1990, Trifunac 1995, Alkhaitib 1994 and Liang 1995 etc). The reason for the use of energy-based Demand is that many seismologists have been quantifying the energy released during earthquakes and have established correlations with common

seismological parameters. Once Demand is quantified in terms of energy, the quantification of Capacity in terms of energy is necessary. The Capacity of the soil to absorb energy is made up of two parts: the energy to overcome viscous resistance and the dissipated pseudo-plastic strain energy. If the accumulation of these energy increments over several load cycles (Capacity) is less than the Demand, then cyclic mobility can occur.

After Nemat-Nasser and Shokooh (1979) have shown a functional relationship between the dissipated energy in laboratory and generated pore pressure, quantification of Capacity in terms of energy is a logical method in the evaluation of liquefaction. Many researchers have proposed energy based models from laboratory tests. However, none of them have attempted to separate viscous resistance of water in the soil. The separation of viscous energy dissipation in the total dissipation of energy will give a more meaningful result in liquefaction potential analysis and pore pressure generation model using dissipated pseudo strain energy from laboratory tests.

CHAPTER VIII
CONCLUSIONS AND RECOMMENDATIONS

8.1 Conclusions

The work presented in this thesis relates to five main areas; the development of ellipsoidal particle model; testing and calculation of surface free energies of soil particles; implementation of the elasto plastic model for unsaturated soil and verification of the model with triaxial testing of unsaturated soils; liquefaction potential analysis of unsaturated soil using the stress-based approach: cyclic triaxial tests on unsaturated soil samples and calculation of dissipated pseudo strain energy.

8.1.1 Particle Model

The pore water in unsaturated soils can be categorized into three forms: adsorbed water, bulk water, and meniscus water. The meniscus water at particle contacts increases the interparticle forces, prevents particle slippages, and changes the soil strength.

The calculation of matric suction and equivalent effective stress using the ellipsoidal particle model is verified first by comparing with spherical particle. As the particles become flatter, suction and interparticle forces increase but are less than those of platy particles. The ability of the ellipsoidal model to adopt various particle shapes is the advantage of the model when compared with the spherical and flat particle models. The inclusion of chemicals in the water changes the surface tension. As a result of decreasing or increasing the surface tension of water, the matric suction and interparticle stress decrease and increase respectively.

8.1.2 Surface Free Energies of Soil Particles

The surface free energies of soil particles were successfully measured by the Universal Sorption Device which is sorption of vapor solvents onto the surface of the soils. By this method, the peculiarity of soil size, irregular shape, and surface texture can be accommodated using this method.

Based on the universal gas sorption testing surface area measurements, the smaller particles have larger surface areas and much rougher surfaces. From the comparison of sand and composite samples, the components of surface free energies increase with a decrease in particle size. The calculation of adhesion of water to a soil particle reveals larger work of adhesion with smaller particles. This suggests that with smaller particles water is more strongly attached to the particles and more difficult to separate.

8.1.3 Suction Controlled Monotonic Triaxial Tests

A series of drained suction controlled triaxial tests were conducted on silty sand specimens to observe soil behavior under different matric suction and pore chemistry. The test results were used to validate the critical state soil model for unsaturated soil proposed by Alonso et al. (1990). In order to do this, a triaxial test apparatus was developed by Barfknecht (2001). The triaxial test apparatus uses the axis-translation technique to be able to raise air pressure above 100 kPa.

8.1.3.1 Behavior under Wetting and Isotropic Stress States

Wetting tests were performed to equalize soil samples. Both at 40 and 80 kPa of matric suction, a small amount of volumetric collapse was observed. No samples have shown a clear yielding point which suggests that all samples consolidated along a virgin compression line. The influence of matric suction on the volumetric compressibility was evident. Test results revealed that the slope of the normal compression line decreases with increasing suction. The presence of sodium chloride in the pore water chemistry has very small effects on volumetric compressibility with the sand-sized particles used in these tests.

When the isotropic test results were compared to the predicted results by the constitutive equation of Alonso et al. (1990), good agreement was found.

8.1.3.2 Behavior during Shear Loading

From the experimental results in this study, it is evident that matric suction has a major influence on the shearing resistance and volumetric characteristics of the unsaturated silty sand samples. The effect of sodium chloride in shearing resistance was observed. However the increase of shearing resistance was very small. When acetone was present in the pore water, the decrease of surface tension was not observed on the soil sample.

In all tests, the incipient critical state was defined at about 8% of shear strain. If the tests had been sheared further, the true critical condition would have been larger than 8% total shear strain. The increase of surface tension due to the presence of sodium chloride in the pore water resulted in the increase of the intercept of the critical state line, k. The slopes of the critical state lines, M, were found to be independent of matric suction as assumed by Alonso et al. (1990).

The experimental stress-pseudo strain response gave stiff behavior in the beginning of the tests. The experimental stress-strain response shows good agreement with the predictions of the elasto-plastic critical state model proposed by Alonso et al. (1990). The test results of the pseudo-strain response show generally good results with the prediction with few exceptions.

8.1.4 Liquefaction Potential in Unsaturated Silty Sand

Without relying on the finite element method, a simple way to do drained analysis along the centerline of a simple pile was presented. This method is used with the elasto-plastic critical state model by Alonso et al. (1990) to calculate the tip resistance of a cone penetrometer in a drained manner.

The calculated tip resistance was used to look at the liquefaction potential of the unsaturated silty sand tested in this investigation. The tip resistance in a hypothetical soil condition showed that unsaturated silty sand can be liquefied. The tip resistance was compared with field CPT test data taken at a site where earthquake damage occurred.

Comparison with the field data revealed that unsaturated silty sand was susceptible to liquefaction, or more precisely, cyclic mobility.

8.1.5 Undrained Cyclic Triaxial Tests

Undrained cyclic triaxial tests were performed on unsaturated silty sand. The results from the cyclic tests were used to calculate dissipated pseudo strain energy. From the dissipated pseudo strain energy calculation, the effect of suction was evident. However the effect of surface tension due to presence of chemicals on the pore water was negligible.

8.2 Recommendations for Future Study

Several recommendations are made on the future testing system and analysis methods on the prediction of cone penetration and liquefaction potential.

The compaction of unsaturated soil sample was not performed directly in the triaxial cell. During the transportation of compacted specimens to the triaxial test cell, the disturbance of the soil specimen is unavoidable. In the future triaxial tests, direct compaction of the soil sample in the test cell is necessary to remove any adverse effects of sample disturbance.

With the establishment of the equipment and testing program, a broad range of matric suction could be examined. But the problem of duration of the time for equilibrium of suction throughout the 15 bar ceramic stone must be addressed. Instead of using an extra high air entry value ceramic stone, less high air entry ceramic stone is necessary.

In this research, only two low matric suction ranges were tested. Complete validation of the proposed critical state based constitutive models can be accomplished. It is also worthwhile to investigate the volume change properties of a soil due to a change in suction.

The prediction of tip resistance using the elasto-plastic model for unsaturated soil is based on centerline analyses. Complete two-dimensional strain path analyses will give

the stress field around cone penetrometer. Also the present model needs to be incorporated into a finite element method. Using coupled consolidation of the proposed model will enable the investigation of the drained analysis with the strain path method.

Limited reliable penetration data exist for uniform silty sand. Further work should include the performance of good quality piezocone tests in a uniform deposit of silty sand. The use of a calibration chamber testing is recommended since it allows for a better control of the test condition.

In order to be able to investigate the liquefaction potential of unsaturated silty sand, new triaxial testing apparatus should be developed. The testing equipment should follow standardized testing procedure as well as controlling initial suction condition before the test.

Modification of a previous energy based liquefaction potential method or the proposal of new energy based liquefaction potential method is recommended based on dissipated pseudo strain energy. This means that the capacity of the soil should be based on dissipated pseudo strain energy. With existing test data on saturated soil samples, only relaxation tests are needed on the same soil sample previously investigated in order to modify the previously proposed energy based liquefaction potential method or the proposed new energy based liquefaction potential method..

REFERENCES

Aitchison, G.D. and Woodburn, J.A. (1969). "Soil Suction in Foundation Design." *Proceedings of 7th ICSMFE,* Mexico City, Mexico, Vol. 2, 1-8.

Alkhaitib, M. (1994). "Liquefaction Assessment by Strain Energy Approach." Ph.D. dissertation, Wayne State University, Detroit, MI.

Alonso, E.E., Gens, A., and Josa, A. (1990). "A Constitutive Model for Partially Saturated Soils." *Geotechnique,* 40(3), 405-430.

Baldi, G., Bellotti, R., Ghionna V.N., Jamiolkowski, M., and Pasqualini E. et al. (1985). "Laboratory Validation of In-Situ Tests." *Proceedings of 11th ICSMFE,* San Francisco, CA, AGI Golden Jubilee Volume, 217-239.

Baligh, M.M. (1985a). "Fundamentals of Deep Penetration I: Soil Shearing and Point Resistance." *Tech. Rep. R85-9, Order No.776,* Department of Civil Engineering, M.I.T., Cambridge, MA.

Baligh, M.M. (1985b). "Fundamentals of Deep Penetration II: Pore Pressures." *Tech. Rep. R85-10, Order No. 777,* Department of Civil Engineering, M.I.T. Cambridge, MA.

Barden, L., Madedor, A.O., and Sides, G.R. (1969). "Volume Change Characteristics of Unsaturated Clay" *Journal of Soil Mechanics and Foundation Division*, ASCE, 95(SM1), 33-52.

Barfknecht, J.E. (2001). "Characterization of the Strength and Plastic Deformation Properties of Unsaturated Soils." Ph.D. dissertation, Texas A&M University, College Station, TX.

Bear, J. (1979). *Hydraulics of Groundwater,* McGraw-Hill Inc., New York.

Berrill, J.B. and Davis, R.O. (1985). "Energy Dissipation and Seismic Liquefaction of Sands: Revised Model." *Soils and Foundations,* 25(2), 106-118.

Biot, M.A. (1941). "General Theory of Three-Dimensional Consolidation." *Journal of Applied Physics,* 12(2), 155-164.

Biot, M.A. (1956). "Theory of Propagation of Elastic Waves in a Fluid Saturated Porous Solid." *Journal of Acoustical Society of America,* 28(2), 168-191.

Bishop, A.W. (1959). “The Principle of Effective Stress.” *Lecture Notes at Norwegian Geotechnical Society*, Oslo, Norway.

Bishop, A.W. and Blight, G.E. (1963). “Some Aspects of Effective Stress in Saturated and Unsaturated Soils.” *Geotechnique*, 13(3), 177-197.

Bishop, A.W. and Donald, I.B. (1961). “The Experimental Study of Partly Saturated Soils in the Triaxial Apparatus.” *Proceedings of 5th ICSMFE*, Paris, France, Vol.1, 13-21.

Blight, G.E. (1967). “Effective stress Evaluation for Unsaturated Soils.” *Journal of Soil Mechanics and Foundation Division*, ASCE, 93(SM2), 125-148.

Bocking, K. and Fredlund, D.G. (1980). “Limitations of the Axis-Translation Technique.” *Proceedings of 4th Int. Conf. on Expansive Soils*, Denver, CO, Vol. 1, 117- 135.

Brackley, I.J.A. (1971). “Partial Collapse in Unsaturated Expansive Clay.” *Proceedings of 5th African Reg. Conf. on Soil Mech. and Found. Engrg*., South Africa, Vol. 1, 23-30.

Briaud, J.L. and Gibbens, R.M. Eds. (1994). “Predicted and Measured Behavior of Five Spread Footing on Sand.” *Geotechnical Special Publications No. 41*, ASCE, New York.

Burland, J.B. (1964). “Some Aspects of Effective Stress in Saturated and Unsaturated Soils.” *Geotechnique*, 14(1), 65-68.

Castro, G. (1969). “Liquefaction of Sands.” Ph.D. dissertation, Harvard Soil Mech. Series, No 81. Pierce Hall, Harvard University, Cambridge, MA.

Castro, G. (1975). “Liquefaction and Cyclic Mobility of Saturated Sands.” *Journal of Geotechnical Engineering Division*, ASCE, 101(GT6), 551-570.

Castro, G. and Poulos, S.J. (1977). “Factors Affecting Liquefaction and Cyclic Mobility.” *Journal of Geotechnical Engineering Division*, ASCE, 103(GT6), 501-516.

Cho, G.C. (2000). “Unsaturated Soil Stiffness and Post-Liquefaction Shear Strength.” Ph.D. dissertation, Georgia Institute of Technology, Atlanta, GA.

Cleveland, G.S. (2001). "A Comparison of the Fracture Properties of Selected Geosynthetic Products Using Pseudo-Strain Damage Theory." M.S. thesis, Texas A&M University, College Station, TX.

Davis, R.O. and Berrill, J.B. (1982). "Energy Dissipation and Seismic Liquefaction in Sands." *Earthquake Engineering and Structural Dynamics*, Vol. 10, 59-68.

Deresiewicz, H. (1974). "Bodies in Contact with Applications to Granular Media." *R.D. Mindlin and Applied Mechanics*, Pergamon Press, Inc., New York.

Dingxin, C. (2002). "Surface Free Energy of Asphalt-Aggregate System and Performance Analysis of Asphalt Concrete Based on Surface Energy." Ph.D. dissertation, Texas A&M University, College Station, TX.

Elghaib, M.K. (1989). "Prediction and Interpretation of Piezocone Data During Undrained, Drained, and Partially Drained Penetration" Ph.D. dissertation, M.I.T., Cambridge, MA.

Fai, C.C. (2001). "Behavior of Unsaturated Loosely Compacted Weathered Materials." Ph.D. dissertation, The Hong Kong University of Science and Technology, Hong Kong.

Fam, M. and Santamarina, J.C. (1996). "Coupled diffusion-fabric-flow phenomena: an effective stress analysis." *Canadian Geotechnical Journal*, 33(3), 515-522.

Fredlund, D.G. (1973). "Volume Change Behavior of Unsaturated Soils." Ph.D. dissertation, University of Alberta, Edmonton, Canada.

Fredlund, D.G. (1989). "Soil Suction Monitoring for Roads and Air Fields." *Proceedings of Symposium on the State of the Art of Pavement Response Monitoring Systems for Roads and Airfields*, Sponsored by the U.S. Army Corps of Engineers, Hanover, NH, 113-121.

Fredlund, D.G. and Morgenstern, N.R. (1977). "Stress State Variable for Unsaturated Soils." *Journal of Geotechnical Engineering Division*, ASCE, 103(GT5), 447-466.

Fredlund, D.G., Morgenstern, N.R., and Widger, R.A. (1978). "The Shear Strength of Unsaturated Soils." *Canadian Geotechnical Journal*, 15(3), 313-321.

Fredlund, D.G. and Rahardjo, H. (1987). “Soil Mechanics Principles for Highway Engineering in Arid Regions.” *Transportation Research Record 1137*, TRB, Washington, DC, 1-11.

Fredlund, D.G. and Rahardjo, H. (1993). *Soil Mechanics for Unsaturated Soils*, John Wiley and Sons, Inc., New York.

Fung, Y.C. (1977). *A First Course in Continuum Mechanics*, Prentice Hall, Englewood Cliffs, NJ.

Gan, J.K.M., Fredlund, D.G., and Rahardjo, H. (1988). “Determination of the Shear Strength Parameters of an Unsaturated Soil Using the Direct Shear Test.” *Canadian Geotechnical Journal*, 25(3), 500-510.

Geiser, F., Laloui, L. and Vulliet, L. (2000). “On the Volume Measurement in Unsaturated Triaxial Test.” *Proceedings of Asian Conference on Unsaturated Soils*, Singapore, 669-674.

Gens,A. and Alonso, E.E.(1992). “A Framework for the Behavior of Unsaturated Expansive Clays.” *Canadian Geotechnical Journal*, Vol. 29, 1013-1032.

Gibbs, H.J. and Coffey, C.T. (1969). “Techniques for Pore Pressure Measurements and Shear Testing of Soils.” *Proceedings of 7th ICSMFE*, Mexico City, Mexico, Vol. 1, 151-157.

Good, R.J. (1992). “Contact Angle, Wetting, and Adhesion: A Critical Review.” *Journal Adhesion Science and Technology*, Vol. 6, 3-36.

Good, R.J., and van Oss, C.J. (1991). “The Modern Theory of Contact Angles and the Hydrogen Bond Components of Surface Energies.” *Modern Approach to Wettability: Theory and Application*, Plenum Press, New York.

Green, R.A. (2001). “Energy Based Evaluation and Remediation of Liquefiable Soils.” Ph. D. dissertation, Virginia Polytechnic Institutive and State University, Blacksburg, VA.

Gutenberg, B. and Richter, C.F. (1956). “Magnitude and Energy of Earthquakes.”, *Ann. Geofis.*, 9, 1-15.

Hall, J.R. (1962). “Effect of Amplitude on Damping and Wave Propagation in Granular Materials.” Ph.D. dissertation, University of Florida, Gainesville, FL.

Hall, J.R., and Richard, F.E. (1963). “Dissipation of Elastic Wave Energy in Granular Soils.” *Journal of Soil Mechanics and Foundations Division,* ASCE, 89(SM6), 25-56.

Hilf, J.W. (1956). *An Investigation of Pore-Water Pressure in Compacted Cohesive Soils*. Denver, Colorado: U.S. Department of the Interior, Bureau of Reclamation, Design and Construction Division.

Ho, D.Y.F and Fredlund, D.G. (1982). “A Multistage Triaxial Test for Unsaturated Soils.” *Geotechnical Testing Journal*, 5(1), 18-25.

Hoyos, L.R. (1998). “Experimental and Computational Modeling of Unsaturated Soil Behavior Under True Triaxial Stress States.” Ph.D. dissertation, Georgia Institute of Technology, Atlanta, GA.

Jeng, F.S. (1992). “Deep Penetration into Frictional Ductile and Brittle Materials.” Ph.D. dissertation, MIT, Cambridge, MA.

Jennings, J.E. and Burland, J.B. (1962). “Limitations to the Use of Effective Stresses in Partly Saturated Soil.” *Geotechnique*, 12(2), 125-144.

Ladd, R.S. (1978). “Preparing Test Specimens Using Undercompaction” *Geotechnical Testing Journal*, 1(1), 16-23.

Lamborn, M.J. (1986). “A Micromechanics Approach to Modeling Partly Saturated Soils” M.S. thesis, Texas A&M University, College Station, TX.

Law, K.T., Cao, Y.L., and He, G.N. (1990). “An Energy Approach for Assessing Seismic Liquefaction Potential.” *Canadian Geotechnical Journal*, 27(3), 320-329.

Lee, H.J. (1996). “Uniaxial Constitutive Modeling of Asphalt Concrete Using Viscoelasticity and Continuum Damage Theory.” Ph.D. dissertation, North Carolina State University, Raleigh, NC.

Lee, H. J., Daniel, J. S., and Kim, Y. R. (2000). "Continuum Damage Mechanics-Based Fatigue Model of Asphalt Concrete." *Journal of Materials in Civil Engineering*, ASCE, 12(2), 105-112.

Lee, H.J. and Kim, Y.R. (1998). "Viscoelastic Constitutive Model for Asphalt Concrete under Cyclic Loading." *Journal of Engineering Mechanics*, 124(1), 32-40.

Lee, H.C. and Wray, W.K. (1995). "Techniques to Evaluate Soil Suction – a Vital Unsaturated Soil Water Variable." *Proceedings of the 1st International Conference on Unsaturated Soils*, Paris, France, Vol. 2, 615-622.

Li, W (1997). "The Measurement of Surface Free Energy of Aggregate SHAP RB." *Final Report of Cahn Balance Thermogravimetry Gas Adsorption Experiments*, Department of Chemical Engineering, Texas A&M University, College Station, TX.

Liang, L. (1995). "Development of an Energy Method for Evaluating the Liquefaction Potential of a Soil Deposit." Ph.D. dissertation, Case Western Reserve University, Cleveland, OH.

Lide, D.R. (2000). *CRC Handbook of Chemistry and Physics*, 80th Edition. CRC Press, Washington, DC.

Lytton, R.L. (1995). "Foundations and Pavements on Unsaturated Soils." *Proceedings of the 1st International Conference on Unsaturated Soils*, Paris, France, Vol.3, 1201-1220.

Lytton, R.L. (2001). Personal Communication, Department of Civil Engineering, Texas A&M University, College Station, TX.

Matyas, E.L. and Radhakrishna, H.S. (1969). "Volume Change Characteristics of Partly Saturated Soils." *Geotechnique*, 18(4), 432-448.

Nagaraj, T.S. and Srinivasa Murthy, B.R. (1985). "Compressibility of Partly Saturated Soils." *Journal of Geotechnical Engineering Division*, ASCE, 111(GT7), 937-942.

NCEER (1997). *Proceedings of the NCEER Workshop on Evaluation of Liquefaction Resistance of Soils*, Technical Report NCEER-97-0022, National Center for

Earthquake for Earthquake Engineering Research, State University of New York at Buffalo, Buffalo, NY.

Nemat-Nasser, S. and Shokooh, A. (1979). "A Unified Approach to Densification and Liquefaction of cohesionless Sand in Cyclic Shearing." *Canadian Geotechnical Journal*, Vol. 16, 659-678.

NRC (1985). *Liquefaction of Soils During Earthquakes*, Committee on Earthquake Engineering, Commission on Engineering and Technical Systems, National Research Council, National Academy Press, Washington, D.C.

Olson, R.E. and Langfelder, L.J. (1965). "Pore-Water Pressures in Unsaturated Soils." *Journal Soil Mechanics and Foundation Division*, ASCE, 91(SM4), 127-160.

Park, S.W. (2000). "Evaluation of Accelerated Rut Development in Unbounded Pavement Foundations and Load Limits on Load-Zoned Pavement" Ph.D. dissertation, Texas A&M University, College Station, TX.

Robertson, P.K. and Wride, C.E. (1998). "Evaluating Cyclic Liquefaction Potential Using the Cone Penetration Test." *Canadian Geotechnical Journal*, 35(3), 442-459.

Roscoe, K.H. and Burland, J.B. (1968). "On the Generalized Stress-Strain Behavior of Wet Clay." *Engineering Plasticity*, Cambridge University Press, New York, 535-609.

Schapery, R. A. (1984). "Correspondence Principles and a Generalized J-Integral for Large Deformation and Fracture Analysis of Viscoelastic Media." *International Journal of Fracture*, 25, 195-223.

Seed, H.B. and Idriss, I.M. (1971). "Simplified Procedures for Evaluating Soil Liquefaction Potential." *Journal of the Soil Mechanics and Foundations Division*, ASCE, 97(SM8), 105-134.

Sharma, R.S. (1998). "Mechanical Behavior of Unsaturated Highly Expansive Clays." Ph.D. dissertation, University of Oxford, UK.

Si, Zhiming (2001). "Characterization of Microdamage and Healing of Asphalt Concrete Mixture." Ph.D. dissertation, Texas A&M University, College Station, TX.

Smith, J.M., Van Ness, H.C., and Abbott, M.M. (1996). *Introduction to Chemical Engineering Thermodynamics*, 5th Edition, McGraw-Hill, New York.

Tand, K.E. (2000). *KETA In-House Summary Report*, Internal Report Written by Tand and Associates, Inc, Houston, TX.

Terzaghi, K. (1936). "The Shear Resistance of Saturated Soils." *Proceedings of 1st ICSMFE*, Harvard University, Cambridge, MA, Vol. 1, 54-56.

Trifunac, M.D. (1995). "Empirical Criteria for Liquefaction in Sands via Standard Penetration Tests and Seismic Wave Energy." *Soil Dynamics and Earthquake Engineering*, Vol. 14, 419-426.

Vanapalli, S.K., Fredlund, D.E., Pufahl, D.E., and Clifton, A.W. (1996). "Model for Prediction of Shear Strength with Respect to Soil Suction." *Canadian Geotechnical Journal*, 33(3), 379-392.

Wheeler, S.J., Gallipoli, D., and Karstunen, M. (2002). "Comments on Use of the Barcelona Basic Model for Unsaturated Soils" *Int. J. Numer. Anal. Meth. in Geomechanics*, 26, 1516-1571.

Wheeler, S.J. and Karube, D. (1996) "State of Art Report: Constitutive Modeling." *Proceedings of the First International Conference on Unsaturated Soils*, Paris, France, Vol.3, 1323-1356.

Wheeler, S.J. and Sivakumar, V. (1995). "An Elasto-Plastic Critical State Framework for Unsaturated Soils." *Geotechnique*, 45(1), 35-53.

Wood, D.M. (1990). *Soil Behavior and Critical State Soil Mechanics*, Cambridge University Press, New York.

Youd, T.L., Idriss, I.M., Andrus, R.D., Arango, I., and Castro, G. et al. (2001). "Liquefaction Resistance of Soils: Summary Report from the 1996 NCEER and 1998 NCEER/NSF Workshops on Evaluation of Liquefaction Resistance of Soils" *Journal of Geotechnical and Geoenvironemntal Eng.*, ASCE, Vol. 127(10), 817-833.

APPENDIX A

CALIBRATION OF PRESSURE TRANSDUCERS AND LOAD CELL

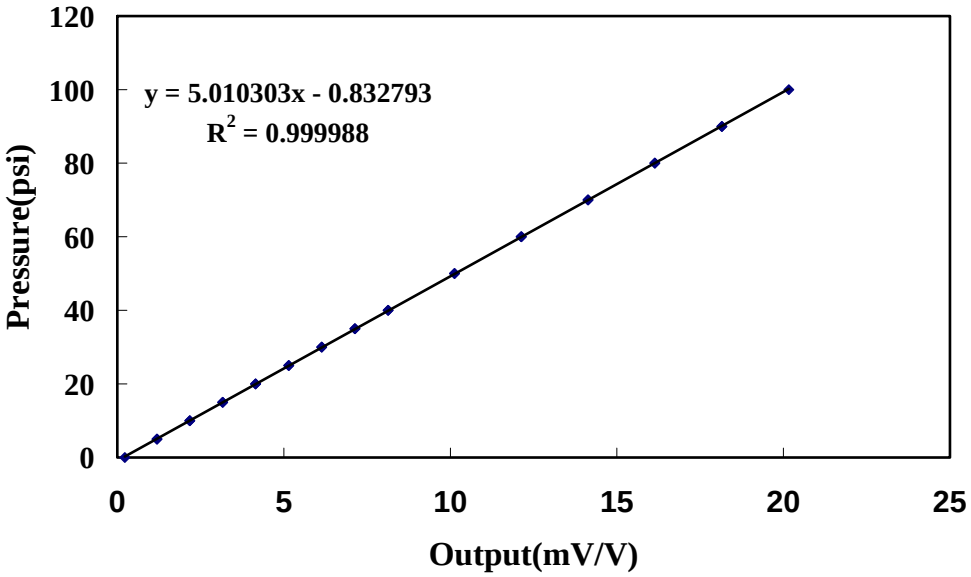

Figure A.1 Calibration of Confining Pressure Transducer

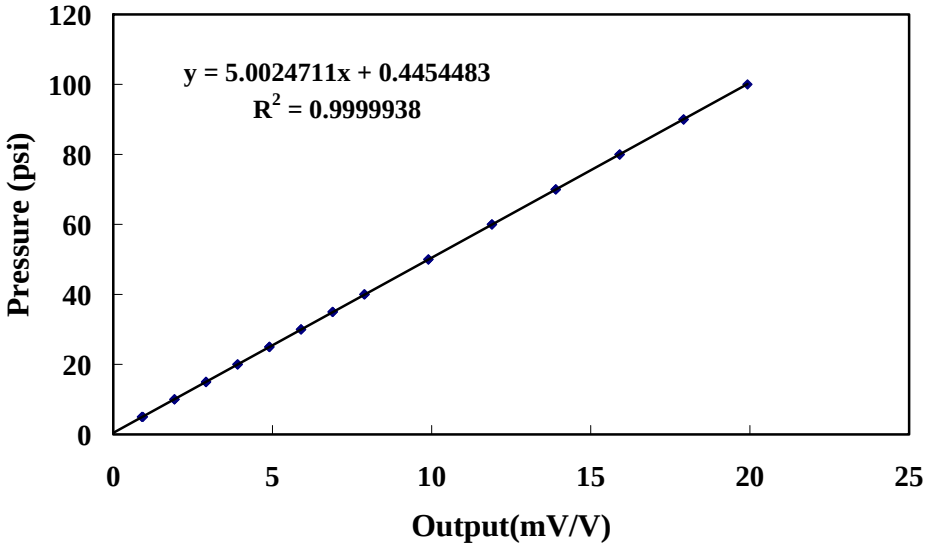

Figure A.2 Calibration of Air Pressure Transducer

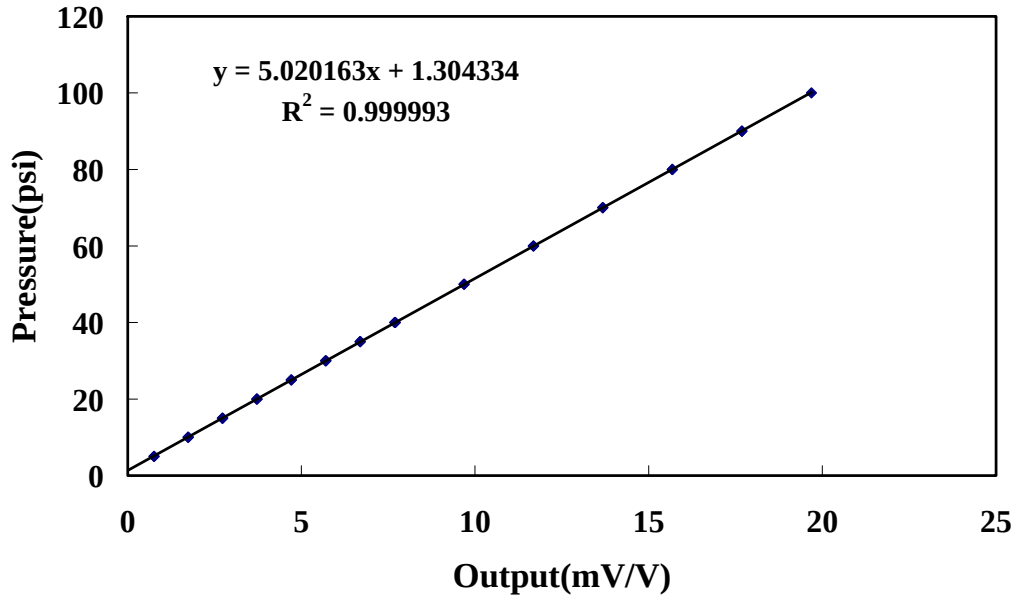

Figure A.3 Calibration of Water Pressure Transducer

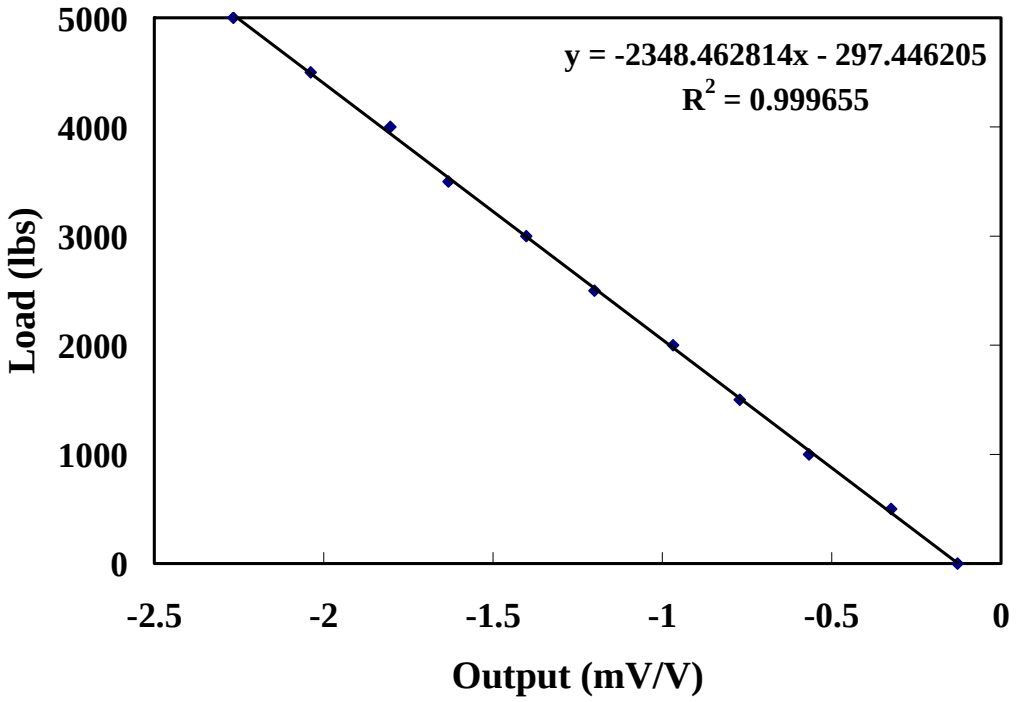

Figure A.4 Calibration of Load Cell

APPENDIX B
CYCLIC TRIAXIAL TEST RESULTS

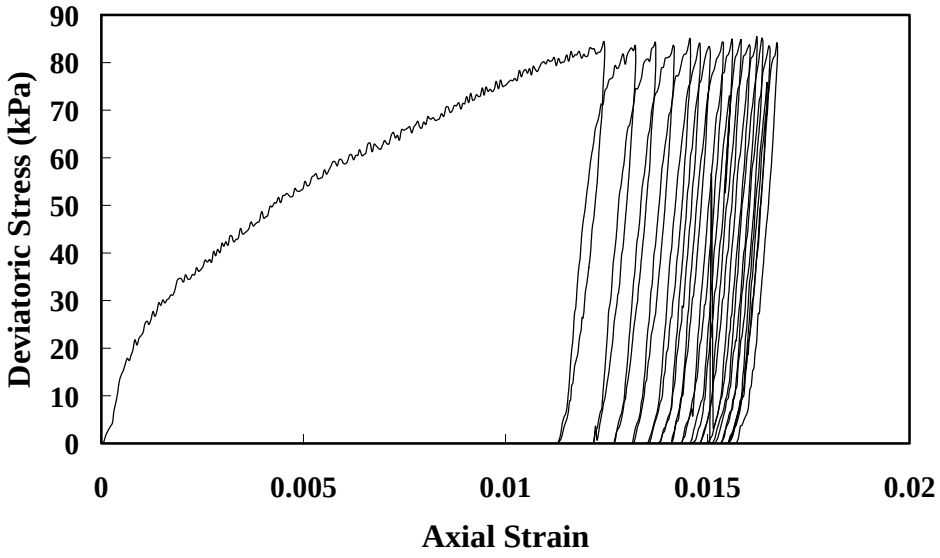

Figure B.1 Stress Strain Response (S40HD)

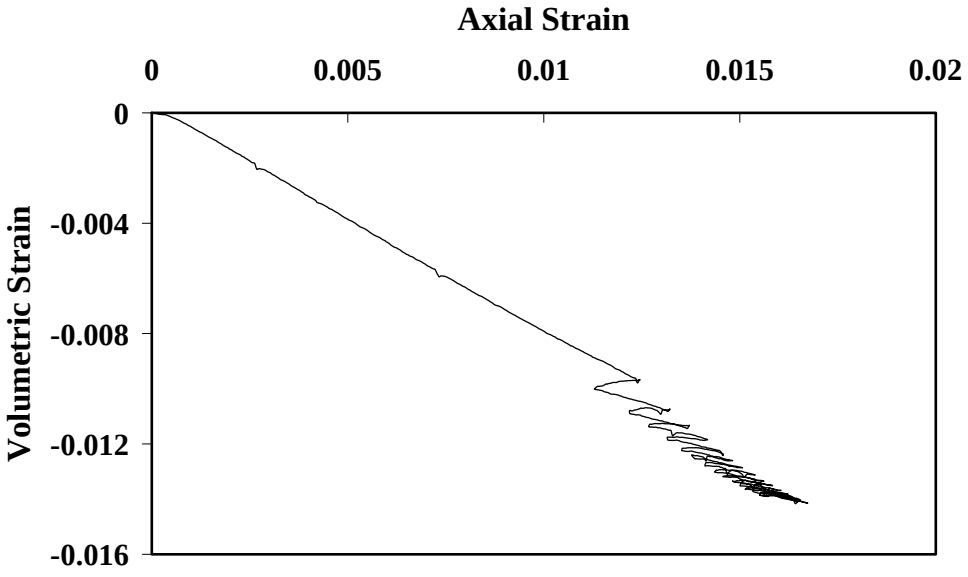

Figure B.2 Axial Strain versus Volumetric Strain (S40HD)

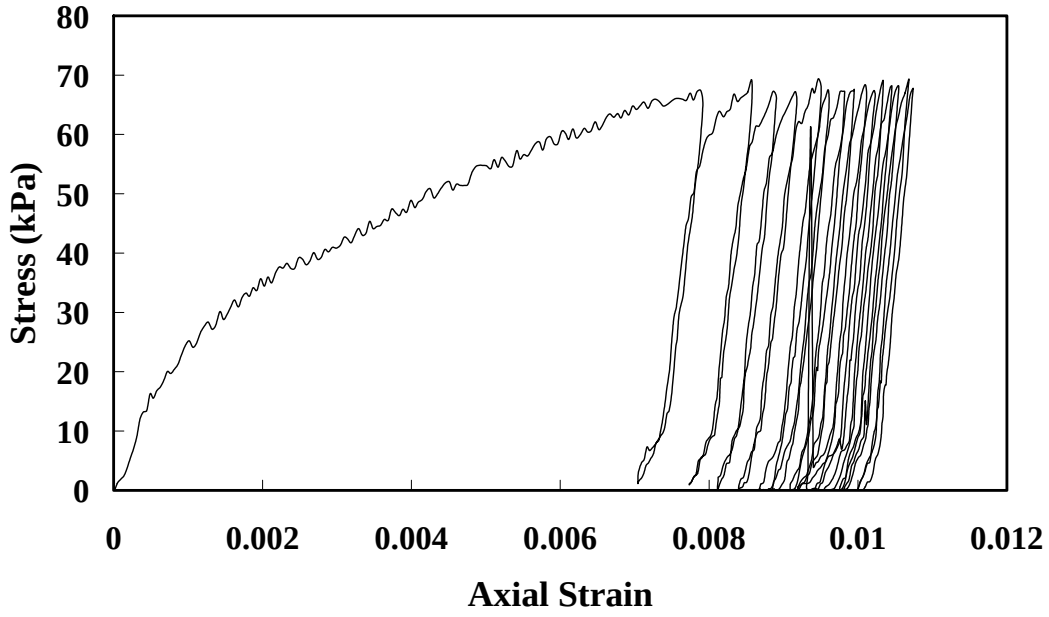

Figure B.3 Stress Strain Response (S40LD)

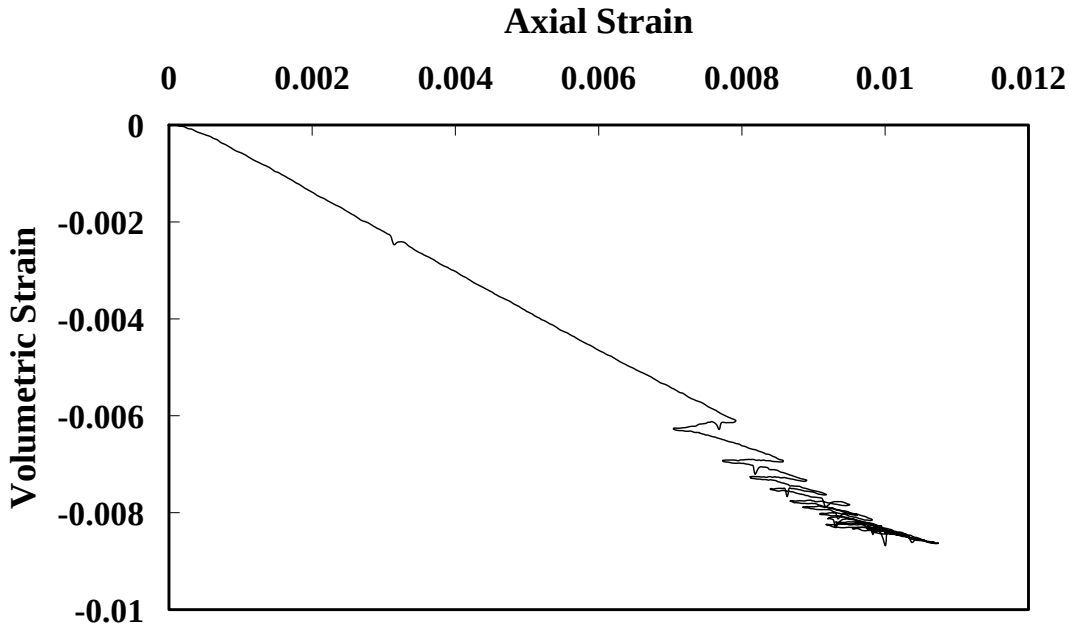

Figure B.4 Axial Strain versus Volumetric Strain (S40LD)

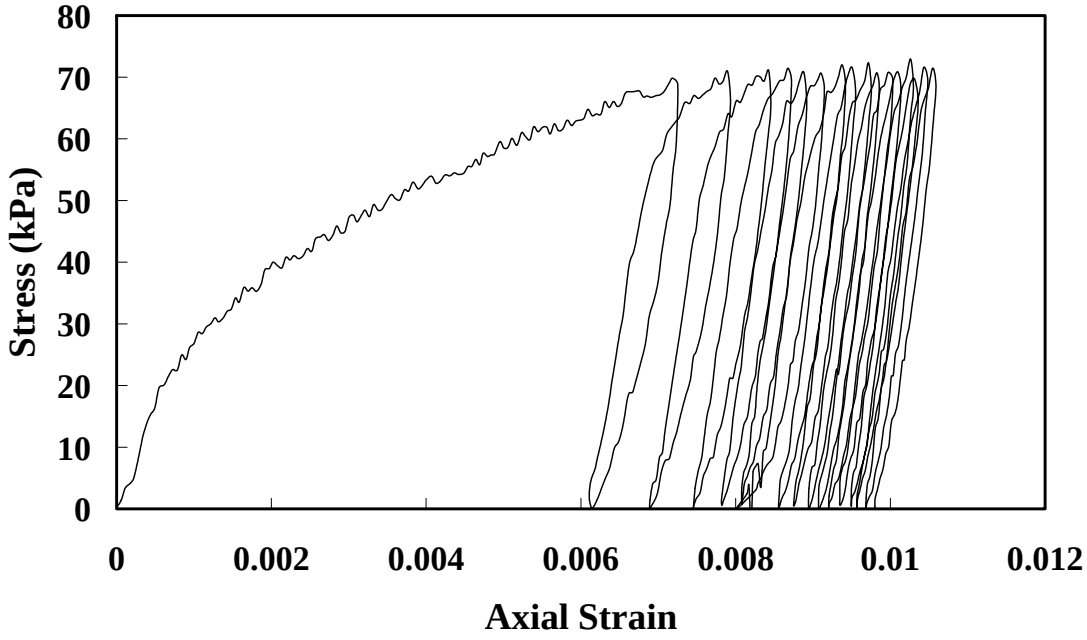

Figure B.5 Stress Strain Response (S80LD)

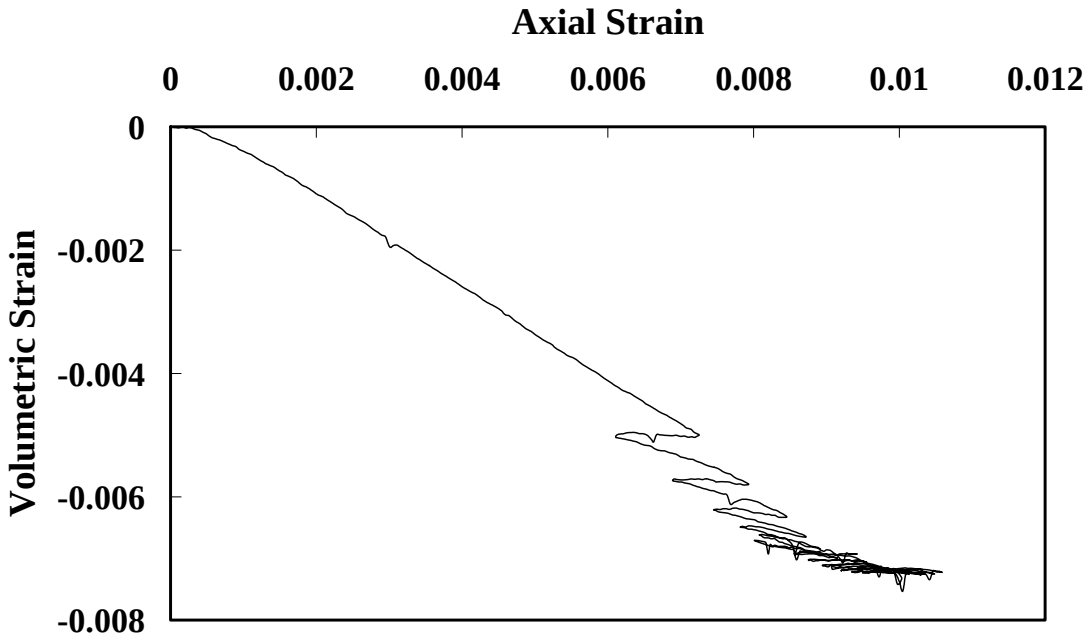

Figure B.6 Axial Strain versus Volumetric Strain (S80LD)

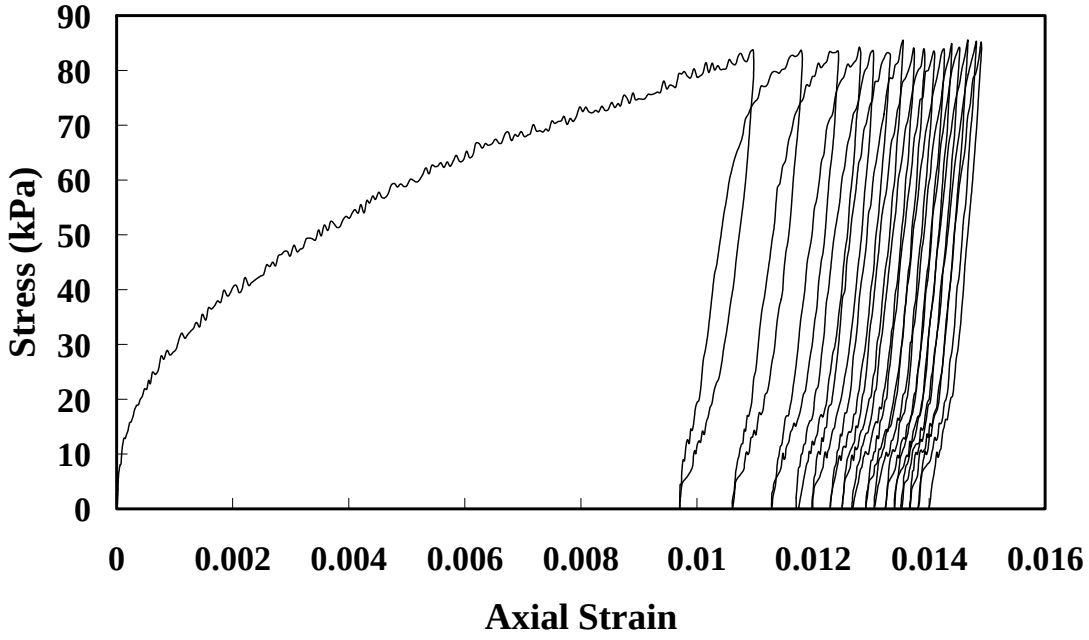

Figure B.7 Stress Strain Response (S80HD)

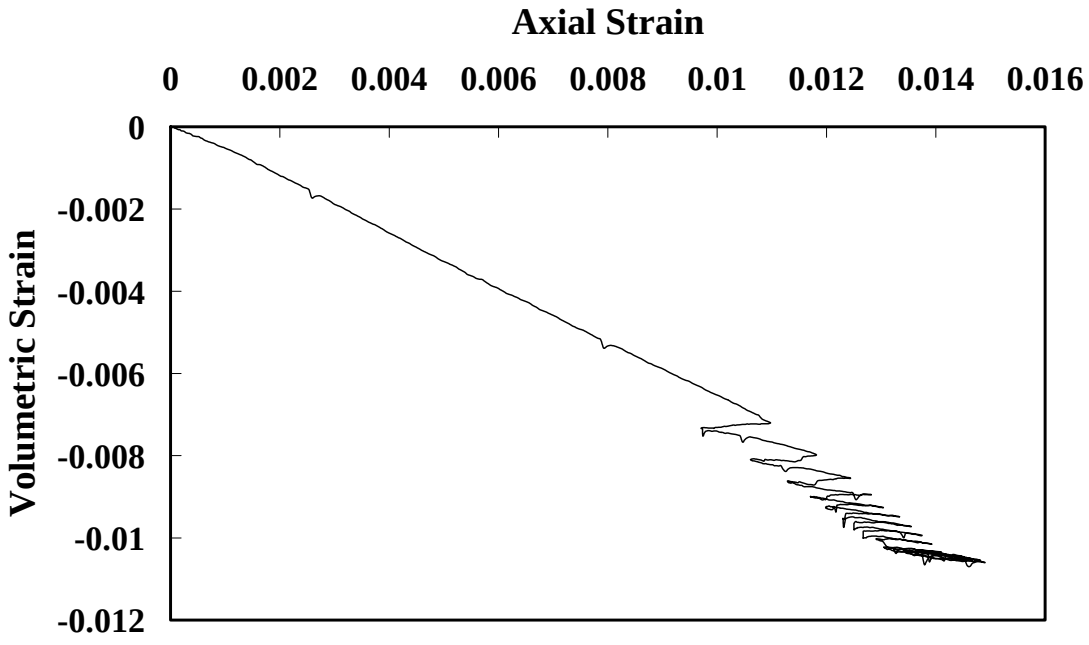

Figure B.8 Axial Strain versus Volumetric Strain (S80HD)

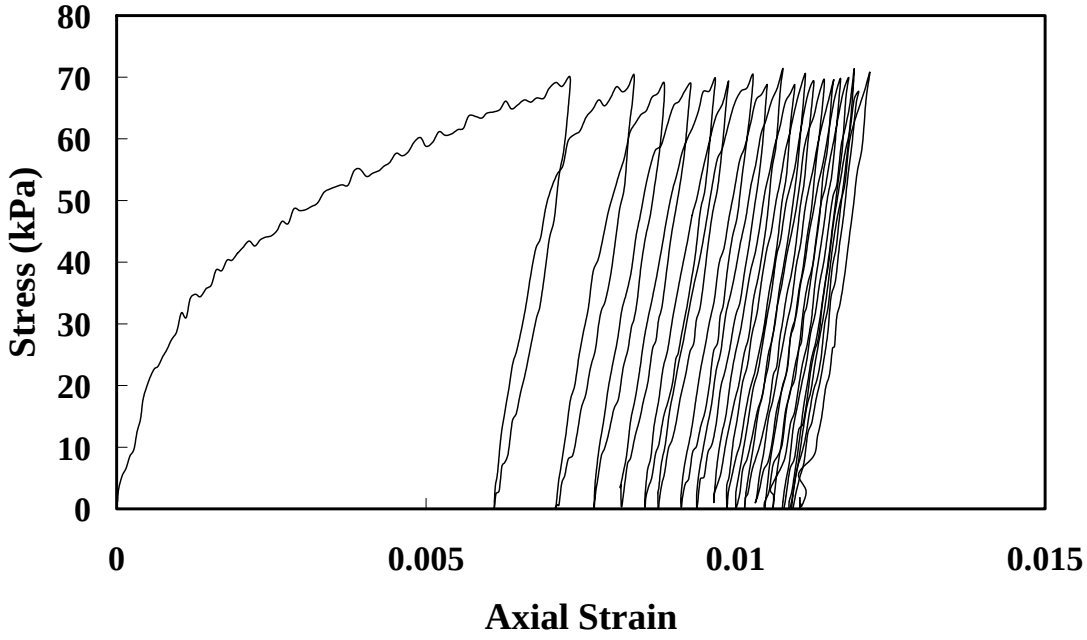

Figure B.9 Stress Strain Response (S40LN)

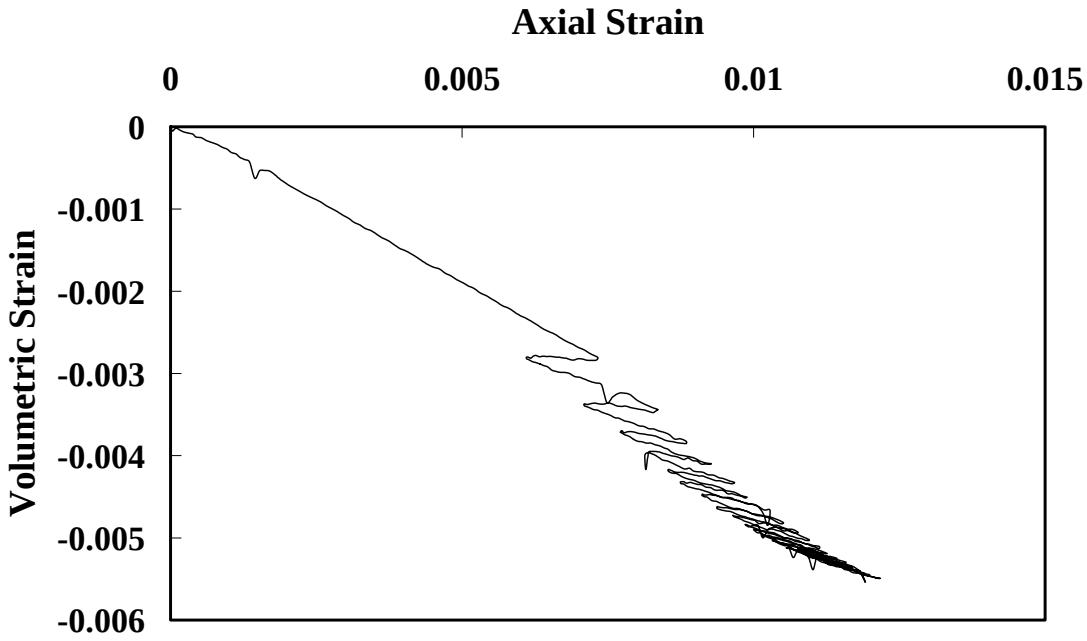

Figure B.10 Axial Strain versus Volumetric Strain (S40LN)

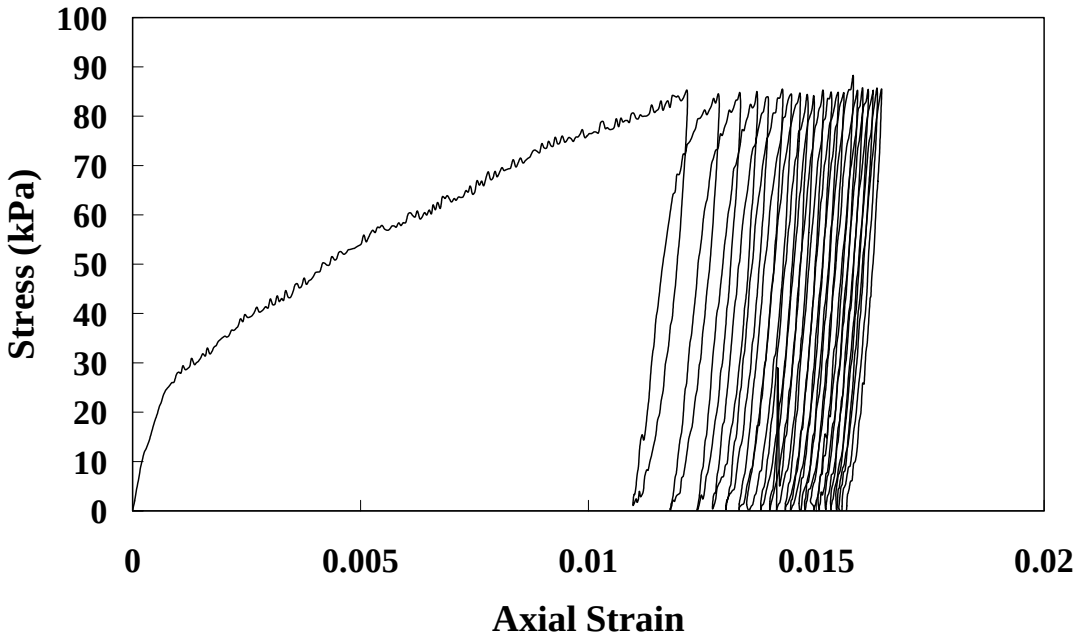

Figure B.11 Stress Strain Response (S40HN)

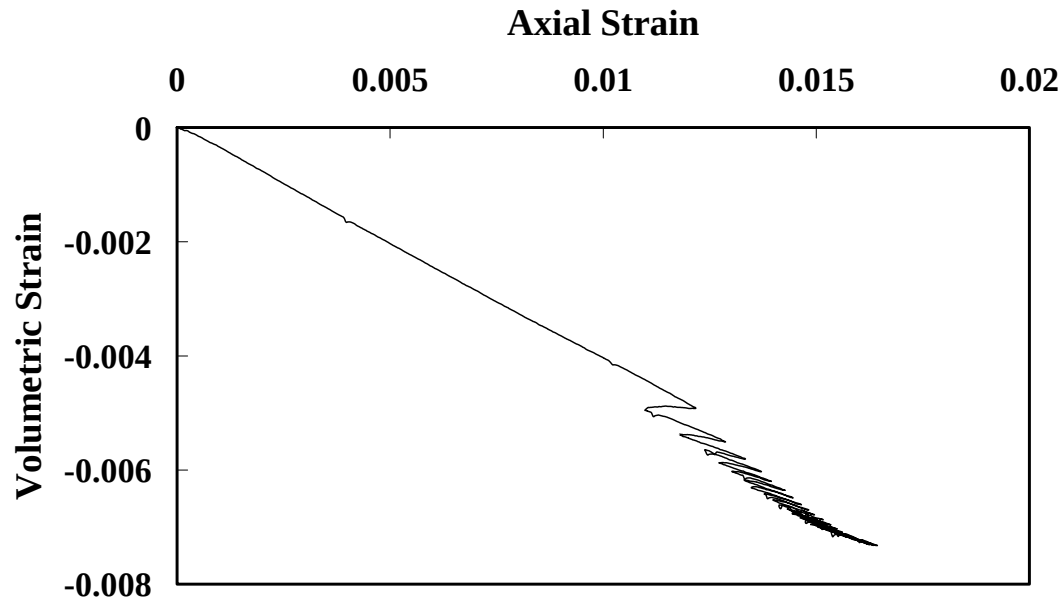

Figure B.12 Axial Strain versus Volumetric Strain (S40HN)

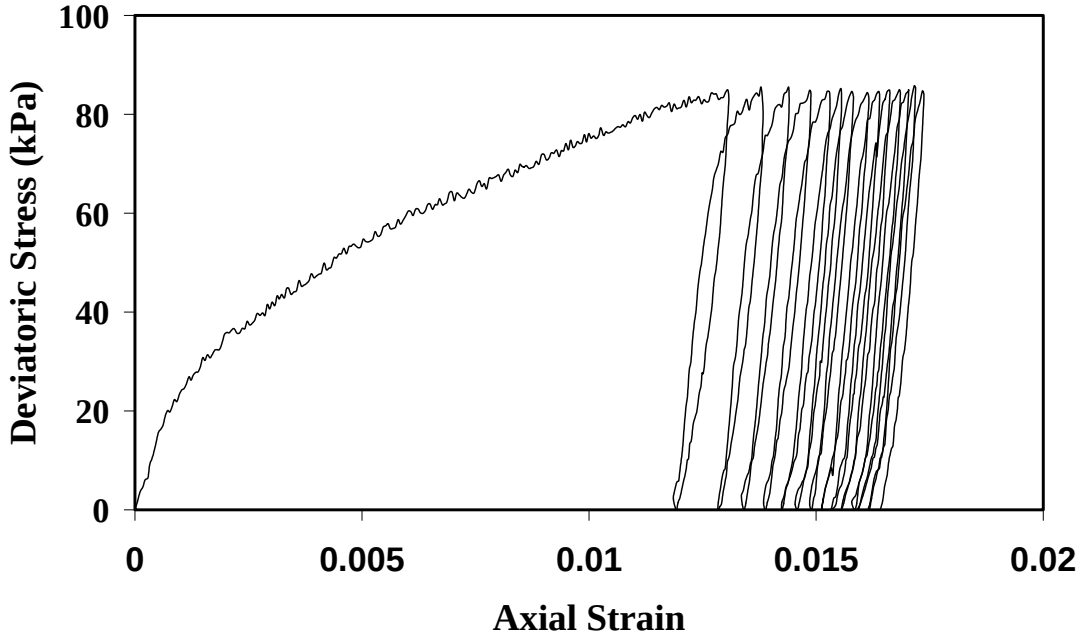

Figure B.13 Stress Strain Response (S40HA)

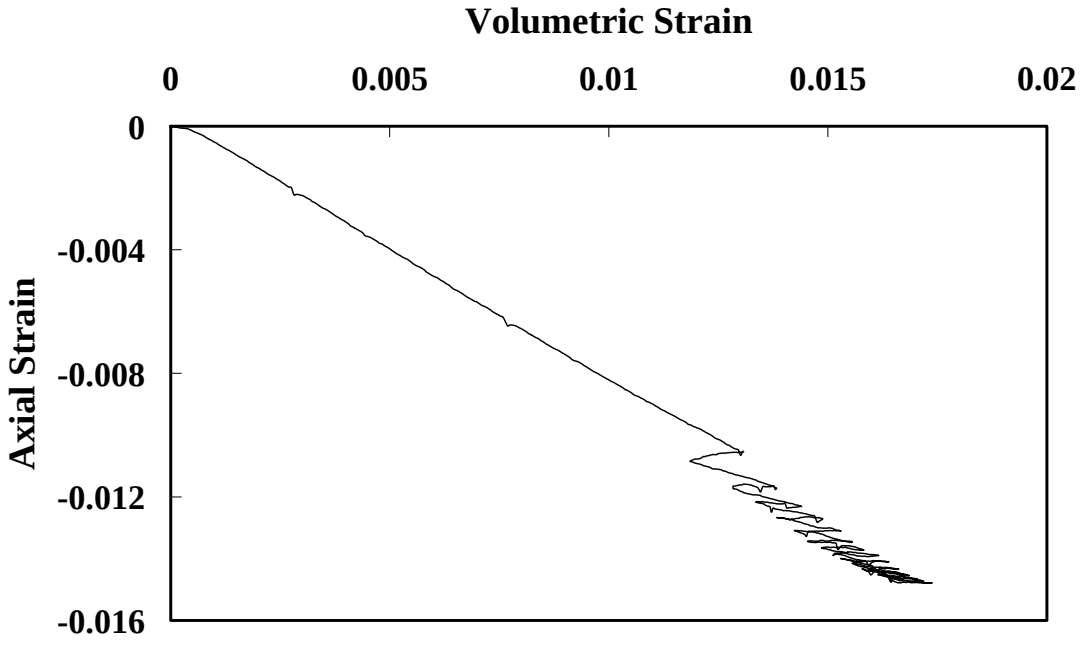

Figure B.14 Axial Strain versus Volumetric Strain (S40HA)

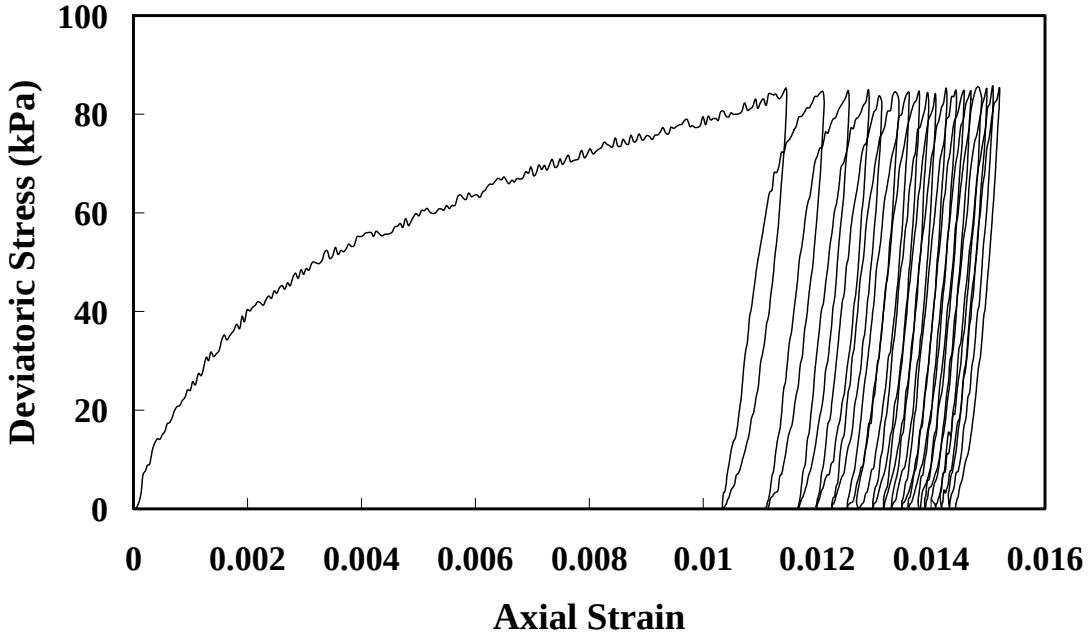

Figure B.15 Stress Strain Response (S80HA)

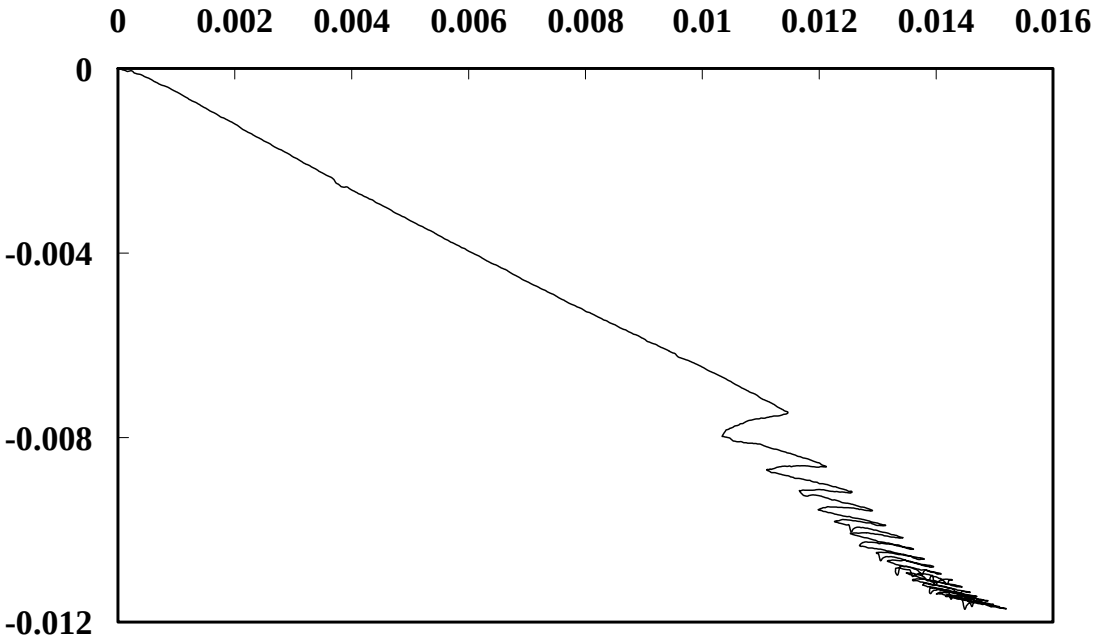

Figure B.16 Axial Strain versus Volumetric Strain (S80HA)

VITA

Byoung-Jae Mun was born on February 23, 1971 in Korea. He enrolled at Chung-Ang University, in Seoul, South Korea, where he received a bachelor of engineering in civil engineering in 1998. Between 1991-1993 he served his country in the Korean Army. In the fall of 1998, he came to America and enrolled at Texas A&M University. He received a masters degree in civil engineering in 2000. During his masters degree plan, he worked under the supervision of Dr. Briaud for a Vertically Earth Reenforced Technology Wall (VERT Wall) project. The following semester he decided to continue his education and he enrolled in the Ph.D. program at Texas A&M University. From June 2001 to December 2004, he worked as a research assistant in the Civil Engineering Department at Texas A&M University. Under the supervision of Dr. Robert L. Lytton, he performed research on unsaturated soil behavior under monotonic and cyclic stress states. He received his Ph.D. in December 2004. He is interested in unsaturated soil model, foundation designs and dynamic problems.

His permanent mailing address is:

61-15 Bonggok Dong, Chang-Won

Kyung-Nam, 641-270, South Korea